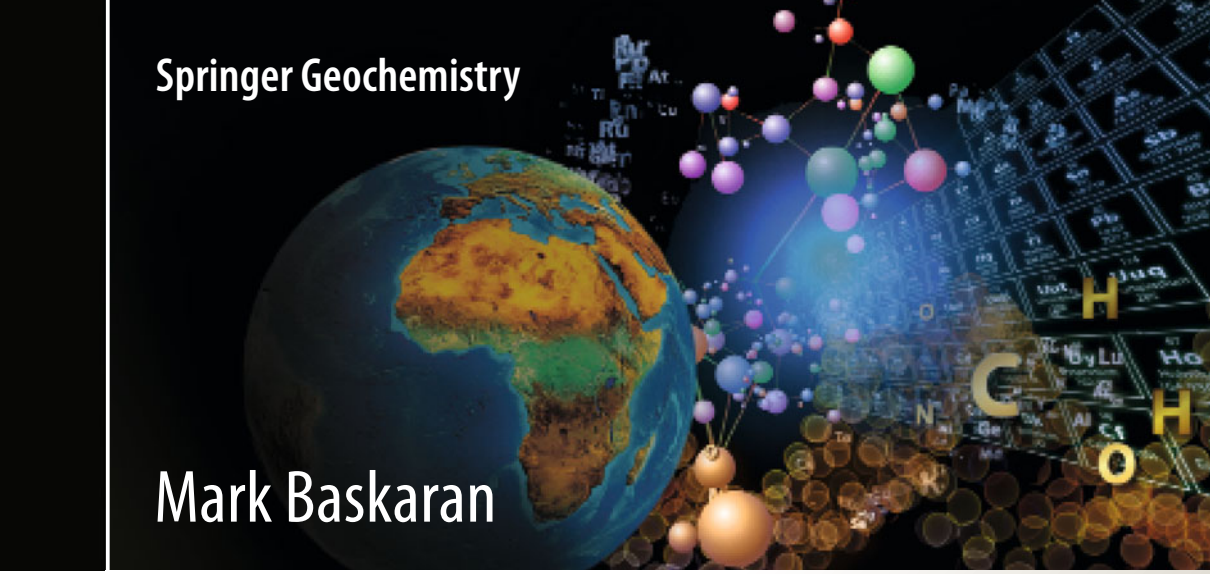Mark Baskaran

Radon: A Tracer for Geological, Geophysical and Geochemical Studies

Springer

Springer Geochemistry

More information about this series at http://www.springer.com/series/13486

Mark Baskaran

Radon: A Tracer for Geological, Geophysical and Geochemical Studies

Mark Baskaran
Wayne State University
Detroit, MI
USA

To my beloved children:
Angelin, Justin and Gracelin
who always motivated me to work harder
and to carry on a passion for learning
for the generations to come

Foreword

A volume covering many roles of radon in the environment is a welcome addition to the geochemical literature. Radon is the maverick element of the noble gas clan. While there are shared familial characteristics, radon is governed by its own rules. It retains no memory of its history beyond a few times the meager half-lives of its natural isotopes, of a few days for ^{222}Rn and under a minute for the more fleeting ^{219}Rn and ^{220}Rn. These have concentrations that are typically maintained by their parent Ra isotopes, whose concentrations are in turn subservient to those of their U and Th progenitors. Radon will sometimes set off from the support of parental secular equilibrium, but this unsupported break is always short-lived. A radon atom can be set free from a solid when brought into existence during the decay that produces it along with a ^{4}He atom sibling, though these recoil from one another at birth, a violent process that projects them in opposite directions, sometimes right out of the solid. It is the subsequent travel that provides the opportunities for using Rn isotopes as a geochemical and geophysical tool, since the rate of decay of these liberated atoms provides a clock on their travel away from the site of production. The modes of transport reflect the chemical group trademarks. As a gas, it will prefer to be in the more mobile volatile, rather than liquid, phase. Being noble, it also generally disdains chemical interactions that can complicate travel. Consequently, radon escaping from minerals can be followed in groundwaters, into surface waters, and into the atmosphere, and following its path is how evidence is collected about radon sources and the flow of transporting waters and gases.

Professor Baskaran has made many valuable contributions to the field of U-series nuclides, and here he has assembled a systematic and comprehensive survey of the behaviour of radon in the environment. Of course, the factors that control harmful human exposure to radon have been extensively studied and reviewed elsewhere, but here the broader environmental occurrences of Rn are on display together. Those with interests in such disparate fields as hydrology, atmospheric processes, and geochemical exploration will discover the unique

insights that can be provided by radon and related short-lived nuclides. These will continue to constitute an essential part of the isotope geochemist's toolkit. This volume will serve both as a reference handbook and as an inspiration to new investigations for professionals as well as graduate students.

Don Porcelli
Department of Earth Sciences, Oxford University

Preface

Radon is the heaviest of all naturally occurring noble gases and it has a total of 36 isotopes, all of which are radioactive (ranging from ^{193}Rn to ^{228}Rn). Only three of these isotopes occur naturally and are constantly produced at a known rate in the ^{238}U-(^{222}Rn, radon), ^{235}U-(^{219}Rn, also known as actinon), and ^{232}Th-(^{220}Rn, also known as thoron) series. Radon has received the most attention among all the noble gases over the last four decades, largely due to the fact that it is the single major contributor to the ionizing radiation dose received by the general population. Radon is the second most frequent cause of lung cancer after smoking, and is classified as a human carcinogen. While the noble gas applications extend from cosmochemistry to different branches of geoscience, applications of radon are generally confined to near-surface Earth processes, due to its short mean life (5.53 days). Note that the presence of mantle ^{3}He in the oceans is indicative of diffusion of helium from much deeper sources inside the Earth, but sources of radon to Earth systems is much more confined to shallower depths. Most review articles and books such as *Noble Gases* by Minoru Ozima and Frank Podosek and the articles in the edited volume *Noble Gases in Geochemistry and Cosmochemistry* by Don Porcelli, Chris Ballentine and R. Wieler in Reviews in Mineralogy and Geochemistry serve as key reference works for the researchers working in noble gas geochemistry, but most of these publications have discounted the utility of radon as a tool to investigate several Earth surface processes. The sensitivity of radon measurement is the highest among all noble gases. In terms of molar concentration, 1 pico Curie (pCi) can be easily measured (1pCi of ^{222}Rn activity contains 1.76×10^4 atoms which corresponds to 2.9×10^{-20} mole of radon). While there are a large number of scientific reports from national and international agencies (e.g., US Environmental Protection Agency, US National Academy of Science, World Health Organization) that describe findings on indoor radon in peer-reviewed journal articles, and many scientific reports pertaining to indoor radon as a health hazard, there is no single book on the applications of radon as a tracer in Earth systems. This book is designed to address that deficiency.

This volume is structured to examine the current body of knowledge in regard to all major aspects of the applications of radon as an environmental tracer. Each chapter is written as a review article, providing a critical synthesis with sufficient details for those who are technically trained but not necessarily working in this or similar area of research. This book is divided into 11 chapters. Chapter 1 is concerned with the physical, chemical, and nuclear properties of radon and the relationship between radon and its progeny. Chapter 2 gives an in-depth review of existing instrumentation for the measurements of radon and its progeny in environmental samples (water, air, and soil gas). The mechanisms of radon emanation and the factors that control the variations of the radon emanation coefficient are presented in Chap. 3. Radon has a simple emanation function from the Earth's surface, and the gradient in radon concentrations in the atmosphere as a function of latitude and longitude serves as a valuable tool to quantify factors and processes in the atmosphere that redistribute the radon released from the Earth's surface (Chap. 4). Progeny of radon, in particular ^{210}Po and ^{210}Pb, have been widely utilized as tracers to quantify a number of atmospheric processes that include source tracking and transport time scale of air masses, residence time and removal rate constant of aerosols and flux to and exchange between environmental systems of other gas species such as CH_4 and Hg^0 (Chap. 5). Radon concentration gradients at key interfaces such as sediment–water and air–water in aqueous systems (oceans, rivers, and lakes) have been utilized to determine exchange rates of gases across these interfaces (Chap. 6). The most widely used chronometer among the U-Th-series radionuclides is ^{210}Pb, which is a progeny of radon, with over 2,300 published articles over the past four decades. Its utility as a tracer and chronometer is presented in Chap. 7. Radon has a high solubility in organic liquids, similar to other noble gases, and hence its usefulness as a tracer for investigating the partitioning of radon between organic solvents and groundwater along with its application in quantifying infiltration of meteoric water and as a dating tool (in conjunction with ^{4}He) are given in Chap. 8. Radon as a tracer in geochemical exploration studies are presented in Chap. 9. In earthquake studies, radon is widely used as a precursor to predict earthquakes and several case studies are presented in Chap. 10. Finally, in Chap. 11, a summary of factors that affect radon entry indoor and potential techniques for radon entry prevention and mitigation are summarized. At the end of each chapter, future research direction is also included.

This book will prove to be a valuable resource for researchers in atmospheric science, marine and environmental sciences, earthquake studies, geochemical exploration studies (including uranium and hydrocarbon), organic pollutant studies in groundwater, noble gas geochemistry, and radon as a health hazard. Sections of the book are expected to be useful as a supplementary text to a number of graduate courses that include Environmental Isotope Geochemistry, Geochronology and Tracer Studies in Groundwater, Atmosphere and Ocean system.

Detroit, USA   Mark Baskaran
July 2016

Acknowledgments

Contents

About the Author

Dr. Mark Baskaran is a tenured Full Professor in the Department of Geology at Wayne State University (Detroit, Michigan). He received his Ph.D. in Physics from Physical Research Laboratory (PRL), a premier research institution in India. After his Ph.D., he spent 2 years at PRL as a postdoctoral fellow before he moved to the Institute of Marine Science at the University of Alaska (Fairbanks, Alaska). After a year, he joined Texas A&M University (Galveston, Texas) where he taught introductory Physics and Geology courses at the Department of Marine Sciences, while conducting research related to atmospheric fluxes of radionuclides, mobility of radionuclides in groundwater, scavenging and particle cycling in marine environment and dating of recent sediments and carbonates. After his eleven-year career as a teacher and a researcher in Texas, he joined Wayne State University where he became a tenured Full Professor in 2007. He teaches both introductory level courses in Oceanography, Meteorology, and Physical Geology as well as upper level courses including Chemical Fate and Transport in the Environment, Nuclear Geology, and Environmental Geochemistry.

Professor Mark Baskaran has published over 130 peer-reviewed articles (with over 5,300 Google Scholar cumulative citations, h-index 43 in July 2016), most of which are related to the applications of isotopes as tracers and chronometers in Earth systems. He edited a two-volume Handbook entitled *Handbook of Environmental Isotope Geochemistry* with 40 articles contributed by eminent scholars in the field in 2011, published by Springer. He spent 3 months as a Senior *Fulbright Scholar* at Ege University (Izmir, Turkey) in 2015. He has given invited and plenary talks/seminars at over 60 national/international conferences, workshops, universities, and research institutions around the world.

Dr. Baskaran's research work includes all subsystems of the Earth system. Most of his work involved collaboration with a large number of researchers from universities and institutions around the world. His work with marine systems (estuarine, coastal, shelf and open-ocean) on the investigations of particular organic carbon export, particle cycling and remineralization, and colloidal thorium scavenging in the Arctic Ocean, Gulf of Mexico, North Atlantic, and East Pacific were funded by several funding agencies in the U.S. that include the National Science

Foundation (NSF), National Oceanic and Atmospheric Administration (NOAA), and the Department of Energy (DOE). His currently funded ongoing research is to investigate sedimentation and sediment dynamics in dams and other freshwater systems. He has been funded by NSF as a part of the U.S. GEOTRACES group in all four phases so far (Intercalibration, North Atlantic, East Pacific, and Western Arctic Ocean sections). He has served as a Chief Scientist in six major oceanographic expeditions in the Gulf of Mexico and Arctic Ocean.

He convened a National Workshop entitled *Recent Changes in the Biogeochemistry of the Great Lakes System* in March 2013 at Wayne State University. He also had convened a number of sessions and meetings at both national and international conferences and workshops.

Dr. Baskaran currently resides in Troy, Michigan with his wife (of 33 years) Inthumathi Baskaran. He has three grown-up children.

Chapter 1
Physical, Chemical and Nuclear Properties of Radon: An Introduction

1.1 Discovery of Radon

Radon is the heaviest of all noble gases, a class of chemically inert gases with low reactivity, and has a total of 36 isotopes ranging from ^{193}Rn to ^{228}Rn. All of the isotopes are radioactive, with three isotopes that are constantly produced from the ^{238}U (^{222}Rn), ^{235}U (^{219}Rn, also known as actinon, derived from its grandparent, ^{227}Ac) and ^{232}Th (^{220}Rn, also known as thoron, derived eventually from ^{232}Th). Only four of 36 radon isotopes have half-lives greater than 1 h. Radon was the last noble gas to be discovered by Friedrich Ernest Dorn, a German scientist in 1898, after the discoveries of four other radionuclides, uranium (U), thorium (Th), radium (Ra) and polonium (Po) by others. The first paper reporting the release of radioactive gas from the decay of radium was published in 1900 (Dorn 1900). One year prior to this publication, Rutherford placed thorium oxide inside a lead box and observed that the rate of leakage of the gold-leaf electroscope was much slower when the door was opened compared to when the door was closed. Based on this result, he concluded that thorium compounds continuously emit radioactive particles which retain their radioactive powers for several minutes and these results were published in 1900 (Rutherford 1900). At around this time, Pierre and Marie Pierre observed that the gas emitted from radium remained radioactive for a month, giving some indication on the half-life of ^{222}Rn (Curie and Curie 1899).

Radon belongs to group 18 (noble gases, p-block and period 6; [Xe] $4f^{14}$ $5d^{10}$ $6s^2$ $6p^2$) in the periodic table. Although noble gases are chemically inert, the interactions of these gases with other species are weaker (comparable to van der Waals type, with energy of bonding on the order of 1–3 eV, compared to ionic and

---

Throughout the book, three terms are synonymously used to represent the concentration of radon in environmental samples, as done in most published literature. Those are: concentration, activity, activity concentration, and specific activity. The units are: for fluids (liquid and gas): Bq L^{-1}/Bq m^{-3} or pCi L^{-1}/pCi m^{-3}; for solids: Bq g^{-1}/Bq kg^{-1} or pCi g^{-1}/pCi kg^{-1}

Table 1.1 Mean atomic velocities (The mean velocity of a particle as a function of Temperature and mass are calculated from: $v_{mean} = (8KT/\pi m)^{1/2}$ where K is Boltzmann constant (1.3806×10^{-23} m^2 kg^{-1} s^{-2} K^{-1}), m is mass in kg, and T is temperature (absolute temperature scale)) at mean global temperature of 14 °C

Isotope	Velocity (m/s)
H	2,456
He	1,232
Ne	549
Ar	390
Kr	269
Xn	215
^{222}Rn	165

covalent bonding (on the order of 3–8 eV)) and the interactions are expected to be less complicated. There is a fair amount of literature that discusses the geochemistry of noble gases other than Rn (e.g., Ozima and Podosek 2002; Porcelli et al. 2002); however, data on the geochemistry of radon is limited. The three radon isotopes in the ^{238}U–^{235}U–^{232}Th series are commonly found in the environment. The molar abundance of these radon isotopes are the lowest among all the other noble gases, but there are several techniques available to measure such low abundance with counting instruments (Chap. 2). The geochemical factors that determine the distribution are similar to those of other noble gases and hence analogies with other noble gases are relevant to the discussion.

The average atomic or molecular velocities of noble gases for the average surface temperature on earth (14 °C or 287 °K) for radon and other noble gases are given in Table 1.1. The mean atomic velocity of radon, 165 m s^{-1}, is significantly lower than other noble gases, as expected.

1.2   Properties of Radon

1.2.1   Chemical Property

The atoms of radon and other noble gases have a closed-shell electronic structure and are extremely stable, as the ionization enthalpies are high. There are no ordinary electron-pair interactions among the noble gas atoms. The weak forces (van der Waals type or London type) are proportional to the polarizability and inversely proportional to the ionization of enthalpies of the atoms (Cotton et al. 1988). The first ionization energy (the energy needed to remove one electron from the outermost filled shell) for radon is 1,037 kJ/mol and it increases with decreasing atomic number for the other noble gases (Fig. 1.1a). The electronegativity in a column on the periodic table decreases with increasing atomic number and hence radon has a lower electronegativity (electronegativity = 2.2 Pauling scale, Table 1.2) compared

Fig. 1.1a First ionization energy (energy required to remove the most loosely held electron from one mole of noble gas ions each with a charge of +1) versus atomic number (data taken from Cotton et al. 1988)
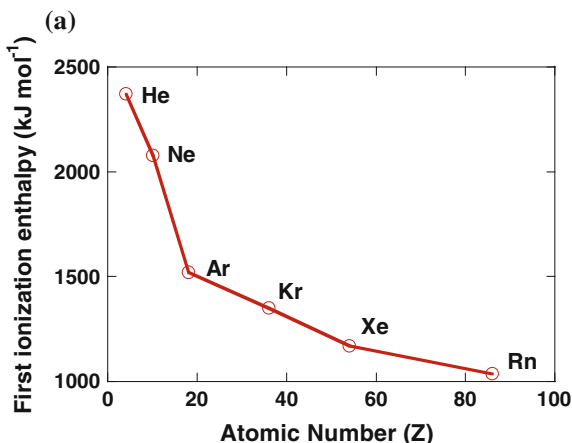
Fig. 1.1b Increase of heat vaporization with increase of the atomic number of noble gases—heat vaporization is the energy needed to overcome interatomic attractive forces (data taken from Cotton et al. 1988)
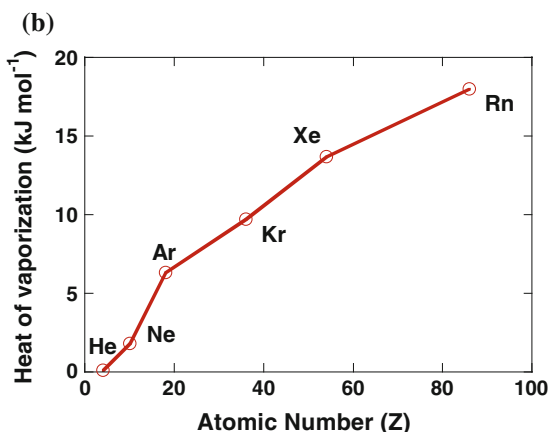
to the element one period before it, xenon (electronegativity = 2.60 Pauling scale) and thus radon is relatively more reactive than xenon. The solubility in a column also increases with increasing atomic number and hence radon is more soluble than xenon. Radon is also more soluble in organic liquids than in water. The heat of vaporization (measure of the work that must be done to overcome atomic attractive forces) also increases with atomic number (Fig. 1.1b).

Radon lies on the diagonal of the periodic table between the metals and non-metals and exhibits some of the characteristics of both groups, hence, it was suggested that radon can be classified as a metalloid element, along with boron, silicon, germanium, arsenic, antimony, tellurium, polonium and astatine (Stein 1987). Radon has been shown to react spontaneously at 25 °C or lower temperatures with fluorine, halogen fluorides (except IF_5) and a number of oxidizing salts (Stein 1987). Although there is no evidence for the existence of radon compounds or ions in aqueous solutions, solutions of cationic radon has been prepared in nonaqueous

Table 1.2 Atomic, physical and chemical properties of Radon

Property	Values
Atomic number	86
Standard atomic weight	222
Outer shell electron configuration	$6s^2 6p^6$
Density	9.73 kg m^{-3} (at 0 °C, 1.013×10^5 Pa)
Melting point (°K)	202
Normal boiling point (°K)	208.2
Heat of fusion (kJ mol^{-1})	3.247
Heat of vaporization (kJ mol^{-1})	18.0
First ionization enthalpy (kJ mol^{-1})	1037
Oxidation states	0, 2, 6
Electronegativity	2.2 (Pauling scale)
Covalent radius (nm)	0.150
van der Waals radius (nm)	0.220

Table 1.3 Nuclear and physical properties for ^{222}Rn, ^{220}Rn and ^{219}Rn

Parameter	Symbol	^{222}Rn	^{220}Rn	^{219}Rn
Half-life	$T_{1/2}$	3.823 d	55.83 s	3.983 s
Decay constant	λ	2.098×10^{-6} s^{-1}	1.242×10^{-2} s^{-1}	0.174 s^{-1}
Average recoil energy on formation	E_r	86 keV	103 keV	104 keV
Diffusion coefficient in air	D_a	1×10^{-5} m^2 s^{-1}	–	–
Diffusion coffficient in water	D_w	1×10^{-9} m^2 s^{-1}	–	–

solvents, such as hydrogen fluoride and halogen fluorides (Stein 1970, 1984). From a comparison of the known properties of krypton and xenon fluorides with that of radon, it has been deduced that radon forms a difluoride, RnF_2, and derivatives of the difluoride, such as $RnF^+SbF_6^-$, $RnF^+TaF_6^-$ and $RnF^+BiF_6^-$. Similar to KrF_2 and XeF_2, RnF_2 is reduced to elemental radon by water (implying that radon exists in +2 oxidation state in RnF_2 and is reduced to elemental Rn (0 oxidation number)):

$$RnF_2 + H_2O \rightarrow Rn + 1/2\,O_2 + 2HF \tag{1.1}$$
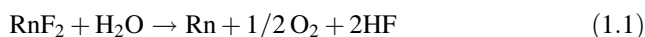
When heated to 400 °C with elemental fluorine, non-volatile radon difluoride is formed:

$$Rn + F_2 \xrightarrow[400\,°C]{} RnF_2 \tag{1.2}$$

When Rn exists in an ionic state, it is able to displace ions of the first group elements (H^+, Na^+, K^+, Cs^+) and some of the second group elements (Ca^{2+}, Ba^{2+}). Quantitative removal of radon has been observed on a column packed with either

Nafion resins or complex salts. The distribution coefficient of cationic radon, K_d, in dilute BrF_3—trichlorotrifluoroethane solution was found to range from $\sim$90 to 4000 L/kg (Stein 1987). The degree of partitioning of radon is a function of the radon partition coefficient between water and air, amounting to $K_{W/Air}$ = 0.2395 at room temperature (296 °K) (Clever 1979). Wong et al. (1992) reported organic-carbon normalized sediment-water partition coefficient values of 21–25 on a suite of sediments from Boston Harbor, Charles River and Buzzards Bay in the United States. The octanol-water partition coefficient (K_{OW}) for radon is given as (Wong et al. 1992):

$$K_{OW} \text{ of } {}^{222}Rn = 32.4 \pm 1.5 \quad (@20\,°C) \tag{1.3}$$

1.2.2 Sorption Behavior of Radon

The general (and expected) chemical sorption behavior of ${}^{222}Rn$ is that it is inert and does not react with other elements or often with compounds. It was assumed that radon did not interact with the surfaces of soil grains. Schery and Whittlestone (1989) reported isolated sorption of radon on to soil and rock grains under certain cases. However, due to the pervasiveness of moisture in moist climate, the contribution from desorption is likely limited compared to other major mechanisms of release of radon to the atmospheric air over much of the Earth's surface. From a comparison of the environmental conditions that exist on the moon with that on the earth's surface, Tanner (1980) concluded that for the dry, low-pressure environment of lunar rocks, sorption seems to be important, but the evidence for significant sorption at temperatures and humidity common at the earth's surface is conflicting.

1.2.3 Partitioning of Radon Between Gas and Aqueous Phases

As radon is a gas, its equilibrium partitioning between the gas and aqueous phases can be described by Henry's law, which is expressed as:

$$C_w = K\,C_a \tag{1.4}$$

where C_a represents radon concentration in the gas phase (Bq per m^3 of pore air), C_w is radon concentration in water (Bq per m^3 of water) and K is the dimensional partition coefficient, which is a function of temperature. The reported partition coefficient for radon between distilled water and air are 0.245 at 20 °C and 0.193 at 31.6 °C (Boyle 1911; Nazaroff 1992).

1.2.4 Physical Properties of Radon

The physical parameters of radon are summarized in Table 1.2. Atomic, physical and chemical properties of radon including density, melting point, heat of fusion, heat of vaporization, oxidation states, electronegativity and first ionization potential (energy needed to remove the outermost (highest energy) electron from a neutral atom in the gaseous state) are given in Table 1.2. The ionization potential of radon is also compared with other noble gases (Table 1.4).

Table 1.4 Comparison of atomic radius and ionization potential in all noble gases

Isotope	Atomic wt.	Atomic radius (Å)	Ionization potential
Rn	222	–	–
Xe	131.29	2.2	12.13
Kr	83.80	2.0	14.00
Ar	39.948	1.9	15.76
Ne	20.1797	1.6	21.56
He	4.002602	1.8	24.59

NM Not measured

Table 1.5 SI units and equivalents for traditional units

Parameter, SI unit	Conversion
Activity, Bq	1 Curie (Ci) = 3.7×10^{10} Bq
1 pico curie (pCi)	2.22 disintegration per minute, dpm
1 Bq	60 dpm (disintegrations per minute) or 1 disintegration per second, 1 dps
Concentration (Bq m^{-3})	1 pCi = 37 Bq m^{-3}
1 Potential alpha-energy concentration (PAEC, J m^{-3})	1 Working level (WL)[a] = 1.3×10^5 meV/L = 2.08×10^{-5} J m^{-3}
Equilibrium-equivalent decay product concentration (EEDC) for ^{222}Rn (Bq m^{-3})	1 Working level (PAEC) = 3,740 Bq m^{-3}
Exposure (J m^{-3} s)	1 Working level month (WLM) = 12.97 J m^{-3} s
Exposure (Bq m^{-3} y)	1 WLM = 73.9 Bq m^{-3} y^{-1}
Exposure rate (J m^{-3})	1 WLM/y = 4.11×10^{-7} J m^{-3}
Exposure rate (Bq m^{-3})	1 WLM/y = 73.9 Bq m^{-3}

The conversion factors for PAEC, EEDC, Exposure and Exposure rate are from Nero (1992f)
[a]In studies of radon-exposed miners radon progeny concentrations are generally expressed in terms of 'working levels' (WL). The working level is defined as any combination of the short-lived progeny in one liter of air that results in the ultimate release of 1.3×10^5 meV of alpha particle energy

1.2.5 Diffusion of Radon

From the published literature on radon transport, it is now established that transport of radon from soil to the atmosphere occurs predominantly by molecular diffusion (Schery et al. 1984; Nazaroff 1992). The activity flux density (J^d, Bq m^{-2} s^{-1}) resulting from random molecular motion is described by Fick's law which states that the radon flux density is linearly proportional to its concentration gradient:

$$J^d = -D_m \nabla C \qquad (1.5)$$

where D_m is the molecular diffusion coefficient (m^2 s^{-1}) and ∇C is the gradient of radon activity concentration (Bq m^{-3}/m). The negative sign is to indicate that radon diffuses from higher to lower concentrations. The molecular diffusion coefficients in air (D_{ma}) and water (D_{mw}) are approximately 1×10^{-5} and 1×10^{-9} m^2 s^{-1}, respectively (Table 1.3).

The rate of radon movement in soil is expected to be slow compared to its movement in a homogenous medium such as pure air for two reasons: (i) the tortuous flow path around particles (tortuosity = τ) and (ii) relatively smaller fluid volume (porosity = n). Taking these two factors into consideration, the bulk radon flux density is given by:

$$J^d = -n_s \tau D_m \nabla C \qquad (1.6)$$

where n_s is the porosity of the soil. Tortuosity (τ) is unity for a pure solution and is generally less than unity in soils. It was found to be 0.66 for closely packed uniform spheres. The terms D_m and τ are lumped together and are collectively known as the diffusion coefficient of the pore fluid such that

$$D = \tau D_m \qquad (1.7)$$

Substituting for D from Eq. (1.7) in (1.6),

$$J^d = -n_s D \nabla C \qquad (1.8)$$

The product of porosity and D can be represented by the notation D_e, the effective bulk diffusion coefficient of the soil. Note that D is directly related to the diffusion length of radon in the matrix and is a more fundamental parameter.

Radon diffusion coefficients in soil depend on the position of the ^{222}Rn location, which generally depends on the soil type, pore size distribution, water content and porosity. Since the molecular diffusion coefficient in air and water differ by a factor of 10^4, moisture effects dominate over other physical factors in the mobility of radon in soil. Earlier studies have shown that diffusion of radon is severely affected when soil moisture exceeds a certain threshold, which depends on the geometry of the soil pore space (Ishimori et al. 2013). The effective diffusion coefficient for radon in soil, comprised of mail tailings, silty sandy clay, compacted silt sands,

clayey sands, compacted inorganic clays, varved clays, mud, loams and alluvial-detrital deposits of granite, has been reported to vary between 2.2×10^{-10} m^2 s^{-1} (mud with 85 % water content) and 7.2×10^{-6} m^2 s^{-1} (mill tailings) (Nazaroff et al. 1992).

1.3 Decay Products of ^{222}Rn

Being an intermediate radioactive decay product in the ^{238}U (^{222}Rn), ^{235}U (^{219}Rn) and ^{232}Th (^{220}Rn) decay chain, radon undergoes radioactive decay (Fig. 1.2). The aggregate mean life of the daughter products of ^{222}Rn (^{218}Po, ^{214}Pb, ^{214}Bi, ^{214}Po) is 71.57 min while the corresponding aggregate mean-lives of the ^{220}Rn (^{216}Po, ^{212}Pb, ^{212}Bi, ^{212}Po) and ^{219}Rn (^{215}Po, ^{211}Pb, ^{211}Bi, ^{207}Tl) are 16.81 h and 1.03 h, respectively. The ^{238}U, ^{235}U and ^{232}Th series with the half-lives, decay mode, energy of emission (alpha, decay and gamma) and yield of the nuclear decay are given in Tables 1.6a, 1.6b and 1.6c.

Within a decay series, the evolution of the abundance of a daughter radioactive isotope is dependent upon its decay rate as well as production from its radioactive parent. Since the abundance of the parent is in turn dependent upon that of its parent, and so on up the decay chain, the systematics can become complicated, although for most applications simplifying circumstances can be found. The evolution of the abundances of isotopes within a decay series is described by the Bateman equations (Porcelli and Baskaran 2011). For a decay series starting from the long-lived parent N_1 and ending with a stable isotope S,

$$N_1 \rightarrow N_2 \rightarrow N_3 \rightarrow N_4 \rightarrow \ldots S \tag{1.9}$$
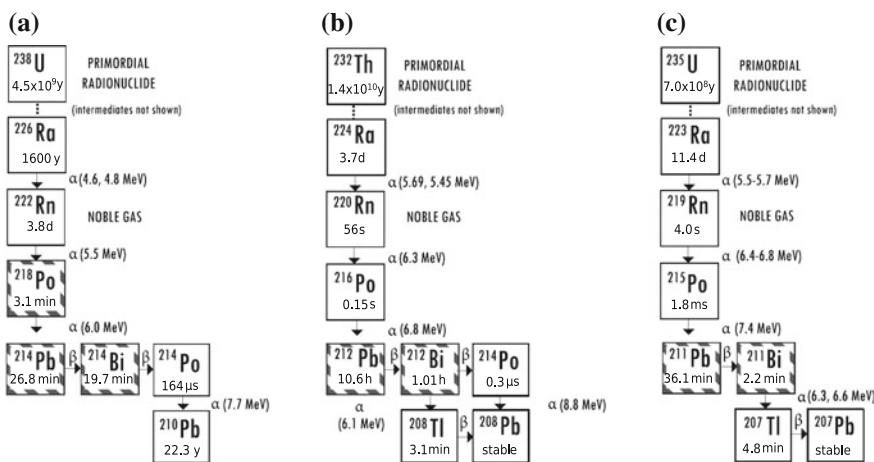
Fig. 1.2 ^{238}U, ^{232}Th and ^{235}U decay chains

Table 1.6a ^{238}U Decay Series—from ^{226}Ra (data taken from Firestone and Shirley 1999)

Isotope	Half-life	Decay	Emission energy (MeV)[a]	Yield (%)
^{226}Ra	1.6×10^3 a	α	4.784 (α_0)	94.55
–	–	–	4.601 (α_1)	5.45
–	–	γ	0.186	3.51
^{222}Rn	3.82 d	α	5.489 (α_0)	$\sim$100
^{218}Po	3.10 min	α	6.002 (α_0)	$\sim$100
^{214}Pb	26.8 min	β^-	1.023 (β_0)	$\sim$100
–	–	γ	0.3519	35.9
–	–	γ	0.2952	18.5
–	–	γ	0.2420	7.5
^{214}Bi	19.7 min	α	5.621 (α_0)	0.021
–	–	β^-	3.272	$\sim$100
–	–	γ	0.609	46.1
–	–	–	1.120	15.0
–	–	–	1.764	15.9
^{214}Po	164 μs	α	7.687 (α_0)	$\sim$100
^{210}Pb	22.3 y	β^-	0.0635 (β_0)	16
–	–	γ	0.0465	4.25
^{210}Bi	5.013 d	β^-	1.163 (β_0)	100
^{210}Po	138.38 d	α	5.304 (α_0)	100
^{206}Pb	Stable	–	–	–

[a]Energies of beta decay are maxima

Table 1.6b   Isotopes of the ^{235}U Decay Series (from ^{223}Ra)—data taken from Firestone and Shirley (1999)

Isotope	Half-life	Decay	Emission energy (MeV)[a]	Yield (%)
^{223}Ra	11.435 d	α	5.539-5.747	96.8
–	–	γ	0.2695	13.7
^{219}Rn	3.96 s	α	6.819 (α_0)	79.4
–	–	–	6.553 (α_1)	12.9
–	–	–	6.425 (α_2)	7.6
^{215}Po	1.78 ms	α	7.386 (α_0)	100
^{211}Pb	36.1 min	β^-	1.373	100
^{211}Bi	2.14 min	α (99.72 %)	6.623	83.8
–	–	–	6.278	16.2
–	–	β^- (0.28 %)	0.579	100
–	–	γ	0.351	13.0
^{207}Tl	4.77 min	β^-	1..423	100
^{207}Pb	Stable	–	–	–

[a]Energies of beta decay are maxima

Table 1.6c Isotopes of the ^{232}Th Decay Series (from ^{224}Ra)—data taken from Firestone and Shirley (1999)

Isotope	Half-life	Decay	Emission energy (MeV)[a]	Yield (%)
^{224}Ra	3.66 d	α	5.685 (α_0)	94.9
–	–	–	5.449 (α_1)	5.1
–	–	γ	0.2410	3.97
^{220}Rn	55.6 s	α	6.288 (α_0)	99.89
–	–	–	5.747 (α_1)	0.11
^{216}Po	0.145 s	α	6.778 (α_0)	∼100
^{212}Pb	10.64 h	β$^-$	0.574	100
–	–	γ	0.2386	43.3
–	–	–	0.3001	3.28
^{212}Bi	60.55	α (35.94 %)	6.051	69.9
–	–	–	6.090	27.1
–	–	β$^-$	2.254	100
–	–	γ	–	–
^{212}Po	0.299 μs	α	8.784 (α_0)	100
^{208}Tl	3.05 min	β$^-$	1.372	100
–	–	γ	0.405	3
–	–	–	0.832	2.8
^{207}Pb	Stable	–	–	–

[a]Energies of beta decay are maxima

The long-lived parent evolves according to the basic decay equation:

$$(N_1) = (N_1)_0 e^{-\lambda_1 t} \tag{1.10}$$

(N_1) is the activity, so that

$$(N_1) = \frac{dN_1}{dt} = \lambda_1 N_1 \tag{1.11}$$

The next two nuclides in the decay series evolves according to the equations

$$(N_2) = \frac{\lambda_2}{\lambda_2 - \lambda_1} (N_1)_0 \left(e^{-\lambda_1 t} - e^{-\lambda_2 t}\right) + (N_2)_0 e^{-\lambda_2 t} \tag{1.12}$$

$$(N_3) = \frac{(N_1)_0 \lambda_2 \lambda_3}{\lambda_2 - \lambda_1} \left(\frac{e^{-\lambda_1 t}}{(\lambda_2 - \lambda_1)(\lambda_3 - \lambda_1)} + \frac{e^{-\lambda_2 t}}{(\lambda_1 - \lambda_2)(\lambda_3 - \lambda_2)} + \frac{e^{-\lambda_3 t}}{(\lambda_1 - \lambda_3)(\lambda_2 - \lambda_3)}\right)$$
$$+ \frac{(N_2)_0 \lambda_3}{(\lambda_3 - \lambda_2)} \left(e^{-\lambda_2 t} - e^{-\lambda_3 t}\right) + (N_3)_0 e^{-\lambda_3 t} \tag{1.13}$$

Where λ_1, λ_2, λ_3 are the decay constants of N_1, N_2 and N_3, respectively. The equations become increasingly complex, but are rarely necessary for environmental

applications. Further, these equations can be greatly simplified under most circumstances.

i. For all environmental timescales, the abundance of the long-lived parent (N_1) of the chain is constant, and $e^{-\lambda_1 t} \approx 1$. When $\lambda_2 \gg \lambda_3$ and $\lambda_1 \gg \lambda_1$, then, $\lambda_2 - \lambda_1 \approx \lambda_2$ and $\lambda_3 - \lambda_1 \approx \lambda_3$.

ii. When a system has been closed for a long time, i.e., when $e^{-\lambda_2 t} \approx e^{-\lambda_3 t} \approx 0$, the above equations reduce to $(N_1 \lambda_1) = (N_2 \lambda_2) = (N_3 \lambda_3)$, so that all the nuclides have the same activity as their parents, i.e., are in secular equilibrium, and the entire chain has the same activity as that of the long-lived parent. This is the state within very long-lived materials, such as unweathered rocks, and is the state all systems evolve towards when nuclides are redistributed.

iii. The activity of the daughter evolves towards secular equilibrium with its parent according to its own half-life (and *not* that of the half life of its parent). This could be grown-in, where the daughter starts with a lower activity, or decay when the daughter starts with a higher activity; in either case, it is the difference in the activities that declines at a rate determined by the half-life of the daughter. Therefore, the half-life of the daughter dictates the time-scale for which it is useful.

The linking of all the isotopes in the chain can lead to considerable complexity, since the parent concentration of each nuclide is changing, and so the concentrations of the entire chain must be potentially considered. However, for most applications, this can be greatly simplified by the following considerations:

(a) When a nuclide is isolated from its parent, then it becomes the head of the decay chain and simply decays away according to the decay equation (Eq. 1.10); that is, it becomes the top of the chain. An example is ^{210}Pb, which is generated in the atmosphere from ^{222}Rn and then transferred to sediments in fallout, where its activity simply diminishes according to Eq. 1.10 with a 22.3 year half-life (Fig. 1.2).

(b) Where the time scale of interest is short compared to the half-life of an isotope, the abundance of that isotope can be considered to be constant. In this case, this nuclide can be considered the head of the decay chain, and the influence of all nuclides higher in the decay series, can be ignored. For example, over periods of 100 years, ^{226}Ra ($t_{1/2} = 1.60$ ky) remains essentially constant, while ^{210}Pb ($t_{1/2} = 22.3$ y) will grow towards secular equilibrium according to Eq. 1.12.

(c) Where the time scale of interest is long compared to the half-life of an isotope, the activity of that isotope can be considered to be equal to that of the parent. For example, in a closed mineral, the ^{222}Rn activity will be equal to that of parent ^{226}Ra after about three weeks, and so while the activity of ^{210}Pb will grow-in towards that of its parent ^{222}Rn, this can be represented by measurements of ^{226}Ra. Therefore, shorter-lived intermediate isotopes (^{218}Po, ^{214}Bi, ^{214}Pb, ^{214}Po) can be ignored.

1.4 Units of Radioactivity

Since all the isotopes of radon are radioactive, the radioactivity units are the most common ones. The different activities and the conversion between them are given in Table 1.5. All noble gases lighter than radon are generally stable and are measured using mass spectrometers. Gases are normally measured by volume and the quantities of all other noble gases are generally reported in terms of cm^3 STP (Standard Temperature and Pressure).

There are a number of units used for reporting radon concentration data. The term 'activity' refers to the number of radioactive decays of a nuclide per unit time and is the product of the decay constant, λ, and the number of atoms, N. Although the International Associations (such as IUPAC) have established\standard units, in practice several units are commonly used in peer-reviewed literature as well in common use. Curie (denoted as Ci) is one of the basic units for radioactivity and it is the activity of 1.000 g of ^{226}Ra and is equal to 37 billion disintegrations per second (3.7×10^{10} dps or 2.22×10^{12} disintegrations per minute, dpm; thus, 1 pCi = 2.22 dpm). The SI (abbreviated **SI** from French: *Le Système international d'unités*) unit of radioactivity is the Becquerel (Bq), which is equal to one atom decaying per second. The amount of natural radioactivity given off by radon and other decay products is very small and is commonly measured in trillionths of one Ci (10^{-12} or pico Curie).

The least commonly used units for radon are the mass unit and radon concentration in terms of cm^3 STP. For ^{222}Ra, the conversion factors for common radioactivity units are 1×10^{-21} mol/mol = 1.52 pCi m^{-3} STP = 5.6×10^{-2} Bq m^{-3} STP (or 56 mBq m^{-3} STP), where pCi is picocuries, 'Bq' is Becquerels and 'm^3 STP' is a standard cubic meter of air at 273.15 K and 1 atmosphere (Table 1.5).

The daughter products of ^{222}Rn can reach secular equilibrium within less than three hours (Fig. 1.2), and the collective activity of ^{222}Rn, ^{218}Po, ^{214}Pb and ^{214}Bi, known as equilibrium-equivalent decay-product, $EEDC_{Rn-222}$, is also used:

$$EEDC_{Rn-222} = 0.106\,A_{Po-218} + 0.513\,A_{Pb-214} + 0.381\,A_{Bi-214} \qquad (1.14)$$

where A_{Po-218}, A_{Pb-214} and A_{Bi-214} are the activities (Bq m^{-3} or pCi L^{-1}) of ^{218}Po, ^{214}Pb and ^{214}Bi, respectively (Nero 1988). In Eq. (1.14), ^{214}Po is not included due to very few atoms of ^{214}Po compared to ^{218}Po, ^{214}Pb, ^{214}Bi, due to half-life of 164 μs (at secular equilibrium between ^{222}Rn and ^{214}Po, $A_{Rn-222} = A_{Po-214}$); number of ^{214}Po atoms = activity of ^{222}Rn/decay constant of ^{214}Po (4.23×10^{-3} s^{-1})). Note that ^{214}Po alpha has the highest energy (7.69 meV).

Similar to Eq. (1.14), one can write equilibrium-equivalent decay product concentration for ^{220}Rn (from the ^{232}Th series) as follows:

$$EEDC_{Rn-220} = 0.913 * I\left(^{212}Pb\right) + 0.087 * I\left(^{212}Bi\right) \qquad (1.15)$$

where A_{Po-218}, A_{Pb-214} and A_{Bi-214} are the activities (Bq m^{-3}) of ^{218}Po, ^{214}Pb and ^{214}Bi, respectively (Nero 1988).

When radon is present in higher activity levels in surface air, it poses health hazard. Due to a short half-life, only a small fraction of sub-surface derived ^{220}Rn reaches surface air and its distance traveled is limited before its decay. Very little of ^{219}Rn, derived from ^{235}U decay chain, is present in air because the abundance of ^{235}U is only ~0.7 % as that of ^{238}U. When ^{222}Rn is inhaled, it is not the ^{222}Rn dose that causes the radiation exposure, but it is the daughter products of ^{222}Rn that includes three alpha particles produced from the decay of ^{222}Rn to ^{210}Pb in the ^{238}U-decay chain.

1.5   A Synopsis of the Applications of Radon

Radon-222, with the longest half-life amongst the three radon isotopes produced from the U-Th series radionuclides, is widely utilized as a tracer in the environment. The concentration gradient of radon in soil-air, surface-air and groundwater have been utilized as tracers for locating subsurface uranium deposits (Chap. 9), predicting earthquakes (Chap. 10), identifying subsurface hydrocarbon deposits (Chap. 9), finding sources of air masses (Chap. 5), quantification of air-sea gas exchange rates in the ocean, estuaries, and lakes, determination of vertical eddy diffusion coefficient in the ocean and other aqueous bodies, quantification of the amount of groundwater discharge, characterization of transport coefficients for chemical exchange between pore waters and overlying waters (Chap. 6), dating of groundwater and as a tracer for monitoring nonaqueous phase liquids (Chap. 8). Radon has been found to be a suitable tracer for use in the development and validation of three-dimensional global circulation and chemical transport models. Furthermore, ^{222}Rn, along with its progeny (mainly ^{210}Pb, ^{210}Bi and ^{210}Po), has provided a wealth of information on the sources of air masses and aerosols, residence times and removal rate constants of aerosols, stability and vertical movements of air masses and deposition velocities of aerosols in the planetary boundary layer (Chap. 5). Radon also provides proxy information for other atmospheric pollutants such as dimethyl sulfide (DMS), mercury, etc. In this book, most of the key applications of radon and its progeny are discussed in depth.

References

Boyle RW (1911) The solubility of radium emanation. Application of Henry's law at low partial pressures. Philos Mag 22:840–854

Clever HL (ed) (1979) Solubility data series, vol 2. Krypton, Xenon and Radon—gas solubilities. Oxford: Pergamon Press

Cotton FA, Wilkinson G, Bochmann M Grimes RN (1988) Advanced inorganic chemistry: a comprehensive text, 5th edn, pp. 1488. Wiley-Interscience

Curie P, Curie, MM (1899) Sur la radioactivite provoquee par les rayons de Becquerel. *Comptes rendus hebdomadaires des séances de l'Académie des sciences* **129**: 714–6

Dorn FE (1900) Die von radioactiven Substanzen ausgesandte Emanation. Emanation". Abhandlungen der Naturforschenden Gesellschaft zu Halle 23:1–15

Firestone RB, Shirley VS (1999) Table of Isotopes, 8th edn. Update with CD-ROM, Wiley-Interscience.

Ishimori Y, Lange K, Martin P, Mayya YS Phaneuf M (2013) Measurement and calculation of radon releases from NORM residues. Technical Reports Series N0. 474, IAEA, Vienna

Nazaroff WW (1992) Radon transport from soil to air. Rev Geophys 30:137–160

Nazaroff WW, Moed BA Sextro RG (1992) Soil as a source indoor radon: generation, migration and entry. In: Nazaroff WW and Nero AV(eds) Radon and its decay products in indoor air. Wiley, pp. 57–112

Nero AV (1988) Estimated risk of lung-cancer from exposure to radon decay products in United States homes—a brief review. Atmos Environ 22(10):2205–2211

Nero AV (1992) Radon and its decay products in indoor air: an overview. In: Nazaroff WW, Nero AV (eds) Radon and its decay products in indoor air. Wiley, pp. 1–53

Ozima M, Podosek FA (2002) Noble gas geochemistry. Cambridge University Press, p. 286

Porcelli D, Baskaran M (2011) An overview of isotope geochemistry in environmental studies. In: Baskaran M (ed) Handbook of environmental isotope geochemistry, advances in isotope geochemistry. Springer, Heidelberg. doi:10.1007/978-3-642-10637-8_2

Porcelli D, Ballentine CJ, Wieler R (2002) Noble gases in geochemistry and cosmochemistry, book series: reviews in mineralogy and geochemistry, vol 47, published: 2002

Rutherford E (1900) A radioactive substance emitted from thorium compounds. Phil Mag 40:1–4

Schery SD, Whittlestone S (1989) Desorptin of radon at the Earth's surface. J Geophys Res 94 (D15):18297–18304

Schery SD, Gaeddert DH, Wilkening MH (1984) Factors affecting exhalation of radon from a gravelly sandy loam. J Geophys Res 89:7299–7309

Stein L (1970) Ionic radon solutions. Science 168:362–364

Stein L (1984) Hydrolytic reactions of radon fluorides. Inorg Chem 23:3670

Stein L (1987) Chemical properties of radon. In: Radon and its decay products; Hopke, P.; ACS symposium series; chapter 18. American Chemical Society; Washington DC, pp. 240–251

Tanner AB (1980) Radon migration in the ground: a supplementary review. In: Gesell TF, Lowder WM (ed) Proceedings of the Natural Environment III, U.S. Department of Commerce Report Conference-780422, National Technical Information Service, Springfield, pp 5–56

Wong CS, Chin Y-P, Gschwend PM (1992) Sorption of Rn-222 to natural sediments. Geochim Cosmochim Acta 56:3923–3932

Chapter 2
Radon Measurement Techniques

2.1 Introduction

A number of techniques have been utilized for measuring the concentrations of radon (^{222}Rn) and its daughter products in the environment. The specific analytical method utilized depends primarily on the concentrations of ^{222}Rn in the medium and the precision needed. The ranges of radon concentrations in environmental samples are given in Fig. 2.1. Radon concentrations in surface waters including ocean waters are much lower compared to subsurface groundwater and the methodology of sampling and/or analytical methods often differ. Radon concentrations in atmospheric air also are generally low compared to soil air.

Radon measurement techniques are classified based on three characteristics (Fig. 2.2): (i) whether the technique measures ^{222}Rn or its daughter products; (ii) time resolution and (iii) radioactive detection of the type of emission—either alpha, or beta particles or gamma radiation resulting from radioactive decay. Most common methods rely on detection of alpha particles. Sometimes a single alpha particle (e.g., ^{218}Po for ^{222}Rn) is detected to measure radon isotopes (as in air-in-monitors, RAD7, Durridge, USA) or by counting all three alpha particles produced in the decay of ^{222}Rn (i.e., ^{222}Rn, ^{218}Po, and ^{214}Po) using scintillation counters (details given later). Some methods are based on the detection of gamma-ray emitted radionuclides during radioactive decay of the progeny of ^{222}Rn (^{214}Bi, ^{214}Pb) and only a few methods utilize beta decays.

There are three broad classes for time resolution when it comes to sampling and analysis (Fig. 2.2): (a) *grab-sample* technique involves measurement of ^{222}Rn in discrete sample of water (or air) collected over a very short time (compared to the mean-life of ^{222}Rn) at a single point. Examples include measurements of radon in groundwater, freshwater and marine waters, and air samples. Radon measurement equipment such as RAD7 can be used to measure ^{222}Rn in air at any time when it is used in 'sniffer' mode in which case radon is typically present with minimal ingrowth of its progeny and large number of measurements can be taken in a relatively short
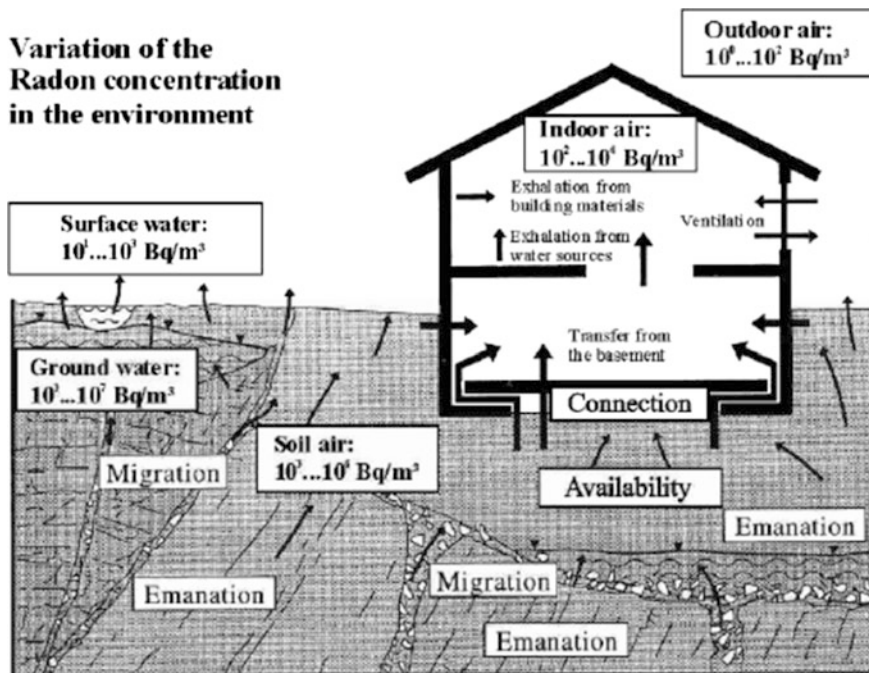
Fig. 2.1 Concentrations of radon in the environment (figure taken from http://www.sarad.de/)
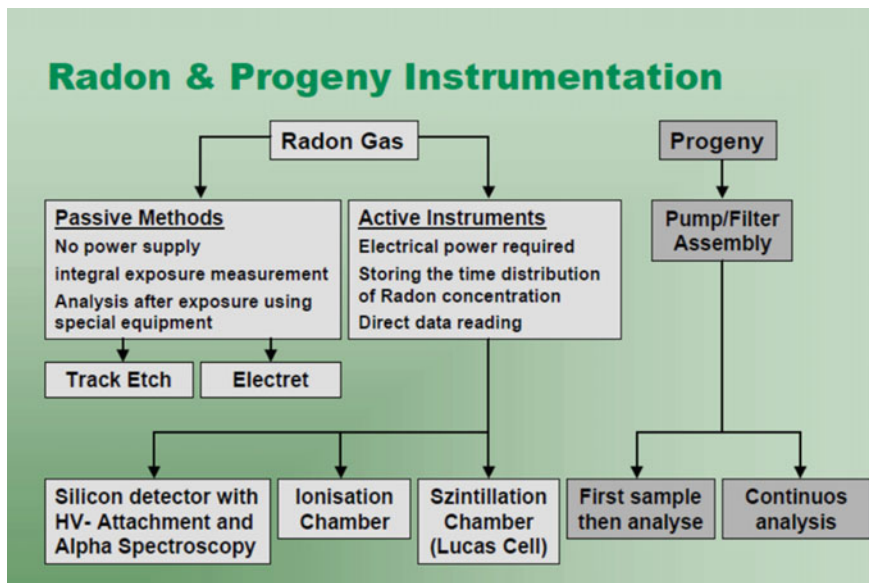
Fig. 2.2 Methods and Instruments to measure radon and its progeny (taken from http://www. SARAD.de/)

period of time; (b) *continuous* technique provide time-series concentrations of ^{222}Rn in samples (soil gas, air, water) and sampling and counting are done simultaneously. Recently developed instruments such as Smart Radon Duo (www.roopcreators.com) and Scintillation Radon Monitors (www.eeipl.in) can also be used for continuous monitoring of ^{222}Rn as well as ^{220}Rn in air, soil gas or water. Such data is quite valuable in the usage of ^{222}Rn as a tracer for predicting earthquakes (Chap. 10). Many of the continuous monitors are portable and nearly all of those are designed to detect alpha radiation (by ionization chamber, gross alpha counting or alpha spectrometry). It is more difficult to build a portable beta detector or gamma-ray spectrometer that has both low background and high sensitivity; and (c) *Integrating* technique provide the integrated concentration over a certain period of time. Such measurements are useful to determine monthly or annual average ^{222}Rn concentration of a specific building. The passive detectors, which are quite inexpensive, are examples of integrating techniques. Such devices are useful to assess the effectiveness of remedial techniques to alleviate indoor radon problems. Additionally, integrated results can also be determined from continuous long-term measurement records.

A review of the most commonly utilized ^{222}Rn measurement techniques are reviewed in this chapter. Furthermore, wherever applicable, the sensitivity and quality assurance/quality control (QA/QC) aspects of these techniques are also explored.

2.2 Techniques for Measuring Radon

2.2.1 Grab Sampling Methods

2.2.1.1 Air Samples

Radon-222 measurements in air (both surface and upper atmospheric) are made either with direct measurement of radon (direct method) or its progeny (indirect method) (e.g., Papastefanou 2002). For direct measurements, grab samples have been collected either in flasks, stainless steel containers, in situ absorption of radon onto cold plates, or activated charcoal. The flasks or steel containers are brought to the laboratory and the radon is extracted onto activated charcoal column and subsequently transferred to Lucas cell (details given in Sect. 2.2.1.4). The cold plates can be heated inside a closed chamber and the released gas is filled in a Lucas cell for assay.

Indirect measurements are based on the collection and counting of radon progeny, but this method is based on the assumption of equilibrium between radon gas and its aerosol progeny. Such an assumption is considered to be valid for sites that are at a significant distance from the radon's terrestrial source and the weather conditions of the air masses are fairly calm en route to the sampling site. This method is likely to fail in the case of precipitating air masses (Chambers et al. 2014). Chambers et al. (2014) have summarized the radon data measured with

different techniques and resolution in the Antarctic over 5 decades (1958–2011; papers published in 1960–2013).

Although a number of sampling methods are available for surface air, the most common method for layers above planetary boundary layer involves collection of air samples using a manifold that is comprised of an inlet, fore-pump, main compressor, pressure monitoring sensors and relief valves, data system, and steel sample cylinder (Fig. 2.3). The sample cylinder has a water volume of 2.5 L and a pressure rating of 1800 psi, so that when it is fully pressurized it can hold 300 STP L (or 0.300 m^3 at STP) of ambient air (details given in Kritz et al. 1998). Williams et al. (2011) used a 10-trap radon sampler installed in an underwing pod of the instrumented motorized glider, and air samples were collected over 5 or 10-min at a flow rate of 20–30 L min^{-1} at standard temperature and pressure. The
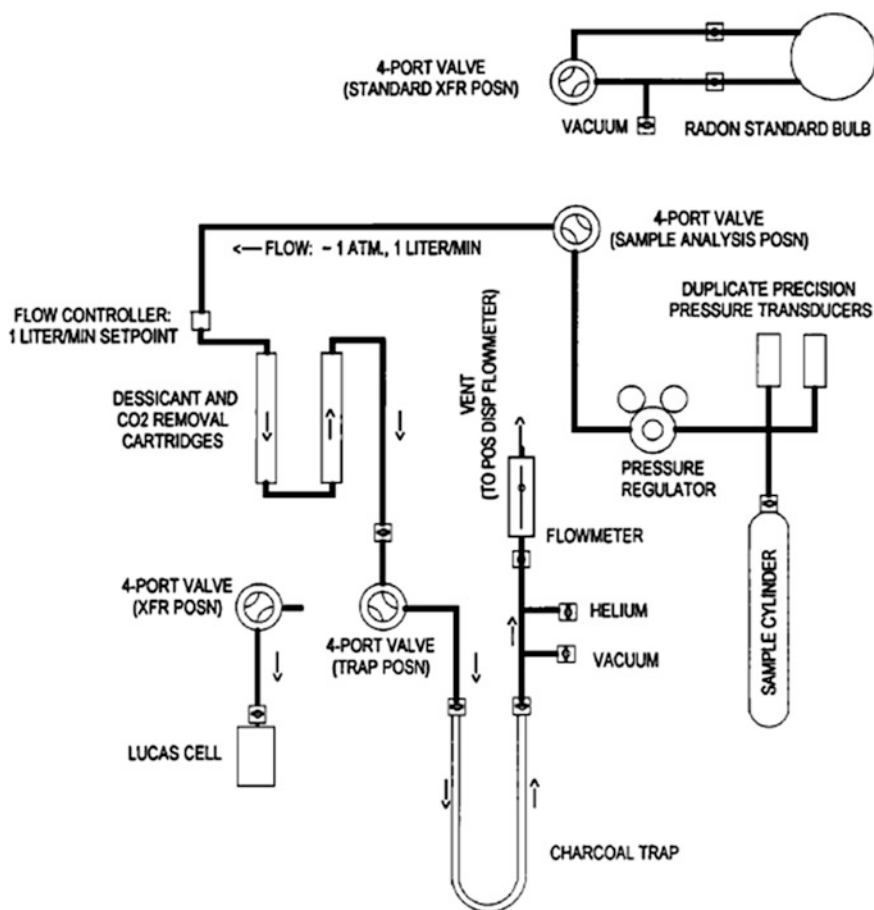
Fig. 2.3 Schematic diagram of ^{222}Rn transfer and extraction system (figure from Kritz et al. 1998, with permission from American Geophysical Union)

filling procedure consisted of a short flush with both valves open, after which the exit value was closed and the sample was collected. The model used by Kritz et al. (1998) had dimension of ~ 4 m^2 of cabin floor space, weighing ~ 500 kg with ~ 4.5 kW of electrical power. The filled cylinders are brought to the laboratory where the Rn was stripped out by cold trapping. The cylinder is connected via ~ 3 mm stainless tubing to the trapping/transfer system. The air from the cylinder (with 2 ports, each one with its own solenoid valve) passes through a regulator, where its pressure is reduced to ~ 1 atm above ambient air through a flow controller where the flow is regulated at a constant 1 STP L/min. After passing through drierite (to remove water vapor) and ascarite (to remove CO_2) columns, the air flows through an activated charcoal column immersed in a dry ice—alcohol mixture at -78 °C,[1] where the radon contained in the air stream is trapped by the charcoal (Fig. 2.3). Note that the design of the trapping-transfer systems and the associated operating procedures and calibration procedures are similar to those described in Broecker and Peng (1971), Mathieu et al. (1988) and are often modified by different groups (e.g., Kritz et al. 1998).

The charcoal column containing radon is then heated to 480 °C (note: Kritz et al. (1998) reported heating to 300 °C) and then, slowly back-flushed with helium to transfer the trapped radon into a Lucas cell for counting. Kritz et al. (1998) reported ~ 8 h to process eight samples in parallel. In the case of large volume air samples collected in stainless containers, the quantity of air passing through each trap is determined from the known volume and the beginning and ending pressures of each sample cylinder. The volume of air is also confirmed by passing air through a calibrated positive displacement flowmeter downstream of the trap. Kritz et al. (1998) reported radon trapping efficiency of >99 % by placing two traps in series (trapping efficiency (%) = [1 – {^{222}Rn trapped in the second trap/^{222}Rn trapped in the first trap}]* 100). The fraction of ^{222}Rn transfer from the trap to the counting was reported to be 95 ± 3 %.

2.2.1.2 Soil Air Samples

Radon concentrations in soil gas is about 2–5 orders of magnitude higher than that in atmospheric air. One of the relatively easier ways of measuring radon in soil gas is using Soil Gas Probe coupled with RAD7 (Fig. 2.4, http://www.durridge.com/products_soil_gas_probe.shtml). This soil probe can be operated anywhere above the water table and is used in conjunction with a drying unit (drierite column). The soil air can be sampled in the GRAB mode or Continuous Monitoring mode using the standard protocol. Continuous monitoring method is simpler and provides time resolution in the event of weather changes. RAD7 will pump air for the first 5 min of every half-hour cycle, and then for 1 min for every 5 min once the relative

---

[1]The author's laboratory experience has shown that the dry ice alone or a mixture of salt and ice is sufficient to quantitatively trap radon in the activated charcoal column.

humidity drops below 10 %. A typical 2 h continuous run would amount to $\sim$20 L
of soil air and the volume of air passed through RAD7 will depend on the porosity
and tortuosity of the soil.

2.2.1.3 Water Samples

Collection of grab water samples for ^{222}Rn measurements (or for any other dis-
solved gases) from rivers, lakes, oceans (including sea water at all depths) and
underground is always challenging. A precaution that need to be exercised in the
collection of any grab water samples is identical in that dissolved gases from the
water should not escape during transfer from the water sample to the storage
container. Aeration of the water sample during collection could result in a loss of
radon, and thus the sampling procedures need to be designed to minimize this
effect. Direct suction of water sample into a 20-L flint glass bottles have been used
in the gas extraction procedures before (Broecker 1965). The bottle should be first
evacuated and sealed off. A length of rubber tubing is usually attached to the
exhaust side of the adaptor. The far end is weighted and lowered into the water to
the desired depth in a lake (or river or sea). The exhaust value is opened and the
water is allowed to flow in until the desired amount is obtained. The container is
then sealed, moved to the laboratory, and attached directly to the gas extraction
system, thus collecting near surface waters with no chance of gas loss.

During GEOSECS (Geochemical Ocean Sections Study, 1968–1978), large
volume ($\sim$20 L) water samples were collected and stored in gas-tight containers

and were analyzed in ships for ^{222}Rn. The protocol adopted during the GEOSECS cruises involved pumping helium through the water sample stored in a gas-tight container to drive all the Rn into an activated charcoal column inside a stainless steel trap that is kept at dry ice (Mathieu et al. 1988). Helium is then re-circulated through the sample trap using a diaphragm pump that comes with the Extraction Board (Mathieu et al. 1988). Water vapor and CO_2 are usually trapped by serially connected Drierite and Ascarite columns, respectively. Radon from the charcoal column is mobilized by heating and subsequently quantitatively transferring it into a Lucas counting cell. After transferring Rn, the cell is stored for ~ 3 h for all the daughter products of ^{222}Rn to reach secular equilibrium (note the long-lived daughter products of ^{222}Rn (before ^{210}Pb) is ^{214}Pb, with a half-life of 26.8 min; in about 2 h, ^{214}Pb/^{222}Ra activity ratio = 0.955; in about 3 h, the activity ratio becomes 0.99). The cell is then counted in an alpha scintillation counter (Mathieu et al. 1988). After the measurement of ^{222}Rn, the water sample can be stored for about 20 days and the concentration of in situ ^{226}Ra can be determined. For in situ ^{222}Rn measurements, appropriate correction for the decay and in-growth should be applied (Mathieu et al. 1988).

More recently, ^{222}Rn has been utilized widely as a tracer to quantify the submarine groundwater discharge in coastal areas. A multi-detector system that measures ^{222}Rn activities continuously in coastal waters has been developed (Fig. 2.5, Dulaiova et al. 2005). The system utilizes a constant stream of water that is delivered by a submersible pump to an air-water exchange system where radon in the water phase equilibrates with radon in a closed air loop. The air stream is then fed to three radon-in-air monitors connected in parallel to determine the activity of ^{222}Rn. The precision in this methodology is approximately ± 5–15 % for typical coastal seawater concentrations (Dulaiova et al. 2005).
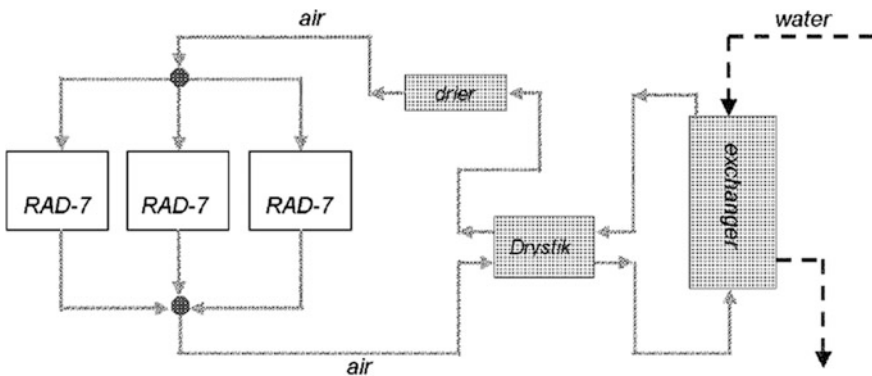
Fig. 2.5 A simplified sketch of an equilibrium three-stage radon measurement system. *Lines* shown represent the water pumped through the exchanger by a submersible pump (*dashed*) and a closed air loop (*solid*) that flows through three RAD-7 radon analyzers in parallel (Dulaiova et al. 2005)

2.2.1.4   Lucas Cell Method of Measurement

One of the most important devices to measure radon is the scintillation flask which was first introduced in 1950s by Henry F. Lucas and is commonly known as Lucas cell (Lucas 1957). The original cell has the shape of right circular cylinder with a hemispherical cap, with 5 cm diameter and a volume of 100 cm^3. Typical efficiency is 70–80 %. In a new cell, the background count rate of ~ 0.1 count/min can be achieved. Commercially, different volumes of cells are available (e.g., 270, 160, 100 cm^3). The inside is coated with silver-activated zinc sulfide (ZnS(Ag)) phosphor and one side (usually the bottom side) has transparent flat surface and constitutes a viewing window. The cell typically has two sampling ports, each fitted with a valve, and a photomultiplier tube is coupled to the transparent window of the cell. When an alpha particle produced within the cell strikes the phosphor, a flash of light is produced and is sensed by the photomultiplier tube which is optically coupled to the cell window and associated electronics (preamplifier and multiplexer) and is counted using a multichannel analyzer (MCA) (recorded as a count, not to be confused with the energy spectrum often used in alpha spectroscopy). Most often, the traditional method of gating amplifier/scalar arrangement has been widely used, but the use of multichannel analyzer advantages include: (i) ability to observe the number of counts above and below the 'window' of the counting region (similar to upper level of detection (ULD) and lower level of detection (LLD) in alpha-ray or gamma-ray spectroscopy); (ii) the overall shape of the distribution allows easy identification of spurious counts resulting from electrical noise or interference (Kritz et al. 1998); (iii) changes in the performance caused by voltage drifts or deterioration of the PMTs; and (iv) MCAs can be programmed to make a set number of individual counts during the counting period.

As mentioned earlier, after radon is filled in a Lucas cell and before it is assayed in a scintillation counter, it is usually stored for about 3 h for the daughter products ^{218}Po, ^{214}Pb, ^{214}Bi and ^{214}Po to reach secular equilibrium with ^{222}Rn (governed by the half-life the longest lived daughter, ^{214}Pb, with a half-life of 26.8 min). In this decay of ^{222}Rn, three alphas (from the decay of ^{222}Rn, ^{218}Po, ^{214}Po) and 2 betas (from the decay of ^{214}Pb and ^{214}Bi) along with a number of gamma-ray lines are produced (summarized in Porcelli and Baskaran 2011). The background of the Luca cell is expected to increase due to its repeated use from the decay of ^{222}Rn daughter products during the time between filling and evacuation of the cell (after counting). In this interval, a finite amount of ^{210}Pb would have been produced from the decay of ^{214}Bi via ^{214}Po. With time, ^{210}Pb decay to ^{210}Po (alpha decay) via ^{210}Bi (beta emitter) takes place and thus periodic monitoring the background of each of the Lucas cell is essential.

2.2.1.5   Comparison of Grab Sample Analysis Versus RAD7-Based Method

While the grab sample analytical method described above for air and water samples is precise (typically $\sim \pm 5$ %) and straight forward, there are two main

disadvantages: (i) radon extraction/transfer method is labor-intensive and this method can only partially be simplified by automation and computer-controlled laboratory processing; and (ii) this grab sample method requires the extraction/transfer and counting facility to be in close proximity to minimize decay and in-growth time in charcoal between sampling and radon extraction. In addition, the throughput is poor. However, more recent methodology with Radon Monitor (RAD7) yields precision ($\sim \pm 10$–15 %) that is less than the previous quantitative extraction methods $\sim \pm 5$ % (e.g., Mathieu et al. 1988). The advantages include (i) the ease of the analysis in the field, (ii) no need to apply decay/growth correction, (iii) no in-growth correction for the progeny of ^{222}Rn; and (iv) a much higher throughput, making this method of analysis distinctly advantageous in the investigation of coastal oceanic processes. Details of this method are given in Sect. 2.2.

2.2.1.6   Calibration, Quality Control, Precision and Accuracy

The extraction/transfer analysis system used for small volume water samples (e.g., groundwater) is calibrated by flushing a known ^{222}Rn content (in equilibrium with ^{226}Ra) of sealed glass containers obtained from the National Institute of Standards or preparing ^{226}Ra standard using RGU-1 (IAEA) primary standard by dissolving a known amount of RGU-1 in which ^{238}U and all its daughter products all the way to ^{210}Po are in secular equilibrium with ^{238}U. Care must be exercised in dissolving the RGU-1 standard (e.g., drying the standard before weighing an aliquot for analysis to ensure the standard is free of water vapor, complete dissolution of the standard with ^{226}Ra-free mineral acids that include HF, HNO_3 and HCl, no loss of ^{226}Ra during digestion and handling/transfer of the solution, etc.). In the case of large-volume seawater (or surface water), 20 L of filtered seawater, with a known in situ ^{226}Ra concentration, is taken in a glass container (to prevent the loss of Rn through diffusion), spiked with a primary ^{226}Ra standard (or RGU-1 standard in solution form) and stored for >1 month. The sample is assayed for ^{222}Rn and the result obtained by this method is compared to the certified value.

Calibration of atmospheric air sampling device is more difficult. An atmospheric air sampling site at which radon concentration is simultaneously determined both with a calibrated device and an uncalibrated instrument. Intercalibration between laboratories that make routine airborne measurements would also be quite useful.

As mentioned earlier, for every alpha particle produced from the decay of ^{222}Rn, there are two other daughters that produce alpha particles: ^{218}Po, with a half-life of 3.10 min and ^{214}Po, with an half-life of 164 µs (effective half-life ($\tau_{eff} = \tau_{Po\text{-}218} + \tau_{Pb\text{-}214} + \tau_{Bi\text{-}214}$) of 71.6 min). Since the normal procedure is to start counting the sample after two to three hours, it is assumed that ^{222}Rn is in secular equilibrium with ^{218}Po, ^{214}Pb, ^{214}Bi and ^{214}Po. The overall error (propagated error) in the determination of ^{222}Rn by this method arises from the errors associated with the following: (i) net counts (=total counts – background counts) for

a given counting cell; If N_t is the total counts n_t is error associated with the total count, and B_t is the total background count and b_t is error associated with the background count, then, the net count (N) and error associated with the net count (n) is given by:

$$N \pm n = (N_t - B_t) \pm \left(n_t^2 + b_t^2\right)^{1/2}$$

(ii) the efficiency (η_c) of the Lucas cell. The total variations in the amount of silver-activated zinc sulfide (ZnS(Ag)) coating can result in slight variations in the counting efficiency of the cell which could also change with time; (iii) counting efficiency of the scintillation counter (η_s) which is determined using a glass-sealed Lucas Cell with a known amount of ^{226}Ra in which ^{226}Ra and ^{222}Rn are in secular equilibrium; and (iv) volume of air used for study. We assume the transfer efficiency of ^{222}Rn from the sample container to the Lucas cell is 100 %. For a typical 1000 counts, the 1 standard deviation (1σ) on the net counts is ~3.2 % (assuming the counting error associated with the cell background is very small compared to the counting error associated with the gross count). Assuming that the 1σ error associated with the counting efficiency of the Lucas cell is 5 %, the 1σ error associated with the efficiency of the counting instrument is 2 %, and the 1σ error associated with the volume of air sample is 1.5 %, then, the propagated 1σ uncertainty of the overall measurement may be estimated by talking the square root of the sum of the squares of the individual elements entering into the calculation as follows: $[(3.2\ \%)^2 + (5\ \%)^2 + (2\ \%)^2 + (1.5\ \%)^2]^{1/2} = 6.4\ \%$. Note that in counting instruments, the most common practice is to report 1σ of the propagated error while in mass spectrometry, the standard practice is to report 2σ values. Williams et al. (2011) reported the following errors: variability associated with the counting efficiency of the cell is ~±5 %, accuracy of the radon calibrated source of ±4 %; and the overall typical error with the measurement of ±8 %. Presence of a small but variable amounts of ^{226}Ra in charcoal contributing to ^{222}Rn has been reported by Williams et al. (2011) and hence blank levels of the extraction/transfer system needs to be periodically monitored.

The activity of the ^{222}Rn in air sample (A, in disintegration per second (dps) per standard cubic meter, Bq m^{-3}) at the time of collection can be calculated as follows:

$$A\left(Bq\,m^{-3}\right) = Ne^{\lambda t}/(3\,t\,\eta_c\,\eta_s\,V\,^*\,60)$$

where t is the time elapsed between sampling and mid-counting (in minutes), λ is the ^{222}Rn decay constant (1.2598×10^{-4} min^{-1}), V is the volume of air samples (per standard m^3), 60 is to convert dpm to dps (or Bq) and the factor '3' is to account for the additional two alpha emissions that occur following each radon decay at secular equilibrium in the counting cell.

2.2.2   Radon Analysis of Surface Water Samples Using RAD7

A relatively new technology based on RAD7 radon-in-air detector (Durridge Co., Billerica, MA) has allowed rapid and inexpensive field measurements of radon in water (Fig. 2.6, Burnett et al. 2001; Dulaiova et al. 2005). Instead of collecting large quantities (~ 20 L) of seawater in gas-tight containers, stripping with helium into cold traps, transferring to Lucas cells on a vacuum line, and counting on photomultiplier tube counters (e.g., Mathieu et al. 1988; Krishnaswami et al. 1991; Corbett et al. 1999), the RAD7 approach provides continuous measurement of radon (^{222}Rn) and thoron (^{220}Rn) in the field.

A single-detector system (Fig. 2.5) analyses ^{222}Rn from a constant stream of water passing through an air-water exchanger ("RAD-AQUA") that distributes radon from the running water to a closed air loop. The air stream is fed to a RAD7 that determines the activity of ^{222}Rn by electrostatic collection and measurement of the α-emitting daughters, ^{214}Po and ^{218}Po (^{220}Rn, if present, may be detected by integrating counts in the ^{216}Po region; Burnett et al. 2007; Dimova et al. 2009). Since the distribution of radon at equilibrium between the air and water phases is governed by a now well-known temperature and salinity dependence (Schubert et al. 2012), the radon activity in the water is easily calculated if one also measures the water temperature and salinity.

The RAD7 uses a high electric field with a silicon semiconductor detector at ground potential to attract the positively-charged polonium daughters, ^{218}Po$^+$ ($T_{1/2} = 3.10$ min; $E_\alpha = 6.00$ MeV) and ^{214}Po$^+$ ($T_{1/2} = 164$ μs; $E_\alpha = 7.67$ MeV) which are then counted as a measure of the radon activity in air. For faster analyses, the ^{218}Po is preferred, as it will reach radioactive equilibrium with ^{222}Rn in only about 15 min (^{214}Po requires about 3 h for equilibrium because of the intermediate ^{214}Pb and ^{214}Bi daughters).

Fig. 2.6 Diagrammatic view of the experimental setup for a single RAD7 exchanger continuous radon-in-water monitor. The "Drystik" is a Nafion drying tube that helps preserve the Drierite desiccant (Burnett et al. 2001)
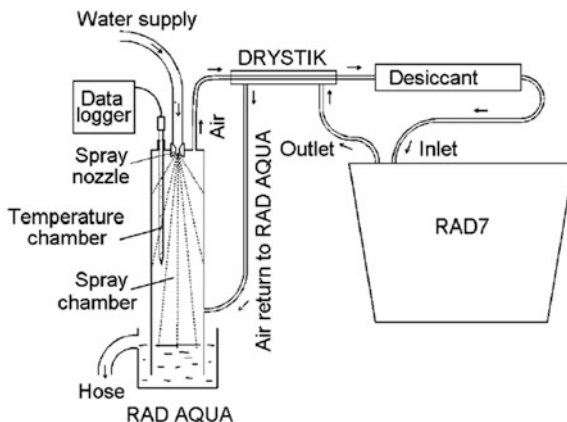
The air–water exchanger (Fig. 2.6) is simply a plastic cylinder that has water entering continuously via a nozzle that aspirates the water into fine droplets so that radon is emanated into a stream of air that is circulated through the exchanger, a drying system, then to the RAD7 for measurement, and then returned to the exchanger to begin another loop. After some time, the radon activity in the air reaches equilibrium with the radon in the water, the ratio at equilibrium being determined by the water temperature and salinity.

In order to increase throughput, several RAD7s can be arranged in parallel with one exchanger (Fig. 2.5). Using 3 RAD7s (Fig. 2.5), it has been shown that typical coastal water radon measurements can be made in 10-min intervals with a precision ranging from 5–15 % depending upon the radon activities present. Thus, a typical day of surveying in a coastal region can result in 50 or more measurements.

2.2.3   Integration Radon Monitors

The Integrated radon monitor method of radon measurement provides time integrated ^{222}Rn concentration for a period of sampling, typically few days to few months. The two requirements for this method to effectively work are: (i) the sampling technique must maintain an integrated record of each alpha particle impacting the measurement device; and (ii) the detector must maintain exposure information from the time of retrieval to the time of analysis in a laboratory.

The solid-state nuclear track detectors (SSNTD) were recognized to hold the powerful potential of recording the primary radioactive signature of radon—alpha particle emission, and enabled the development of simple and quantitative methods of measuring the radon isotopes. Original discovery on the alpha particle tracks were seen in cellulosic materials such as cellulose nitrate and cellulose acetate butyrate. Subsequently, alpha particle tracks were also seen in polycarbonates such as bisphenol-A polycarbonate, i.e., Lexan and allyl diglycol carbonate, CR-39 (summarized in Fleischer 1988). Due to good ionization sensitivity and stability against various environmental factors, the CR-39 (polycarbonate material) has been used as the state-of-the-art track detector for environmental radon. More recently, LR-115 track detector-based twin-cup dosimeter has been developed and are used for indoor Rn-222 and Rn-220 measurements (Eappen and Mayya 2004).

Using the solid-state detector technique, radon concentrations have been measured in air, water and other earth material, with other applications spanning from biological dosimetry and home-ventilation design to prospecting for hydrocarbon and uranium resources, and to measurements of the respiration of the Earth, which can provide warnings of impending geological hazards such as earthquakes and volcanic eruption (Fleischer 1988). The technique is simple to use and relatively inexpensive. For the measurements of environmental radon levels, exposure of few weeks to a year are normally necessary to obtain desirable precision at relatively low analytical cost. Following the exposure, the film is etched in an alkaline solution (typically NaOH or KOH) to enhance the size of the tracks so that the track

density (number of tracks per unit area) can be easily determined by optical microscopy or by automated scanning and counting technology. Although this method is less reliable for rapidly obtaining information on indoor ^{222}Rn concentrations, it is well-suited for obtaining annual average concentrations.

A typical ^{222}Rn-only measuring device comprised of an enclosure that allows ^{222}Rn to enter through a permeable, anti-^{220}Rn membrane is shown (Fig. 2.7). This enclosure excludes condensed alpha emitters and the membrane area and thickness are chosen so as to exclude the unwanted gaseous alpha emitters including ^{219}Rn (it is derived from <1 % of uranium (^{235}U) and its half-life is 3.96 s) and ^{220}Rn, without significantly affecting the ^{222}Rn. Thus, only ^{222}Rn enters the enclosure and the three alpha particles emitted (^{222}Rn, ^{218}Po and ^{214}Po (note that the rate of production of ^{214}Po is determined by half-lives of ^{214}Pb and ^{214}Bi; details in Chap. 1)). Some of the radon measurements made with the Terradex Track Etch system were designed to give integrated readings that minimize the effects of diurnal and barometric pressure. For sampling in soils, detector cups were buried at a depth of 40 cm (Fig. 2.7). The alpha tracks can be counted and it yields a highly reproducible unambiguous measure of ^{222}Rn (Fleischer et al. 1980).

Fig. 2.7 Alpha particle detector mounted on a plastic cup and this instrument is usually kept at 40 cm below ground

HOLE COVER

ALPHA PARTICLE DETECTOR

PLASTIC CUP
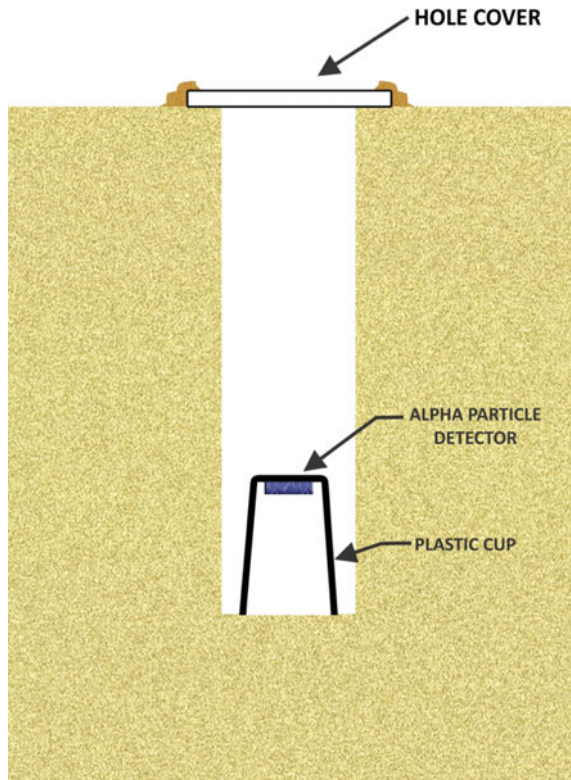
The unique advantages of solid-track nuclear track detectors include: (i) the energy of the alpha particles produced from the decay of ^{222}Rn and its progeny (alpha particles from the decay of ^{222}Rn, ^{218}Po and ^{214}Po) are sufficiently ionizing to produce etchable damage tracks in a variety of polymeric solids; and (ii) other lightly ionizing radiation such as β- and γ-rays from other natural radioactivity and from cosmic-rays are not recorded.

2.2.4 Continuous Monitors

The passive integrating-type detectors are frequently deployed for indoor radon surveys. The on-line radon monitors are commonly used for special radon diagnostic measurements in residential environments, in particular build-up in confined spaces, as well as in quality assurance programs. Real-time data not only help in deciding control measures to minimize radon exposure in the environment, but also are useful along active fault zones where radon concentrations may change significantly and rapidly.

A large amount of efforts have gone into the development of fast responding, highly sensitive radon monitors. The most common ones available in the market are: (i) RAD7 (Durridge, Boston, USA (http://durridge.com); (ii) Radon Scout Plus (SARAD, GmbH, Dresden, Germany, (http://www.sarad.de)); (iii) RTM 2200 (SARAD, Dresden, Germany, (http://www.sarad.de) and (iv) CRM (BARC, Mumbai, India; Ashokkumar et al. 2014). Conventional detectors used in the development of radon monitors include pulse ionization chambers, scintillation detectors coupled with photomultiplier tubes and silicon PIN diodes. Of these, the silicon PIN diode detectors are found to be better in terms of low bias (<100 V), intrinsic alpha detection efficiency (approaching near 100 % for alpha particles), energy resolution, its simplicity, robustness and its cost (Ashokkumar et al. 2014). A comparison of the sensitivity of these four commonly used silicon-detector-based radon monitors are shown in Table 2.1. The CRM developed at the Bhabha Atomic Research Center appears to have higher sensitivity (=counts per hour, CPH/radon

Table 2.1 Comparison of sensitivity of various silicon-based radon monitors (from Ashokkumar et al. 2014)

Instrument	Radiation detector	Mode of operation	Sensitivity (CPH/Bq m^{-3})
RAD7, Durridge[1]	Si-PIPS	Sniff	0.32
		Normal	0.65
Radon Scout, SARAD[2]	Si detector	Diffusion	0.12
RTM2200, SARAD[2]	Si detector	^{214}Po-excluded	0.19
		^{214}Po-included	0.42
CRM, BARC[3]	Si PIN	Fast	0.91
	Diode array	Sensitive	1.76

[1]www.durridge.com; [2]www.SARAD.de; [3]Ashokkumar et al. (2014)

Fig. 2.8 *Top*: Diagram of the continuous radon monitor developed at the Bhabha Atomic Research Center; *Bottom*: Typical alpha spectrum acquired during calibration (courtesy of Ashokkumar, 2016; details given in Ashokkumar et al. 2014)
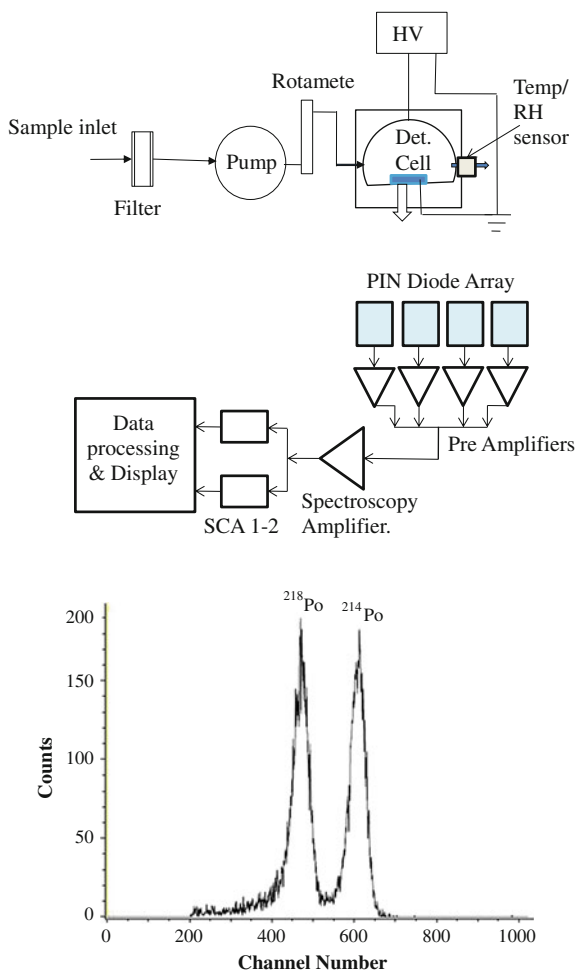
concentration, Bq m^{-3}, CPH/Bq m^{-3}; Ashokkumar et al. 2014). The CRM instrument (Fig. 2.8 top) seems to be less dependent on the humidity of the air compared to other existing systems. It has been shown earlier that the electro-deposition efficiency of radon progeny depends strongly on the relative humidity (RH) of the sampled air. The minimum detection level, C_{MDL} [=2* standard deviation of background counts/(sensitivity factor, CPH/Bq m^{-3})* counting time] of 0.80 Bq m^{-3} for 1 h counting appears to be significantly lower than other instruments (in the fast mode with a 15 min cycle time, CMDL is 3.1 Bq m^{-3} (Ashokkumar et al. 2014)). Furthermore, the volume of the hemispherical metal collection chamber (1 L) is substantially larger than the other systems (0.150–0.750 L).

Scintillation cell-based continuous radon monitors (Smart Radon Duo and Scintillation Radon Monitors) have been developed by the Bhabha Atomic Research Center in Mumbai (Bombay, India). These are based on a software that takes into

account the ingrowth of progeny in a given counting interval without making equilibrium assumptions. An advantage of this technique is that its performance is not affected by relative humidity and hence does not require silica-gel or any other dehumidifying agents. The performance of this instrument has been satisfactorily compared against Alphaguard and RAD7 and has been extensively used for radon and thoron measurements in India (Kumar et al. 2013; Chauhan et al. 2014).

In addition to these air monitors discussed above, continuous radon concentrations in groundwaters are monitored by means of an electronic automatic probe, known as Clipperton (CNRD-URA 1767, Universite Montpellier II, F-34094, Montpellier, France). It is based on the detection of alpha-particles using 1 cm^2 area solid-state electronic sensor. The Clipperton probe allows the measurement of radon activity levels in a range between 100 and 1,000 kBq m^{-3}, with an accuracy of $\sim \pm 7.5$ % (Monnin and Seidel 2002). In addition to the Rn sensor, probes for other geochemical, geophysical and hydrological parameters (such as CO_2, CH_4, N_2, Eh, pH, DO, electrical conductivity, temperature, water level fluctuations, microseismicity) can also be simultaneously deployed which are useful for earthquake research (Streil et al. 1997).

2.2.5   Analysis of ^{222}Rn Using Its Progeny

The decay of ^{222}Rn results in the formation of a series of short-lived daughters before ^{210}Pb:

$\rightarrow$ ^{222}Rn   (3.82   d) $\rightarrow$ ^{218}Po   (3.10 min) $\rightarrow$ ^{214}Pb   (26.8 min) $\rightarrow$ ^{214}Bi (19.7 min) $\rightarrow$ ^{214}Po   (<0.2 ms) $\rightarrow$ ^{210}Pb   (22.3 yr) $\rightarrow$ ^{210}Bi   (5.0   d) $\rightarrow$ ^{210}Po (138.4 d) $\rightarrow$ …
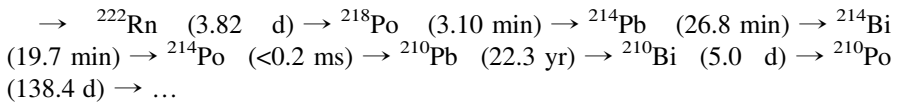
While radon is a noble gas, all of its daughter products are metals (although Po is sometimes classified as metalloid because of its position in the periodic table). As mentioned earlier, the longest-lived daughter product between ^{222}Rn and ^{210}Pb in the decay chain (Chap. 1) is ^{214}Pb, and hence in about 3 h, we expect the activities of: ^{222}Rn = ^{218}Po = ^{214}Pb = ^{214}Bi = ^{214}Po. Polonium, Pb and Bi are highly particle-reactive and hence upon formation quickly and irreversibly attach to submicron-sized aerosol particles of the ambient air. In an isolated air mass when there are no major preferential removal of Pb-Po-Bi-laden aerosol particles from the air, ^{222}Rn concentrations can be determined from the measurements of any of the daughter products.

The alpha particles from the decay of ^{218}Po (6.002 MeV), ^{214}Po (7.687 MeV) or ^{222}Rn   (5.489 MeV),   or   the   beta   particles   from   the   decay   of ^{214}Pb (β_{max} = 1.023 MeV) and ^{214}Bi (β_{max} = 3.272 MeV) using Geiger-Muller counter or the gamma-emissions associated with the decay of ^{214}Bi (0.609 MeV ($\sim$100 %), 1.120 MeV; (1.120 MeV 15.0 %), 1.764 MeV, 15.9 %)), and ^{214}Pb (0.3159 MeV (35.9 %), 0.2952 MeV (18.5 %); (0.2420 MeV (7.5 %)), using gamma spectrometry (non-destructive) can be utilized to assess the activities of ^{222}Rn.

2.2.5.1   Determination of ^{222}Rn Using Its Progeny in a Solid Surface-Barrier Detector

The alpha-emitting progeny of ^{222}Rn can be quantitatively determined using alpha spectrometry. A known volume of air is drawn through a cylindrical system through two in-line filters. The first filter retains the particular matter and radon progeny so that only radon passes through the first filter. As the filtered air from the first filter moves to the 2nd filter, ingrowth of radon progeny occurs. This radon progeny is collected on a second filter which faces the surface barrier detector. An alpha-spectrum of ^{214}Po and ^{218}Po are shown in Fig. 2.8 bottom.

Another simple method involves collecting the +ively charged decay products onto a metal surface maintained at a negative potential placed inside a metallic chamber. The positively charged ^{218}Po collected on the metal surface is then counted using surface-barrier detector.

Advantages of a surface-barrier detector includes very low background (<0.1 count per hour in the regions of interest), high energy resolution and ruggedness, ability to spectrally separate the signals of progeny of ^{222}Rn and ^{220}Rn (they have different alpha energies). However, the alpha spectrometer requires electrical power and associated equipment, vacuum pump and the cost of the instrument is relatively high.

2.2.5.2   Determination of ^{222}Rn Using Electret

Electrets are passive, lightweight, integrating and relatively inexpensive detectors (Kotrappa et al. 1992). It is electrically charged Teflon disc, serving both as a source of an electric field and sensor. When an alpha particle decays in the detector chamber, ionization of the air takes place leading to a decrease in the total charge on the electret. The decrease in the total charge results in the voltage drop (charge, Q = capacitance, C^* potential difference, V) over the measurement period and is used to quantify the ^{222}Rn concentration.

2.2.5.3   Determination of ^{222}Rn Using Beta Counter

Radon concentrations can be determined by measuring the beta activity of ^{214}Pb and ^{214}Bi collected on filter papers, assuming secular equilibrium between ^{222}Rn and its progeny in the air. The beta activity can be assayed with plastic scintillators mounted on photomultiplier tubes or the filter paper can be directly counted in a beta counter (a Geiger-Muller counter), with appropriate use of absorber film (such as Mylar, with suitable mass density). The assumption of secular equilibrium between ^{222}Rn and its daughter products has been observed in the atmosphere over the ocean even after rain and during fog, although uncertainties of up to 15 % have been reported (i.e., ^{214}Pb/^{222}Rn = ^{214}Bi/^{222}Rn = 1.00 ± 0.15 (Larson 1978). However, due to short-term atmospheric turbulence and other short-term events, it

may be necessary to check the secular equilibrium between radon and its progeny periodically due to differences in the geochemical properties of radon and its progeny.

2.2.5.4   Radon Measurements Using Gamma-Ray Spectrometry

Atmospheric ^{222}Rn concentrations can be measured by measuring ^{214}Pb and ^{214}Bi by gamma spectrometry (e.g., Duenas et al. 1994). This particular method may be appropriate where there is temperature inversion leading to very little or no vertical movement of air masses. Also, no major wet precipitation event should have taken place within $\sim$2 h of sampling, as wet precipitation events will most likely remove ^{218}Po, ^{214}Pb, ^{214}Bi, but not ^{222}Rn.

2.2.5.5   Radon Measurements Based on Direct Progeny Monitoring Technique

Direct radon (and thoron) progeny sensors have been developed (Mishra et al. 2009a, b; Mayya et al. 2012) to measure directly time integrated radon progeny concentrations indoor. The direct radon progeny sensor (DRPS) and direct thoron progeny sensor (DTPS) are absorbers mounted on solid-state nuclear track detector on which alpha particles emitted from the progeny atoms deposit on the surface during deployment in the field. The absorber offers the right energy window to detect either ^{214}Po or ^{212}Po alpha emission and virtually cuts-off alpha contributions from other air-based emissions. DRPS has a 37 μm absorber to detect mainly the alpha particles emitted from ^{214}Po (7.69 MeV) formed from the eventual decay of ^{218}Po, ^{214}Pb and ^{214}Bi atoms deposited on it (Mishra et al. 2009a, b).

2.2.6   Indoor Radon Measurements

There are three inexpensive and widely used methods to measure indoor ^{222}Rn concentrations (charcoal canisters, electrets, and alpha-track detectors), all of these methods require long-term (48 h to 3 months) exposure durations. Following the exposure of activated charcoal, the quantity of radon adsorbed can be analyzed, either by gamma-ray spectrometry (via ^{214}Pb and ^{214}Bi) or desorption followed by scintillation counting. Due to the short half-life of ^{222}Rn, 3.82 days, the exposure period is useful for only about a week following exposure and the sampler has to be returned to the laboratory for prompt analysis. This method could complement the etched-track detector in survey work. However, none of these methods seem suitable for measurement of radon concentrations in soil gas below buildings because the measurement devices are relatively large and cannot easily be placed below a building foundation for the required sampling period. In addition, the high

moisture levels in soil gas interfere with the sorption of radon onto charcoal canisters, and the gaseous diffusion constant for radon in the vadose zone is unknown. As a result, grab samples are the most effective means to measure radon concentration in soil gas. Track etch detectors placed inside two cups one of which cuts-off thoron completely is most popularly used for indoor radon measurements (Eappen and Mayya 2004).

2.2.7 Identification of Entry Points of Radon Inside Buildings Using RAD7

The soil gas released from Earth surface contains ^{222}Rn and ^{220}Rn and they start to decay. Thoron has half-life 55.6 s, and so soil gas that has been out of the soil for 5 min will have lost $\sim$97 % of thoron. Assuming that the soil gas moves about 20 cm/min, by the time it has moved about 1 m, most of the thoron (>97 %) has decayed. It is reported that at one half meter away from the hotspot thoron, it is barely detectable. If the air is sampled near an entry point in the building and thoron is detected, then, the Rn entry hot spot is <1 m from the point of sampling. The first daughter of thoron is ^{216}Po (half-life = 150 ms) and so we need to have the instrument that can measure instantaneously and RAD7 that is currently available in the market has been demonstrated to be useful for this purpose. A fast monitoring of thoron level is to set RAD7 by listening to the beeps, with the tone set to Geiger mode, and monitoring the status display which will show if the beep is in the B (thoron) window. The sample location corresponding to the highest count rate of thoron is the entry point of radon.

2.2.8 Summary and Future Direction

A large number of methods have been developed for ^{222}Rn (and a few methods for thoron) for a number of sample matrices and for different applications. The precision/accuracy of measurements depends on the applications. Indoor radiation dose assessment requires generally lower precision compared to grab samples from a marine environment where it is used as a tracer for gas-exchange studies. The spatial and temporal variability of radon in subsurface media (soil air and groundwater) limits the desired precision. However, in oceanic and limnological studies where radon is used as a tracer, higher precision is desired. The throughput for such a study is low and enhancing throughput with higher precision is needed. Overall, there are sufficient methodologies and instruments exist in recent literature which overall meets the research needs.

References

Ashokkumar P, Sahoo BK, Raman A, Mayya YS (2014) Development and characterization of a silicon PIN diode array based highly sensitive portable continuous radon monitor. J Radiol Prot 34:149–160

Broecker WS (1965) An application of natural radon to problems in oceanic circulation. In: Ichiye DT (ed) Symposium on diffusion in ocean and fresh waters, pp. 116–45. Lamont-Doherty Geological Observatory, Palisades, NY [5.5.3, 10.4.2, 10.5, 10.5.1, 11.5]

Broecker WS, Peng T-H (1971) The vertical distribution of radon in the BOMEX area. Earth Planet Sci Lett 11:99–108

Burnett WC, Kim G, Lane-Smith D (2001) A continuous radon monitor for assessment of radon in coastal ocean waters. J Radioanal Nucl Chem 249:167–172

Burnett WC, Dimova N, Dulaiova H, Lane-Smith D, Parsa B, Szabo Z (2007) Measuring thoron (^{220}Rn) in natural waters. In: Warwick P (ed) Environmental radiochemical analysis III. Royal Society of Chemistry, RSC Publishing, Cambridge, pp 24–37

Chambers SD, Hong S-B, Williams AG, Crawford J, Griffiths AD, Park S-J (2014) Characterizing terrestrial influences of Antarctic air masses using Radon-222 measurements at King George Island. Atmos Chem Phys 14:9903–9916. doi:10.5194/acp-14-9903-2014

Chauhan RP, Kumar A, Chauhan N, Joshi M, Aggarwal P, Sahoo BK (2014) Ventilation effect on indoor radon-thoron levels in dwellings and correlation with soil exhalation rates. Indoor Built Environ. doi:10.1177/1420326X1454288

Corbett DR, Chanton J, Burnett W, Dillon K, Rutkowski C, Fourqurean J (1999) Patterns of groundwater discharge into Florida Bay. Limnol Oceanogr 44:1045–1055

Dimova N, Burnett WC, Lane-Smith D (2009) Improved automated analysis of radon (^{222}Rn) and thoron (^{220}Rn) in natural waters. Environ Sci Technol 43:8599–8603

Duenas C, Perez M, Fernandez MC, Carretero J (1994) Disequilibrium of radon and its short-lived daughters near the ground with atmospheric stability. J Geophys Res 99(D6):12865–12872

Dulaiova H, Peterson R, Burnett WC, Lane-Smith D (2005) A multi-detector continuous monitor for assessment of ^{222}Rn in the coastal ocean. J Radioanal Nucl Chem 263(2):361–365

Eappen KP, Mayya YS (2004) Calibration factors for LR-115 (Type-II) based radon-thoron discriminating dosimeter. Radiat Meas 38:5–17

Fleischer RL (1988) Radon in the environment—opportunities and hazards. Geochim Cosmochim Acta 14(4):421–435

Fleischer RL, Giard WR, Mogro-Campero A, Turner LG, Alter HW, Gingrich JE (1980) Dosimetry of environmental radon: methods and theory for low-dose integrated measurements. Health Phys 39:957–962

Kotrappa P, Brubaker T, Dempsey JC, Stieff LR (1992) Electret ion chamber system for measurement of environmental radon and environmental gamma radiation. Radiat Prot Dosim 45:107–110

Krishnaswami S, Bhushan R, Baskaran M (1991) Radium isotopes and 222Rn in shallow brines, Kharagoda (India). Chem Geol 87:125–136

Kritz MA, Rosner SW, Stockwell DZ (1998) Validation of an off-line three-dimensional chemical transport model using observed radon profiles 1. Observations. J Geophys Res 103(D7):8425–8432

Kumar A, Chauhan RP, Joshi M, Sahoo BK (2013) Modeling of indoor radon concentration from radon exhalation rates of building materials and validation through measurements. J Environ Radioact 127C:50–55

Larson RE (1978) Radon measurements during marine fog events off Nova Scotia. J Geophys Res 83(C1):415–418

Lucas HF (1957) Improved low-level scintillation counter for radon. Rev Sci Instrum 28:680–683

Mathieu GG, Biscaye PE, Lupton RA, Hammond DE (1988) System for measurement of Rn-222 at low-levels in natural waters. Health Phys 55(6):989–992

Mayya YS, Mishra R, Prajith R, Gole AC, Sapra BK, Chougaonkar MP et al (2012) Deposition based passive monitors for assigning radon, thoron inhalation doses for epidemiological studies. Radiat Prot Dosim 152:18–24

Mishra R, Sapra BK, Mayya YS (2009a) Development of an integrated sampler based on direct $^{222}Rn/^{220}Rn$ progeny sensors in flow-mode for estimating unattached/attached progeny concentration. Nucl Instrum Methods Phys Res B 267:3574–3579

Mishra R, Mayya YS, Kushwaha HS (2009b) Measurement of $^{220}Rn/^{222}Rn$ progeny deposition velocities on surfaces and their comparison with theoretical models. J Aerosol Sci 40:1–15

Monnin M, Seidel JL (2002) Pressure response of radon detecting devices placed at depth in aquifers. Geofisica Int 41(3):229–232

Papastefanou C (2002) An overview of instrumentation for measuring radon in soil gas and groundwaters. J Environ Radioact 63:271–283

Porcelli D, Baskaran M (2011) An overview of Isotope Geochemistry in Environmental Studies. In: Baskaran M (ed) Handbook of environmental isotope geochemistry, pp. 11–32. Springer (ISBN: 978-3-642-10636-1)

Schubert M, Paschke A, Lieberman E, Burnett WC (2012) Air-water partitioning of ^{222}Rn and its dependence on water temperature and salinity. Environ Sci Technol 46:3905–3911

Streil T, Heinecke J, Koch U, Oeser V, Wiegand J (1997) EPOS 1-A multiparameter measuring system for earthquake prediction research. In: Biagi PF (ed) IVth International Conference on Rare Gas Geochemistry, University of Rome III, Rome, Italy, 8–10 December 1997

Williams AG, Zahorowski W, Chambers S, Griffiths A, Hacker JM et al (2011) The vertical distribution of radon in clear and cloudy daytime terrestrial boundary layers. J Atmos Sci 68:155–174. doi:10.1175/2010JAS3576.1

Chapter 3
Mechanisms of Radon Emanation and Long-Term Radon Flux Studies

3.1 Introduction

Investigations of radon emanation rates from Earth's surface have implications for many fields in Earth and atmospheric sciences. The temporal and spatial variations in the release rates of radon emanation to air and water have been utilized as tracers for locating subsurface uranium and hydrocarbon deposits (Chap. 9), predicting earthquakes (Chap. 10), and sources of air masses (Chap. 4). Radon and its progeny are utilized as powerful tracers to quantify atmospheric processes including source tracking and transport (within and between the troposphere and stratosphere), time scales of air mass stability and vertical movement, removal rates and residence times of aerosols, sources of continental dust in an air mass, and gas exchange studies at air-sea interfaces (e.g., Baskaran 2011). For all these studies, a thorough understanding of the factors and processes that control the radon emanation rates from rocks/minerals/soils is essential.

Radon atoms located within a solid grain are unlikely to escape the mineral grain due to low diffusion coefficients in solids (10^{-25}–10^{-27} m^2 s^{-1}). However, it is widely recognized that radon escapes from a mineral grain as a result of its recoil when its parent, radium, undergoes radioactive decay. When radon atoms formed from the decay of radium escape from the grains, mainly because of recoil, and go into the interstitial space between the grains, they can be transported by diffusion (molecular diffusion coefficient in air and water are 1×10^{-5} m^2 s^{-1} and 1×10^{-8} m^2 s^{-1}, respectively) and advection causing the movement of the emanated radon atoms towards Earth's surface. Processes leading to the release of radon from subsurface and eventual transport to the atmosphere are shown in Fig. 3.1.

The number of radon atoms released per number of atoms generated is known as radon emanation coefficient (also known as emanation fraction, emanation power). The radon emanation coefficient in naturally-occurring earth materials (rocks, soils, minerals, uranium mine tailings) varies over 4 orders of magnitude, with the lowest values reported for zircon (0.00001) and highest value of 0.7 for volcanic ash—deep
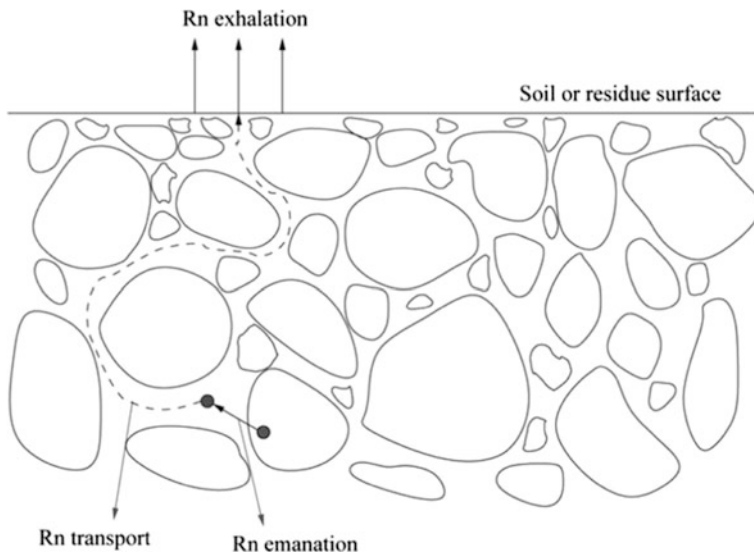
Fig. 3.1 Mechanism leading to radon release to the atmosphere

agricultural soils from Tuxedo, New Mexico, USA (from a summary of radon emanation coefficients for over 1000 data points given in Nazaroff 1992; Sakoda et al. 2011; Eakin et al. 2016). There is a large variation even within one mineral, zircon, from 0.001 to 2.2 % (excluding a weathered zircon sample) (data summarized in Eakin et al. 2016). From a synthesis of a large sets of data, Sakoda et al. (2011) reported REC values ranging over 2–4 orders magnitude (minerals: 0.0001–0.25), rocks (0.0051–0.40), soils (0.001–0.83, mill tailings (0.02–0.33) and fly ashes (0.00096–0.35)). Generally, higher REC values for soil and tailings arise from radium-enriched grain surface.

In this chapter, the mechanisms of radon emanation and the factors that control the variations in radon emanation coefficient are discussed. A brief summary of radon emanation studied at lunar surfaces (where there is only a diffusional component of transport with no advection component) is also presented.

3.2 Comparison of Recoil Length to Diffusion Length for ^{222}Rn

From the conservation of momentum of a system of ^{226}Ra (parent)-^{222}Rn (daughter) and alpha particle produced from the decay of ^{226}Ra, one can calculate that a ^{222}Rn atom will possess a kinetic energy of 86 keV (Bossus 1984). The recoil distance traveled by the newly formed Rn atom, which is a measure of the distance between the site of generation and the point where its kinetic energy is transferred

Table 3.1 Alpha recoil ranges of [220]Rn and [222]Rn in various matrices

Medium	Density (g cm^{-3})	Range (nm) [220]Rn	Range (nm) [222]Rn
Air	1.58×10^{-3}	60,000	53,000
Water	1.00	87	77
Quartz (SiO$_2$)	2.65	38	38

Data taken from IAEA (2013)

to the host material, depends on the density, lattice structure and composition of the material. The range of recoil distances have been reported to be 20–70 nm for common minerals, ~ 77 nm for water and 5.3×10^4 nm (53 μm) in air (Table 3.1). One can compare these recoil distances to the diffusion lengths in minerals.

The diffusion coefficients (D) for radon has been reported to vary between 10^{-25} and 10^{-27} m^2 s^{-1} (Ishmori et al. 2013). The corresponding diffusion length (L) can be calculated as follows:

$$L = \sqrt{(D\tau)} \tag{3.1}$$

where τ is the mean-life of radon (=5.51 days). The diffusion length ranges between 0.02–0.2 nm, which is one to three orders of magnitude lower than that of the recoil distances and hence the escape of radon from intact mineral grains by diffusion is negligible. Furthermore, one can determine the in situ radon diffusion length from the vertical depth profile of [222]Rn in soil gas. From diffusion theory, the radon concentration C(z) at depth z follows the equation:

$$C(z) = C_\infty(1 - \exp(-z/L_r)) \tag{3.2}$$

where C_∞ is [222]Rn concentration at infinite depth (Bq m^{-3} of soil gas), z is the thickness of the material and L_r is the radon diffusion length. From a plot of [222]Rn activity concentration (Bq m^{-3} soil gas) versus depth from surface, one can estimate L_z based on the relationship given in Eq. (3.2) (Ishmori et al. 2013).

3.3   Radon Emanation Rates from Earth's Surface

3.3.1   Radon Diffusive Transport in Soil Pores

The random molecular motion of radon is such that in the presence of horizontal or vertical concentration gradients, there is a net migration of Rn from regions of high concentration to low concentration. A major mechanism of transport of radon from the surface soils to the atmosphere is by molecular diffusion (e.g., Tanner 1980; Nazaroff 1992). The flux density, J_d, resulting from molecular diffusion, is the amount of [222]Rn passing through a given cross section per unit area per unit time and is proportional to the concentration gradient (dC_{Rn}/dx) (known as Fick's law). If D_0 is the molecular diffusivity (m^2 s^{-1}), C_{Rn} is the concentration of [222]Rn (Bq m^{-3}),

$$F_d \left(\mathrm{Bqm}^{-2}\, \mathrm{s}^{-1} \right) = -D_0\, dC_{Rn}/dx \tag{3.3}$$

where C_{Rn} is ^{222}Rn concentration per volume of soil gas; dC_{Rn}/dx is a negative quantity in the direction of diffusion. The diffusivity of radon in free air is 1.2×10^{-5} m^2 s^{-1} but in soil gas the diffusion is constrained by the solid grains. The area through which radon can diffuse is reduced in solid grains and the average path length to reach the surface soil (Fig. 3.1) is increased. Thus, the diffusion coefficient in soil air needs to be modified, with an effective diffusion coefficient (D_e), which incorporates porosity of the soil and diffusion coefficient in air. The diffusive flux density of ^{222}Rn activity per unit of air filled pore area of the soil (J_s^d) is given by:

$$J_s^d = -D_e\, dC_{Rn}/dx \tag{3.4}$$

The effective diffusion coefficient is reported to vary between 2.5×10^{-6} m^2 s^{-1} in compacted inorganic clays to 6.0×10^{-8} m^2 s^{-1} in silty sandy clay with a moisture content of 17.3 % of dry weight (values summarized in Nazaroff 1992). The typical effective diffusion coefficient value of 3×10^{-6} m^2 s^{-1} in a typical subsurface material is about a factor of 4 smaller than the diffusion coefficient of radon in open air (Nazaroff 1992).

3.3.2   Diffusive Flux into the Atmosphere

Using the conservation of radon concept in the soil pores, a mass balance equation for the soil gas ^{222}Rn can be written (Nazaroff 1992). If C_a is the concentration of ^{222}Rn in the gas phase (Bq per m^3 of pore air), the total ^{222}Rn accumulated (or input) = diffusive transport ($\varepsilon_a D_e \nabla^2 C_a$) + generation rate of mobile ^{222}Rn ($f A_{Ra} \lambda_{Rn} \rho$)—radioactive decay ($-\lambda_{Rn} C_a [\varepsilon_a + k\varepsilon_w + \rho K]$).

$$
\begin{aligned}
[\varepsilon_a + k\varepsilon_w + \rho K]\frac{\partial C_a}{\partial t} = {}& \varepsilon_a D_e \nabla^2 C_a \\
& - \lambda_{Rn} C_a [\varepsilon_a + k\varepsilon_w + \rho K] + f A_{Ra} \lambda_{Rn} \rho
\end{aligned}
\tag{3.5}
$$

where $\varepsilon_a, k, \varepsilon_w,$ and ρ are the air-filled porosity, intrinsic permeability of soil (m^2), water-filled soil porosity, and dry bulk density of soil (kg m^{-3}) respectively; K, D_e, and f are the partition coefficient for sorption (m^3 kg^{-1}), effective diffusion coefficient (m^2 s^{-1}) and emanation coefficient, respectively; A_{Ra} and λ_{Rn} are the radium content of the soil (Bq kg^{-1}) and radioactive decay constant of radon (2.10×10^{-6} s^{-1}), respectively. The first term in the right-hand side (RHS) stands for changes due to Fickian transport if there is spatially varying concentration gradient of ^{222}Rn. The second term in RHS is for the radioactive decay of ^{222}Rn and the last term in RHS stands for the generation rate of mobile ^{222}Rn from the decay of its parent, ^{226}Ra.

In Eq. (3.5), the implicit assumptions are: (i) equilibrium partitioning between sorbed, aqueous and gas-phase of radon; (ii) the values of ε_a and D_e are assumed to be constant throughout the soil; (iii) transport is only by gas phase diffusion; and (iv) the fractional area of any plane through the soil that is occupied by pore air is equal to the air-filled porosity. The accumulation is denoted by the time derivative of the LHS, and the terms on RHS account, respectively, for diffusive transport, decay and production of radon.

One special case is where Eq. (3.5) can be utilized for diffusive radon migration through uncovered, uniform soil of infinite depth. The steady-state solution to the one-dimensional form of Eq. (3.5), assuming that ^{222}Rn concentration at the surface is 0, yields the radon activity concentration in soil pore air at a depth z′ below the surface is given by Eq. (3.6):

$$I_a(z') = I_\infty \left(1 - e^{-z'/\vartheta} \right) \tag{3.6}$$

where

$$I_\infty = \frac{A_{Ra} f \rho}{(\varepsilon_a + k\varepsilon_w + K\rho)} \tag{3.7}$$

$$\vartheta = \left[\frac{D_e}{\lambda_{Rn}} \right]^{1/2} \left[\frac{\varepsilon_a}{(\varepsilon_a + k\varepsilon_w + K\rho)} \right]^{1/2} \tag{3.8}$$

I_∞ represents the activity concentration of radon in the pore air at large depths (z′ ≫ ϑ) and ϑ is the diffusion length which is a characteristic distance over which radon may diffuse through soil during the mean-life of ^{222}Rn. The typical distance for ^{222}Rn for dry moist soils is ∼1 m, but in wet soils, it will be much smaller because of smaller effective diffusivities (Nazaroff 1992).

The radon activity flux density (J^d) due to diffusion is given by:

$$J^d = \varepsilon_a D_e I_\infty / \vartheta = A_{Ra} f \rho (\lambda_{Ra} D_e)^{1/2} \left[\frac{\varepsilon_a}{(\varepsilon_a + k\varepsilon_w + K\rho)} \right]^{1/2} \tag{3.9}$$

For typical values for the parameters in Eq. (3.9) (A_{Ra} = 30 Bq kg^{-1}; emanation coefficient, f = 0.2; soil dry density, ρ = 1600 kg m^{-3}; effective diffusivity, D_e = 3 × 10^{-6} m^2 s^{-1}; air-filled porosity, ε_a = 0.27; water-filled porosity, ε_w = 0.13; aqueous-gaseous partition coefficient, k = 0.25; and sorbed-gaseous partition coefficient, K = 1.4 × 10^{-5} m^3 kg^{-1}), Nazaroff (1992) reported a surface flux density, J_D = 0.022 Bq m^{-2}s^{-1}. This value can be compared to other published values reported in literature (mean worldwide flux from Earth's surface to be approximately 0.015 Bq m^{-2}s^{-1} by Wilkening et al. (1972); for Australian soils, average, seasonally-adjusted value of 0.022 ± 0.005 Bq m^{-2} s^{-1} by Schery et al. (1989); and mean flux from North American soils of 0.040–0.048 Bq m^{-2} s^{-1} by Graustein and Turekian (1990)). Note that the prediction of radon flux requires D_e (=porosity ×

diffusion coefficient) which can be directly estimated using the in situ accumulator technique (Ishmori et al. 2013).

3.4   Mechanisms of and Factors Affecting Radon Release Rates

3.4.1   Mechanisms of Radon Release from Mineral Grains

The radon emanation process includes a direct component from alpha recoil from outer and inner surfaces of grains and diffusion in grains. The indirect component includes diffusion in the inner pores of grains, adsorption on the inner surfaces of grains, embedding into adjacent grain and diffusion-based release after embedding (Sakoda et al. 2011) and these processes are illustrated in Fig. 3.2.
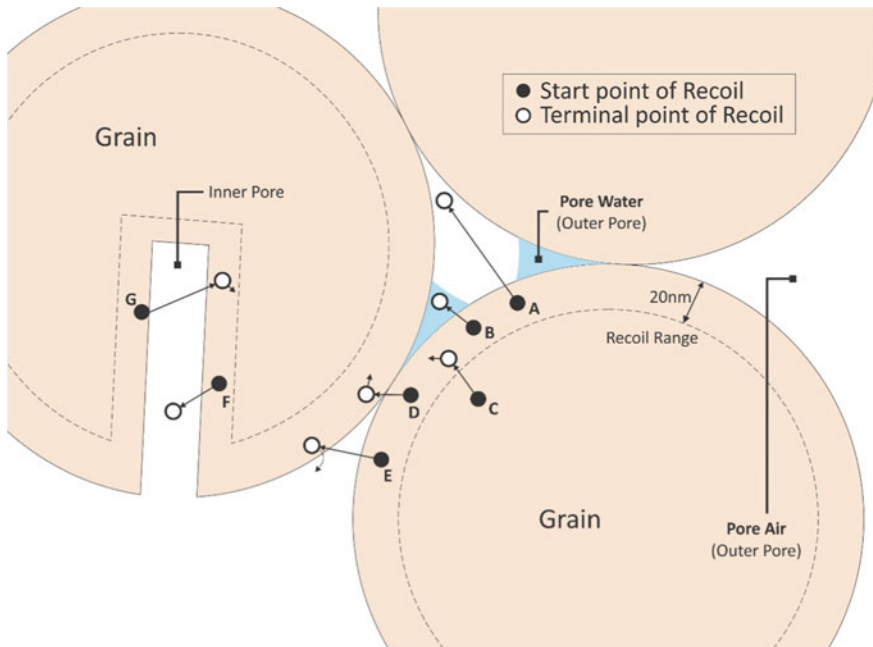
Fig. 3.2 Schematic illustration of radon emanation. The start point (*filled circle*) is where ^{226}Ra undergoes radioactive decay and the terminal point (*open circle*) is where the ^{222}Rn atom ends after losing all its kinetic energy after recoil. The recoil range for a spherical grain is illustrated. Atoms *A*, *B*, *E*, and *F* will undergo emanation. Atom *C* is located not in the recoil range and hence it ends up close to the surface of the mineral grain, but will not undergo emanation; atoms *D*, *E* and *G* located within the recoil distance land onto adjacent grain (or deeper inside the grain) and does not emanate. *Arrows* following terminal points of recoil represent movement due to diffusion process (not to scale). From Sakoda et al. 2011, with permission from Elsevier

The measured emanation coefficient from undamaged soil grains in which radium is distributed uniformly is much higher than expected. One can estimate the fraction of ^{222}Rn escape from a spherical grain of 15 μm diameter (size), assuming that ^{226}Ra is distributed uniformly. Taking the upper range of 0.070 μm as the recoil range, the fractional volume of the outer 0.070 μm [=(volume of whole sphere of radius 7.5 μm—volume of inner sphere of radius 7.43 μm)/volume of whole sphere of radius 7.5 μm] is 2.8 %. The computed escape probability for ^{222}Rn atoms generated within the recoil range of a spherical particle surface is reported to be 25 % (Bossus 1984). Thus, for the 15 μm diameter particle, only 0.7 % of the ^{222}Rn atoms generated will leave the grain during recoil. Several hypotheses have been proposed to explain for the large discrepancy between measured emanation coefficients and those predicted by the theory (Tanner 1980). The main hypotheses are: (i) inhomogeneous distribution of mineral grains, mainly incorporation of ^{226}Ra in accessory minerals (Krishnaswami and Seidemann 1988); (ii) radiation damage caused by both alpha decay and recoil nuclear tracks to the crystalline structure in the vicinity of radium atoms and chemical erosion caused in the minerals. These damages in the lattice structure facilitate the leaching of the mineral in the damaged zone, thereby increasing the emanation coefficient. U- and Th-enriched minerals such as uraninite, betafite, cerite, thorite, etc. have very high concentrations of ^{238}U and/or ^{232}Th, and are commonly in secular equilibrium with their daughter products. However, it was later shown that radiation damage alone does not significantly increase radon escape by diffusion; and (iii) existence of submicronic pores within the mineral result in the formation of a network of channels through which enhanced amounts of radon can diffuse (Rama and Moore 1984, 1990). However, subsequent experiments with argon did not support the nanopore hypothesis and the high radon emanation rate of ^{222}Rn was attributed to the presence of U and its daughter products in accessory minerals in grain boundaries (Krishnaswami and Seidemann 1988). Recent studies on heated zircon minerals indicate fission tracks and radiation damage exert control over radon emanation rates and the radon emanation coefficient decreased inversely with the fission track density (Eakin et al. 2016). Complete annealing of fission and recoil tracks led to the highest radon emanation coefficient indicating that criss-crossed networks of tracks could serve as 'resistance' to the transport of radon in the crystal lattice structure.

3.4.2 Factors that Affect Radon Emanation Rates in the Environment

3.4.2.1 Radium Distribution and Granulometric Parameters

The particle size, shape and location of ^{226}Ra determines the amount of radon that can escape into interstitial pores. If radium is distributed uniformly within a grain, the radon emanation fraction from a spherical grain can be expressed as follows:

(1) Homogenous radium distribution in the grain:

Amount of Ra α V (volume of the grain); amount of Rn emanating α S (surface area of the grain) → Radon emanation fraction, F, α S/V α 1/diameter of the grain, d

(2) Radium distribution concentrated on the grain surface, either via sorption of Ra-enriched Fe/Mn-oxyhydroxide precipitates and other sedimentary deposits and residues such as sand filters, or sorbed Ra on the surface or Ra in accessory minerals at grain boundaries:

Amount of Ra α S; amount of Rn emanation fraction α S → F ∼ constant.

For a grain with homogeneous Ra distribution, the radon emanation fraction, $F_{uniform}$, in the single-grain model is given by Morawska and Phillips (1993):

$$F_{uniform} = (3R/2d) - (1/16) * (2R/d)^3 \qquad (3.10)$$

where R is the recoil length (μm) of radon in the grain. It can be observed from Fig. 3.3 that for grains more than 10 μm size (diameter), very little radon escapes the grain. In cases where (R/d) ≪ 1, the radon emanation fraction will be inversely proportional to grain size. The radon emanation fraction estimated using Eq. (3.10) is an upper limit, since the fraction of radon getting implanted on another adjacent grain is not taken into account. Measured radon coefficient values are significantly higher than those predicted from Eq. (3.10) and hence the assumption of uniform radium distribution in mineral grains has been questioned. Calculation for a single-grain model for the radon emanation fraction, under the assumption that radium exists only on the grain surface, is given by Morawska and Phillips (1993) as follows:

$$F_{surface} = (1/2) * (1 + R/d) \qquad (3.11)$$

Fig. 3.3 Calculated variations in the ^{222}Rn emanation coefficient with particle diameter and surface coating of ^{226}Ra versus homogenously distributed within mineral grains. Thickness of the surface coating is assumed to be 40 nm, comparable to the recoil range (Greeman and Rose 1996, with permission from Elsevier)
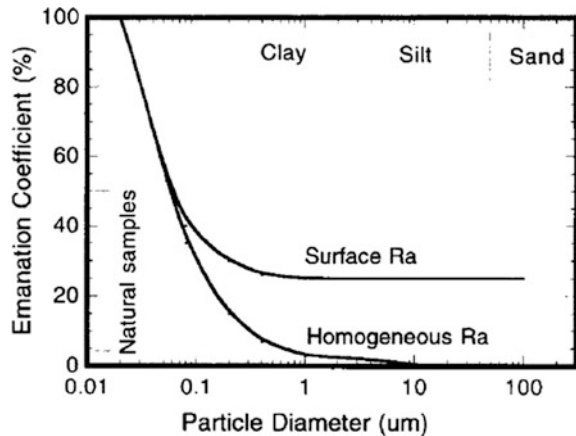
In Fig. 3.3, the radon emanation fraction from radium located on the surface of a grain first decreases and then reaches a constant value of ~ 0.5 with increasing grain size. From the measurements of radon emanation from uranium waste residue repository in 40 locations, it was shown that the calculated in situ ^{222}Rn diffusion length, radon emanation coefficient (both in situ and dry), total porosity and bulk dry density remained the same in all four seasons (within 2σ; Ishmori et al. 2013). Rama and Moore (1990) showed that the radon emanation coefficient from a large block $(30 \times 30 \times 30$ cm) of granite yielded values similar to that for millimeter size grains $(\sim 15$ %) and they attributed this to internal openings within a grain that connected and extended over large distances. The emanation coefficient for ^{220}Rn in large crystals was found to be lower than that of ^{222}Rn and was attributed differences in the diffusion lengths of ^{220}Rn and ^{222}Rn. Dry and large size crystals (masses are given in Table 3.2)

Table 3.2 Comparison of the emanation rates of ^{220}Rn and ^{222}Rn and emanation coefficient in single crystals of a suite of apatite, monazite uraninite and zircon minerals

Sample	Emanation rate (atoms min^{-1} gm^{-1})		Activity of parent radium (disintegration min^{-1} gm^{-1})		Emanation coefficient from ^{222}Rn (%)
	E^{220}Rn	E^{222}Rn	^{224}Ra	^{226}Ra	
1. Apatite conglomerate (~ 5 mm size, 180 g)	0.08 ± 0.01	0.070 ± 0.005	28	15	0.5
2. Apatite crystals ~ 5 mm size (91 g)	0.12 ± 0.01	0.072 ± 0.005	28	15	0.5
3. Apatite twined crystals of $\sim$ equal size joined at one point (70 g)	0.61 ± 0.03	1.4 ± 0.1	14	5.7	25
4. Monazite single crystal-A, 222 g	177 ± 10	23 ± 1	11,200	400	6
5. Monazite single crystal-B 68 g	206 ± 10	76 ± 3	10,700	500	15
6. Monazite (0.224 g)	158 ± 5	4 ± 1	10,000	400	1
7. Uraninite (0.455 g)	56 ± 5	7600 ± 500	3,600	393,000	1.9
8. Zircon, 12.0 g	0.08 ± 0.05	0.034 ± 0.002	108	270	0.01
9. Zircon, 7.0 g	0.05 ± 0.05	0.005 ± 0.001	122	467	0.001
10. Zircon tuxedo, 11.1 g	0.06 ± 0.05	0.055 ± 0.003	87	378	0.01
11. Zircon tuxedo	0.140 ± 0.08	0.014 ± 0.001	95	327	0.004

Data from Rama and Moore (1990)

of apatite, monazite and uraninite have large emanation coefficients (up to 25 %) compared to zircon (0.01–0.001 %, Table 3.2, Rama and Moore 1990). An emanation coefficient of 15 % can be viewed as emanating minerals comprised of micrometer size grains with air gaps in between and a millimeter grain comprised of one billion granulates of micrometer size, with air gaps in between. Since the porosity of the minerals is small (<1 %), Rama and Moore (1990) proposed that the gaps are expected to be narrow, of the order of a few nanometers. Cracks and fissures on grain surfaces from previous radioactive decays and chemical and/or physical weathering effects can also increase the surface area of the grain leading to higher radon emanation coefficient.

3.4.2.2 Effects of Moisture Content and Mineralogy on Radon Emanation Coefficient

Moisture content and mineralogy have strong effects on the emanation coefficient. The recoil range for radon in water is much less than that in air (air: 53,000 nm; water: 77 nm; quart (SiO_2): 34 nm for ^{222}Rn; Table 3.1; Ishmori et al. 2013) and hence water is more effective at stopping ^{222}Rn atoms within the pore space. Effects of moisture content on the ^{222}Rn emanation coefficient for a sample of uranium mill tailing is shown in Fig. 3.4 (Strong and Levins 1982). Several studies have shown that the emanation coefficient is much lower if the source material is dry rather than moist or wet. If we take an average pore dimension of 0.5–50 μm, a radon atom will have a much higher probability of terminating its recoil in a pore that is filled (or partially filled) with water compared to one that is dry. A radon emanation study with 200–800 μm saprolite showed that ∼18 % of the ^{222}Rn generated in the bulk of the sand emanated into the water that could be easily drained from the sand

Fig. 3.4 Effect of moisture content on radon emanation coefficient for a sample of uranium mill tailings (Figure is taken from Strong and Levins 1982, with permission of Health Physics Society)
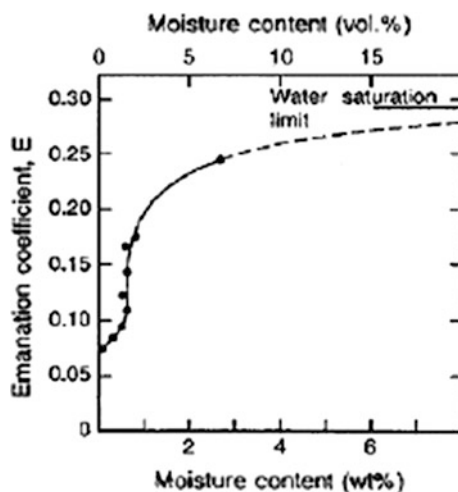
(Rama and Moore 1984). Dissolution of solids could not explain this high radon rate and thus, radon must be escaping in other ways. Washing the saprolite with a mild leachant to remove adsorbed ^{226}Ra did not result in any change in the radon emanation rate. Rama and Moore (1984) reported that saprolite is permeated with pores, with a width opening at the surface of less than a micron, and they suggested that radon diffusing out of these body pores into intergranular pores which have dimensions of hundreds of microns. The empirical equation that relates the radon emanation in dry conditions to moisture saturation is given by Zhuo et al. (2006):

$$\text{Emanation coefficient}, E = E_0[1 + 1.85(1 - \exp(-18.8m)] \qquad (3.12)$$

where E_0 is the radon emanation coefficient in dry condition, and m is the fraction of pore space filled with water.

Several mineralogical aspects such as grain sizes and shape, lattice structure, internal porosity, and elemental composition also affect the radon emanation coefficient. Residues from the mining and milling operations of uranium ores and other resource extraction industries (e.g., phosphogypsum from the phosphate industry, from the oil, gas and coal industries and residues from mineral sands) contain higher concentrations of uranium and/or thorium series radionuclides and are referred to as naturally occurring radioactive materials, most commonly known as NORM. Release of radon from NORM residues is one of the radiological impacts in the environment. Mineralogical characteristics of NORM residues are an important factor in the emanation rates of radon.

3.4.2.3   Effect of Temperature on Radon Emanation Coefficients

Temperature differences between air and soil have also been found to be a factor influencing ^{222}Rn flux (Nazaroff 1992). It is widely known that radon from an air stream can be trapped at temperatures below −10 °C on activated charcoal (Chap. 2), soil CO_2 at −78.5 °C or on glass wool cooled to the temperature of liquid N_2, −196 °C. Since the partial pressure of ^{222}Rn in environmental conditions is very low, radon condenses on surfaces at approximately −150 °C (Rutherford and Soddy 1903). Since the air temperature and relative humidity in air are inversely related, the moisture content of surface soil is related to air temperature and the radon emanation rate is expected to be higher at warmer air and soil temperatures compared to colder temperatures.

3.4.2.4   Effect of Pressure on Radon Emanation Coefficients

It has been shown that the variations in atmospheric pressure can affect ^{222}Rn flux from the Earth's surface. For example, a pressure variation of 6.8 mb ($\sim$0.2 in Hg) can result in a modest enhancement of flux of $\sim$10 % (Schery and Gaeddert 1982).

Pressure changes of 1–2 % associated with the passage of frontal systems is reported to have resulted in variations in ^{222}Rn flux of 20–60 % from Earth surface (Clements and Wilkening 1974). In a majority of houses where high indoor radon concentrations are observed, these concentrations are attributed to a small pressure differential between the basement and living place, resulting in a suction effect due to the lower pressure at the basement. When the soil air pressure is slightly higher than at the soil-air interface, more ^{222}Rn is likely to be released to the air.

3.4.3   Radon in Emanation in Lunar Surface

Radon is constantly transported from the earth by a combination of convection and diffusion while on the lunar surface it is primarily transported by diffusion. For all consideration, the lunar surface is considered to be surrounded by a vacuum, due to very low atmospheric density, 10^{-14} as that of the Earth's atmospheric density. Hence, the rates of diffusion of radon in the lunar surface is also expected to be much higher, as much as a factor of 10, due to existing vacuum conditions above the lunar surface (Kraner et al. 1966). The escape velocity (v_e) on the lunar surface with respect to the Moon's gravity is 2.4 km s^{-1} (v_e = 11.2 km s^{-1} on Earth's surface) and hence the Rn that escapes from lunar surfaces is expected to return back to the lunar surface, primarily due to the lack of convection currents in the atmosphere. The calculated thermal velocities of a radon atom of 0.04 and 0.12 km s^{-1} for the corresponding night and day time extreme temperatures of −233 °C (40 °K) and 123 °C (396 °K), respectively, are much lower than that of the escape velocity. In the Apollo 15 mission, for the first time in human history, mapping the spatial distribution of atomic and nuclear radiation at the lunar surface and relating the spectral quality of the fluxes to the chemical composition of the physical conditions at the lunar surface was attempted. The ^{222}Rn alpha particle density was reported to be higher by a factor of at least 4 at the vicinity of the crater Aristarcus compared to the lunar average (Gorenstein and Bjorkholm 1973). Although the concentrations of U and Th in lunar surface material are comparable to that of the average terrestrial flux values, the average radon emanation rate 9–13 atoms m^{-2} s^{-1} (a wide range of values, < 5,000 to 13,000 atoms m^{-2} s^{-1}, based on equilibrium ^{210}Po activity summarized in Brodzinski (1972)), is two to three orders of magnitude smaller than that of the Earth, 5,000–10,000 atoms m^{-2} s^{-1} (Gorenstein and Bjorkholm 1973; Baskaran 2011). Factors such as grain size, porosity or permeability do affect radon emanation rates, but are of secondary importance. The interaction between the soil and the lower atmosphere, mainly atmospheric conditions above the soil, is the primary driver that results in much higher Rn emanation rate on the Earth compared to the moon where interaction between soil and atmosphere does not exist.

3.4.4   *Methods of Radon Flux Measurements*

A large body of data exists on the ^{222}Rn flux (Bq m^{-2} s^{-1}) obtained both by direct measurements (measured directly from the collection of air samples containing ^{222}Rn emitted from a known area of soil) and from the integration of ^{222}Rn profiles in the atmosphere or excess ^{210}Pb profiles in soils, ice cores or sediment cores from lakes and coastal oceans by estimating the flux and assuming balance between ^{222}Rn emanation and decay (summarized in Robbins 1978; Turekian et al. 1977; Turekian and Graustein 2003). Each of these methods have their own limitations. Direct measurements are from very narrow areas and the assumption of steady state between emanation and decay is questionable when a maritime air mass intrudes a continental air mass (such as maritime tropical air masses mixing with continental and continental polar air masses). Radon accumulated in chamber method provides snapshot data at a particular site under certain types of conditions (e.g., variable amounts of soil moisture, temperature, humidity, pressure conditions) and the practical difficulty in having spatial and temporal measurements is the limiting factor. Radon flux obtained from the measured vertical profiles of ^{222}Rn in the atmosphere provides data integrated over a period of its mean-life of ^{222}Rn (flux = inventory (Bq m^{-2}) /mean life of ^{222}Rn (4.76×10^5 s)). Indirect method includes (i) Measurements of ^{222}Rn in interstitial gas in soils and modeling the ^{222}Rn data to determine diffusive flux (Dorr and Munnich 1990); (ii) Determination of long-term ^{222}Rn flux from the measurements of ^{210}Pb depositional flux or inventory of ^{210}Pb in ice cores, sediment cores from lakes and coastal oceans and soil profiles; and (iii) Terrestrial gamma radiation (TGR) method. Other long-term radon flux data have been analyzed by researchers (Lopez-Coto et al. 2013; Karstens et al. 2015). Some of the commonly used indirect methods of ^{222}Rn flux determination are described below.

3.4.5   *Radon Flux from Soils Using Terrestrial Gamma Radiation*

Terrestrial gamma radiation (TGR also known as gamma dose rate, GDR) is used as a proxy to calculate the radon flux density. The TGR values are also determined from different techniques that include in situ gamma spectrometry, high pressure ionization chambers, thermoluminescent dosimeters, and dose calculations from the activity concentrations of ^{238}U, ^{232}Th and ^{40}K. The TGR from any soil originates from the top 20–30 cm in the soil, primarily from the decay of ^{238}U, ^{235}U- and ^{232}Th-series radionuclides and ^{40}K. Automated radiation monitoring networks are common in several countries and estimation of the radon emanation rates from these data requires delineation of local influence, radiation from anthropogenic radionuclides, and other background radiation than those released from the decay of ^{222}Rn daughter products. For example, automatic monitoring has been networked in 25 European countries by the Institute for Environmental Sustainability at the Joint

Research Center (JRC IES) in Ispra, Italy (Szegvary et al. 2007). The TGR at 1 m above ground level can be calculated as follows (*United Nations Scientific Committee on the Effects of Atomic Radiation*, UNSCEAR 2000):

$$TGR = 0.3234(^{238}U) + 0.423(^{232}Th) + 0.0292(^{40}K) \qquad (3.13)$$

where 0.3234, 0.4230, and 0.0292 are the dose conversion factors (nSv h^{-1} per Bq kg^{-1}) and (^{238}U), (^{232}Th) and (^{40}K) are the activities (Bq kg^{-1}) of ^{238}U, ^{232}Th and ^{40}K, respectively, in dry soils.

A number of radon flux measurements from large areas have been attempted (e.g., Zhou et al. 2008; Griffiths et al. 2010; Manohar et al. 2013; Karstens et al. 2015). For example, Zhuo et al. (2008) developed a comprehensive radon flux map for China and Szegvary et al. (2007) developed a European scale (based on a correlation between radon flux and the TGR from a network of 25 European countries). These large scale maps have their limitations. For example, Zhou et al. (2008) divided China into six regions that represent different climatic regimes. Within one region, there is a large variation in ^{222}Rn flux density. The Huainan and Jiangnan zone (II) has some of the highest ^{222}Rn flux (>60 mBq m^{-2} s^{-1}) as well as lowest (<20 mBq m^{-2} s^{-1}) fluxes and taking an average value for the whole zone
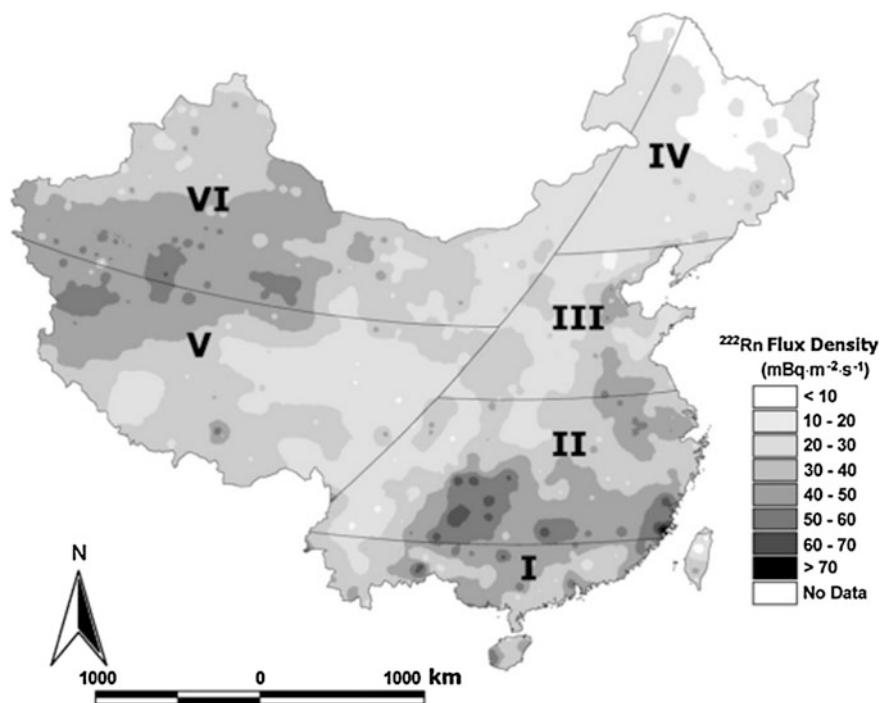
Fig. 3.5 Distribution of the annual average ^{222}Rn flux density from surface soil across China (from Zhou et al. 2008, JER-Elsevier)

will introduce a large uncertainty. Radon fluxes calculated from the depositional fluxes of ^{210}Pb for Xiamen, 8–10 mBq m^{-2} s^{-1}, is lower by a factor >3 reported in the ^{222}Rn flux map for China (Fig. 3.5). Most of these larger-scale maps are extrapolations from limited field data or model-based results. Based on the correlation between the measured ^{222}Rn flux and TGR, a relationship between these two are established. Szegvary et al. (2007) reported an empirical relationship between the terrestrial gamma radiation and radon flux through simultaneous measurements of both as:

$$^{222}\text{Rn flux (atoms cm}^{-2}\text{ s}^{-1}) = (11.8 \pm 1.3) * \text{TGR} (\mu\text{Sv h}^{-1}) - (0.15 \pm 0.11)$$

$$(3.14)$$

The TGR values are normalized for a value measured at 1 m above the ground surface (typical detector height; note that the TGR measured at 3.5 m above ground level is ~ 5 % lower than that measured at 1 m above the ground, Manohar et al. 2013). Other factors that affect the TGR values include local influence (such as gamma radiation emitted from building materials adjacent to the sites where background radiation is measured), variations in the anthropogenic radionuclides (e.g., ^{137}Cs), contributions from short-lived gamma-emitting radionuclides such as ^{212}Pb, ^{214}Pb, ^{214}Bi from the ambient air, and daughter products of ^{220}Rn. The presence of moisture in the soil pores could attenuate the transmission of the gamma radiation dose reaching the detector. Variations in the bulk density of soil also can affect the attenuation of gamma radiation. Variations in total pore space and tortuosity in the upper 20–30 cm are important variables that could affect the ^{222}Rn, but not TGR (Nazaroff 1992; Szegvary et al. 2007). As a result, Rn escape will be higher in soils with coarse grained (e.g., sand grains) than fine grained material such as clays and finer silt. The contribution to TGR value from the Chernobyl-derived ^{137}Cs in Netherlands is estimated to be 1 nSv h^{-1} (Manohar et al. 2013). However, this value is expected to be higher in the Baltic countries where the fallout was much higher whereas the fallout in North America was much lower and hence the Chernobyl-derived TGR value is expected to be negligible compared to the Baltic countries.

3.4.6 Radon Ocean Flux Density

The concentration of ^{226}Ra in water (mBq per gram of water) is very low compared to that in soils (mBq per gram of solid) on the Earth's surface. The average concentration of ^{226}Ra in the upper crust is ~ 31 mBq g^{-1} (assuming ^{238}U and ^{226}Ra are in secular equilibrium; ^{238}U concentration = 2.5 ppm; Wedepohl 1995) while the concentration in surface ocean water is $\sim 1.2 \times 10^{-3}$ mBq g^{-1} (average value, weighted for surface area) calculated based on ^{226}Ra activities in the coastal waters (3.3 mBq g^{-1}), Pacific Ocean (1.07 mBq g^{-1}) and Atlantic Ocean (1.23 mBq g^{-1}), Baskaran 2011).

The ^{222}Rn flux (F_{av}) from the ocean surface can be estimated from the following equation:

$$F_{av} \ (\text{mBq m}^{-2} \ \text{s}^{-1}) = C_{Ra226} v_w^2 \ \alpha_{Rn222}/\sqrt{S} \qquad (3.15)$$

where C_{Ra226} is concentration of ^{226}Ra (mBq m^{-3}) in the mixed layer, v_w is wind speed (m s^{-1}) at 10 m above the sea surface, α_{Rn222} is aeration coefficient (or inversion of the dimension of piston velocity, s m^{-1}), and S is the Schmidt number of radon in seawater which depends on the temperature of water. Although Schery and Huang (2004) divided the ocean into sectors and estimated 1180 mBq m^{-3} for latitude belts of −40° to + 40°, they did not take into account the natural ^{222}Rn variations in the coastal, shelf and slope waters and hence this estimate is of limited use. If we take the average width of the coastal ocean to be 2.4 km (=global ocean continental shelf surface area to be 1.4 10^6 km^2 /total global ocean coastal line length = 5.95 × 10^5 km; ∼7 % of the global surface ocean area), then ^{222}Rn and ^{226}Ra concentrations in coastal waters are expected to be significantly different compared to shelf/slope waters due to contributions of ^{222}Rn from radium and/or radon-enriched waters from SGD, rivers/streams, and industrial activities (e.g., phosphate production industries, etc.). Smethie et al. (1985) determined ^{222}Rn/^{226}Ra activity ratio of ∼0.7 in the surface mixed layer of the tropical Atlantic Ocean. The ratio of ^{222}Rn/^{226}Ra in groundwater varies widely (Chap. 8) and hence in the coastal waters this ratio is likely dominated by the amounts and frequency of submarine groundwater discharge as well. The lowest average annual flux density of 0.038 mBq m^{-2} s^{-1} (0.00182 atom cm^{-2} s^{-1}) for the entire ocean by Schery and Huang (2004) can be compared to other estimates: 0.14 mBq m^{-2} s^{-1} for the global ocean (Schery and Wasiolek 1998); 0.105 mBq m^{-2} s^{-1} for oceans from 60° N and 60° N (Jacob et al. 1997); and 0.21 mBq m^{-2} s^{-1} for 60° N and 60° N (Table 3.3, Taguchi et al. 2002). This range of ^{222}Rn flux from ocean surface, 0.0315–0.21 mBq m^{-2} s^{-1}, can be compared to a wide-range of corresponding values reported for the continents, from 14 mBq m^{-2} s^{-1} to 62 mBq m^{-2} s^{-1} (0.7–2.0 atom cm^{-2} s^{-1}).

Modelers of atmospheric transport of ^{222}Rn have assumed a constant flux density from the oceans, but Schery and Huang (2004) argued that there is variation by a factor of 10 or more between major areas of the ocean, such as large variations between January and July for the Southern Pacific Ocean, mainly due to variations in wind speed. The ocean radon flux has been estimated using the model of Wanninkhof (1992) where there is a quadratic dependence between the gas transfer velocity and wind speed. While this relationship between wind speed and gas exchange rate over the ocean is for the time-averaged fluxes, there are significant variations in the ^{222}Rn flux from surface coastal waters due to variable ^{222}Rn activity concentration compared to the open ocean. In areas where there is large submarine groundwater discharge fluxes, the ^{222}Rn concentration is expected to be higher and thus the ^{222}Rn/^{226}Ra ratio is expected to be highly variable.

There is no information on the radon flux from sea ice, but based on the molecular and turbulent diffusion coefficients of Rn, a reduction by a factor of 10 is estimated (Schery and Huang 2004). Although the model-predicted averaged

Table 3.3 Comparison of model predicted radon flux density to that of the measured values from ocean surface waters[a]

Model—average ^{222}Rn flux (mBq m^{-2} s^{-1})	Measured—average ^{222}Rn flux (mBq m^{-2} s^{-1})	Reference	Comments
0.0473	0.155	Wilkening and Clements (1975)	n = 1, offshore Hawaii, accumulator technique
0.0796	0.0432	Smethie et al. (1985)	n = 21, tropical Atlantic, radon deficiency method
0.0837	0.0503	Chambers et al. (2014)	From atmospheric ^{222}Rn in the Southern Ocean (40°–60° S; 70–140° E)
0.0315	0.0844	Kawabata et al. (2003)	N = 13, NW Pacific, radon deficiency technique
0.0415	–	Schery and Huang (2004)	60° N–60° S-calculated
0.105		Jacob et al. (1997)	60° N–60° S-calculated
0.21	–	Taguchi et al. (2002)	60° N–60° S-calculated
0.14	–	Schery and Wasiolek (1998)	Whole ocean-calculated
0.0382	–	Schery and Huang (2004)	Whole ocean-calculated

[a]Most reported values from continent range between 15 and 42 mBq m^{-2} s^{-1} (0.7–2.0 atoms cm^{-2} s^{-1}) and thus, the fractional emanation from ocean surface range from 0.08 to 1.5 % as that of the continents. Conversion factor: 1 atom cm^{-2} s^{-1} is equivalent to 21 mBq m^{-2} s^{-1}

annual global ^{222}Rn flux density for ocean is estimated to be 0.038 mBq cm^{-2} s^{-1}, corresponding to much lower fractional emanation flux of ^{222}Rn from the ocean (0.1–0.2 % as that from the land), the differences of model-predicted and measured values differ by factors 2–3 and hence more field data are needed on the relative ^{222}Rn flux from the ocean.

3.4.7 Radon Flux Studies from Continents

The temporal variations in radon release rates from soils at a given site depend on a number of factors including the concentrations of ^{226}Ra, and their distribution in mineral grains, physical properties of the mineral grains, porosity and water content of the soil (which implies the frequency and amount of precipitation), atmospheric

Fig. 3.6 Seasonal variation of average ^{222}Rn flux for **a** 5° latitudinal bands and **b** 5° longitudinal bands (Figure is taken from Szegvary et al. 2009; permission from Elsevier Ltd.)
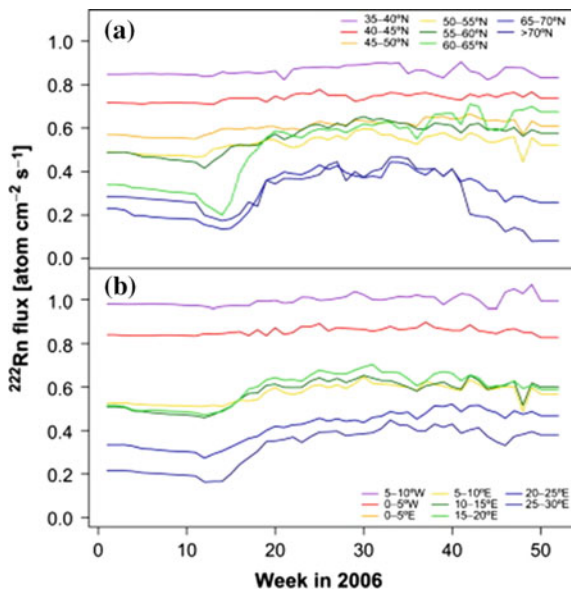
pressure, wind velocity, etc. The radon flux from land varies widely over shorter time-scale, diurnally, monthly and seasonally (Fig. 3.6). Using the emanation rate of 0.75 atom cm^{-2} s^{-1} of ^{222}Rn (corresponding to 15.8 mBq m^{-2} s^{-1} of ^{222}Rn or 23.3 mBq cm^{-2} y^{-1} of ^{210}Pb or 233 Bq m^{-2} y^{-1}) from all continental area (1.50 × 10^{18} cm^2), the corresponding atmospheric depositional flux of ^{210}Pb is estimated to be 3.50 × 10^{16} Bq y^{-1}.[1] However, 24 % of the total land area on Earth's surface is covered by glaciers and permafrost with negligible ^{222}Rn release. Thus, this 0.75 atom cm^{-2} y^{-1} for the whole land area corresponds to 1.00 atom cm^{-2} s^{-1} from the productive areas (1.12 × 10^{18} cm^2). A mean ^{222}Rn world flux value of 25 mBq m^{-2} s^{-1} (1.19 atom cm^{-2} s^{-1}) was obtained from the atmospheric ^{210}Pb fallout by Turekian et al. (1977), which is higher than an earlier estimate of 15 mBq m^{-2} s^{-1} by Wilkening et al. (1972). Assuming an average radon escape rate of 1 atom cm^{-2} s^{-1} (=31.1 mBq ^{210}Pb cm^{-2} y^{-1} or 1.865 dpm ^{210}Pb cm^{-2} y^{-1}) from the land surface, Turekian and Graustein (2003) estimated the total inventory of ^{222}Rn in the atmosphere to be ~1.5 × 10^{18} Bq. Using the accumulator technique where a chamber with an open bottom is placed upon a soil to deduce the flux density from the build-up of radon is obtained, Schery et al. (1989) obtained a flux density of 25.1 mBq m^{-2} s^{-1} from 78 Australia soils.

The weekly mean emanation rates of ^{222}Rn between 65° and 70° N in summer was higher by a factor of 2.5 than the winter and this was attributed to snow and soil moisture dominating the winter time and significantly drier conditions in summer (Szegvary et al. 2009). The ^{222}Rn emanation rates decrease with increasing latitude,

---

[1] 1 atom ^{222}Rn cm^{-2} s^{-1} = 31.08 mBq ^{210}Pb cm^{-2} y^{-1} or 310.8 Bq ^{210}Pb m^{-2} y^{-1}.

Table 3.4 Compilation[a] of long-term ^{222}Rn flux around the globe

Latitude	^{210}Pb Flux (mBq cm^{-2}y^{-1})	Number of sites	^{222}Rn Flux (atom cm^{-2}s^{-1})	Nature of samples
North				
0–10	15.8 ± 11.3	3	0.51 ± 0.36	1 Coa, 1 O, and 1 C
10–20	13.3 ± 8.3	3	0.43 ± 0.27	1 Coa, 2 C
20–30	19.8 ± 11.2	13	0.64 ± 0.36	4 Coa, 5 C, and A 4
30–40	17.8 ± 11.8	46	0.57 ± 0.38	14 Coa, 10 C, 9 Coa/C and 13 A
40–50	15.6 ± 7.5	52	0.50 ± 0.24	6 Coa, 26 C,13 Coa/C and 7 A
50–60	9.3 ± 4.5	10	0.30 ± 0.15	5 Coa, 4 C
60–70	3.7 ± 3.5	9	0.12 ± 0.11	2 Coa, 4 C, 3 IC
70–80	2.0 ± 1.5	10	0.064 ± 0.048	1 Coa, 2 C, 7 IC
South				
[b]0–10	11.7	1	0.38	1 C
10–20	6.7	2	0.21	2 Co
20–30	6.5 ± 2.7	5	0.21 ± 0.09	4 Co, 1 C
30–40	6.1 ± 0.2	5	0.197 ± 0.006	5 Co
40–50	4.2	2	0.135	2 CI
50–60	3.3	1	0.1060	1 O
60–70	0.63 ± 0.22	11	0.020 ± 0.007	I C
70–80	0.21 ± 0.12	7	0.0067 ± 0.0040	I C
80–90	0.18 ± 0.0.08	11	0.0056 ± 0.0025	I C

Co: Coastal; C: Continental; O: Ocean; IC: Ice core/sheet; A: Atmospheric depositional
Only the coastal and continental samples are included; however, in areas where the number of samples are limited (n < 3), the ocean samples (when available) were included
[a]Data are taken from Preiss and Genthon (1997); Baskaran and Naidu (1995) and Du et al. (2015)
[b]Data is from the ^{222}Rn flux calculated for April and May (Trumbore et al. 1990)

from 1 atom cm^{-2} s^{-1} at 30° N to 0.2 atom cm^{-2} s^{-1} at 70° N and even lower south 70° N (Table 3.4), and was attributed to the increased water saturation in the soils with increasing latitude (Conan and Robertson 2002). The commonly used ^{222}Rn flux of 21.0 mBq m^{-2} s^{-1} (1 atom cm^{-2} s^{-1}) is sometimes different in certain areas, and these anomalous values are not often taken into consideration in the regional modeling.

It has been proposed that there are several localized areas with anomalously high ^{222}Rn fluxes, as often evidenced by higher ^{210}Pb atmospheric depositional fluxes. For example, in Shanghai, the average annual depositional flux of ^{210}Pb over a period of 6 years during 2006 and 2013 is 385 Bq m^{-2} y^{-1} which corresponds to a ^{222}Rn flux of 26.0 mBq m^{-2} s^{-1} which is ∼24 % higher than the average values assumed for the continent. In Tatsunokuchi, Japan, the annual ^{210}Pb depositional flux of 840 Bq m^{-2} y^{-1} which corresponds to a ^{222}Rn flux of 56.8 of mBq m^{-2} s^{-1}, is 2.7 times the global average value of 21.0 mBq m^{-2} s^{-1}. In plate boundaries,

frequent tremors and small earthquakes (micro earthquakes) will result in fractures through which more radon could escape resulting in higher radon fluxes. For example, in the "Ring of Fire," a circle of quake-prone areas on the Pacific Rim, >70 % of the world's earthquakes (81 % of the world's largest earthquakes) occur. Other tectonically-active areas where much higher ^{222}Rn fluxes occur likely include Alpine belt which extends from Java to Sumatra through the Himalayas, the Mediterranean and out into the Atlantic.

3.4.8 ^{210}Pb Inventory-Based Long-Term Global ^{222}Rn Flux Estimate and Its Limitation

If one assumes the upward flux of ^{222}Rn equals the downward flux of ^{210}Pb (^{210}Pb flux = ^{222}Rn flux × mean life of ^{222}Rn/mean life of ^{210}Pb), one can calculate the radon emanation flux from the atmospheric depositional flux. This is a reasonable assumption as 100 % of the radon undergoing decay is brought down from the atmosphere eventually and there is no loss of ^{222}Rn or the progenies of ^{222}Rn to the upper stratosphere or mesosphere from either upper troposphere or lower stratosphere reported in literature.

One can convert the ^{210}Pb inventory to the average ^{222}Rn emanation flux integrated over the mean-life of ^{210}Pb. If A_{Rn222} is the activity ($=N_{Rn222} \lambda_{Rn222}$) of ^{222}Rn, when it undergoes radioactive decay, in 38.2 days, 99.9 % of ^{222}Rn would have decayed to ^{210}Pb and the activity of ^{210}Pb can be calculated. The number of original ^{222}Rn atom (N_{Rn222}) equals to the total number of ^{210}Pb atom produced (N_{Pb210}). The total activity of ^{210}Pb (A_{Pb210}) produced from the decay of A_{Rn222} is given by:

$$(A_{Pb210}) = (A_{Rn222}) * (\lambda_{Pb210}/\lambda_{Rn222}) \tag{3.16}$$

The ^{210}Pb annual flux (F_{Pb210}) can be converted to ^{222}Rn flux (F_{Rn222}) as follows:

$$(F_{Rn222}) = (F_{Pb210}) * (\lambda_{Rn222}/\lambda_{Pb210}) \tag{3.17}$$

The conversion factor between ^{222}Rn emanation rate (atom cm^{-2} s^{-1}) to the radon flux (mBq m^{-2} s^{-1}) and to ^{210}Pb flux is given by:

1 atom ^{222}Rn cm^{-2} s^{-1} ≡ 21.0 mBq ^{222}Rn m^{-2} s^{-1} ≡ 31.08 mBq ^{210}Pb cm^{-2} y^{-1} = 310.8 Bq m^{-2} y^{-1}.

The fundamental assumption in this approach is that the overhead atmospheric delivery is removed quantitatively by suspended particulate matter and reaches the sea floor and there is no additional input from sources such as riverine erosional input, ^{210}Pb derived from the discharge of submarine groundwater, either from ^{226}Ra and/or ^{222}Rn. The mean ^{222}Rn flux from continents range from 0.004 atom cm^{-2}s^{-1} (0.12 mBq cm^{-2} y^{-1} ^{210}Pb) to 2.5 atom cm^{-2} y^{-1} (77.7 mBq cm^{-2} y^{-1} ^{210}Pb;

summarized in Table 3.3, Turekian et al. 1977). Using the inventory of ^{210}Pb in a number of soil profiles in the continental United States, higher ^{222}Rn fluxes, 1.5–2.0 atoms cm^{-2} s^{-1}, have also been reported (Turekian and Graustein 2003).

The advantages of the ^{210}Pb flux-based estimate are: (i) it integrates the effects of terrain (e.g., forests) which cannot be studied using the accumulator-on-soil technique; and (ii) ^{210}Pb$_{xs}$-inventory-based approach for ^{222}Rn flux yields the average value integrated over its mean life, ~ 32 yrs. The inter-annual variability of ^{210}Pb depositional flux could be $\sim \pm 10$–15 % depending on the frequency and amount of precipitation and changes in the sources of air masses in the coastal stations (data analyzed from the published data for South Germany by Winkler and Rosner (2000)). Although the ^{222}Rn flux through the ice core and snow is likely negligible, a finite amount of ^{210}Pb flux is likely due to air masses derived from other regions. The major problem with the sediment-inventory approach is the sediment focusing in lakes and coastal ocean. Much higher inventories of excess ^{210}Pb, 2–10 times higher than what is expected from overhead fallout + production from dissolved ^{226}Ra in the overhead water column, have been reported in marine system (e.g., Baskaran and Santschi 2002; Swarzenski et al. 2006). There are oceanic areas where the sediments undergo erosion or in ocean margins where boundary scavenging takes place leading to much higher ^{210}Pb deposition. For example, Moore et al. (1981) reported the fluxes of ^{210}Pb measured by sediment traps in the Santa Barbara Basin off southern California are many times greater than the production rate of ^{210}Pb plus atmospheric fallout in the basin water, which was attributed to advection of ^{210}Pb-enriched particulate matter in water which eventually got trapped in the basin. Measured ^{210}Pb fluxes in the continental shelf off of Washington were found to be much higher than that expected from overhead fallout and in situ production from ^{226}Ra (Carpenter et al. 1981). From the measured inventories of ^{210}Pb in the water column and sediments, Baskaran and Santschi (2002) reported presence of regional differences and attributed to both vertical scavenging and lateral transport. To summarize, ^{210}Pb$_{xs}$-inventory in lakes and coastal ocean-based approaches to obtain ^{222}Rn fluxes remain less reliable.

3.5 Global Radon Emanation Rate Curve

While there is a large amount of ^{210}Pb fallout data from 20° to 45° N, there is very limited data from the Southern Hemisphere and at latitudes north of 50° N (Table 3.4). In areas where there is no data, the inventory of excess ^{210}Pb (^{210}Pb$_{xs}$ excess = total ^{210}Pb—parent-supported ^{210}Pb), is often taken to be the same as the activity of ^{226}Ra, although escape of ^{222}Rn from either diffusion loss or from recoil could result in loss of ^{222}Rn and hence loss of ^{210}Pb. Imboden and Stiller (1982) developed a model to correct for the loss of Rn in the sediments of Lake Geneva, Switzerland. Ravichandran et al. (1995) observed that the radon loss correction was calculated to be very small, <1–2 % of the excess ^{210}Pb.

There are three other global emanation graphs published in literature. Conan and Robertson (2002) reported a latitudinal gradient in terrestrial ^{222}Rn flux, decreasing north of 30° N, although this is not rigorously valid. For example, the latitudinal difference between the islands of Hok Tsui (22° 12′ N) and Gosan (33° 18′ N) is expected to be less than 10–15 %, based on Conan and Robertson (2002) gradient in the ^{222}Rn flux with latitude, but the reported median values are 3456 and 2685 mBq m^{-3}, respectively and one possible explanation for this difference is the frequent or intense injection of boundary layer air to the troposphere in the 30–40° N latitude band compared to the 20–30° N latitude band from frontal and convective activity (Zahorowski et al. 2005). Radon flux as a function of latitude plotted by Conan and Robertson (2002), Szegvary et al. (2009; Fig. 3.7) and Manohar et al. (2013) indicates three humps, which are attributed to higher fluxes due to underlying volcanic geology in the regions of Portugal, Spain, Italy, France, Slovakia and the Cech Republic (Manohar et al. 2013). Conen and Robertson suggest a ^{222}Rn flux of 21.0 mBq m^{-2} s^{-1} (1 atom cm^{-2} s^{-1}) over the ice-free land areas south of 30° N and a linear decrease northwards to reach 4.2 mBq m^{-2} s^{-1} (0.2 atom cm^{-2} s^{-1}). The global radon emanation rates based on published values of long-term ^{210}Pb depositional fallout (Du et al. 2015), sediment core-derived excess ^{210}Pb inventories from marine system and ice cores are given in Fig. 3.7. This figure represents 191 different sites around the globe (including 24 direct atmospheric depositional flux, 10 ice core sites). A majority of these sites are either

Fig. 3.7 Global ^{222}Rn flux based on ^{210}Pb inventories in sediment cores from marine system, ice cores and direct atmospheric depositional fluxes from 191 different global sites (details of the source of data are given in Table 3.4) at different latitude belts (10° belt)
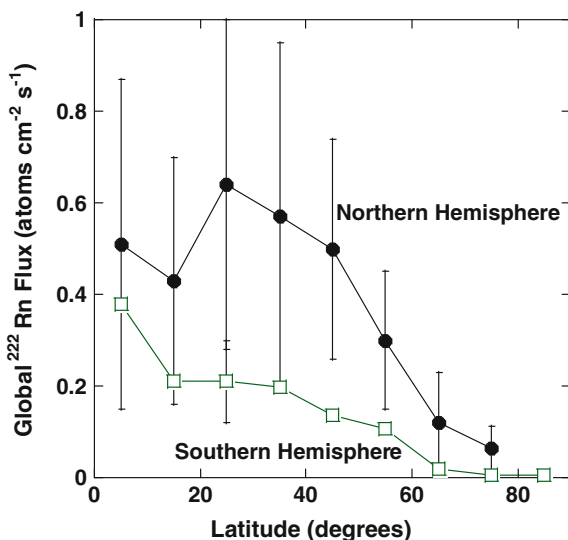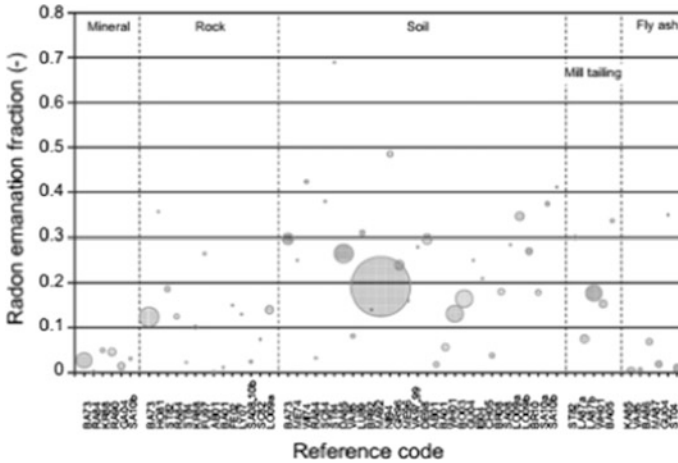
Fig. 3.8 Radon emanation fraction (or coefficient) measured for various materials. Size of *filled circle* is a measure of the number of samples (Figure is taken from Sakoda et al. 2011, with permission from Elsevier)

coastal or continental samples. In areas where the number of samples are less than 3, ocean samples were also included (Table 3.4).

3.6 Summary and Future Research Direction

A large body of data exist on the radon emanation coefficient from soils, rocks and minerals (Fig. 3.8). Still, a large number of minerals for which no data on REC exist. It has been proposed that radon release rates (^{220}Rn and ^{222}Rn) can be useful in quantifying the existence of openings in common rock minerals. Presence of networks of zones of submicronic porosity have been proposed to play a key role in radon emanation rates. More systematic studies are needed to investigate how zones of submicronic porosity and the network of these zones in different minerals affect RECs. More studies on the use of 'radonography' to investigate regions of submicronic porosity in mineral grains and on how different defects and radiation damages in minerals affect REC in minerals.

References

Baskaran M, Naidu AS (1995) ^{210}Pb-derived chronology and the fluxes of ^{210}Pb and ^{137}Cs isotopes into continental shelf sediments, East Chukchi Sea, Alaskan Arctic. Geochim Cosmochim Acta 59:4435–4448

Baskaran M (2011) ^{210}Po and ^{210}Pb as atmospheric tracers and global atmospheric ^{210}Pb Fallout: a review. J Environ Radioact 102:500–513

Baskaran M, Santschi PH (2002) Particulate and dissolved ^{210}Pb activities in the shelf and slope regions of the Gulf of Mexico waters. Continent Shelf Res 22:1493–1510

Bossus DAW (1984) Emanating power and specific surface area. Radiat. Prot. Dosim. 7:73–76

Brodzinski RL (1972) Radon-222 in Lunar atmosphere. Nature 238:107–109

Burnett WC et al. (2006) Quantifying submarine groundwater discharge in the coastal zone via multiple methods. Sci Total Environ 367:498–543

Carpenter R, Bennett JT, Peterson ML (1981) Pb-210 activities in and fluxes to sediments of the Washington continental slope and shelf. Geochim Cosmochim Acta 45:1155–1172

Chambers SD, Hong S-B, Williams AG, Crawford J, Griffiths AD, Park S-J (2014) Characterizing terrestrial influences of Antarctic air masses using Radon-222 measurements at King George Island. Atmos Chem Phys 14:9903–9916. doi:10.5194/acp-14-9903-2014

Clements WE, Wilkening MH (1974) Atmospheric pressure effects on ^{222}Rn transport across the Earth-air interface. J Geophys Res 79:5025–5029

Conan F, Robertson LB (2002) Latitudinal distribution of radon-222 flux from continents. Tellus 54B:127–133

Dorr H, Munnich KO (1990) Gasoline lead in West-German soils. Naturwissenschaften 77 (9):428–430

Du J, Du J, Baskaran M, Bi Q, Huang D, Jiang Y (2015) Temporal variations of atmospheric depositional fluxes of ^{7}Be and ^{210}Pb over 8 years (2006–2013) at Shanghai, China and Synthesis of global fallout data. J Geophys Res 120. doi:10.1002/2014JD022807

Eakin M, Brownlee SJ, Baskaran M, Barbero L (2016) Mechanisms of radon loss from zircon: microstructural controls on emanation and diffusion. Geochim Cosmochim Acta 184:212–228

Gorenstein P, Bjorkholm P (1973) Detection of radon emanation from the crater Aristarchus by the Apollo 15 alpha particle spectrometer. Science 179:792–794

Graustein WC, Turekian KK (1990) Radon fluxes from soils to the atmosphere measured by Pb-210-Ra-226 disequilibrium in soils. Geophys Res Let 18:841–844

Greeman DA, Rose AW (1996) Factors controlling the emanation of radon and thoron in soils of the eastern USA. Chem Geol 129:1–14

Griffiths AD, Zahorowski W, Element A, Werczynski S (2010) A map of radon flux at the Australian land surface. Atmos Chem Phys 10(18):8969–8982

Imboden DM, Stiller M (1982) The influence of radon diffusion on the ^{210}Pb distribution in sediments. J Geophys Res 87:557–565

Ishmori Y, Lange Y, Martin P, Mayya YS, Phenauf M (2013) Measurement and calculation of radon releases from NORM residues. Technical Reports Series No. 474, ISSN 0074-1914; International Atomic Energy Agency, Vienna

Jacob DJ, Prather MJ, Rasch PJ et al (1997) Evaluation and intercomparison of global atmospheric transport models using ^{222}Rn and other short-lived tracers. J Geophys Res 102:5953–5970

Karstens U, Schwingshackl C, Schmithusen D, Levin I (2015) A process-based ^{222}Rn flux map for Europe and its comparison to long-term observations. Atmos Chem Phys 15:12845–12865. doi:10.5914/acp-15-12845-2015

Kawabata H, Narita H, Harada K et al (2003) Air-sea gas transfer velocity in stormy winter estimated from radon deficiency. J Oceanogr 59:651–661

Kraner HW, Schroeder GL, Davidson G, Carpenter JW (1966) Radioactivity in the lunar surface. Science 152:1235–1236

Krishnaswami S, Seidemann DE (1988) Comparative study of ^{222}Rn, ^{40}Ar, ^{39}Ar and ^{37}Ar leakage from rocks and minerals: implications for the role of nanopores in gas transport through natural silicates. Geochim Cosmochim Acta 52:655–658

Lopez-Coto I, Mas JL, Bolivar JP (2013) A 40-year retrospective European radon flux inventory including climatological variability. Atmos Environ 73:22–33

Manohar SN, Meijer HAJ, Herber MA (2013) Radon flux maps for the Netherlands and Europe using terrestrial gamma radiation derived from soil radionuclides. Atmos Environ 81:399–412

Moore WS, Bruland KW, Michel J (1981) Fluxes of uranium and thorium series isotopes in the Santa Barbara Basin. Earth Planet Sci Lett 53:391–399

Morawska L, Phillips L (1993) Dependence of the radon emanation coefficient on radium distribution and internal structure of the material. Geochim Cosmochim Acta 57:1783–1797

Nazaroff WW (1992) Radon transport from soil to air. Rev Geophys 30:137–160

Preiss N, Genthon C (1997) Use of a new database of lead 210 for global aerosol model validation. J Geophys Res 102:25347–25357

Rama, Moore WS (1984) Mechanism of transport of U-Th series radioisotopes from solids into groundwater. Geochim Cosmochim Acta 48:395–399

Rama, Moore WS (1990) Micro-crystallinity in radioactive materials. Int J Radiat Appl Instrum Part E, Nucl Geophys 4:475–478

Ravichandran M, Baskaran M, Sanstschi PH, Bianchi TS (1995) Geochronology of sediments in the Sabine-Neches estuary, Texas, U.S.A. Chem Geol 125:291–306

Robbins JA (1978) Geochemical and geophysical applications of radioactive lead. In: Triage JO (ed) The biogeochemistry of lead in the environment, pp 285–393

Rutherford E, Soddy F (1903) Condensation of radioactive emanations. Phil Mag Ser 6(5):561

Sakoda A, Ishmori Y, Yamaoka K (2011) A comprehensive review of radon emanation measurements for mineral, rock, soil, mill tailing and fly ash. J Appl Radiat Isot 69:1422–1435

Schery SD, Huang S (2004) An estimate of the global distribution of radon emissions from the ocean. Geophys Res Lett 31(L19104):2004. doi:10.1029/2004GL021051

Schery SD, Whittlestone S, Hart KP et al (1989) The flux of radon and thoron from Australian soils. J Geophys Res 94:8567–8576

Schery SD, Wasiolek MA (1998) Modeling radon flux from the earth's surface. In: Katase A, Shimo M (eds) Radon and thoron in the human environment, pp 207–217

Schery SD, Gaeddert (1982) Measurements of the effect of cyclic atmospheric-pressure variation on the flux of Rn-222 from the soil. Geophys Res Lett 9(9):835–838

Smethie WM Jr, Takahashi T, Chipman DW, Ledwell JR (1985) Gas exchange and CO_2 flux in the tropical Atlantic Ocean determined from ^{222}Rn and pCO_2 measurements. J Geophys Res 90:7005–7022

Strong KP, Levins DM (1982) Effect of moisture content on radon emanation from uranium ore and tailings. Health Phys 42:27–32

Swarzenski PW, Baskaran M, Rosenbauer RJ, Orem WH (2006) Historical trace element distribution in sediments from the Mississippi River delta. Estuar Coast 29:1094–1107

Szegvary T, Leuenberger MC, Conen F (2007) Predicting terrestrial Rn-222 flux using gamma dose rate as proxy. Atmos Chem Phys 7:2789–2795

Szegvary T, Conen F, Ciais P (2009) European ^{222}Rn inventory for applied atmospheric studies. Atmos Env 43:1536–1539

Taguchi S, Lida T, Moriizumi J (2002) Evaluation of the atmospheric transport model NIRE-CTM-96 by using measured radon-222 concentrations. Tellus 54(3):250–268

Tanner AB (1980) Radon migration in the ground: a supplementary review. In: Gesell TF, Lowder WM (eds) Proceedings of the natural environment III, pp 5–56, U.S. Dep. Of Comm. Rep. CONF-780422, National Technical Information Service, Springfield, VA

Trumbore SE, Keller M, Bosky SC, Ad Costa (1990) Measurements of soil and canopy exchange rates in the Amazon rain forest using ^{222}Rn. J Geophys Res 95:16865–16873

Turekian KK, Graustein WC (2003) Natural radionuclides in the atmosphere. In: Treatise in geochemistry, 4.10, pp 261–279

Turekian KK, Nozaki Y, Benninger LK (1977) Geochemistry of atmospheric radon and radon products. Ann Rev Earth Planet Sci 5:227–255

UNSCEAR (United Nations Scientific Committee on the Effects of Atomic Radiation) (2000) Sources and Effects of Ionizing Radiation. UNSCEAR 2000 Report to the General Assembly, with Scientific Annexes. UNSCEAR, United Nations, New York

Wanninkhof R (1992) Relationship between gas exchange and wind speed over the ocean. J Geophys Res 97(C5):7373–7381. doi:10.1029/92JC00188

Wedepohl KH (1995) The composition of the continental crust. Geochim Cosmochim Acta 59:1217–1232

Wilkening MH, Clements WE (1975) Radon-222 from the ocean surface. J Geophys Res 80:3828–3830

Wilkening MH, Clements WE, Stanley D (1972) Radon-222 flux measurements in widely separated regions. In: Adams JAS et al. (ed) Proceedings of the natural radiation environment II, pp 717–730, U.S. Dept. of Comm. Rep. Conf-720805, Natural Technical Information Service, Springfield, VA

Winkler R, Rosner G (2000) Seasonal and long-term variation of ^{210}Pb concentration in air, atmospheric deposition rate and total deposition velocity in south Germany. Sci Total Environ 263:57–68

Zahorowski W, Chambers SD, Wang T et al (2005) Radon-222 in boundary layer and free tropospheric continental outflow events at three ACE-Asia sites. Tellus B 57(2):124–140

Zhuo W, Iida T, Furukawa M (2006) Modeling radon flux density from the Earth's surface. J Nucl Sci Technol 43(4):479–482

Zhou W, Guo Q, Chen B, Cheng G (2008) Estimating the amount and distribution of radon flux density from the soil surface in China. J Environ Radioact 99(7):1143–1148

Chapter 4
Radon: A Tracer for Atmospheric Studies

4.1 Introduction

Radioactive isotopes that occur in the atmosphere (more than 30) can be grouped into three major categories: (i) anthropogenic, mainly derived from open-air nuclear weapons testing and occasional nuclear accidents (e.g., Fukushima in 2011, Chernobyl in 1986); (ii) cosmogenic, produced by cosmic rays from interaction with the gaseous components of the atmosphere (e.g., N_2, O_2, Ar, etc.); and (iii) naturally-occurring, mainly ^{222}Rn and its daughter products.

Anthropogenic radionuclides (transient tracers) in the atmosphere were introduced on a continuing basis since 1952 from the detonation of a number of nuclear weapon detonations (note that the first two nuclear detonations were conducted in 1945 at Nagasaki and Hiroshima) and almost ended by end of 1960s. The uneven spatial and temporal distribution of the fallout nuclides such as ^{90}Sr, ^{3}H and ^{14}C, at different latitude belts (heaviest fallout in the northern hemisphere with a peak in fallout between 30° and 60° and lowest in the polar and equatorial regions) provided deeper insight on the time scales of inter-hemispheric exchange of air masses in the troposphere, rates of meridional transport within hemispheres, mixing time scales of airmasses within Hadley and Polar cells, time scales of meridional mixing in the Northern hemisphere, and cross-Equator mixing time scale in the troposphere (Lal and Rama 1966; review paper by Lal 2002).

Cosmogenic nuclides are produced continually, primarily in the stratosphere and upper troposphere, and serve as tracers for studying the nature of large-scale motions of the atmosphere. Long-lived human-induced trace species such as chlorofluorocarbons (CFCs) and SF6 in conjunction with atmospheric radionuclides (both cosmogenic and anthropogenic) have been used to evaluate and validate large-scale atmospheric transport features such as inter-hemispheric exchange and stratosphere-troposphere exchange studies (e.g., Prather et al. 1987; Turekian and Graustein 2003; Lal and Baskaran 2011).

Radon-222 and its progeny (mainly ^{210}Pb, ^{210}Bi and ^{210}Po; Fig. 6.1) have provided a wealth of information on the sources of air masses and aerosols, residence times and removal rate constants of aerosols, stability and vertical movements of air masses and deposition velocities of aerosols in the planetary boundary layer (review papers by Turekian et al. 1977; Turekian and Graustein 2003; Baskaran 2011). The utility of ^{222}Rn as an atmospheric tracer stems from the fact that its mean-life (=half-life (3.82 d)/ln 2 = 5.51 days, also referred as e-folding life time) is long compared to typical turbulent time scales (<1 h), but short enough to constrain ^{222}Rn concentrations in the free troposphere where the concentrations are about two orders of magnitude lower than typical atmospheric boundary layer values. Its mean life is generally comparable to the transit time of air masses across major continents and/or some oceans but much shorter compared to the global mixing time scale of the atmosphere and hence, it is widely dispersed in the atmosphere. The simple source, released exclusively from the earth's surface (∼99 % from continents ∼1 % from oceans), and sink, by removal with a first-order decay rate constant (2.1 × 10^{-6} s^{-1}) enables to quantify both with ease.

There are three isotopes of radon: ^{219}Rn, ^{220}Rn and ^{222}Rn. Radon-219, derived from ^{235}U series, is much less abundant than ^{222}Rn due to the relative abundance of ^{238}U and ^{235}U (^{238}U/^{235}U atomic ratio = 137.7) and its half-life (3.9 s), so it is not useful for atmospheric studies. Radon-220 ("thoron") is a decay product in the ^{232}Th series. Since its half-life is 55.6 s it is well suited for studying vertical mixing close to the Earth's surface (in the "surface layer"), and for distinguishing local from remote terrestrial influence at coastal and island sites.

The concentrations of ^{226}Ra in rocks and minerals (upper crustal average of ∼31 mBq g^{-1}, assuming ^{238}U and ^{226}Ra are in secular equilibrium; average ^{238}U concentration in the upper crust = 2.5 ppm; Wedepohl 1995) is about 4 orders of magnitude higher than that of surface ocean waters (∼1.2 × 10^{-3} mBq g^{-1}; details given in Baskaran 2011). Consequently, the radon emanation rate from land is about 2 orders of magnitude higher than that from the surface ocean waters (1,300–1,800 Bq m^{-2} d^{-1} from continents as opposed to ∼17 Bq m^{-2} d^{-1} from oceanic areas; Samuelsson et al. 1986; Nazaroff 1992).

Once ^{222}Rn escapes from the rocks and minerals of Earth's upper crust, it embarks on an atmospheric journey via diffusion and advection. Along the way, some of the ^{222}Rn undergoes radioactive decay, producing a series of radionuclides (Fig. 6.1). Radon is an ideal atmospheric tracer for local, regional and global scales because: (i) its inert nature, its synoptic-timescale mean lifetime, and its well-characterized source function; and (ii) the residence times of water vapor, aerosols and many important aspects of atmospheric dynamics are comparable to the mean-life of radon (e.g., Zahorowski et al. 2004, 2005). In particular, the large gradient in the concentrations of radon between oceanic and terrestrial radon sources aid in identifying the sources of air masses (continental versus maritime) and serve as an unambiguous indicator of recent terrestrial influence on the oceanic air mass (e.g. Polian et al. 1996). In this chapter, a summary of key applications of ^{222}Rn as an atmospheric tracer is given and future direction is presented.

4.2 ^{222}Rn Activity Variations in the Planetary Boundary Layer

Radon activity in the planetary boundary layer above continental and oceanic areas differ widely (Rama 1969; Wilkening and Clements 1975; Schery and Huang 2004). If there is equilibrium between radon in surface waters and atmosphere, then, there will not be any exchange of radon between these two systems. However, it has been shown that there is always nonequilibrium between these two systems and the concentrations in the atmosphere is significantly lower than that in the surface waters (Wilkening and Clements 1975; more discussion in Chap. 6-Ocean Studies). Radon has also been used as a major dust storm indicator. For example, air containing high atmospheric dust concentrations (indicative of a continental source), was reported to have radon peaks (Bressan et al. 1973; Prospero and Carlson 1970). Note that the higher dust concentrations were found always to be accompanied by radon pulses, but radon pulses were not always accompanied by higher dust concentrations and this was attributed to removal of dust by rainout and washout, whereas radon is only removed by radioactive decay. Dust-laden air over the equatorial Atlantic originating from the arid regions of western Africa was found to contain high concentrations of ^{222}Rn $\sim$1.9 Bq m^{-3} compared to the background level of <0.07 Bq m^{-3} (Prospero and Carlson 1970; note all values are for standard cubic meter). Radon activities at different areas of a weather front differ widely. ^{222}Rn concentrations ahead of a front over the Greenland Sea (0.15 Bq m^{-3}) were found to be much lower than that near the leading edge of the frontal system (1.00 Bq m^{-3}, Bressan et al. 1973). The factors that affect the activities of ^{222}Rn in the planetary boundary layer above the continent and ocean are discussed below.

4.2.1 ^{222}Rn Activity Variations in the PBL Above Land

The activity of ^{222}Rn in the planetary boundary layer (PBL) over land depends on a number of factors that include seasonal variations in the radon source which in turn depends on soil moisture, pressure gradients, seasonal variations in the strength, frequency and/or efficiency of mechanisms that lift the boundary layer air to the mid-troposphere (e.g., cold fronts, wet/dry convection, etc.) (Schery and Gaeddert 1982; Merrill et al. 1989; Nazaroff 1992), seasonal variations in the latitudinal axis of convection and seasonal variations in the sources of air mass (Talbot et al. 1997). The diurnal cycle (daily changes in mixing depth) usually have the dominant influence on changing radon concentrations near the land surface. In Lisbon, Portugal, ^{222}Rn variations of about 2–3 orders of magnitude (0.02 to $\sim$10 Bq m^{-3}) were reported and attributed to changes in the relative portion of air masses derived from continental Europe and maritime air mass from the Atlantic Ocean (Carvalho 1995).

4.2.2 ^{222}Rn Activity Variations in the PBL Above Ocean

Large variations in surface air ^{222}Rn concentrations at specific sites have been widely reported (Table 4.1), and are primarily attributed to variations in the source of air masses. For example, ^{222}Rn activity in maritime air mass at ~ 10 m above the ocean surface is reported to vary between ~ 70 and 150 mBq m^{-3} while in the continent, generally it is found to be >4 Bq m^{-3} at ~ 10 m above the land surface (excluding the permafrost regions) (Moore et al. 1973). In PBL above open ocean, activities as low 20 mBq m^{-3} have also been reported (Zahorowski et al. 2013). In remote ocean areas the advection/fetch effects on radon are dominant (Table 4.1).

Table 4.1 Radon activities in air samples at different locations around the globe

Location	^{222}Rn activity (mBq m^{-3})	Site	Reference
Mid-North Pacific	30–50	MBL, mid-North Pacific	Balkanski et al. (1992), Lambert et al. (1982)
Mid-North Pacific	8.7–66.1 (29.2)	Deep-baseline air	Chambers et al. (2013)
N. Pacific clean air	8–39		Balkanski et al. (1992), Lambert et al. (1982), Moore et al. (1977)
Pacific Ocean	74–518	North of 5° N	Wilkness et al. (1974)
Northeastern Pacific	190–300	<50 m from ocean surface	Andrea et al. (1988)
Arabian Sea	37–74	Surface air	Subramanian et al. (1977)
Arctic (at 305 m)	37–829	82°–87° N; 24°–99° W	Wilkniss and Larson (1984)
Southern Hemisphere	37	Surface air	Wilkness et al. (1974)
Southern Hemisphere	19–93	South of 40° S	Lambert et al. (1970)
Antarctic	18	South Pole	Maenhaut et al. (1979)
Cape Grim in Tasmania	27–44	S. Australia	Zahorowski et al. (2013)
Southern Ocean—south of S. America	44–72	47–53° S	Chambers et al. (2014)
Central USA	220–400	PBL	Liu et al. (1984)

4.3 Radon Concentrations in Polar Regions

The major sources of radon for the atmospheric air in the deep Arctic Ocean basin are the North America for west of Greenland and the Northern Europe for east of Greenland, through the meridional transport of continental air. During Arctic haze events, ^{222}Rn concentrations of 35–75 mBq m^{-3} were found to be associated with fog and clouds, suggesting that this air mass had been in touch with a continental source for 1–4 weeks. The normal background level of radon over the Arctic Ocean is reported to be 35–70 mBq m^{-3}, which is lower than the background values of 70–150 mBq m^{-3} encountered in remote Northern Hemisphere oceanic areas (Wilkniss and Larson 1984). Note that the range for oceanic air, 70–150 mBq m^{-3}, is high compared to other areas above the ocean such as in the Arabian Sea (more details later in this chapter). The radon emanation rates measured in the northern regions of Russia, Alaska and Canadian polar regions in high latitudes were in the range of 0.05–0.37 atom cm^{-2} s^{-1} (summarized in Baskaran and Naidu 1995; compare this with 1.0 atom cm^{-2} s^{-1} assumed in the model calculation for 60° N–60° S; 1 dpm cm^{-2} y^{-1} = 0.53 atom cm^{-2} s^{-1}; 1 atom cm^{-2} s^{-1} = 31.4 mBq cm^{-2} s^{-1}). The lowest ^{222}Rn activity was reported to be ∼19 mBq m^{-3} near South Pole in Antarctic and this was attributed to the presence of solid ice and heavy snow cover that inhibit or impede radon release from land areas (Maenhaut et al. 1979). Most recent high-precision direct ^{222}Rn measurements made at King George Island 62.217° W) are compared with historic and ongoing radon measurements from other Antarctic sites in Chambers et al. (2014). It is to be noted that the convective activities are much less intense above mid-latitudes (north of mid-latitudes in the Northern Hemisphere and south of Southern Hemisphere), including Polar Regions. However, 'radonic storms' with very high ^{222}Rn activities have been reported in the Arctic and Antarctic regions (see Sect. 4.7: role of atmospheric rivers in the transport of radon).

4.4 Vertical Profiles of Atmospheric ^{222}Rn

The vertical distribution of ^{222}Rn over the continents is a direct result of supply from continental material (soils, exposed rocks and minerals), and space- and time-dependent vertical transport processes that include turbulent mixing, convective mixing, mesoscale motions, frontal uplift, etc. which alter the vertical profile of ^{222}Rn. As was discussed earlier, Rn is not removed by precipitation scavenging while its daughter products are. Four vertical ^{222}Rn profiles at on site but different times are shown in Fig. 4.1 (data taken from Moore et al. 1977). Highest concentrations of ^{222}Rn are commonly found in the continental boundary layer (3–8 Bq m^{-3}), decreasing by an order of magnitude, to ∼40 mBq m^{-3} near the tropopause (Moore et al. 1977; Liu et al. 1984; Kritz et al. 1993; Williams et al. 2011). The height of the troposphere (marked by the tropopause), changes

Fig. 4.1 Temporal changes in the vertical profiles of ^{222}Rn at the atmosphere. TP stands for tropopause. Tropopause serves as a barrier where the ^{222}Rn activity drops off. The sampling site is offshore near San Francisco, CA, USA. Data is taken from Moore et al. (1977)
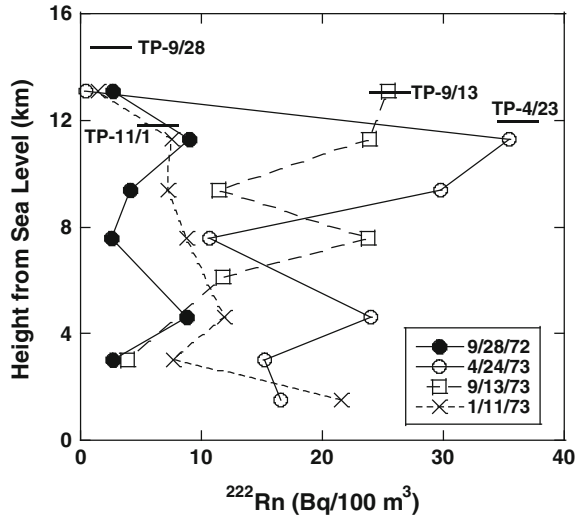
significantly with both season and latitude. Typically the tropopause serves as an impermeable barrier to radon and other atmospheric constituents originating at the earth's surface, except during strong convective updrafts when some of the ^{222}Rn can reach the lower stratosphere leading to production of ^{210}Pb (Baskaran 2011) in the lower stratosphere. Strong fronts also can cause tropopause folding events, major volcanic eruptions and nuclear detonations can also force material of surface origins through the tropopause. In principle, combining radon decay products such as ^{210}Po and ^{210}Pb and other cosmogenic isotopes (e.g. ^{7}Be and ^{10}Be) can be used to estimate or evaluate rates of cross-tropospheric exchange (more details in Chap. 5).

Factors that affect the vertical radon distribution include most of the common processes such as vertical mixing of different strengths and spatial extent, variations of the sources of air masses, and ambient meteorological conditions affecting the air masses in the atmospheric layers. One of the most extensive databases on free tropospheric ^{222}Rn profiles was obtained in the summer of 1994 on flights operating from Moffett Field, California (37.4° N, 122.0° W; Kritz et al. 1998). The profiles extend from the surface to 11.5 km, obtained from 11 flights flown in the period of June 3 to August 16, 1994. From a synthesis of earlier published vertical ^{222}Rn profile data, Liu et al. (1984) estimated the fraction of ^{222}Rn transported from the PBL into the free troposphere. Information on the fractional escape of radon is useful in the estimation of escape of the short-lived chemically reactive species from the PBL to free troposphere. Williams et al. (2011) compared the rates of exchange from the PBL to the lower troposphere under different conditions: clear sky, stratoform cloud cover and convective cloud cover.

The range of concentrations of ^{222}Rn at different atmospheric layers commonly found overlying the northern Pacific Basin are shown in Fig. 4.2 (from Chambers et al. 2013) that include: (i) mixed layer ($\sim$400–1000 m above sea level (asl));

(ii) cloud condensation layer (CCL, ~200–2500 m deep); (iii) trade-wind inversion layer above the CCL (TWI, ~100–300 m deep); (iv) lower troposphere (LT, extending from TWI to ~3–5 km asl); (v) upper troposphere (UT, ≥5 km asl); (vi) the tropopause (8–10 km asl in winter and 15–17 km asl in summer), and (vii) the stratosphere above (Fig. 4.2). The envelop represents the spread of ^{222}Rn data of 11 vertical profiles obtained by Kritz et al. (1998) (figure is adapted from Chambers et al. 2013). Figure 4.2 shows the following: Highest concentrations are found below the cloud condensation layer, with values as high as 2.2 Bq m^{-3} (July 7, 1997 at 800 m) and this is attributed to major advectional fraction of air mass from the adjacent continent. The activity generally decreases to minimum values (as low as 0.05 Bq m^{-3}) between 2 and 4.5 km; however, in some of the profiles, the values at 2.0–4.0 km are relatively high (e.g., June 14, July 7, 1994). The activity range generally increases at 4–6 km above sea level and this is attributed to increasing terrestrial influence in the summer. The air mass below 5 km is from the dominant influence of light northeasterly trade-wind while above 5 km, it is influenced by the westerly jet-stream flow (e.g., Balkanski et al. 1992; Gupta et al. 2004; Chambers et al. 2013). The activity near the tropopause as well as in the upper troposphere and lower stratosphere is generally <~40 mBq m^{-3} (Liu et al. 1984) and the observed ^{222}Rn levels at that altitude is attributed to rapid convection transporting radon from the lower troposphere.
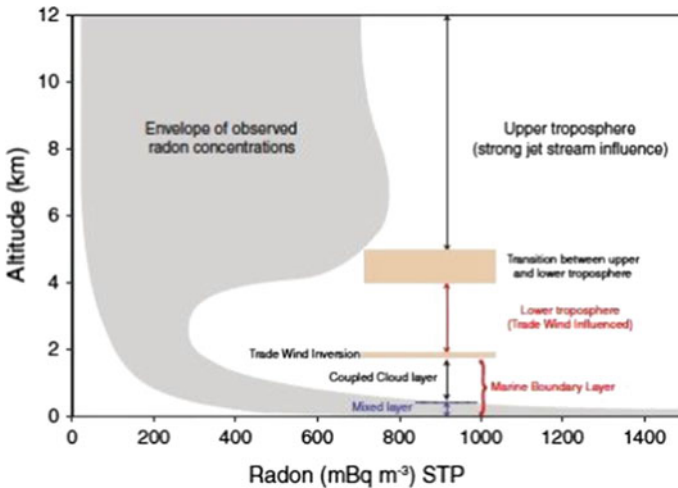
Fig. 4.2 Radon profiles obtained in the summer 1994 on flights originating from Moffett Field, California, USA (27.4° N, 122.0° W). The spread of ^{222}Rn activity indicates the range of values from 11 flights in the period June 3 to August 16, 1994 (figure is adapted from Chambers et al. 2014, with permission from American Geophysical Union)

4.5   Case Studies: Temporal and Spatial Profiles of ^{222}Rn

The temporal variations of ^{222}Rn at different time scales (viz., hourly, daily, monthly, seasonally and annually) have been widely reported. While it is not possible to present results from every station studied, three stations from 3 different islands, including one at very high elevation, are presented as a model study to understand the processes that affect the temporal and spatial variations of ^{222}Rn. The discussions include: (i) temporal variations at a given site, and (ii) spatial variations from three different sites carried out by the Australian group.

A relatively recent study of three stations in the central- to west-Pacific Basin is presented by Zahorowski et al. (2005). The study sites include: (i) Mauna Loa Observatory, on the northern face of the Mauna Loa volcano (19° 32.3′ N, 155° 34.7′ E), on the island of Hawaii at an elevation of 3397 m above mean sea level (AMSL) in the central Pacific Ocean; (ii) Gosan station, on the western coast of Jeju Island (dimension: 73 km east-west and 42 km north-south), South Korea (33° 18′ N, 126° 09′ E); sampling at 55 m AMSL on a bluff; and (iii) Hok Tsui, on the southeastern corner of Hong Kong Island at Cape D'Aguilar (22° 12′ N, 114° 15′ E; sampling at 75 m AMSL on a bluff).

The annual (a–c), seasonal (d–f) and composite diurnal ^{222}Rn concentrations at the three sites (Hok Tsui, Gosan and Mauna Loa) are given in Fig. 4.3, and corresponding monthly values presented in Fig. 4.4. The overall background ^{222}Rn
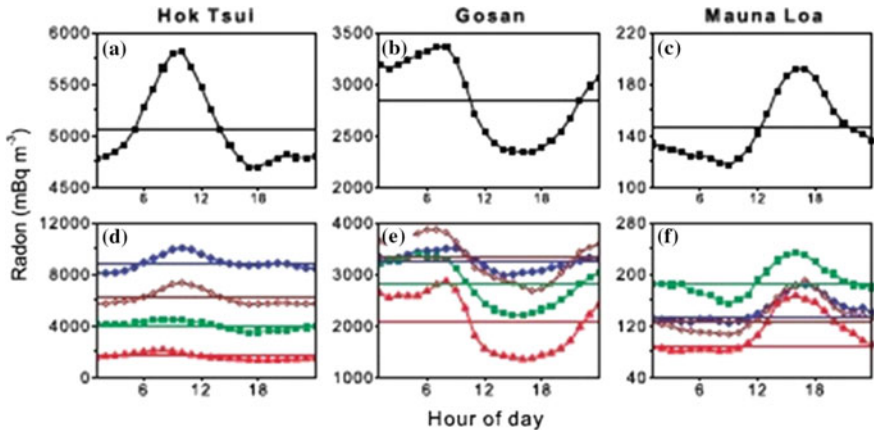
Fig. 4.3 Composite diurnal variations of ^{222}Rn concentrations (mBq m^{-3}) averaged over: annual (a–c), seasonal (d–f). For the seasonal plots: winter: *diamond*; *squares*: spring; *triangle*: summer and *circles*: autumn. *Horizontal dotted lines* represent the respective mean concentrations. Hok Tsui is on the southeastern corner of Hong Kong Island (22° 12′ N, 114° 15′ E, sampled at 15 m above ground level (agl)); Gosan site in on the western coast of Jeju Island, South Korea (33° 18′ N, 126° 09′ E, sampled at 5 m agl); Mauna Loa Observatory is on the northern face of the Mauna Loa volcano (19° 32.3′ N, 155° 34.7′ W, sampled at 40 m). This figure is taken from Zahorowski et al. (2005). Note that the shape of the MLO diurnal reported in Chambers et al. (2013) is different and it is attributed to the issues involved in the data collection in Zahorowski et al. (2005)

Fig. 4.4 Mean monthly ^{222}Rn activity at. **a** Hok Tsui on the southeastern corner of Hong Kong Island; **b** Gosan on the western coast of Jeju Island in South Korea; and **c** Mauna Loa Observatory on the northern face of the Mauna Loa volcano, on the island of Hawaii, USA. The *bars* represent means based on daily minimum concentrations whereas the *open circles* represent means based on all hourly data. Whiskers on *bars* denote ±1 standard deviation. Note that the *vertical scales* are different. The figure is taken from Zahorowski et al. (2005) with permission from *Blackwell Munskgaard*
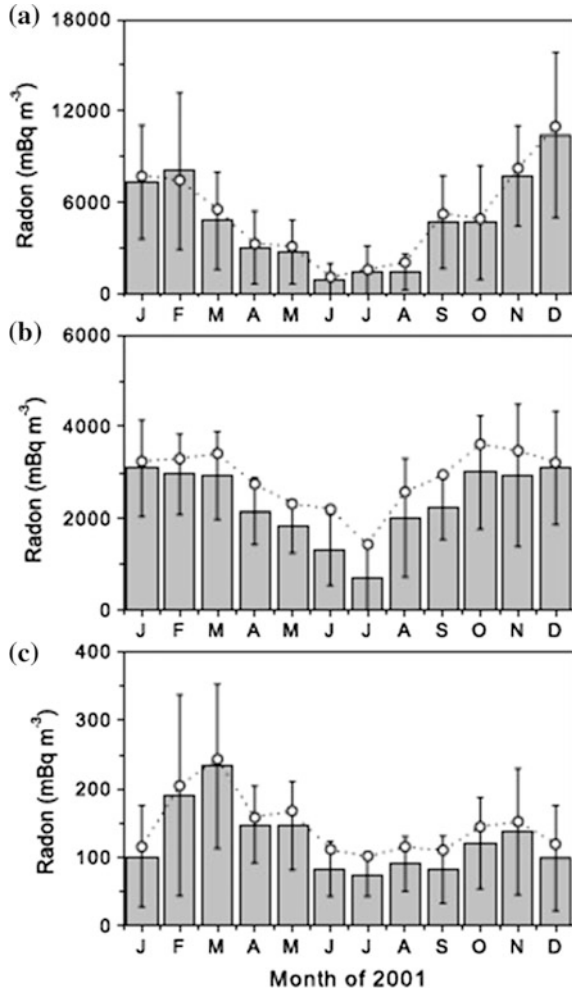
activity in these sites can be that of the marine baseline value, as the radon emanation rate from ocean water likely does not change significantly, partly due to higher heat capacity of water and the changes in air pressure do not change much. Wind speed is one of the main factors that causes observed changes in ocean fluxes. Large heat capacity of water results in a fairly constant PBL depth when the wind fetch is over the ocean. When there is little diurnal change in PBL depth, then, there is usually little diurnal change in radon concentrations measured near the surface. The stations near sea level show clear diurnal cycle of ^{222}Rn concentrations when recent air mass fetch is mostly over land (i.e. not summer, at Hok Tsui, or winter at Gosan station), with a maximum in the morning and minimum in the afternoon (between 1:00 p.m. and 6:00 p.m.), whereas in the high altitude station (MLO), the converse is true (Fig. 4.4). Similar observation is expected in a majority of

continental stations, since heating of Earth's surface will result in active convective updraft of air mass leading to the dilution of boundary layer air mass that are enriched in ^{222}Rn with that airmass with lower ^{222}Rn activity at higher altitude. The ratio of diurnal amplitude to mean ^{222}Rn activity was the highest in summer in Gosan station and MLO and is attributed to dynamic vertical movement of air masses resulting in large variations in ^{222}Rn concentrations, while the winter season has the lowest diurnal amplitude to mean ^{222}Rn activity ratio (Zahorowski et al. 2005; Chambers et al. 2013). The surface concentrations of ^{222}Rn during the day are much smaller because of deep convective vertical mixing (Williams et al. 2011). The smaller diurnal amplitude at Gosan compared to Hok Tsui is attributed to the strong marine influence on boundary layer depth. A closer look Fig. 4.3 a and b, indicates that the amplitudes of the diurnal cycle at Hok Tsui and Gosan are actually quite similar. However, the absolute radon concentrations at Hok Tsui are much higher than at Gosan. This is because Hok Tsui has a much larger, close, terrestrial fetch than Gosan. The radon source function in SE China is also very high. The ratio of diurnal amplitude to mean activity is the lowest in the MLO station, with the daily minimum activity occurring at night, a time when observations are representative of tropospheric conditions and such variations are attributed to the up-slope (anabatic) and down-scale (katabatic) winds during the day and night, respectively (Zahorowski et al. 2005). Chambers et al. (2013) identified a 3-hour mid-morning window that is most representative of tropospheric conditions. The seasonal variations of ^{222}Rn activity indicate that they are pronounced, with the maximum concentrations in the winter months and minimum concentrations in the summer months. In Hok Tsui and Gosan sites (and certain other places in continental setting) such variations are commonly found and are attributed to monsoonal circulation patterns, and extent of vertical and horizontal mixing of air masses arising from differences in the amount of solar insolation (e.g., Japan and China: Iida et al. 2000; India: Debaje et al. 1996). In coastal stations where sources of air masses are highly influenced from the maritime air, the offshore and onshore flow of airmasses taking place at different timescales (seasonal (monsoonal changes)) and synoptic (with the passing of synoptic systems and subsequent changes in air mass fetch) could be the major factor that controls the activity of ^{222}Rn in air. From the temporal variations of ^{222}Rn in MLO, it has been observed that the vertical distribution of tropospheric radon above MLO is more uniform in summer and winter than in spring and autumn (Chambers et al. 2013).

4.6   Variations in the Inventories of ^{222}Rn in the Atmosphere

In a vertical column of the atmosphere, if nonfrontal weather conditions exist and if there is no advection, then, a dynamic balance is expected to exist between influx of radon from the ground to the atmosphere and its removal via radioactive decay. If Q

represents the inventory of all ^{222}Rn (Bq m^{-2}) in the atmosphere to a height of 11 km, then, this ^{222}Rn inventory can be expressed as:

$$Q = \int\limits_{0}^{\infty} (q_z) dz$$

where q(z) is the activity of ^{222}Rn (Bq m^{-3}) at layer z.

The removal rate of ^{222}Rn by radioactive decay (E$_R$, Bq m^{-2} s^{-1}) is given by:

$$E_R = \lambda_{Rn222} * Q$$

where λ is the decay constant = 2.1×10^{-6} s^{-1}.

The inventories of ^{222}Rn for the upper 11 km from Earth's surface, calculated from the data given in Kritz et al. (1998), are given in Table 4.2. Inventories for the 11 profiles varied by a factor of 5.4, from 1412 to 7690 Bq m^{-2}, and such large variations were attributed to varying influences of continental and oceanic air masses to these sampling sites. Overall, the ^{222}Rn inventories in June were significantly higher than that in August 1994 (Table 4.2) and the highest inventory was found on July 7. These variations are likely due to varying fractional inputs of continental air masses.

Table 4.2 Concentrations at 100 m from sea level and total inventory in 11 km of ^{222}Rn from Earth's surface from 11 vertical profiles from Moffett Field, California, USA (37.4° N, 122.0° W)—data from Kritz et al. (1998)

Date	Latitude (°N)	Longitude (°W)	^{222}Rn (100 m) (mBq m^{-3})	^{222}Rn inventory (Bq m^{-2})
June 3, 1994	34.8–37.4	118.9–122.0	0.84	4528
June 7, 1994	37.4–37.8	122.1–125.5	0.47	5485
June 14, 1994	37.4–37.9	119.9–122.1	0.84	3941
June 16, 1994	36.7–37.8	121.6–122.1	0.64	3091
June 23, 1994	37.2–40.2	121.0–122.0	0.77	1528
June 24, 1994	37.2–39.8	120.3–122.1	0.61	1412
June 28, 1994	37.4–39.7	122.1–123.3	1.39	2908
July 7, 1994	37.3–38.9	120.0–122.0	2.23[*]	7690
August 10, 1994	36.8–37.5	120.1–122.0	0.69	2272
August 12, 1994	37.4–39.0	122.1–123.5	1.40	2360
August 16, 1994	37.1–38.0	118.4–122.0	0.89[*]	1609

[*]June 28 and August 16 were from 200 m asl and July 7 was from 800 m

4.7 Role of Atmospheric Rivers in the Transport of ^{222}Rn and Radon Storms

It has been reported that a large amount of tropospheric water vapor is transported poleward (e.g., the typical flow in a South American tropospheric river is very close to that of the Amazon ($\sim 165 \times 10^5$ kg s^{-1} or 1.65×10^4 m^3 s^{-1} or 16.5 million liters of water per second from one river; Newell et al. 1992)- ~ 50 million liters of water per second, equivalent to a 68-m-wide cylindrical pipe gushing water at 50 km/h (modified from Kerr 2006) from the tropics). Newell et al. (1992) from filamentary structures and the filaments are called '*tropospheric rivers*'. The finding of atmospheric river came as a serendipity when explanation(s) for the observed anomalous distribution of carbon monoxide was sought from the computations of daily global tropospheric water vapor flux values. Presence of high concentrations of CO well removed from potential sources and in regions where neither vertical transport into the free troposphere from the boundary layer nor horizontal transport by the prevailing wind existed but could be explained by the flow of large quantities of heat, moisture and westerly momentum poleward and upward as a 'warm conveyor belt' (Newell et al. 1992; Zhu and Newell 1994) and it is likely that radon also could be transported similar to carbon monoxide. Radon in upper air can be carried by the five rivers leading into the middle latitudes of the Southern Hemisphere and 4–5 rivers leading into the Northern Hemisphere; these rivers persist for 10 days or more and travel at ~ 22 km h^{-1} (~ 6 m s^{-1}) which corresponds to the mean zonal wind speed at 750 hecta Pascal (hPa or 750 mb) (Newell et al. 1992). Although these rivers in each hemisphere at any one time occupied ~ 10 % of the mid-latitudes, the rivers were reported to be carrying ~ 90 % of the moisture moving poleward (Kerr 2006). Anomalously high ^{222}Rn concentrations have been reported in remote areas (e.g., Antarctic, Artic South Pacific), far away from the land in several places. For example, ^{222}Rn concentrations at the south pole are usually extremely low (lowest observed in surface air), around 11–15 mBq/STD m^{-3}, similar to concentrations observed under marine conditions in the South Pacific (Wilkniss et al. 1974), but a high ^{222}Rn pulse of 555 mBq STD m^{-3} was observed on January 25 in 1975 (austral summer season). Similar 'radonic storms' have been reported in other regions that include Arctic, Antarctic (at Terre Adelie, 66° 40′ S; 140° E, ~ 555 mBq STD m^{-3} and in a few cases radonics storms occurred simultaneously in several stations, Lambert et al. 1970), and South Pacific. Note that the filamentary structure has also been observed of air entering the troposphere from the stratosphere from aircraft observations and computations (Newell et al. 1992), but these airmasses are dry and significantly older and hence the contribution of ^{222}Rn is likely negligible. Recently, Chambers et al. (2014) reported concentrations >1000 mBq m^{-3} during radonic storm and such events were widely reported throughout the network of Antarctic stations (Fig. 4.5). Medium sized radon events were attributed to rapid transport of air from an 'upstream' continent with a synoptic system in the boundary layer or accumulation/release of locally sourced radon, although the last possibility is highly unlikely. The large radon events were attributed to rapid transport from South America.
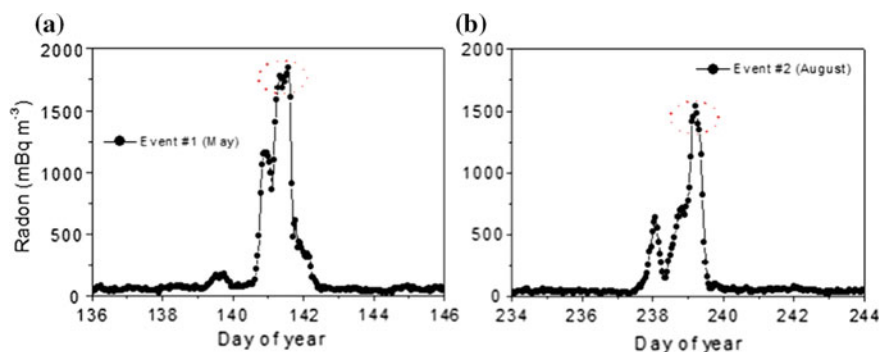
Fig. 4.5 Hourly ^{222}Rn concentrations measured at King Sejong station (62.217° S, 58.783° W) at the tip of the Antarctic Peninsula on Baton Peninsula, King George Island. Two of the largest radon events, one in May 2013 and another in August 2013 are shown. Figure is taken from Chambers et al. (2014)

4.8   Modeling the Atmospheric Distribution of ^{222}Rn

Distribution of radon in the atmosphere is not only useful in the identification of the least-perturbed marine air masses, but also in tracing terrestrial air mass movements, in the refinement of source footprints for aerosols in continental outflow events, calibration of regionally integrated emissions of important greenhouse gases, evaluation of the performance of transport and mixing schemes in weather, climate, and chemical transport model (Williams et al. 2011 and the references cited therein). It has been shown that the deep convection, which is characterized by rapid motion between the planetary boundary layer (PBL) and middle and upper atmosphere plays a dominant role in the transport of ^{222}Rn to the upper troposphere and stratosphere (Donner et al. 2007). The mesoscale updrafts and downdrafts in the atmosphere will directly affect the extent of vertical transport and injection of ^{222}Rn, and such updrafts and downdrafts are fueled by the latent heat released during cloud condensation, in particular from the stratiform cloud systems (Donner et al. 2007). Due to maximum solar insolation in the summer months in the Northern Hemisphere, the vertical mixing of air masses are strong and convection transport are dominant resulting in deep convection transport and lower ^{222}Rn concentrations in the PBL in the daytime. However, in many continental sites, clear sky summer conditions lead to very stable nights, and high nocturnal radon concentrations at night. So, averaged over the diurnal cycle, radon in the PBL may not be lower in summer.

All these atmospheric models require the ^{222}Rn flux data from earth's surface. Radon flux estimates for some of the countries/continents have been reported (e.g. Global: Conen and Robertson 2002; Europe: Szegvary et al. 2009; Karstens et al. 2015; Australia: Griffiths et al. 2010; China: Zhou et al. 2008) and discussions on the latitudinal variability are given in a number of papers (e.g., Conen and Robertson 2002;

Williams et al. 2009). Most of the models employed so far have relied on a simple assumption of ^{222}Rn flux from land surfaces of 1 atom cm^{-2} s^{-1} (or 10^4 atoms m^{-2} s^{-1}) between 60° S and 60° N, and 0.5 atom cm^{-2} s^{-1} between 60°–70° S and 60°–70° N (e.g., Rasch et al. 2000). However, it was shown that a globally uniform land-based ^{222}Rn surface flux of 1.0 atom cm^{-2} s^{-1}, with in ±60°, overpredicts atmospheric Rn in both hemispheres. Utilizing a value of 0.72 atom cm^{-2} s^{-1} within ±60° produces atmospheric distributions of ^{222}Rn that compare well with the observed Northern Hemisphere distributions (Gupta et al. 2004).

From a compilation 38 measured tropospheric vertical profiles of ^{222}Rn from global data set (up to 9 km above ground level from eastern United States that include central Illinois in 1967, Ohio in 1950; western United States (up to 12 km above ground) that include Limon, Colorado in 1969, Scottsbluff, Nebraska in 1971, Salt Lake City, Utah in August 1971, and Scottsbluff, Nebraska in 1971 and 1972; and former Soviet Union that include European USSR (up to 9 km above ground level that include near Moscow in 1967, eastern Ukraine in 1966); Arizona in the southwestern United States during summer 1971 up to 5 km above ground level; Yukon Valley of Alaska during winter 1972, up to 5 km above ground), Liu et al. (1984) observed that the average ^{222}Rn profiles for summer, spring-fall and winter, indicate there are distinct differences in the vertical profiles of ^{222}Rn. From the analysis of these vertical ^{222}Rn profiles, it was reported that about 55 % of the ^{222}Rn is transported above the planetary boundary layer in summer, considerably more than the other seasons. Williams et al. (2011) considered the transport of radon from the PBL under different meteorological conditions, and highlighted the importance of convective cells. They also reported that in summer about 20 % of the ^{222}Rn in the planetary boundary layer rises to over 5.5 km ($\sim$500 milli bar). From the average profiles obtained from a large data set, they calculated the vertical eddy diffusion coefficients with maximum values of 50–70 × 10^4 cm^2 s^{-1} in the mid-troposphere, 0.8–5 × 10^4 cm^2 s^{-1} near the surface and a decrease as the tropopause is approached (Table 4.3). The slope of the summer profile changes relatively steeply below 3 km and gradually levels off between 3 and 8 km. The eddy coefficient obtained above was used to estimate the fractions of trace gases that escape PBL that are reactive and have lifetimes of 1, 3 and 10 days to be 20, 40, and 70 %, respectively, assuming that the top of the boundary layer to be 2 km in the summer (Liu et al. 1984). Thus, by inference, for a pollutant with a lifetime similar to ^{222}Rn and surface source, >50 % would reach the troposphere above the PBL (also known as atmospheric boundary layer) in the summer, but significantly less in other seasons (Liu et al. 1984).

Table 4.3 Radon based Vertical diffusion constant

Location	Diffusion coefficient (m^2 s^{-1})	Reference
Tropics	50	Jacob et al. (1997)
Non-tropics	10	Jacob et al. (1997)
Average of global dataset	50–70 (mid-troposphere)	Liu et al. (1984)
Average of global dataset	0.8–5.0 near surface	Liu et al. (1984)

From a consensus on the need to assess different global models to compare the scavenging and deposition processes, World Climate Research Program (WCRP) organized a workshop in 1995 at Downing College at Cambridge, UK. An evaluation of scavenging and deposition process of 15 global models by comparing simulations of ^{222}Rn, ^{210}Pb, SO_2, and SO_4^{2-} against each other, and against observations for these constituents indicate that the predicted model-based ^{222}Rn concentrations vary by more than an order of magnitude in Antarctica. For example, 11 different models-predicted seasonal variations of ^{222}Rn to vary an order of magnitude, from <1 mBq/SCD m^{-3} to >50 mBq SCD m^{-3} for Antarctica (Fig. 4.6) during all four seasons, with the largest differences in June–July–August (winter time in the southern hemisphere), although all these modelers were asked to use a source distribution of 1.0 atom cm^{-2} s^{-1} over land between 60° S and 60° N, and 0.5 atom cm^{-2} s^{-1} over land between 60° N and 70° N, except Greenland, where the surface was assumed to be ice-covered (Rasch et al. 2000). Model-predicted ^{222}Rn concentrations in Bermuda were often 2-4 times too high compared to observational

Fig. 4.6 Seasonal variations in radon over Bermuda (*top*) and Antarctica (*bottom*) for the models (various *thin line* patterns) and the observational estimate (heavy *black line*). Figure is taken from Rasch et al. (2000)
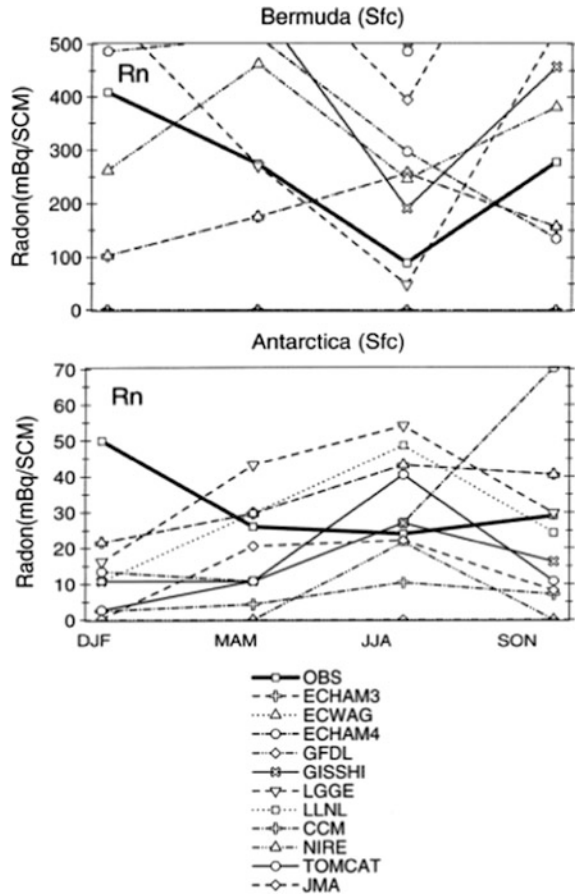
estimate (Fig. 4.6). It appears that a number of models are not well constrained and more work needs to be done in this area of research in calibrating each of the models and identify the reasons for the differences in the results obtained between these 11 groups.

4.9 Application of ^{222}Rn as Indian Monsoon Air Circulation Tracer

Radon has been utilized as a tracer in quantifying the interaction and moisture transport between two constituent air masses: (i) maritime equatorial air mass and (ii) continental African air mass in the Indian subcontinent region. In the Arabian Sea, the monsoon current was found to consist of two very distinct air masses: the lower maritime air mass from sea surface to ~ 1 km level, with a very low ^{222}Rn activity (17–67 mBq m^{-3} STD; Fig. 4.7a), mainly derived from the southern hemisphere and the upper relatively dry continental air mass, from 1 to ~ 5 km, with 10–20 times higher ^{222}Rn activity (Rama 1969, 1970). The ^{222}Rn activity started increasing from the Western Arabian Sea eastward to values of 330–500 mBq m^{-3}, and was attributed to the mixing of continental air mass from above. During the winter months, the air mass from the Indian subcontinent is known to pervade over the Arabian Sea, with the average ^{222}Rn activity in the winter months of ~ 670 mBq m^{-3} which is significantly higher than the maritime air mass values (Rama 1969; Fig. 4.7b). The surface monsoon air over the east Arabian Sea is found to have a range between 80–500 mBq m^{-3}, with a mean value of 330 mBq m^{-3}. From the average ^{222}Rn activity in continental air of 670 mBq m^{-3} and average maritime air mass ^{222}Rn activity in the east Arabian Sea of 330 mBq m^{-3}, Rama (1969) estimated that the component of continental air in surface air exceeds 50 % near the coast. Reliable ^{222}Rn data in the upper air in conjunction with air trajectory analysis could provide insight on the monsoon dynamics in the subcontinent and possibly as to why there are inter-annual variations in the amounts of monsoon in the Indian subcontinent.

4.10 Applications of ^{222}Rn as a Proxy for Other Pollutants

Radon being a noble gas is not susceptible to removal by wet or dry atmospheric removal processes, and hence flow and mixing of atmospheric vapor and other gases can be tracked using radon. In the atmosphere, the mean-life of ^{222}Rn is comparable to the lifetimes of short-lived atmospheric pollutants such as NO_x (oxides of nitrogen, the major ones being NO, NO_2), SO_x (oxides of sulphur, the major ones being SO_2 and SO_3), propane, butane and other particle-reactive hydrocarbons. Accumulation of ^{222}Rn in the nocturnal boundary layer is widely used to characterize atmospheric stability influences on air pollution (e.g. Chambers et al. 2015), and to estimate emissions of CO_2, CH_4, N_2O, Hg^0 and other species by

Fig. 4.7a Activity of [222]Rn in surface air over the Arabian Sea and the Indian Ocean during monsoon period (in dpm m^{-3}; 1 dpm m^{-3} = 16.67 mBq m^{-3}); (figure is taken from Rama, J. Geophys. Res. 1970, with permission from AGU)

Fig. 4.7b Activity of [222]Rn in surface air over the Arabian Sea during post-monsoon period (in dpm m^{-3}; 1 dpm m^{-3} = 16.67 mBq m^{-3}); figure is taken from Rama, J. Geophys. Res. 1970, with permission from AGU

mass balance approach (Szegvary et al. 2009; Zahorowski et al. 2004). Radon flux has been used to estimate Hg^0 emissions during stable nocturnal boundary layers (during non-turbulent atmospheric conditions; Obrist et al. 2006; Slemr et al. 2013). Other gases released from the ocean surface can also be traced using [222]Rn. For example, biogenic dimethylsufide ((CH$_3$)$_2$S, DMS) is an important precursor for sulfur dioxide (SO$_2$) and methanesulfonic acid (CH$_3$SO$_2$(OH), MSA) due to its reaction with the hydroxyl radical (OH) during the day and the nitrate radical (NO$_3$) at night (Andrea et al. 1988). It is released from the oceans to the atmosphere and is considered to be the major natural source in the atmospheric sulfur budget. The DMS/[222]Rn ratio in air samples could be a useful tracer for tracing the sources of

DMS. Radon has also been used in particulate matter source apportionment, as a parameter for source dilution (Crawford et al. 2013, 2015).

4.11   Summary and Future Research Directions

Utility of radon as an effective atmospheric tracer requires precise radon flux determination mainly from continent and to a lesser extent from the ocean surface. Although diurnal, monthly and seasonal changes of radon fluxes have been widely reported, using long-term direct atmospheric depositional fluxes of ^{210}Pb, one can estimate the annual average ^{210}Pb flux for a specific region. However, validation of atmospheric modeling studies require average radon flux over a period of the mean-life of ^{222}Rn and hence more precise regional ^{222}Rn flux is a prerequisite for atmospheric studies. A number of attempts have been made towards this effort, but more concentrated efforts are needed.

Oceanic radon fluxes are anticipated to be high from certain regions such as coastal areas around the world, mainly due to much larger discharge of ^{222}Rn and ^{226}Ra via submarine groundwater discharge. Specific regions in Northeast Asia (e.g., some parts of Japan [note also that the southeast coastal region of China also has high radon fluxes]) is anticipated to have the highest ^{222}Rn flux (as observed from the highest ^{210}Pb atmospheric depositional flux) and accordingly global modeling community is required to take these factors into consideration.

Temporal variations of ^{222}Rn activity data in the upper air in conjunction with air trajectory analysis in the marginal seas surrounding Indian subcontinent could provide insight on the northeast and southwest monsoon dynamics that impacts the Indian subcontinent in a major way and possibly factors and atmospheric processes that affect the interannual variations in the amount of precipitation during monsoon in the Indian subcontinent. The role of atmospheric rivers in the transport of ^{222}Rn to different latitudes are not included in any of the existing models. Although ^{222}Rn activity in surface air in Antarctic is very low, there are 'radonic storms' reported, where ^{222}Rn activity increases by more than an order of magnitude, and it remains unknown what causes this spike in ^{222}Rn activity and whether the transport of ^{222}Rn via atmospheric rivers play a role on this. Eleven different models that predicted the seasonal variations of ^{222}Rn concentrations in air, assuming constant ^{222}Rn emanation rates, vary over an order of magnitude both in Antarctic and Bermuda and thus it appears that a number of models are not well constrained and more work needs to be done in this area of research in calibrating each of the models and identify the reasons for the differences between these 11 groups. Future radon measurements in Antarctic should help improve the parametrization of convection and tropospheric transport in models.

References

Andrea MO, Berresheim H, Andreae TW (1988) Vertical distribution of dimethelsulfide, sulfur dioxide, aerosol ions, and radon over the northeast Pacific Ocean. J Atmos Chem 6:149–173

Balkanski YJ, Jacob DJ, Arimoto R et al (1992) Distribution of Rn-222 over the North Pacific—implications for continental influences. J Atmos Chem 14:353–373

Baskaran M (2011) Po-210 and Pb-210 as atmospheric tracers and global atmospheric Pb-210 fallout: a Review. J. Environ Radioact 102:500–513. doi:10.1016/j.jenvrad.2010.10.007

Baskaran M, Naidu AS (1995) ^{210}Pb-derived chronology and the fluxes of ^{210}Pb and ^{137}Cs isotopes into continental shelf sediments, East Chukchi Sea, Alaskan Arctic. Geochim Cosmochim Acta 59:4435–4448

Bressan DJ, Larson RE, Wilkniss PE (1973) Atmospheric radon and dust, air mass trajectories and meteorological conditions over the Greenland Sea. Nature 245:74–77

Carvalho FP (1995) Origins and concentrations of ^{222}Rn, ^{210}Pb, ^{210}Bi and ^{210}Po in the surface air at Lisbon, Portugal, at the Atlantic edge of the European continental landmass. Atmos Environ 29:1809–1919

Chambers SD, Zahorowski W, Williams AG et al (2013) Identifying tropospheric baseline air masses at Mauna Loa Observatory between 2004 and 2010 using Radon-222 and back trajectories. J Geophys Res 118(2):992–1004

Chambers SD, Hong S-B, Williams AG, Crawford J, Griffiths AD, Park S-J (2014) Characterizing terrestrial influences of Antarctic air masses using Radon-222 measurements at King George Island. Atmos Chem Phys 14:9903–9916. doi:10.5194/acp-14-9903-2014

Chambers SD, Wang F, Williams AG, Xiaodong D, Zhang H, Lonati G, Crawford J, Griffiths AD, Ianniello A, Allegrini I (2015) Quantifying the influences of atmospheric stability on air pollution in Lanzhou, China, using a radon-based stability monitor. Atmos Environ 107:233–243

Conan F, Robertson LB (2002) Latitudinal distribution of radon-222 flux from continents. Tellus 54B, 127–133

Crawford J, Cohen DD, Chambers S, Williams A, Stelcer E (2013) Incorporation of Radon-222 as a parameter in ME-2 to improve apportionment of PM2.5 sources in the Sydney region. Atmos Environ 80:378–388

Crawford J, Chambers S, Cohen DD, Griffiths A, Williams A, Stelcer E (2015) Using Radon-222 as an indicator of atmospheric mixing depth in ME-2 for PM2.5 source apportionment. Aerosol Air Qual Res 15:611–624

Debaje SB, Vernekar KG, Ramachandran TV (1996) Study of atmospheric radon-222 concentration at Pune. Indian J Environ Prot 16(10):755–760

Donner LJ, Horowitz LW, Fiore AM, Seman CJ, Blake DR, Blake NJ (2007) Transport of radon-222 and methyl iodide by deep convection in the GFDL Global atmospheric model AM2. J Geophys Res 112:D17303. doi:10.1029/2006JD007548

Gupta ML, Douglass AR, Kawa R et al (2004) Use of radon for evaluation of atmospheric transport models: sensitivity to emissions. Tellus B 56(5):404–412

Griffiths AD, Zahorowski W, Element A, Werczynski S (2010) A map of radon flux at the Australian land surface. Atmos Chem Phys 10:8969–8982

Iida TK, Yamada K, Hashiguchi Y, Morizumi J et al (2000) Measurements of atmospheric radon concentrations at various locations in east Asia. In: Inaba J, Hisamatsu S, Ohtsuka Y (eds) Distribution and speciation of radionuclides in the environment. Rokkasho, Aomori, pp 123–132

Jacob DJ, Prather MJ, Rasch PJ et al (1997) Evaluation and intercomparison of global atmospheric transport models using ^{222}Rn and other short-lived tracers. J Geophys Res 102:5953–5970

Karstens U, Schwingshackl C, Schmithusen D, Levin I (2015) A process-based ^{222}Rn flux map for Europe and its comparison to long-term observations. Atmos Chem Phys 15:12845–12865. doi:10.5914/acp-15-12845-2015

Kerr RA (2006) Rivers in the sky are flooding the world with tropical waters. Science 313:435

Kritz MA, Rosner SW, Kelly KK, Loewenstein M, Chan KR (1993) Radon measurements in the lower tropical stratosphere: evidence for rapid vertical transport and dehydration of tropospheric air. J Geophys Res 98:8725–8736

Kritz MA, Rosner SW, Stockwell DZ (1998) Validation of an off-line three-dimensional chemical transport model using observed radon profiles −1. Observations. J Geophys Res 104 (D7):8425–8432

Lal D (2002) Cosmogenic radionuclides. In: Holton JR, Pyle J, Curry JA (eds) Encyclopedia of atmospheric sciences. Academic, London, pp 1891–1900

Lal D, Baskaran M (2011) Application of cosmogenic isotopes as atmospheric tracers. In: Baskaran M (ed) Handbook of environmental isotope geochemistry, pp 575–589

Lal D, Rama (1966) Characteristics of global tropospheric mixing based on man-made ^{14}C, ^{3}He, and ^{90}Sr. J Geophys Res 71:2865–2874

Lambert G, Polian G, Taupin D (1970) Existence of periodicity in radon concentrations in the Large-Scale circulation at lower latitudes between 40 and 70 South. J Geophys Res 75: 2341–2345

Lambert G, Polian G, Sanak J et al (1982) Radon cycle and its descendants to the study of troposphere stratosphere changes. Annales de Geophysique 38(4):497–531

Liu SC, McAfee JR, Cicerone RJ (1984) Radon 222 and tropospheric vertical transport. J Geophys Res 89:7291–7297

Maenhaut W, Zoller WH, Coles DG (1979) Radio nuclides in the South Pole atmosphere. J Geophys Res 84:3131–3138

Merrill JT, Uematsu M, Beck R (1989) Meteorological analysis of long range transport of mineral aerosols over the North Pacific. J Geophys Res 94(D6):8584–8598

Moore HE, Poet SE, Martell EA (1973) ^{222}Rn, ^{210}Pb, ^{210}Bi, and ^{210}Po profiles and aerosol residence times versus altitude. J Geophys Res 78:7065–7075

Moore HE, Poet SE, Martell EA (1977) Vertical profiles of ^{222}Rn and its long-lived daughters over the eastern Pacific. Environ Sci Technol 11:1207–1210

Newell RE, Newell NE, Zhu Y, Scott C (1992) Tropospheric Rivers? A pilot study. Geophys Res Lett 19(24):2401–2404

Nazaroff WW (1992) Radon transport from soil to air. Rev Geophys 30:137–160

Obrist D, Conen F, Vogt R, Siegwolf R, Alewell C (2006) Estimation of Hg^{0} exchange between ecosystems and the atmosphere using ^{222}Rn and Hg^{0} concentration changes in the stable nocturnal boundary layer. Atmos Environ 40:856–866

Polian G, Lambert G, Ardouin B, Jegou A (1996) Long-range transport of continental radon in subantarctic areas. Tellus 38B:178–189

Prather MJ, McElroy MB, Wofsy SC, Russell G, Ring D (1987) Chemistry of the global troposphere: Fluorocarbons as tracers of air motion. J Geophys Res 92:6579–6613

Prospero JM, Carlson TN (1970) Radon-222 in the North Atlantic Trade Winds: its relationship to dust transport from Africa. Science 167:974–977

Rama (1969) Monsoon circulation from observations of natural radon. Earth Planet Sci Lett 6:56–60

Rama (1970) Using natural radon for delineating monsoon circulation. J Geophys Res 75 (12):2227–2229

Rasch PJ, Feichter J, Law K, Mahowald N et al (2000) A comparison of scavenging and deposition processes in global models: results from the WCRP Cambridge Workshop of 1995. Tellus 52B:1025–1056

Samuelsson C, Hallstadius L, Persson B, Hedvall R, Holm E (1986) ^{222}Rn and ^{210}Pb in the Arctic summer air. J Environ Radioact 3:35–54

Schery SD, Gaeddert DH (1982) Measurement of the effect of cyclic atmospheric pressure variation on the flux of ^{222}Rn from the soil. Geophys Res Lett 9(8):835–838

Schery SD, Huang S (2004) An estimate of the global distribution of radon emissions from the ocean. Geophys Res Lett 31(L19104):2004. doi:10.1029/2004GL021051

Slemr F, Brunke E-G, Whittlestone S, Zahorowski W, Ebinghaus R, Kock HH, Labuschagne C (2013) 222Rn-calibrated mercury fluxes from terrestrial surface of southern Africa. Atmos Chem Phys 13:6421–6428

Subramanian SK, Rangarajan C, Gopalakrishnan SS, Eapen CD (1977) Radon daughters radioactivity levels over Arabian Sea as indicators of air mass mixing. J Appl Meteorol 16(5):487–492

Szegvary T, Conen F, Ciais P (2009) European ^{222}Rn inventory for applied atmospheric studies. Atmos Environ 43:1536–1539

Talbot RW, Dibb JE, Lefer BL, Bradshaw JD, Sandholm ST et al (1997) Chemical characteristics of continental outflow from Asia to the troposphere over the western Pacific Ocean during February-March 1994: results from PEM-West B. J Geophys Res 102(D23):28255–28274

Turekian KK, Graustein WC (2003) Natural radionuclides in the atmosphere. In: Treatise in geochemistry, 4.10, pp 261–279

Turekian KK, Nozaki Y, Benninger LK (1977) Geochemistry of atmospheric radon and radon products. Annu Rev Earth Planet Sci 5:227–255

Wedepohl KH (1995) The composition of the continental crust. Geochim Cosmochim Acta 59:1217–1232

Wilkening MH, Clements WE (1975) Radon-222 from the ocean surface. J Geophys Res 80: 3828–3830

Wilkniss PE, Larson RE (1984) Atmospheric radon measurements in the Arctic: Fronts, seasonal observations, and transport of continental air to polar regions. J Atmos Sci 41:2347–2358

Wilkniss PE, Larson RE, Bressan DJ, Steranka J (1974) Atmospheric radon and continental dust near Antarctic and their correlation with air mass trajectories computed from NIMBUS-5 satellite photographs. J Appl Meteorol 13(4):512–515

Williams A, Chambers S, Zahorowski W, Crawford J, Matsumoto K, Uematsu M (2009) Estimating the Asian radon flux density and its latitudinal gradient in winter using ground-based radon observations at Sado Island. Tellus B 61:732–746. doi:10.1111/j.1600-0889.2009.00438.x

Williams AG, Zahorowski W, Chambers S, Griffiths A, Hacker JM et al (2011) The vertical distribution of radon in clear and cloudy daytime terrestrial boundary layers. J Atmos Sci 68:155–174. doi:10.1175/2010JAS3576.1

Zahorowski W, Chambers SD, Henderson-Sellers A (2004) Ground based radon-222 observations and their application to atmospheric studies. J Environ Radioact 76:3–33

Zahorowski W, Chambers SD, Wang T et al (2005) Radon-222 in boundary layer and free tropospheric continental outflow events at three ACE-Asia sites. Tellus B 57(2):124–140

Zahorowski W, Griffiths S, Chambers SD et al (2013) Constraining annual and seasonal radon-222 flux density from the Southern Ocean using radon-222 concentrations in the boundary layer at Cape Grim. Tellus B 65(19622):2013

Zhu Y, Newell RE (1994) Atmospheric rivers and bombs. Geophys Res Lett 21(18):1999–2002

Zhou W, Guo Q, Chen B, Cheng G (2008) Estimating the amount and distribution of radon flux density from the soil surface in China. J Environ Radioact 99:1143–1148

Chapter 5
Applications of Radon Progeny in Atmospheric Studies

5.1 Introduction

The decay products of ^{222}Rn include 11 isotopes (7 from the major decay pathway; Fig. 5.1) that are continuously produced in the atmosphere. Of the 6 elements (Po, Bi, At, Tl, Hg and Pb) that are produced in the decay of ^{222}Rn, the branching ratio of the decay that goes through ^{214}Hg, ^{206}Tl and ^{210}Tl are small (<0.1 %, Fig. 5.1). The 6.0 MeV energy of the alpha particle emitted by the ^{222}Rn decay in the atmosphere causes the daughter ^{218}Po nuclide to recoil with a velocity much greater than that of the ambient gas molecules or atoms and diminish until its energy is the same as that of the ambient air, at which time the ^{218}Po diffuses through the air until it encounters a surface, typically an aerosol particle, to which it attaches (Turekian and Graustein 2003). Almost 100 % of atmospheric radon are derived from emanation from continental (>99 %) and oceanic (<1 %) surfaces. Due to its chemical nature, atmospheric radon traces the sources of air masses in the atmosphere. The mean life of radon (t = 5.53 days) is generally comparable to the transit time of air masses across major continents and/or oceans and hence it is widely dispersed in the atmosphere. Radon is chemically inert and is not removed from the atmosphere by physical or chemical means and hence it is exclusively lost from its radioactive decay making it to be the primary source of most of ^{214}Pb, ^{214}Bi, ^{214}Po, ^{210}Pb, ^{210}Bi and ^{210}Po in the atmosphere. Soon after the production of ^{210}Pb from the decay of ^{214}Po, ^{210}Pb rapidly associates with aerosols in the 0.1–0.5 µm diameter size range (Knuth et al. 1983; Turekian and Graustein 2003). Lead-210-laden aerosols of this size range, known as 'accumulation mode', are large enough so that their velocity due to Brownian motion is so small that diffusion is not a significant method of transport. Their Stokian gravitational settling velocity is much less than the typical rates of vertical motions in the atmosphere. Scavenging by precipitation is the primary mechanism of removal of the Rn-progeny-laden atmospheric aerosols. The activities of the long-lived daughter products of ^{222}Rn, viz., ^{210}Pb, ^{210}Bi and ^{210}Po
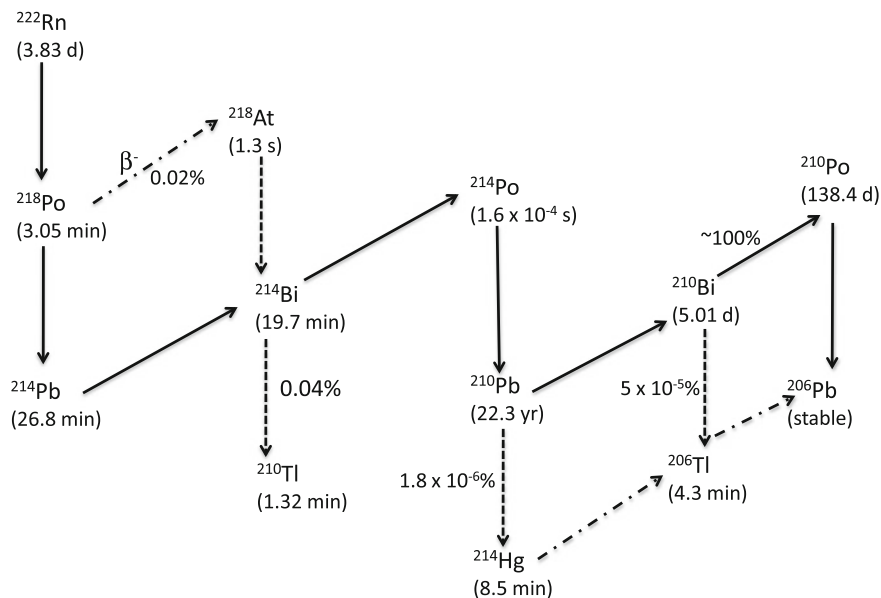
Fig. 5.1 Radon-222 and its decay chain

in the atmosphere are governed, to a large extent, by their production rates, rates of decay and removal by scavenging by atmospheric aerosols.

Some of the progeny of ^{222}Rn in the atmosphere have been widely utilized as tracers to quantify processes that include: (i) source tracking and transport (within and between troposphere and stratosphere) time scales of air masses including vertical movement and stability of air masses; (ii) residence times and removal rate constants of aerosols; (iii) deposition velocities and washout ratios of aerosols; (iv) flux to and exchange between environmental systems of other gases species such as CH$_4$, Hg^0; and (v) processes of attachment of metal ions to atmospheric aerosols (e.g., Turekian et al. 1977, 1989; Church and Sarin 2008; Baskaran 2011 and the references therein). Lead-210 also has been used as a surrogate for other atmospheric components (e.g., atmospheric sulfate—its precursor SO$_2$ is a gas similar to ^{210}Pb's precursor ^{222}Rn, Mattsson 1988; mercury which exists as a gaseous element (only oxidized species of mercury is removed by precipitation); hydrocarbons).

In this chapter, the utility of ^{210}Po and ^{210}Pb as atmospheric tracers are reviewed. The global database for the depositional fluxes of atmospheric ^{210}Pb is evaluated and a global fallout curve for ^{210}Pb is included. The factors and processes that cause spatial and temporal variations of ^{210}Pb fluxes are discussed. The long-term average ^{222}Rn emanation rates based on the atmospheric depositional fluxes, inventory of excess ^{210}Pb in sediment cores and ice cores are given. The residence times of bulk and size-fractionated aerosols are compared and the possible causes for the discordancy of residence times obtained from three different pairs (^{210}Pb/^{222}Rn,

^{210}Bi/^{210}Pb and ^{210}Po/^{210}Pb) are discussed. We evaluate the importance of resuspended dust and how its contribution can lead to discordant residence time of aerosols obtained between ^{210}Bi/^{210}Pb and ^{210}Po/^{210}Pb pairs.

5.2 Sources, Fluxes and Distributions of Radon and Its Progeny

5.2.1 Radon Flux to and Distribution in the Atmosphere

A large body of data exists on the ^{222}Rn flux data obtained both by direct measurements (measured directly from the collection of air samples containing ^{222}Rn emitted from a known area of soil) and from the integration of ^{222}Rn profiles in the atmosphere by estimating the flux and assuming balance between ^{222}Rn emanation and decay (summarized in Robbins 1978; Turekian et al. 1977, 2003; Church and Sarin 2008). Each of these methods have their own limitations. For example, the direct measurements are from very narrow area and assumption of steady state between emanation and decay is questionable when maritime air mass intrudes prevailing continental air mass, such as maritime tropical air mass mixing with continental and continental polar air masses. The radon flux from different mineral grains is also variable and more details on the factors and processes that affect radon emanation flux are given in Chap. 3.

About 10 % of the ^{222}Rn produced from the decay of ^{226}Ra in the upper one meter of the soil is released to the atmosphere (Turekian et al. 1989). The mean diffusion length of ^{222}Rn in soil water is ~ 1 mm which is about 1000 times smaller than that in the air and hence in regions where there is frequent precipitation and the pore spaces of the soil are saturated, the ^{222}Rn emanation is expected to be suppressed.

The long-term global ^{222}Rn fluxes from continents range from 0.0056 atom cm^{-2} s^{-1} to 2.0 atom cm^{-2} y^{-1} (Turekian et al. 1977; Turekian and Graustein 2003). Using the inventory of ^{210}Pb in a number of soil profiles in the continental United States, higher ^{222}Rn fluxes, 1.5–2.0 atoms cm^{-2} s^{-1}, have also been reported (Table 5.1; Turekian and Graustein 2003). From the long-term (>1 year) data of the atmospheric depositional fluxes of ^{210}Pb from 35 different sites, the calculated radon emanation rates varied between 0.19 and 2.70 atom cm^{-2} s^{-1} (Table 5.2, Du et al. 2015). The weekly mean emanation rates of ^{222}Rn between 65° and 70° N in summer was found to be higher by a factor of 2.5 than the winter and this was attributed to snow and soil moisture dominating the winter time and significantly drier conditions existing in summer (Szegvary et al. 2009). The ^{222}Rn emanation rates decrease with increasing latitude, from 1 atom cm^{-2} s^{-1} at 30° N to 0.2 atom cm^{-2} s^{-1} at 70° N, and was attributed to the increased water saturation in the soils with increasing latitude (Conen and Robertson 2002). High radon emanation rates close to Japan and a relatively low flux across the rest of the North Pacific including

Table 5.1 Compilation of long-term ^{210}Pb flux around the globe (Data are taken from Preiss and Genthon (1997), Baskaran and Naidu (1995) and Du et al. (2015))

Latitude	[210]Pb flux (mBq cm^{-2} y^{-1})	Number of sites	Nature of samples
North			
0–10	15.8 ± 11.3	3	1 Coa, 1 O, and 1 C
10–20	13.3 ± 8.3	3	1 Coa, 2 C
20–30	19.8 ± 11.2	13	4 Coa, 5 C, and 4 A
30–40	17.8 ± 11.8	46	14 Coa, 10 C, 9 Coa/C, and 13 A
40–50	15.6 ± 7.5	52	6 Coa, 26 C, 13 Coa/C and 7 A
50–60	9.3 ± 4.5	10	5 Coa, 4 C
60–70	3.7 ± 3.5	9	2 Coa, 4 C, 3 IC
70–80	2.0 ± 1.5	10	1 Coa, 2 C, 7 IC
South			
0–10*	11.7	1	1 C
10–20	6.7	2	2 Co
20–30	6.5 ± 2.7	5	4 Co, 1 C
30–40	6.1 ± 0.2	5	5 Co
40–50	4.2	2	2 CI
50–60	3.3	1	1 O
60–70	0.63 ± 0.22	11	I C
70–80	0.21 ± 0.12	7	I C
80–90	0.18 ± 0.08	11	I C

Co Coastal; *C* Continental; *O* Ocean; *IC* Ice core/sheet; *A* direct atmospheric depositional flux
Only the coastal and continental samples are included; however, in areas where the number of samples are limited (n < 3), the ocean samples (when available) were included
*Data is from the [222]Rn flux calculated for April and May (Trumbore et al. 1990)

the California coast have been reported. High radon emanation rates in some regions in Japan (2.70 atom cm^{-2} s^{-1}) and the regions of the 'ring of fire' could be due to large number of micro and macro earthquakes (>70 % of the global earthquakes) that could allow higher escape of [222]Rn.

5.2.2 Activities of [210]Po and ^{210}Pb in Surface Air and Upper Atmosphere

Temporal and spatial variations of ^{210}Pb and [210]Po in surface air:
    Burton and Stewart (1960) made the first measurement of atmospheric [210]Po (known as Radium-F), [210]Bi (Radium-E) and [210]Pb (Radium-D) in air samples. Following this study, a number of studies have been conducted. In both continental and marine setting, the ^{210}Pb activity in air varies widely. The factors that affect the

Table 5.2 Global fallout data of latitudinal variations of measured ^{210}Pb flux and calculated ^{222}Rn flux

Study area	Sample date	Latitude	Longitude	Distance between location and ocean (km)	Annual rainfall (mm)	Volume-weighted ^{210}Pb activity (Bq L^{-1})	^{210}Pb flux (Bq m^{-2} year^{-1})	^{222}Rn flux (at cm^{-2} s^{-1})	References
College station, TX	1989.6–1992.2	30.6° N	96.4° W	200	1220	0.15	179	0.58	Baskaran et al. (1993)
New Haven	1977–1978	41° N		10	1480	0.14	200	0.64	Turekian et al. (1983)
Los Angeles, CA		33.93° N	118.4° W	<5	360	0.097	35	0.11	Fuller and Hammond (1983)
Palo Alto, CA		37.78° N	122.2° W	5 km	490	0.051	25	0.08	Turekian et al. (1983)
Bermuda	1977–1978	33° N		2	1700	0.07	115	0.37	Turekian et al. (1983)
Norfolk	1983.1–1984.12	36.9° N	76.3° W	45	1360	0.1	137	0.44	Olsen et al. (1985)
Galveston, TX	1988.12–1992.2	29.3° N	94.8° W	2	1167	0.15	172	0.55	Baskaran et al. (1993)
Stillpond	1995.9–1996.8	39° N	70.1° W	100	1260	0.1	130	0.42	Kim et al. (2000)
Lake Constance	1993	47.7° N	9.2° E	400	–	–	108	0.35	Vogler et al. (1996)
Zurich Lake	1984–1987	47.3° N	8.6° E	350	1100	0.13	138	0.44	Schuler et al. (1991)

(continued)

Table 5.2 (continued)

Study area	Sample date	Latitude	Longitude	Distance between location and ocean (km)	Annual rainfall (mm)	Volume-weighted ^{210}Pb activity (Bq L^{-1})	^{210}Pb flux (Bq m^{-2} year^{-1})	^{222}Rn flux (at cm^{-2} s^{-1})	References
Oak Ridge, TN	1982.9–1984.12	36° N	84.3° W	500	1270	0.09	114	0.37	Olsen et al. (1985)
Nankang, Taiwan	1996–2001	25° N	121.6° E	17	1945	0.16	317	1.02	Su et al. (2003)
Peng-Chia Yü, Taiwan	1996–2001	25.7° N	122.1° E	0.5	1929	0.09	183	0.59	
Ansan, Korea	1992–1993	37.3° N	126.8° E	20	1120	0.22	248	0.80	Kim et al. (1998)
Seoul, Korea	2009–2010	37.5° N	127° E	30	1816	0.16	273	0.88	Yan et al. (2012)
Huelva, Spain	2009–2010	37.2° N	6.7° E	1	1000	0.06	59	0.19	Lozano et al. (2011)
Western Mediterranean Sea (9 sites)		36–44° N	0.5–11° W	<5	400–1500	0.12–0.26	47–390	0.15–1.3	Garcia-Orellana et al. (2006)
Detroit, Michigan	1999–2001	42.4° N	83° W	770	760	0.35	235	0.76	McNeary and Baskaran (2003)
Gironde estuary, France	2006–2007	45.2° N	0.4° W	55	923	0.11	103	0.33	Saari et al. (2010)
Ahmedabad, India	2000–2002	23.0° N	72.6° E	180	650	0.075	68	0.22	Rastogi and Sarin (2008)
Xiamen, China	2001–2003	24.4° N	118.1° E	2	1618	0.09	150	0.48	Jia et al. (2003)

(continued)

Table 5.2 (continued)

Study area	Sample date	Latitude	Longitude	Distance between location and ocean (km)	Annual rainfall (mm)	Volume-weighted ^{210}Pb activity	^{210}Pb flux	^{222}Rn flux	References
						$(Bq\ L^{-1})$	$(Bq\ m^{-2}\ year^{-1})$	$(at\ cm^{-2}\ s^{-1})$	
Qingdao, China	2002	36.1° N	120.3° E	2	421	0.28	117	0.38	Yi et al. (2005)
	2004	36.1° N	120.3° E	2	376	0.49	186	0.60	
Stony Brook, NY	2008.4–2009.12	40.9° N	73.1° W	25	1277	0.11	146	0.47	Renfro et al. (2013)
Tatsunokuchi, Japan	1991.1–2002.12	36.44° N	136.8° E	14	2208	0.38	840	2.70	Yamamoto et al. (2006)
Tsukuba, Japan	2000–2001	36° N	140.1° E	40	1305	0.14	179	0.58	Hirose et al. (2004)
Nagasaki, Japan	2001	32.75° N	129.8° E	3	1471	0.16	234	0.75	Hirose et al. (2004)
Monaco	1998–2010	43.83° N	7.5° E	1	622	0.33	205	0.66	Pham et al. (2013)
Shanghai, China	2006–2011	31.2° N	123.4° E	50	1168	0.31	366	1.18	Du et al. (2015)

^{210}Pb activities in air include the seasons, atmospheric pressure variations that affect the sources of air masses as well as local radon emanation rates, height of the atmospheric boundary layer, temperature inversions, diurnal and seasonal variations of meteorological parameters, soil moisture content (which affect the emanation rates), and frequency and amount of precipitation, presence of snow cover, etc. The long-term temporal variations of ^{210}Pb activity in aerosols collected from Detroit over a period of 18 months (weekly to monthly sampling) varied over an order of magnitude, from 0.30 to 4.22 mBq m^{-3}, with a mean of 1.2 mBq m^{-3} (n = 30; McNeary and Baskaran 2003). Monthly ^{210}Pb activities measured over a period of 12 years in Belgrade (Central Serbia) varied between 0.30 and 3.17 mBq m^{-3}. A large number of values (average) fall within a range of 0.2–1.2 mBq m^{-3} (0.58 mBq m^{-3} in New Haven, Connecticut, Turekian et al. 1983; 0.45 mBq m^{-3} in Tsukuba, Japan, Sato et al. 1994; 0.74 mBq m^{-3} in Palermo, Italy, Cannizaro et al. 1999; 0.57 mBq m^{-3} in South Germany, Winkler and Rosner 2000; 0.62 mBq m^{-3} in Grenade, Southeastern Spain: 0.28–0.92 mBq m^{-3} (geometric mean: 0.52 mBq m^{-3}), Azahra et al. 2004; 1.15 mBq m^{-3} in Detroit, USA, McNeary and Baskaran 2003). In Lisbon, Portugal the ^{210}Pb activity varied between 0.036 and 0.524 mBq m^{-3}, with the lowest values corresponding to oceanic air masses (Carvalho 1995). High ^{210}Pb activities have been reported in Milan, Italy when prolonged anti-cyclonic conditions with high air temperature existed (Vecchi et al. 2005). A significant correlation between the maximum temperature and pressure and ^{210}Pb activity in air has been reported (Dueñas et al. 2005). ^{210}Pb activities at Svalbard varied between 0.011 and 0.62 mBq m^{-3} during 2001 and are lower than stations in the northern Finland. The ^{210}Pb activity in aerosols collected from the North Pacific was found to be ~ 2 times higher than that of the South Pacific, reflecting higher land/sea ratio in the Northern Hemisphere compared to the Southern Hemisphere.

Generally, the activities of ^{210}Pb in aerosols are high in winter due to low mixing height and low in the summer due to efficient mixing of the troposphere caused by solar heating. (e.g., Paatero et al. 1998). Based on 30-year (1967–1996) long-term of daily ^{210}Pb measurements in Finland, Paatero et al. (1998) reported that the daily variations are due to synoptic-scale weather situations while the seasonal variations are attributed to the efficiency of vertical mixing of the lower atmosphere. However, there are sites where higher ^{210}Pb in the summer months have also been reported (e.g., in Spain, Garcia-Talavera et al. 2001; Azahara et al. 2004; Dueñas et al. 2005, 2009). Overall, wintertime stability over continents inhibits the transfer of surface-source ^{210}Pb-laden aerosols to the free atmosphere and limits their transport distance while spring and summer convective mixing over continents results in an efficient exchange between the boundary layer and free troposphere, which enhances long-range transport of aerosols (Turekian and Graustein 2003).

The specific activities of ^{210}Pb (Bq per gram of aerosol mass) in aerosols are one to two orders of magnitude higher than that found in the top soils. For example, the specific activities of ^{210}Pb in aerosols collected in Detroit over 18-months period varied between 2.7–23.0 Bq g^{-1}, compared to ~ 0.08–0.17 Bq g^{-1} in the surficial soils (McNeary and Baskaran 2003). The efficiency of ^{210}Pb entrainment into the

atmospheric aerosols is very high and hence the specific activity of ^{210}Pb in aerosols is usually far greater than other elements commonly found, such as Al (Turekian et al. 1989). For example, ^{210}Pb/Al ratio in aerosols collected in the SEAREX program was found to be 10^4–10^5 times higher than that in the soils (Turekian et al. 1989). The activities of ^{210}Pb in size-fractionated aerosols collected using a 5-stage impact collector showed that 83 % of the total ^{210}Pb was associated with <0.95 μm (Baskaran, unpublished data). This is similar to the observation reported by Martell and Moore (1974) that 90 % of ^{210}Pb in aerosols is associated with particles ≤0.3 μm. The activities of ^{210}Po in surface air also vary widely, ranging from 0.01 to 0.26 mBq m^{-3} (Moore et al. 1973; Talbot and Andren 1983; McNeary and Baskaran 2007).

5.2.3   Importance of Long-Range Atmospheric Desert Dust to the Activities of ^{210}Po and ^{210}Pb

The single largest contributor to the global particulate burden of the troposphere, except sporadic release of massive volcanic eruptions, is the wind-blown dust (Andreae 1995). A major portion of these dusts are derived from dust storms in subtropical highs at latitudes 30°–35° where most of the deserts occur. The 'dust belt' includes deserts in North Africa, Central and South Asia, the Middle East and China. Saharan dusts have been documented to have been transported to the Caribbean and Florida; dust transported across the Pacific from Asia has been detected in the west coast of USA (Prospero 1999; Bollhöfer and Rosman 2001); and yellow dust storm from China was reported in S. Korea (Kim et al. 1998). Analysis of ^{210}Pb on dust collected at different places in the Mediterranean Sea (central, eastern and western) showed that the dust deposition accounted for 1.2–3.5 mg cm^{-2} y^{-1}, with ^{210}Pb activities ranging between 0.39–9.7 Bq/g (mean: 4.2 Bq/g). The highly varying (spatially and temporally) amounts of Saharan dust is estimated to contribute >50 % of the total ^{210}Pb flux in sites where the precipitation is low, with expected low ^{210}Pb fallout (Garcia-Orellana et al. 2006). At a site north of Barcelona in the western Mediterranean Sea, Garcia-Orellana et al. (2006) estimated the atmospheric fallout from pulse dust input to represent ∼16 % of the total atmospheric deposition of ^{210}Pb.

5.2.4   Vertical Profiles of ^{210}Pb Activity Above Cloud Cover

The activities of ^{210}Pb and ^{210}Po in two vertical profiles, one from Limon, Colorado and the other from Scottsbluff, Nebraska showed that the vertical activity profiles vary widely (Fig. 5.2). The activities of ^{210}Pb in the upper troposphere (i.e. above cloud cover) remain relatively constant within a factor of ∼2 (data from Moore et al. 1973). It has been shown that the stratospheric ^{210}Pb activity varies very little,

Fig. 5.2 Vertical profiles of ^{210}Po and ^{210}Pb in air from Limon, Colorado (April 2, 1969) and Scottsbluff, Nebraska (January 19, 1971). Data is taken from Moore et al. (1973)
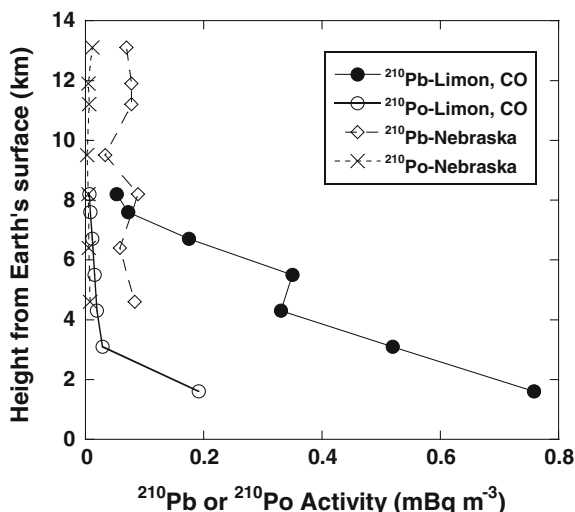
with a mean stratospheric activity of 0.3 mBq m^{-3} while its activity in the upper troposphere is much lower ($\sim$0.04 mBq m^{-3}; Lambert et al. 1982; Moore et al. 1973, 1977). This is similar to the observation for ^{222}Rn in the lower stratosphere and upper troposphere (Kritz et al. 1993). Due to infrequent precipitation in the upper troposphere (because cloud condensation heights are below the upper troposphere), the residence times of aerosols are longer in the free troposphere above the cloud cover than in the planetary boundary layer and hence the activities of ^{210}Pb are expected to be higher in the free troposphere above the cloud cover, in particular near the tropopause. The variations in the ^{210}Pb activities in the lower stratosphere could result from the rates of vertical transport processes (Feely and Seitz 1970). In particular, during major updrafts, ^{222}Rn could reach heights significantly above the cloud condensation height (upper troposphere and lower stratosphere) leading to higher production rates of ^{210}Pb. As discussed in Chap. 4, major volcanic eruptions and nuclear detonations can also force material of surface origins, including ^{222}Rn, through the tropopause.

5.2.5 Volume-Weighted Activities of ^{210}Pb and ^{210}Po

A compilation of the published data of the volume-weighted activities of ^{210}Pb (=annual ^{210}Pb activity deposited/ annual precipitation, Bq L^{-1}) given in Table 5.2, shows that the values vary within a factor of $\sim$10 (0.05–0.49 Bq L^{-1}), although world-wide distribution of ^{210}Pb in rain (including Polar Regions) vary over a factor of 20 (Rangarajan et al. 1976). The monthly volume-weighted activities of ^{210}Pb over a period of 97 months (December 2005–December 2013) varied from 0.05 to 3.40 Bq L^{-1} (mean: 0.55 Bq L^{-1}) in Shanghai, China (Du et al. 2015). Variations

in the activities of ^{210}Pb by a factor of >100 in individual rain events are common. However, from the data presented in Table 5.2, certain features emerge. The lowest value is found in the west coast of USA and some areas in the Mediterranean coast (Huelva, Spain) where the amount of precipitation is low and the depositional flux is predominantly controlled by high fluxes in 2–3 months in a given year (Fuller and Hammond 1983; Lozano et al. 2011). The maritime air mass from the Pacific brings ^{210}Pb-depleted air resulting in lower volume-weighted activities of [210]Pb. The island site Bermuda also has low value due to dominant maritime air mass. At different sites in the western Mediterranean Sea, the values vary over a factor of 2, again mainly due to varying inputs of continental and oceanic air masses. The values reported for Ahmedabad (India), a semi-arid region where the dry fallout is quite significant, is also low, 0.075 Bq L^{-1} (average). A plot of the volume-weighted activities of ^{210}Pb and amount of precipitation did not show any correlation, affirming the hypothesis that the relative fraction of continental air mass and oceanic air mass along with amount and frequency of precipitation determine the volume-weighted activities of [210]Pb.

The volume-weighted [210]Po activity in rain samples during the 18-months collected in Detroit was found to be 10.3 mBq L^{-1}, which are about two orders of magnitude lower than that of [210]Pb. The volume-weighted [210]Po/^{210}Pb ratio of 0.029 is lower than that in the precipitation reported in other places and this was attributed to many samples having below detection limits of [210]Po in precipitation, as the samples were processed after a time delay and the in-growth correction for [210]Po was high (McNeary and Baskaran 2007). There is very limited data in the literature to compare the volume-weighted activities of [210]Po. Yan et al. (2012) reported volume-weighted activity of [210]Po in precipitation from Seoul (12 months) to be 21.3 mBq L^{-1}, with a [210]Po/^{210}Pb activity ratio of 0.13.

5.2.6   Depositional Fluxes of [210]Po and [210]Pb

5.2.6.1   Variations in the Depositional Flux of [210]Pb

The three major types under which the scavenging of ^{210}Pb in the atmosphere takes place are: (i) scavenging in convective updrafts; (ii) scavenging by large-scale precipitation and (iii) dry deposition. Using a global three-dimensional simulation of ^{210}Pb on aerosol scavenging, the relative importance of convective precipitation and large-scale precipitation generated by two research groups differed considerably while the contribution of dry deposition was estimated to account for 13–14 % of the total depositional flux (Feichter et al. 1991; Balkanski et al. 1993). Monthly variations of the depositional fluxes vary by more than an order of magnitude. During washout, activities of ^{210}Pb tend to be relatively higher in the early stages of rainfall and in short duration rainfall than the latter stages and rainfall that persists for many days.

5.2.6.2   Different Methods of Obtaining Depositional Flux of ^{210}Pb

Long-term depositional fluxes of ^{210}Pb can be obtained from direct measurements (by deploying atmospheric collectors, usually for short-term, less than 2–3 years) or from natural repositories (long-term over its mean life, 33 years), such as lake sediments, snow fields, and soils. Note that the collection of direct ^{210}Pb atmospheric depositional flux samples require addition of acids to the container prior to collection to prevent loss of ^{210}Pb onto the walls of the atmospheric collector. In principle, one can also estimate the flux from the measured activity of ^{210}Pb in surface air and deposition velocity as:

^{210}Pb depositional flux (F) = ^{210}Pb activity in air (C_{air}, in Bq m^{-3}) x deposition velocity of aerosol (V_d, in m s^{-1}).

However, the ^{210}Pb in air could vary over an order of magnitude and the deposition velocity of aerosols also likely will vary with time and hence there will be large uncertainty on the depositional fluxes determined using this approach. Depositional fluxes obtained from undisturbed soil cores (^{210}Pb annual depositional flux = inventories of ^{210}Pb/mean life of ^{210}Pb, 32.2 year) could be affected by the vertical transport of ^{210}Pb via colloidal transport. Although a major portion of the atmospherically-delivered ^{210}Pb is retained in the upper ~ 30 cm of the soil, some of the humic substances could form a complex with Pb and could result in the downward migration, although this fraction is expected to be small (<10 %). Long-term depositional fluxes obtained from the sediment cores in aqueous systems (such as coastal ocean and lake systems) have the inherent uncertainty of sediment focusing or erosion as well as boundary scavenging that could result in varying sediment inventories of ^{210}Pb. Furthermore, in coastal areas, the submarine groundwater discharge could contribute high levels of ^{222}Rn and ^{226}Ra which could result in additional ^{210}Pb production (note that ^{222}Rn discharge will result in excess ^{210}Pb while ^{226}Ra will result in increased parent-supported ^{210}Pb).

5.2.6.3   Factors Affecting the Depositional Fluxes of ^{210}Pb

The reported depositional fluxes in a continental setting in a 10° belt almost vary by an order of magnitude. For example, the depositional flux of ^{210}Pb in Tatsunokuchi, Japan (36.44° N, 136.8° E) with ~ 84 mBq cm^{-2} y^{-1} is about 10 times higher than the value reported for the west coast of the United States, 3.3–5.0 mBq cm^{-2} y^{-1} (33.93° N, 118.4° W; Table 5.2, Fuller and Hammond 1983). This lower depositional flux in the west coast of the United States is attributed to two factors: (i) lower amounts of precipitation in those places where the data is reported (2.5 mBq cm^{-2} y^{-1} in San Francisco, CA with 49 cm y^{-1}, with very little rainfall during the summer and early fall months, and 3.5 mBq cm^{-2} y^{-1} in Los Angeles, CA with 36 cm y^{-1} annual rainfall, with very little (<5 % of the total) rainfall during summer months; Fuller and Hammond 1983); and (ii) predominantly ^{210}Pb-depleted oceanic air masses. This is in contrast to the prediction based on one-dimensional model in which vertical air column was assumed as if it is

well-mixed with a globally invariant removal rate constant (i.e., constant residence time of ^{210}Pb-laden aerosol) (Turekian et al. 1977). Although both areas are tectonically-active, ^{222}Rn emanation rates are likely elevated in both places, but the relative proportion of maritime and continental air masses along with the differences in the amount and frequency of precipitation are likely the key factors for the differences in the depositional fluxes. The second highest annual depositional fluxes of ^{210}Pb was reported from Shanghai, China, with a flux of 36.6 mBq cm^{-2} y^{-1} (Du et al. 2015) (Table 5.3).

Table 5.3   Current Global Budget (Contributions from plant exudates and forest fires are basically recycled components and included in the atmospheric dust; contributions from cement manufacturing, uranium ore mining and milling operations, lead smelting are considered negligible compared to the production from ^{222}Rn) for ^{210}Pb and ^{210}Po

Source	^{210}Pb flux (Bq y^{-1})	^{210}Po flux (Bq y^{-1})
Natural		
^{222}Rn emanation from Land[a]	3.50×10^{16}	1.05×10^{15}
^{222}Rn emanation from waters[a] (Oceans, rivers, lakes)	0.095×10^{16}	0.029×10^{15}
Resuspension of soils[b]	0.033×10^{16}	0.033×10^{16}
Sea salt spray[c]	3.7×10^{11}	7.4×10^{11}
Volcanic activity[d]	6.0×10^{13}	2.4×10^{15}
Artificial		
Nuclear detonations	0	0
Fossil fuel burning[e]	7.5×10^{12}	7.5×10^{12}
Tetraethyl lead combustion[f]	$<10^{11}$	$<10^{11}$
Dispersion of phosphate fertilizers[g] and gypsum byproducts	1.7×10^{13}	5.1×10^{11}
Measured Fluxes		
Northern Hemisphere	2.66×10^{16} Bq	
Southern Hemisphere	1.11×10^{16} Bq	
Total Flux	3.64×10^{16} y	3.82×10^{15} y

[a]^{210}Pb flux was calculated based on fluxes given in Table 5.1; assuming a residence time of 10 days, the ^{210}Po/^{210}Pb ratio = 0.03 was used in calculating the ^{210}Po activity
[b]The flux from resuspended dust was estimated for ^{210}Pb by Robbins (1978); ^{210}Po flux was calculated assuming ^{210}Po/^{210}Pb AR = 1.0
[c]^{210}Pb estimate is from Robbins (1978); ^{210}Po/^{210}Pb ratio of 2 in the microlayer was assumed (Bacon and Elzerman, 1980)
[d]Annual flux for ^{210}Pb and ^{210}Po was taken from Lambert et al. (1982)
[e]Burning of coal in 1970 was estimated to contribute 3.7×10^{12} Bq of ^{210}Pb (Jaworowski et al. 1972) assuming a 2 % annual increase in consumption, the estimated contribution is 7.5×10^{12} Bq in year 2015; it was assumed that ^{210}Po and ^{210}Pb are in equilibrium
[f]Robbins (1978) estimated this to be 1.1×10^{12} Bq; its use has decreased >90 % and hence it is estimated to contribute $<10^{11}$ Bq y^{-1}
[g]^{210}Pb flux from use of phosphate fertilizer was reported in Robbins (1978) and a 3 % annual increase in phosphate use was assumed; most of the ^{210}Pb flux is derived from higher ^{222}Rn release and the ^{210}Po/^{210}Pb ratio of 0.03 is used to estimate ^{210}Po flux

It has been shown that the atmospheric depositional flux is strongly correlated with the amounts of precipitation (Nevissi 1985; Baskaran et al. 1993; Kim et al. 1998; Caillet et al. 2001; Garcia-Orellana et al. 2006). However, there are other places where such correlation was not found (e.g., Texel and Groningen, Netherlands, Beks et al. 1998). Beks et al. (1998) reported that the variations in the annual depositional flux at two sites in Netherlands appear to be correlated to the number of heavy rains and thunderstorms. It was shown that 4 % of the total rainy days account for ∼25–30 % of the total annual depositional flux of ^{210}Pb (McNeary and Baskaran 2003). The higher depositional fluxes during thunderstorm may be related to the variations in the cloud condensation height for normal rainfall and thunderstorms as well as weather systems/type of air masses (continental vs. maritime) in which thunderstorms frequently occur. It was shown that precipitation-normalized depositional fluxes of ^{210}Pb are generally higher during spring and summer seasons, and this is likely due to frequency and amounts of rainfall (Baskaran 1995; Du et al. 2015).

## 5.2.7 Specific Activity and Depositional Flux of ^{210}Po

Excess ^{210}Po have been reported in the global atmospheric studies and the possible sources of ^{210}Po include resuspension of top soils, stratospheric aerosols, volcanic emission, bio-volatile ^{210}Po, release from ^{210}Po-enriched sea surface microlayer and escape of volatile ^{210}Po through gas exchange (Kim and Church 2011). The specific activity of atmospheric ^{210}Po vary widely, from 0.01 to 0.26 mBq m^{-3} (Moore et al. 1973; Talbot and Andren 1983; Baskaran and Shaw 2001; McNeary and Baskaran 2007). Kim and Church (2000) reported excess ^{210}Po on aerosols in the coastal atmosphere of the Chesapeake and Delaware Bays in the United States and hypothesized that the excess ^{210}Po originates mainly from surface waters either by the sea-spray of the surface microlayer or by gas exchange. Momoshima et al. (2001) observed biologically mediated emission of Po from culture solution suggesting the possibility of biotic source for atmospheric Po in the environment. McNeary and Baskaran (2007) observed that the correlation between ^{210}Po specific activity and precipitation was found to be weaker than that of ^{210}Pb and attributed this observation to the possible presence of volatile Po in the atmosphere which could escape from scavenging by the water droplets (McNeary and Baskaran 2007). Kim et al. (2005), from a suite of precipitation samples, reported high level of excess ^{210}Po in urban air of Seoul and they attributed to anthropogenic sources. From a comparison of the δ ^{34}S and ^{210}Po in aerosols, Kim et al. interpreted the source of ^{210}Po to be the urban air of anthropogenic origin. Tateda and Iwao (2008) reported the highest depositional fluxes of ^{210}Po along the coastal regions of Japan (13–58 Bq m^{-2} y^{-1}) ever reported in literature, in particular the highest value in

summer 1997 and the source(s) for this high value was not identified. Yan et al. (2012) reported an average value of 36 Bq m^{-2} y^{-1} for ^{210}Po and 0.02–0.78 (mean: 0.18) for ^{210}Po/^{210}Pb activity ratio in precipitation samples at Seoul, S. Korea. Compared to the depositional flux data for ^{210}Pb, the ^{210}Po depositional flux data are limited, and further studies are needed to address the importance of volatile Po in the atmospheric scavenging of Po.

5.2.8 ^{210}Po/^{210}Pb Activity Ratios in the Bulk Precipitation and Aerosols

The ^{210}Po/^{210}Pb ratios in precipitation samples also vary considerably: 0–0.15 (mean: 0.05, San Francisco, USA, Fuller and Hammond 1983), 0.11–0.42 (mean: 0.24, Hussain et al. 1998), and 0.005–0.284 (mean: 0.072 in Detroit, USA, McNeary and Baskaran 2007). The activity ratios of ^{210}Po/^{210}Pb in bulk precipitation were found to be slightly higher than that in the aerosols, indicating possible presence of ^{210}Po that are not completely scavenged by precipitation condensation (McNeary and Baskaran 2007). A plot of the ^{210}Po/^{210}Pb ratios in precipitation versus ^{210}Po/^{210}Pb ratios (data taken from McNeary and Baskaran 2007) in aerosols indicates considerable scatter in the plot (Fig. 5.3) and the activity ratios in aerosols vary in short time scales compared to the period of collection of the precipitation (2–5 weeks). If all the atmospheric ^{210}Po is completely derived from the decay of atmospheric ^{210}Pb, then, for a typical residence time of atmospheric water vapor of ∼10 days, we expect the ^{210}Po/^{210}Pb activity ratio to be ∼0.03.

Fig. 5.3 ^{210}Po/^{210}Pb ratios in precipitation versus aerosols. If there is uniform washout of the atmospheric aerosols, then, we expect the line to fall on a straight line given above. There is considerable scatter indicating that there is large scale heterogeneity in the samples. The aerosol collection is over 24 h while the precipitation samples integrate much longer (weeks to a month). Data is from McNeary and Baskaran (2007)
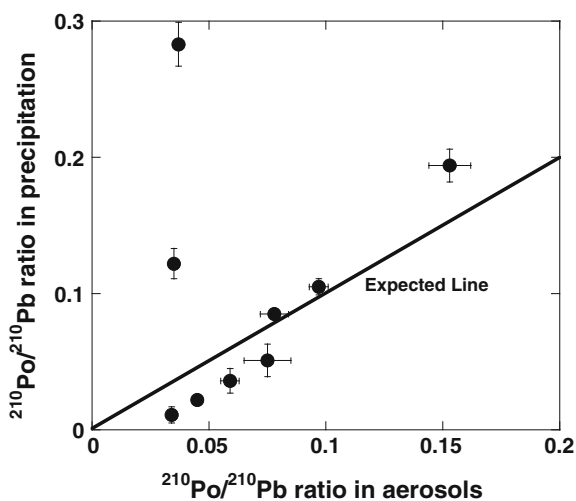
5.2.9 Dry Depositional Flux of ^{210}Po and ^{210}Pb

The fraction of dry depositional flux varies widely, depending on a number of factors including rural versus urban areas, proximity to the point of emission of aerosols near factories, amounts and frequency of precipitation, etc. Globally, the fraction of dry fallout is estimated to be ~ 10 % of the bulk fallout. However, in semi-arid regions and areas where the amount of precipitation is low (e.g., sub-tropical deserts that extend from $\sim 30°–35°$ latitude and in large continental regions of the middle latitudes; southern California, Arizona, etc.), the dry depositional flux could be more important than the wet fallout. In Ahmedabad, a high-dust semi-arid region in western India, the dry fallout of ^{210}Pb accounted for 24–44 % (mean: 35 %) over a period of 3 years (2000–2002, Rastogi and Sarin 2008). The activity ratio of ^{210}Po/^{210}Pb in most of the bulk precipitation and aerosol samples was found to vary between 0.01 and 0.20, but in dry precipitation samples, this ratio was found to be much higher (0.05–0.64, mean = 0.33) in Detroit, Michigan, USA (McNeary and Baskaran 2007). It is evident that the dry depositional samples and the amount of fallout are highly biased by resuspended dust resulting in higher ^{210}Po/^{210}Pb ratios in dry fallout.

5.3 Global Fallout Curve for ^{210}Pb

Depositional flux of ^{210}Pb at any given site primarily depends on the ^{222}Rn activity in the air and the scavenging efficiency of ^{210}Pb by rain. Global depositional flux of ^{210}Pb integrated over 10° latitude belt for the Northern and Southern Hemisphere are given in Table 5.1 (Fig. 5.4). Most of the data for this plot is taken from Preiss and Genthon (1997), and Du et al. (2015). Only data from continents, coastal oceans, ice cores/sheets and direct atmospheric depositional flux data are included in plotting this figure. Due to sediment focusing/erosion issues, the inventories from lakes and oceans (except coastal oceans where no other data available) are not included in the plot. The ^{210}Pb flux at high latitudes (>70° N and S) is less than 10 % of the fallout of the tropical and sub-tropical regions, and this is likely due to low radon emanation rates and low amounts of precipitation (Table 5.1). Overall, the depositional flux in the Southern Hemisphere is distinctly lower than that in the Northern Hemisphere, mainly due to larger landmass in the Northern Hemisphere. Although there are isolated areas where the ^{210}Pb depositional flux is higher than that reported in Table 5.1 (such as coastal areas of Japan), overall, the depositional flux is significantly lower than 20 mBq cm^{-2} y^{-1}. It has been shown that there are very little variations in the atmospheric depositional fluxes of ^{210}Pb (based on the activities of ^{210}Pb in lichens in Sweden and Finland) in the northern Europe (north

Fig. 5.4 Global atmospheric depositional fluxes of ^{210}Pb at different latitude belts (10° belt). This figure represents 191 different sites around the globe. Details of the sources of data are given in Table 5.1. Data is taken from the compiled data set by Preiss and Genthon (1997) and Du et al. (2015)
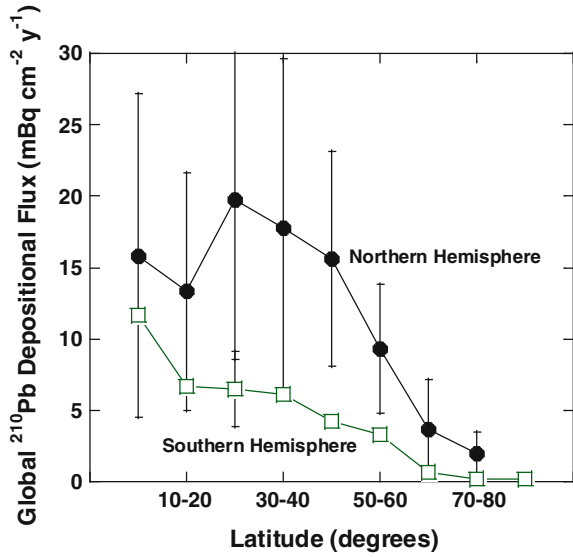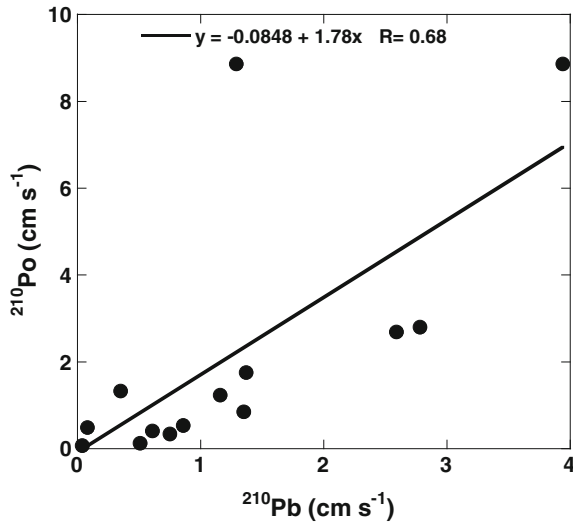

Fig. 5.5 Deposition velocity based on ^{210}Po versus ^{210}Pb in Detroit, Michigan, USA (data are taken from McNeary and Baskaran 2007)

of 60° N, Kauranen and Miettinen 1969). The ^{210}Pb flux in ice caps in Antarctica is about 20 times lower than that in Greenland and this is attributed to the differences in the release rates of ^{222}Rn in the surrounding areas (Turekian et al. 1977) (Fig. 5.5).

5.4   Applications of Radon Progeny to Aerosol Deposition Velocity and Residence Times

5.4.1   Depositional Velocities of Aerosols Using Daughter Products of ^{222}Rn

As was shown above, the deposition velocity (V_d) is utilized to transform concentration of a species (C_s) in air to its flux (F) to the Earth's surface. In principle, one can calculate V_d for any species based on the concentration in air and its flux. However, the advantage of using ^{210}Po or ^{210}Pb are the following: (i) The distribution of ^{210}Po and ^{210}Pb in aerosols are similar to other particle-reactive contaminants of interest (i.e. similar distribution coefficients) and therefore can be used to determine the fluxes of these contaminants to the Earth's surface; (ii) Both of these species are derived primarily from Earth's surface and thus the deposition velocity obtained for ^{210}Po and ^{210}Pb can be used for other earth-borne species such as Hg; and (iii) the activities of ^{210}Po and ^{210}Pb in aerosol and precipitation samples can be easily measured. The deposition velocity is calculated as follows:

$$V_d(cm/s) = F\left(mBq\,cm^{-2}s^{-1}\right)/C_s\left(mBq\,cm^{-3}\right)$$

A comparison of the deposition velocities obtained based on ^{210}Pb activities with that of ^{210}Po indicates that the ^{210}Po-based deposition velocity is 1.8 times higher than that of the ^{210}Pb-based values and the differences were attributed to presence of more volatile ^{210}Po which are not captured by the aerosol filters utilized to measure C_s (Fig. 5.4). Although a large range of V_d values have been reported, the average values agree within factor of ~3 (0.6–1.9 cm s^{-1}; summarized in Baskaran 2011). A linear best-fit line between total deposition velocities (either ^{210}Po or ^{210}Pb-based) and total particulate matter collected on to the filter does not show any significant correlation suggesting that the aerosol mass does not control the amount of ^{210}Pb scavenged by aerosols. Based on this observation, it was proposed that only a small portion of the atmospheric aerosols participate in the scavenging of atmospheric ^{210}Po or ^{210}Pb and a major portion of the aerosols do not actively participate in the removal of these nuclides from the atmosphere (McNeary and Baskaran 2007; Baskaran 2011). This experimental observation can be compared to results from a simple calculation: If we assume clear background air to contain aerosol mass number concentration of 10^3 particle cm^{-3} and the activity of ^{210}Po to be 1.2 mBq m^{-3} (average over 18 months in Detroit, MI), then, there are 1.2×10^6 atoms m^{-3} of ^{210}Po is present while the number of aerosol particles is ~10^9 particles m^{-3}. Thus, three orders of magnitude of higher particles are available than the number of ^{210}Pb ions (at the time of production, it is in ionic state) and hence only ~0.1 % or less of the aerosol particles will have ^{210}Po atom.

5.4.2   Washout Ratios Using Daughter Products of ^{222}Rn

The ratio of the average concentrations of ^{210}Pb (or ^{210}Po) in earth's surface level precipitation to its average activity in unwashed earth surface level air, known as washout ratio (W), is calculated as follows:

$$W = \rho C_{rain}/C_{air}$$

where ρ is the density of air at standard conditions (1.2 kg m^{-3} at 20 °C and 0.76 m Hg) and C_{rain} and C_{air} are the concentrations of radionuclide (^{210}Pb or ^{210}Po) in bulk deposition (in Bq kg^{-1}) and surface air (in Bq m^{-3}), respectively. The inherent assumption in this calculation is that the specific activity of ^{210}Pb or ^{210}Po of the air in the precipitation cloud is the same as that measured at the surface level in aerosol. A wide range of washout ratios for ^{210}Pb have been reported, varying between 30 and 2500, with a mean value of 780 (summarized in Baskaran 2011). However, there is only one set of data exist for the washout ratio based on ^{210}Po and it varied between 68 and 4522 (mean: 762) for Detroit, Michigan, USA, implying that the mean value is comparable to that of ^{210}Pb. If any volatile ^{210}Po species is present in the atmosphere, then, this ratio is expected to be lower. Future additional studies could shed more light on this.

5.4.3   Residence Times of Aerosols Based on the Daughter Products of ^{222}Rn

From a series of samples collected at various latitudes in the troposphere and stratosphere over central North America, Moore et al. (1973) discussed their implications for aerosol residence times. Samples collected from the lower strato-sphere yielded model ages from 40 days to 2 years, with the bulk of the samples between 100 and 180 days. In the lower stratosphere, the vertical mixing is sup-pressed and precipitation scavenging is virtually nil. These ages are generally consistent with the estimates of stratospheric residence times derived from the behavior of fission products injected into the stratosphere by atmospheric testing of nuclear weapons. From a synthesis of published data of Moore et al. (1973), Turekian and Graustein (2003) obtained residence times of aerosols of 20–30 days in the troposphere. A single aerosol sample always contains material from parcels of widely varying history and hence the residence time is basically an average of different aerosols types and origin. Also, if a fraction of aerosols with age of 1–2 days mix with another fraction of aerosols with age of 50 d, the age of the com-posite aerosol pool will fall in between these two ages. Martell and Moore (1974) and Moore et al. (1973) interpreted their data to yield a mean age of aerosols in the lower troposphere of less than 4 days, increasing by a factor of 3 toward the top of the troposphere. From the modeling of vertical profiles of ^{210}Pb, Balkanski et al. (1993) showed that the mean residence time of ^{210}Pb increased with latitude.

5.4.3.1 Intercomparison of the Residence Time Based on the Activity Ratios of ^{210}Po/^{210}Pb, ^{210}Bi/^{210}Pb and ^{222}Rn/^{210}Pb

The mean-lives of ^{222}Rn ($\tau = 5.51$d) and its daughter products (^{210}Pb: $\tau = 32.18$y; ^{210}Po: $\tau = 199.7$ d; ^{210}Bi: $\tau = 7.23$ d) are comparable to some of the time scales of atmospheric processes and hence the disequilibrium between the daughter-parent nuclides are useful to obtain the time scale of atmospheric processes. The disequilibrium between ^{222}Rn, ^{210}Pb, ^{210}Bi and ^{210}Po (i.e., ^{210}Pb/^{222}Ra, ^{210}Bi/^{210}Pb and ^{210}Po/^{210}Pb activity ratios) have been utilized to determine the residence time and removal rate constant of aerosols, with often discordant values resulting from these pairs.

The major removal mechanism of atmospheric ^{222}Rn daughter products is by wet scavenging and hence the intensity of scavenging is expected to vary with latitudes and longitudes, mainly depending on the amount and frequency of precipitation. In low latitudes (0–20° N/S) due to high amounts of precipitation, the scavenging of aerosols is rapid in the planetary boundary layer than above it and hence the residence time of aerosols are expected to be shorter. However, in the horse latitudes (30°-38° N/S; or subtropical highs), the dry fallout will relatively be high compared to the wet fallout. In a well-mixed, isolated atmospheric box where the rate of supply of ^{222}Rn is constant, the rate of change of decay product activities is given by:

$$dN_d/dt = \lambda_p N_p - \lambda_d N_d - \lambda_r N_d \qquad (5.1)$$

where N_p and N_d denote number of atoms of parent and daughter products, λ_p and λ_d are their respective decay constants, and λ_r is the first-order removal rate constant. The following assumptions are inherent in writing Eq. (5.1): (i) the short-lived daughters of ^{222}Rn (^{218}Po, ^{214}Pb and ^{214}Bi; Fig. 5.1) are in secular equilibrium with ^{222}Rn which implies that the time scales that we are tracing is much longer than 3 h and the system is in steady state during this time scale (during which these daughters reach secular equilibrium with ^{222}Rn); (ii) The source of ^{210}Pb, ^{210}Bi and ^{210}Po in the air are derived from the radioactive decay of ^{222}Rn in a parcel of air and that parcel of air does not mix with any other air masses that have different activities of ^{222}Rn and its progeny and there is no other sources for any of the daughter products (basically the system is assumed to be a 'closed system'); and (iii) the removal of the radionuclides follows a first-order kinetics. Rearranging this equation for ^{210}Pb/^{222}Rn and ^{210}Bi/^{210}Pb yields the following equations:

$$\tau_{r(Pb-Rn)} = (A_{Pb}/A_{Rn}) \times \tau_{Pb}/(1 - A_{Pb}/A_{Rn}) \qquad (5.2)$$

$$\tau_{r(Bi-Pb)} = A_{Bi} \times \tau_{Bi}/(A_{Pb} - A_{Bi}) \qquad (5.3)$$

where A_{Rn}, A_{Pb}, A_{Bi} and A_{Po} are activities of ^{222}Rn, ^{210}Pb, ^{210}Bi and ^{210}Po, respectively; $\tau_{r\,(Pb-Rn)}$, $\tau_{r\,(Bi-Pb)}$ $\tau_{r\,(Po-Pb)}$ are residence times based on ^{210}Pb/^{222}Rn, ^{210}Bi/^{210}Pb and ^{210}Po/^{210}Pb activity ratios, respectively; and τ_{Pb} and τ_{Pb} are mean

lives of ^{210}Pb and ^{210}Po, respectively. Because of the intermediate daughter (^{210}Bi) in the decay between ^{210}Pb and ^{210}Po, the temporal relationship between the activities of ^{210}Po and ^{210}Pb is given as follows (Moore et al. 1973):

$$\tau_{r(Po-Pb)} = \left[-b \, + \, \left(b^2 - 4ac\right)^{1/2}\right] 2a \qquad (5.4)$$

where $a = A_{Pb} - A_{Po}; b = -A_{Po}(\tau_{Bi} + \tau_{Po})$; and $c = -A_{Po}(\tau_{Bi}\tau_{Po})$

If ^{222}Rn and all its decay products are closed with respect to their inputs and outputs and the inputs and outputs are only governed by the radioactive decay and first-order removal (scavenging (or sorption), gravitational settling, removal by coagulation, etc.), then we anticipate the residence time obtained by both ^{210}Bi/^{210}Pb and ^{210}Po/^{210}Pb methods to be similar. But discrepancies obtained by these two methods are frequent, due to deviations from these ideal conditions (Figs. 5.6 and 5.7). Furthermore, possible additional sources contributing to the measured activities of the progeny are the reason why discordant residence times have been reported. Note that Lozano et al. (2010) pointed that the decay of in situ ^{210}Bi could contribute to ^{210}Po and in studies where only ^{210}Po and ^{210}Pb are measured and reported, the correction for this component of ^{210}Po should be applied.

5.4.3.2   Extraneous Sources of ^{210}Po and Advantages of ^{210}Bi/^{210}Pb Over ^{210}Po/^{210}Pb Pair in Obtaining Residence Time

In the calculation of the tropospheric residence times of aerosols, it is assumed that ^{210}Po, ^{210}Bi and ^{210}Po are derived from the decay of ^{222}Rn in the atmosphere and

Fig. 5.6 Comparison of residence time of aerosols obtained using ^{210}Po/^{210}Pb pair with that of ^{210}Bi/^{210}Pb pair (data taken from Poet et al. 1972)
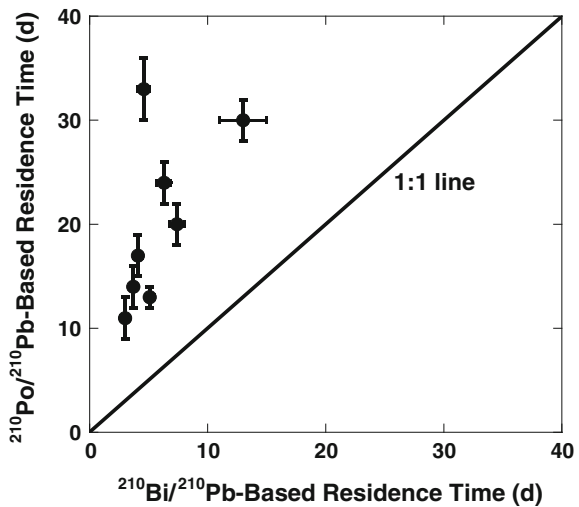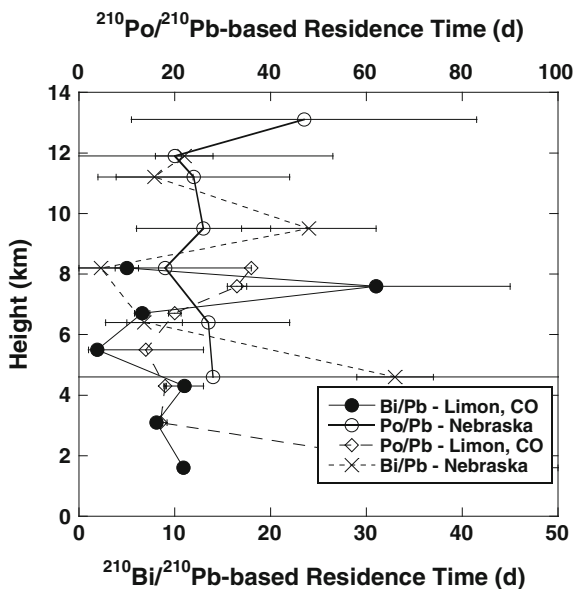
Fig. 5.7 Vertical profiles of residence times of aerosols in from Limon, Colorado (April 2, 1969) and Scottsbluff, Nebraska (January 19, 1971) based on ^{210}Bi/^{210}Pb and ^{210}Po/^{210}Pb pairs. Data is taken from Moore et al. (1973)

the contribution from all other sources are negligible. However, commonly other sources for atmospheric ^{210}Po have been recognized. The advantages of ^{210}Bi method over ^{210}Po method are: (i) the mean life of ^{210}Bi (7.2 d) is comparable to the mean residence time of aerosols and water vapor in the lower atmosphere and is less sensitive to extraneous sources than ^{210}Po (e.g., Papastefanou and Bondietti 1991); (ii) volatile nature of ^{210}Po compared to ^{210}Pb or ^{210}Bi could result in additional sources of ^{210}Po to the atmosphere which could alter the residence time based on ^{210}Po/^{210}Pb pair (such as large amounts of ^{210}Po are released to the atmosphere from major volcanic events; (Hussain et al. 1995; Le Cloarec et al. 1995; Nho et al. 1996, 1997; Kim et al. 2000; Su and Huh 2002). For example, about 60 of the Earth's 550 historically-active volcanoes are erupting each year (excluding those under ocean floor; Simkin et al. 1994). High enrichment of ^{210}Po in in volcanic gases with ^{210}Po/^{210}Pb activity ratios up to about 600 (57–614) in the Stromboli's plume have been reported (Gauthier et al. 2000). In the same plume, ^{210}Bi/^{210}Pb and ^{210}Po/^{210}Bi activity ratios have been reported to vary between 5 and 92 and 1.5 and 18.9, respectively. Weeks and in some cases months before the major volcanic eruption, the ^{210}Po activity in air were found to be extremely higher than the background levels (Nevissi 1984; Sheng and Kuroda 1985; Su and Huh 2002). For example, the depositional fluxes of ^{210}Po in Taiwan 2–3 days before Mayan volcanic eruption on the island of Luzon, Philippines, which is >1000 km away from Taiwan, reported to be 2–3 orders of magnitude higher than reported when there is no volcanic eruption-derived ^{210}Po present (Fig. 5.8; Su and Huh 2002); and (iii) in surface air sampling, finite amount of resuspended dust will have ^{210}Po/^{210}Pb activity ratio of $\sim$1.0 (as evidenced by higher ^{210}Po/^{210}Pb activity ratio dry fallout
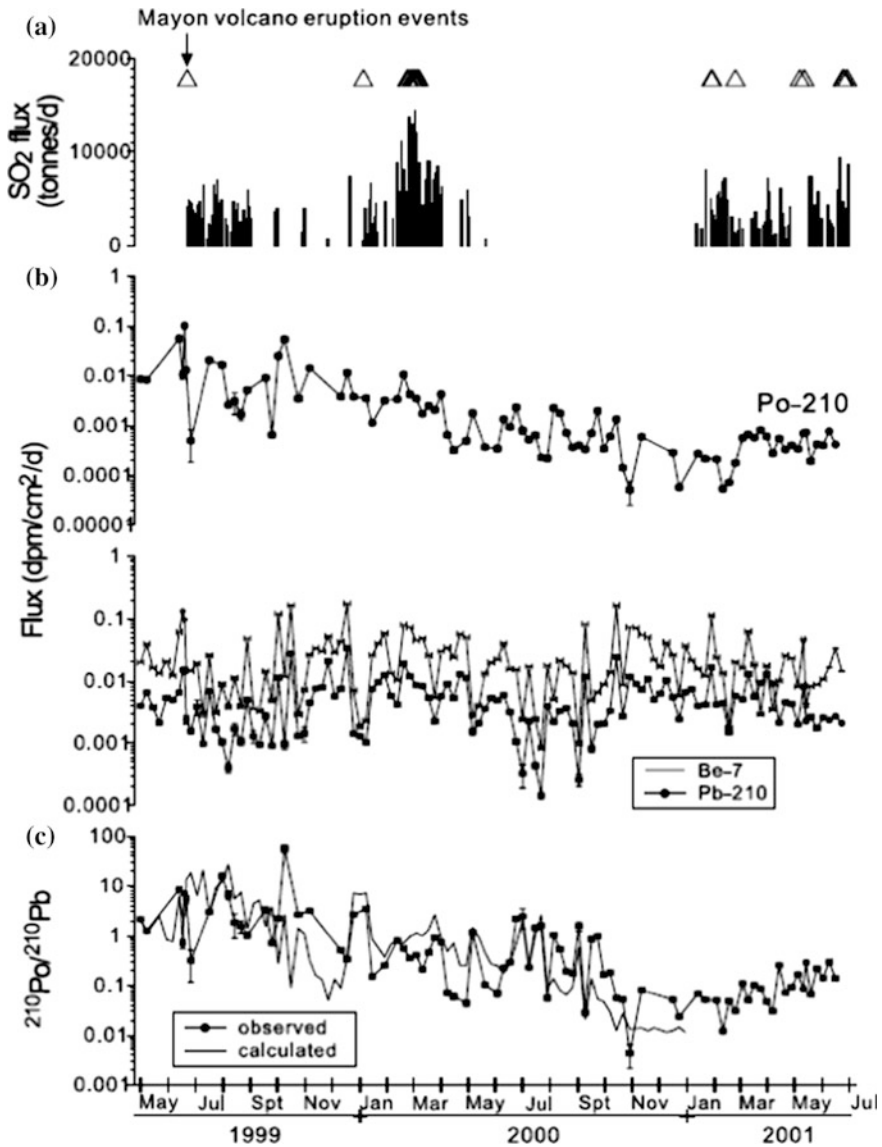
Fig. 5.8 The time series of **a** SO$_2$ flux; **b** ^{210}Po, ^{7}Be and ^{210}Pb fluxes and **c** ^{210}Po/^{210}Pb activity ratios. The sampling for radionuclides were conducted at Nankang (figure is adapted from Suh and Huh 2002)

samples) which will drastically affect ^{210}Po/^{210}Pb residence times. The only disadvantage with ^{210}Bi/^{210}Pb is the time-sensitive nature of this pair. It has been well-documented that the ^{210}Bi/^{210}Pb-based residence time is always lower than the

^{210}Po/^{210}Pb-based residence times (e.g., residence times obtained by both pairs are summarized in Papastefanou 2009).

One of the important sources of ^{210}Po and ^{210}Pb to the atmosphere is the fine dust likely contributing a significant portion to the rain. Finer particulate matter (<10 μm) that can be carried by wind to longer distances likely will have ^{210}Po/^{210}Pb and ^{210}Bi/^{210}Pb activity ratios of ~1.0. However, as the dust traverses through the atmosphere it could pick-up additional ^{210}Po and ^{210}Pb, with ratios ^{210}Po/^{210}Pb < 0.1. Thus, the wind-blown dust when collected at sites far away from the place of origin will likely have ^{210}Po/^{210}Pb AR < 1, but its value will likely depend on the trajectory distance of the air mass. Back trajectory analysis combined with the spatial sampling from the source region of the dust storm (such as from Sahara along its trajectory) to the site of interest (to quantify input from surface soils along the trajectory) for ^{210}Po, ^{210}Pb, and ^{210}Bi is expected to yield better insight on how the ^{210}Po/^{210}Pb ratios in aerosols vary with distance from the source. Such studies involving collection and analysis for ^{210}Pb-^{210}Bi-^{210}Po from source to sink is not yet attempted. As was discussed earlier, even a small amount of dust (5–10 %) could significantly affect the residence time obtained by ^{210}Po as opposed to ^{210}Bi pair. The importance of recycling dust can be assessed from the published data for ^{10}Be, another atmospherically-delivered radionuclide produced in the atmosphere by cosmic-ray spallation reaction (half-life = 1.4 ma). It has been shown that recycling of ^{10}Be from continents to the atmosphere has resulted in significant variations in the activities of ^{10}Be (atoms/g aerosol) and Heikkilä et al. (2008) estimated that recycled ^{10}Be from atmospheric dust could contribute up to 10–20 % of the bulk activity. In order to quantify the amount of dust contribution to the ^{210}Po and ^{210}Pb, it is important to measure index elements such as Al or Ti or ^{232}Th to quantify the terrigenous dust by direct measurements on aerosols. In principle, the Al/^{210}Po, Al/^{210}Bi and Al/^{210}Pb ratios in the dust can be used to make corrections for dust-derived ^{210}Po, ^{210}Bi and ^{210}Pb, although there is uncertainty on how much ^{210}Po, ^{210}Bi and ^{210}Pb in the dust are picked-up along its transit from the place of origin to the place of dust collection.

The effects of addition of equal amounts of ^{210}Bi and ^{210}Po from sources other than the radioactive decay of ^{210}Pb in the atmosphere can be evaluated as follows: If an air parcel with a finite initial amount of ^{210}Pb is 5 days old and all the ^{210}Bi and ^{210}Po in that air parcel are derived from the decay of this initial ^{210}Pb, then, the expected activity ratios of ^{210}Bi/^{210}Pb and ^{210}Po/^{210}Pb are 0.5 and 0.010, respectively. If there is a 10 % additional input of ^{210}Pb from the atmospheric dust, with ^{210}Bi and ^{210}Pb in secular equilibrium, then, the apparent residence times calculated using ^{210}Bi/^{210}Pb and ^{210}Po/^{210}Pb will yield 5.7 d and 29 d, respectively. Thus, a smaller contribution of ^{210}Po will affect the ^{210}Po/^{210}Pb-based residence time drastically. Note that the ^{210}Po/^{210}Pb ratio in wet and dry precipitation is generally <0.1 and thus the uppermost soil layer will likely have ^{210}Po/^{210}Pb activity ratio <1.0, but in about 2 years this ratio will be close to ~1, assuming that there is no escape of volatile ^{210}Po from this layer.

5.4.3.3   Residence Times Based on $^{210}Po/^{210}Pb$ and $^{210}Bi/^{210}Pb$ Ratios Size-Fractionated Aerosols

The residence times obtained on the bulk as well as size-fractionated aerosols are given in Fig. 5.9. The gross discrepancy between the ^{210}Po- and ^{210}Bi-based residence times in the bulk aerosol samples is evident. On the other hand, in the size-fractionated aerosol samples, there is a strong correlation between ^{210}Po- and ^{210}Bi-based residence times (data taken from Marley et al. 2000). Thus, it appears that the extraneous ^{210}Po is primarily confined to the larger-size aerosols which is likely due to larger dust particles. The sorption of ^{210}Po or ^{210}Pb (or any other particle-reactive species) depends on the surface area of the aerosols and hence the small-size aerosols more efficiently scavenge Po derived from the decay of atmospheric ^{210}Pb. Wallner et al. (2002) reported $^{210}Po/^{210}Pb$ ratios ranging between 0.6 and 2.5 in >1 μm-sized aerosols collected with impactor while in sizes with <2 μm, this ratio was lower. One another possibility is the input of aerosols from the lower stratosphere into the troposphere. The residence time of aerosols in the whole stratosphere is ∼1–2 years and hence the $^{210}Po/^{210}Pb$ AR in stratospheric aerosols is expected to be ∼1.0. However, the ^{210}Pb and ^{210}Po input of stratospheric air to the lower tropospheric air is likely negligible. From earlier studies during the time when nuclear-weapons-derived ^{90}Sr was present in the stratosphere, based on $^{90}Sr/^{210}Pb$ ratios in the aerosols, it was found that there was no stratospheric source for these nuclides (Moore et al. 1976). Turekian et al. (1989) reported that in about half of the aerosol samples collected at the New Zealand site and in the North Pacific westerlies showed no trend in $^{210}Po/^{210}Pb$ ratios with increasing size, but in the remaining samples, there was some increasing trend in >2 μm samples. Using modeling approach, it was estimated that the residence time of aerosols produced at

Fig. 5.9 Comparison of the residence times based on $^{210}Po/^{210}Pb$ and $^{210}Bi/^{210}Pb$ in bulk (Poet et al. 1972) and size-fractionated aerosol (Marley et al. 2000) samples from several sites in North America. Strong correlation in size-fractionated samples indicates that the additional sources of ^{210}Po are likely confined to the courser fractions
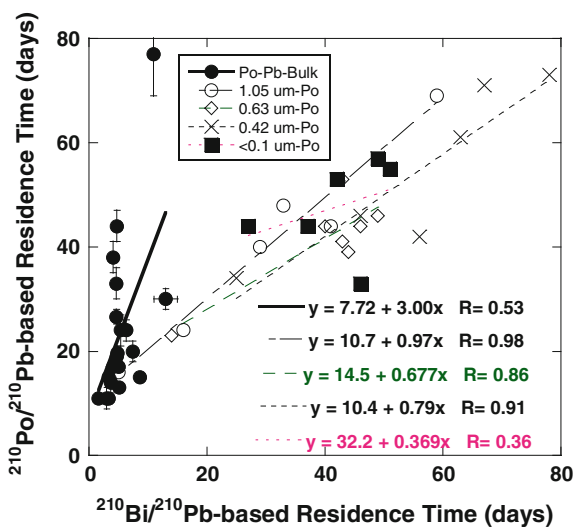
9-km altitude is about four times longer than that for aerosol produced in the lowest 500 m of atmosphere (Balkanski et al. 1993). From the vertical profiles of ^{222}Rn, ^{210}Pb, ^{210}Bi and ^{210}Po, Moore et al. (1973) observed that the mean residence time of aerosols increased with altitude in the troposphere within a factor 3 and the mean aerosol residence time in the lower stratosphere is about 1–2 years. The vertical profiles of the residence time obtained by both ^{210}Bi/^{210}Po and ^{210}Po/^{210}Pb pair is given. The discordancy between ^{210}Po/^{210}Pb and ^{210}Bi/^{210}Po residence time was attributed to the ^{210}Po derived from resuspended material (Poet et al. 1972; Moore et al. 1973). More systematic study is required to address the importance of volatile Po in the atmosphere and how it affects the determination of the residence time.

There are specific cases where the residence time of aerosols could be longer than the mean life of ^{210}Bi (e.g., arctic haze) where ^{210}Po will likely serve as a suitable tracer (Baskaran and Shaw 2001). For example, very low activities of ^{222}Rn (37 to 74 mBq m^{-3}) in air associated with the arctic haze, fog and clouds as well as low amounts of precipitation during winter months was attributed to isolation of this arctic haze from the continental source for 3–4 weeks (Wilkniss and Larson 1984). Temporal evolutions of ^{210}Po/^{210}Bi ratios from the time of formation of the haze to its disappearance need to be evaluated to determine if ^{210}Po is a better atmospheric tracer.

5.5 Global Atmospheric Inventory of ^{210}Po and ^{210}Pb

A number of factors that could potentially affect the atmospheric inventory of ^{210}Po and ^{210}Pb over the past 4-5 decades include: (i) virtually no ^{210}Pb derived from nuclear weapons test in the atmosphere; (ii) increased phosphate fertilizer and fossil fuel usage; (iii) elimination of leaded gasoline in most countries in the world resulting in the decrease in the release of ^{210}Pb (and ^{210}Po) to the atmosphere; (iv) better characterization of atmospheric ^{210}Pb production rates and removal rates; and (v) better characterization of other possible sources. Furthermore, we have a very large data set on the depositional fluxes of ^{210}Pb for the whole Earth (Preiss and Genthon 1997 + several direct atmospheric depositional flux studies; summarized in Du et al. 2015). Using the present day information on the possible sources and sinks of atmospheric ^{210}Po and ^{210}Pb, a revised mass balance is made.

Synthesis of global ^{210}Pb depositional flux from >190 sites on Earth's surface indicate that there are highly varying depositional fluxes at various latitudes and using one 'global average' value would not be accurate. Using the average value of the atmospheric depositional fluxes of ^{210}Pb (obtained from atmospheric collectors, coastal sediment cores, soil profiles in continents, ice cores; Table 5.1, Fig. 5.4) for each of the latitude belt, the global atmospheric depositional flux curve for ^{210}Pb is established (Fig. 5.4).

A finite amount of ^{210}Po in the atmosphere is produced from the decay of ^{210}Pb (via ^{210}Bi). One of the extraneous sources for ^{210}Po is the volcanic gases. Bennett et al. (1982) estimated the contribution of ^{210}Po to the atmosphere from the May

18th, 1980 eruption of Mt. St. Helens to be in the range of 1.0×10^{13} Bq to $\sim 17 \times 10^{13}$ Bq, which is significantly higher than that supplied from coal burning, phosphate fertilizer production and lead smelting. Lambert et al. (1982) estimated a global volcanic ^{210}Po output of 2.4×10^{15} Bq y^{-1} of ^{210}Po, with a median ^{210}Po/^{210}Pb activity ratio of 40, resulting in a ^{210}Pb contribution of 6.0×10^{13} Bq y^{-1}. The volcanic eruption is episodic and is not in steady-state, and hence it is difficult to estimate the annual flux.

Using the ^{222}Rn emanation rate of 0.75 atom cm^{-2} s^{-1} (Wilkening et al. 1975) from all the continental area (1.50×10^{18} cm^2), the corresponding ^{210}Pb flux is estimated to be 3.50×10^{16} Bq y^{-1} (1 atom ^{222}Rn cm^{-2} s^{-1} = 31.08 mBq ^{210}Pb cm^{-2} y^{-1}), under the assumption that the upward flux of ^{222}Rn equals the downward flux of ^{210}Pb (^{210}Pb flux = ^{222}Rn flux X mean-life of ^{222}Rn/mean-life of ^{210}Pb). However, 24 % of the land area is covered by glaciers and permafrost with negligible ^{222}Rn release. This 0.75 atom cm^{-2} s^{-1} for the whole land area corresponds to 1.00 atom cm^{-2} s^{-1} from the productive areas (1.12×10^{18} cm^2). ^{222}Rn emanation rate from surface waters (ocean, rivers and lakes) is 0.088 atom cm^{-2} s^{-1} (Wilkening and Clements 1975). This corresponds to ^{210}Pb flux of 0.095×10^{16} Bq y^{-1} (area = 3.50×10^{18} cm^2). One another importance source is the atmospheric dust. The atmospheric dust contribution varies both spatially and temporally, with episodic events contributing to most of the atmospheric dust. Moore et al. (1976) estimated as much as 60 % of the atmospheric ^{210}Po is derived from the atmospheric dust. Using the surface flux of ^{210}Po obtained by Moore et al. (1976), Robbins (1978) estimated the ^{210}Pb global flux (assuming ^{210}Po and ^{210}Pb are in equilibrium) from resuspended dust to be 0.033×10^{16} Bq y^{-1}. The ^{210}Po/^{210}Pb AR in the very top surface soils is less than 1, mainly due to low atmospheric deposition of ^{210}Po, with ^{210}Po/^{210}Pb values of <0.1–0.2. However, the ^{210}Po is anticipated to reach secular equilibrium in about 2 years. When fine dust from surface soils is resuspended with less certain ^{210}Po/^{210}Pb ratios, it is likely that as the dust moves through the atmosphere, it will scavenge additional ^{210}Pb, with ^{210}Po/^{210}Pb ratios <0.01–0.10. Thus, the assumption that ^{210}Po and ^{210}Pb are in equilibrium could underestimate the dust-derived flux estimate for ^{210}Pb.

Extensive use of phosphate fertilizers could contribute to the release of ^{222}Rn. Phosphate ores have much higher activities of ^{238}U (20 to 300 ppm corresponding to 0.25 to 3.75 Bq g^{-1}) and its daughter products, including ^{226}Ra. Resuspension and radon exhalation from the widespread dispersal of phosphate fertilizers in land areas around the globe along with the gypsum byproducts of fertilizer production has been estimated to contribute 3.7–7.4×10^{12} Bq y^{-1} (Moore et al. 1976; Robbins 1978). Assuming a global increase of 3 % in the consumption of phosphate fertilizers with similar ^{226}Ra activities, could result in an atmospheric flux of 11.5–23.0×10^{12} Bq y^{-1} (mean: 1.7×10^{13} Bq y^{-1}) in year 2015. Retention of atmospheric ^{210}Pb on to plant leaf surfaces could alter the distribution of ^{210}Pb in the atmosphere, although this source may not affect the global mass balance estimates. Forest fires are confined to selected regions and also are sporadic and it is unlikely to contribute any significant amounts to the global budget of ^{210}Pb or ^{210}Po. Use of leaded gasoline through the combustion of tetraethyl lead in the globe

has decreased drastically (>95 % since 1970s; lead usually into the atmosphere as a volatile compound and subsequently formed an aerosol by photolytic processes) and hence its contribution to the atmospheric ^{210}Pb or ^{210}Po budget is likely negligible. Evidences of ^{210}Pb derived from weapons testing, possibly derived from the ^{208}Pb (2n, γ) reaction with the lead structural materials in the nuclear devices, are discussed in Robbins (1978). Since the cessation of nuclear weapons testing, this component is also negligible. Even in historical records, this component would have decreased to ∼20 % of the total delivered from weapons testing. ^{210}Pb and ^{210}Po derived from fossil fuel consumption is another significant source. It was estimated that ∼3.7×10^{12} Bq y^{-1} of ^{210}Pb is derived from the burning of coal which has high activity of ^{210}Pb compared to other fossil fuel (Jaworowski et al. 1972). In several countries usage of peat in power plants as fuel could be a significant source of natural radionuclides. The amount of ^{210}Po and ^{210}Pb derived from these sources are expected to be significantly lower than that of the fossil fuels. The average increase in the use of coal is 2.0 % (from 4129 million short tons in 1980 to 7075 million short tons in 2007; http://www.eia.doe.gov/aer/txt/ptb1115. html, downloaded on 15 May 2010). This corresponds to 7.5×10^{12} Bq y^{-1} of ^{210}Pb in year 2015, assuming that the amount of ^{210}Pb/^{210}Po released to the atmosphere per unit mass of coal has remained constant during the past 40 years.

It has been shown that the ocean microlayers are highly enriched in ^{210}Po (Bacon and Elzerman 1980; Heyraud and Cherry 1983). It is widely known that dimethyl sulfide is formed in the ocean waters and released to the atmosphere. As a metalloid in the sulfur-selenium-tellurium group XVI, Po can form a volatile dimethyl polonide and could be released to the atmosphere (summarized in Church and Sarin 2008). Turekian et al. (1989) used ^{210}Pb as a tracer of SO_4^{2-} in precipitation. They used SO_4^{2-}/^{210}Pb ratios in aerosols and showed that the SO_4^{2-}/^{210}Pb ratio in aerosols from regions of high biological productivity was higher than normal relatively unpolluted air indicating a sulfate source from the oxidation of dimethyl sulfide.

5.6 Summary and Future Direction

The daughter products of ^{222}Rn, in particular, ^{210}Po and ^{210}Pb, can be more effectively used as atmospheric tracers in the future, provided we improve our understanding of their sources and pathways. Recent results of the residence time of aerosols calculated using ^{210}Po/^{210}Pb and ^{210}Bi/^{210}Pb in the finer fraction of the size-fractionated aerosols seem to yield consistent values and more studies are needed to validate this observation. Presence of atmospheric Po in the volatile form and its effect on the first-order scavenging by aerosols needs to be assessed. Release of ^{210}Po to the atmosphere from ocean surface layers in the form of methyl polonide and other volatile forms of Po needs to be quantified. It has been hypothesized that only a small fraction of the aerosol particles in the atmosphere actively participate

in the removal of Po, Pb and other particle-reactive species. Chemical characterization of the aerosol particles and their role in the removal of Po and Pb will aid to test this hypothesis. Now that some of the sources of ^{210}Po and ^{210}Pb to the atmosphere are eliminated or diminished (such as nuclear weapons, leaded gasoline), we can quantify other sources and pathways of ^{210}Po (such as plant exudates, fertilizers, forest fires, volcanic activity, etc.) better.

Ongoing major environmental changes have resulted in accelerated soil erosion in highly populated areas around the world. Climate change has resulted in changes in the surface air temperature and frequency and amounts of precipitation. All these factors will impact the release rates of radon from Earth surface and the production rates of its progeny in the atmosphere.

Some linkages between oscillations of surface ^{210}Pb activities in the air in Southern Finland and state of the northeastern part of the Atlantic Ocean have been observed, with the warmer surface water in the North Atlantic resulting in low ^{210}Pb activities. Higher amounts of warm and saline-water in the North Sea have been linked to enhanced cyclonic activity and low ^{210}Pb air activity. More studies linking surface water temperature of the source area to the continental ^{210}Pb activities will provide insight on the long-term environmental changes and coupling between the oceans and continents. The time scale involved in the transport of source to sink of dust plume and arctic haze are of great interest and such studies require measurements of ^{210}Po, ^{210}Bi and ^{210}Pb in size-fractionated aerosols and future studies hopefully will provide answers to some of these questions.

References

Andrea MO (1995) Climatic effects of changing atmospheric levels. In: Henderson-Sellers A (ed) Future climates of the world: a modeling perspective, world survey of climatology, vol 16. Elsevier, Amsterdam, pp 341–392

Azahra M, Lopez-Penalver JJ, Camacho-Garcia MA et al (2004) Atmospheric concentrations of Be-7 and Pb-210 in Granada, Spain. J Radioanal Nucl Chem 261(2):401–405

Bacon MP, Elzerman AW (1980) Enrichment of ^{210}Pb and ^{210}Po in the sea-surface microlayer. Nature 284:332–334

Balkanski YJ, Jacon DJ, Gardner GM, Graustein WC, Turekian KK (1993) Transport and residence times of tropospheric aerosols inferred from a global three-dimensional simulation of ^{210}Pb. J Geophys Res 98:20573–20586

Baskaran M (1995) A search for the seasonal variability on the depositional fluxes of ^{7}Be and ^{210}Pb. J Geophys Res 100:2833–2840

Baskaran M (2011) ^{210}Po and ^{210}Pb as atmospheric tracers and global atmospheric ^{210}Pb Fallout: a review. J Environ Radioact 102:500–513

Baskaran M, Naidu AS (1995) ^{210}Pb-derived chronology and the fluxes of ^{210}Pb and ^{137}Cs isotopes into continental shelf sediments, East Chukchi Sea, Alaskan Arctic. Geochim Cosmochim Acta 59:4435–4448

Baskaran M, Shaw GE (2001) Residence time of Arctic haze aerosols using the activities and activity ratios of ^{210}Po, ^{210}Pb and ^{7}Be. J Aerosol Sci 32:443–452

Baskaran M, Coleman CH, Santschi PH (1993) Atmospheric depositional fluxes of ^{7}Be and ^{210}Pb at Galveston and College Station, Texas. J Geophys Res 98:20555–20571

Beks JP, Eisma D, van der Plicht J (1998) A record of atmospheric ^{210}Pb deposition in The Netherlands. Sci Total Environ 222:35–44

Bennett JT, Krishnaswami S, Turekian KK et al (1982) The uranium and thorium decay series nuclides in Mt. St. Helens effusives. Earth Planet Sci Lett 60:61–69

Bollhöfer A, Rosman KJR (2001) Isotopic source signatures for atmospheric lead: The Northern Hemisphere. Geochim Cosmochim Acta 65:1727–1740

Burton WM, Stewart NG (1960) Use of long-lived natural radioactivity as an atmospheric tracer. Nature 186:584–589

Caillet S, Arpagaus P, Monna F, Dominik J (2001) Factors controlling ^{7}Be and ^{210}Pb atmospheric deposition as revealed by sampling individual rain events in the region of Geneva, Switzerland. J Environ Radioact 53:241–256

Carvalho FP (1995) Origins and concentrations of ^{222}Rn, ^{210}Pb, ^{210}Bi and ^{210}Po in the surface air at Lisbon, Portugal, at the Atlantic edge of the European continental landmass. Atmos Environ 29:1809–1919

Church TM, Sarin MM (2008) U- and The-series nuclides in the atmosphere: supply, exchange, scavenging and applications to aquatic processes. In: Radioactivity in the environment, vol. 13. Elsevier, Amsterdam, pp 11–45

Conan F, Robertson LB (2002) Latitudinal distribution of radon-222 flux from continents. Tellus 54B:127–133

Cannizaro F, Greco G, Ranelli M, Spitale MC, Tomarchio E (1999) Determination of ^{210}Pb concentration in the air ground-level by gamma spectrometry. Appl Radiat Isot 51:239–245

Du J, Du J, Baskaran M, Bi Q, Huang D, Jiang Y (2015) Temporal variations of atmospheric depositional fluxes of ^{7}Be and ^{210}Pb over 8 years (2006–2013) at Shanghai, China and Synthesis of global fallout data. J Geophys Res 120. doi:10.1002/2014JD022807

Dueñas C, Fernandez MC, Carretero J, Liger E, Cañete S (2005) Deposition velocities and washout ratios on a coastal site (southeastern Spain) calculated from ^{7}Be and ^{210}Pb measurements. Atmos Environ 39:6897–6908

Dueñas C, Fernandez MC, Canete S, Perez M (2009) ^{7}Be and ^{210}Pb concentration ratio in ground level air in Malaga (36.7° N, 4.5° W). Atmos Res 92:49–57

Feely HW, Seitz H (1970) Use of lead-210 as a tracer of transport processes in the stratosphere. J Geophys Res 75:2885–2894

Feichter J, Brost RA, Heimann M (1991) Three-dimensional modeling of the concentration and deposition of ^{210}Pb aerosols. J Geophys Res 96:22447–22460

Fuller C, Hammond DE (1983) The fallout rate of Pb-210 on the western coast of the United States. Geophys Res Lett 12:1164–1167

Garcia-Orellana J, Sanchez-Cabeza JA, Masqué P, Àvila A, Costa E, Loÿe-Pilot MD, Bruach-Menchén JM (2006) Atmospheric fluxes of ^{210}Pb to the western Mediterranean Sea and the Saharan dust influence. J Geophys Res 111:D15305. doi:10.1029/2005JD006660

Garcia-Talavera M, Quintana B, Garcia-Diez E, Fernandez F (2001) Studies on the radioactivity in aerosols as function of meteorological variables in Salamanca (Spain). Atmos Environ 35:221–229

Gauthier P-J, Le Cloarec M-F, Condomines M (2000) Degassing processes at Stromboli volcano inferred from short-lived disequilibria (^{210}Pb-^{210}Bi-^{210}Po) in volcanic gases. J Volcanool Geoth Res 102:1–19

Heikkilä U, Beer J, Alfimov V (2008) Beryllium-10 and beryllium-7 in precipitation in Dubendorf (440 m) and at Jungfraujoch (3580 m), Switzerland (1998–2005). J Geophys Res 113 (D11104):2008. doi:10.1029/2007JD0091960

Heyraud M, Cherry RD (1983) Correlation of ^{210}Po and ^{210}Pb enrichments in the sea-surface microlayer with neuston biomass. Cont Shelf Res 1:283–293

Hirose K, Honda T, Yagishita S, Igarashi Y, Aoyama M (2004) Deposition of behaviors of ^{210}Pb, ^{7}Be and thorium isotopes observed in Tsukuba and Nagasaki, Japan. Atmos Environ 38:6601–6608

Hussain N, Ferdelman TG, Church TM, Luther G III (1995) Bio-volatilization of polonium: Results from laboratory analyses. Aquatic Geochem 1:175–188

Hussain N, Church TM, Veron AJ, Larson RE (1998) Radon-daughter disequilibria and lead systematic in the western North Atlantic. J Geophys Res 103:16059–16071

Jaworowski Z, Bilkiewicz J, Kownacka L, Wlodek S (1972) Artificial sources of natural radionuclides in environment. In: Adams JAS, Lowder WM, Gesell RF (eds) The natural radiation environment II, vol. 2, Proceedings 2nd international conference on the natural radiation environment, Houston, Texas, 1972. CONF-720805-P2, pp 809–818

Jia C, Liu G, Yang W, Zhang L, Huang Y (2003) Atmospheric depositional fluxes of ^{7}Be and ^{210}Pb at Ziamen (in Chinese with English abstract). J Xiamen Univ Nat Sci 42(3):352–357

Kauranen P, Miettinen JK (1969) ^{210}Po and ^{210}Pb in the arctic food chain and the natural radiation exposure of Lapps. Health Phys 16:287–295

Kim SH, Hong G-H, Baskaran M, Park KM, Chung CS, Kim KH (1998) Wet removal of atmospheric ^{7}Be and ^{210}Pb at the Korean Yellow Sea coast. Yellow Sea 4:58–68

Kim G, Church TM (2011) Po-210 in the Environment: Biogeochemical cycling and bioavailability. In: Handbook of Environmental Isotope Geochemistry (Ed. M Baskaran), Advances in Isotope Geochemistry series, pp 271–284

Kim G, Hussain N, Church TM (2000) Excess ^{210}Po in the coastal atmosphere. Tellus B 52:74–80

Kim G, Hong Y-L, Jang J, Lee I, Hwang D-W, Yang H-S (2005) Evidence for anthropogenic ^{210}Po in the urban atmosphere of Seoul, Korea. Environ Sci Technol 39:1519–1522

Knuth RH, Knutson EO, Feely HW, Volchock HL (1983) Size distribution of atmospheric Pb and Pb-210 in rural New Jersey: implications for wet and dry deposition. In: Pruppacher HR, Semonin RG, Slinn WGN (eds) Precipitation scavenging, dry deposition, and resuspension. Elsevier, Amsterdam and Oxford, pp 1325–1334

Kritz MA, Rosner SW, Kelly KK, Loewenstein M, Chan KR (1993) Radon measurements in the lower tropical stratosphere: evidence for rapid vertical transport and dehydration of tropospheric air. J Geophys Res 98:8725–8736

Lambert G, Ardouin B, Polian G (1982) Volcanic output of long-lived radon daughters. J Geophys Res 87:11103–11108

Le Cloarec MF, Neveu S, Nho E-Y (1995) ^{210}Po in savanna burning plumes. J Atmos Chem 22:111–122

Lozano RL San Miguel EG, Bolivar JP (2011) Assessment of the influence of in situ Bi-210 in the calculation of in situ Po-210 in air aerosols: Implications on residence time calculations using Po-210/Pb-210 activity ratios. J Geophys Res 116:D08206. doi: 10.1029/2010JD014915

Lozano RL, San Miguel EG, Bolivar JP, Baskaran M (2011) Depositional fluxes and concentrations of ^{7}Be and ^{210}Pb in bulk precipitation and aerosols at the interface of Atlantic and Mediterranean coasts in Spain. J Geophys Res 116:D18213

Marley NA, Gaffney JS, Drayton PJ (2000) Measurement of ^{210}Pb, ^{210}Po, and ^{210}Bi in size-fractionated atmospheric aerosols: an estimate of fine-aerosol residence times. Aerosol Sci Technol 32:569–583

Martell EA, Moore HE (1974) Tropospheric aerosol residence times: a critical review. J Rech Atmosph 8:903–910

Mattsson R (1988) ^{210}Pb and ^{222}Rn as guides in adjudicating SO_4^{2-} and SO_2 air concentrations sulphate in the air in Finland 1962 … 1985. Sci Total Environ 69:211–224

McNeary D, Baskaran M (2003) Depositional characteristics of ^{7}Be and ^{210}Pb in southeastern Michigan. J Geophys Res 108:4210. doi:10.1029/2002JD003021

McNeary D, Baskaran M (2007) Residence times and temporal variations of ^{210}Po in aerosols and precipitation from southeastern Michigan, United States. J Geophys Res 112:D04028. doi:10.1029/2006JD007639

Momoshima N, Song LX, Osaki S, Maeda Y (2001) Formation and emission of volatile polonium compound by microbial activity and polonium methylation with methylcobalamin. Environ Sci Technol 35(14):2956–2960

Moore HE, Poet SE, Martell EA (1973) ^{222}Rn, ^{210}Pb, ^{210}Bi, and ^{210}Po profiles and aerosol residence times versus altitude. J Geophys Res 78:7065–7075

Moore HE, Martell EA, Poet SE (1976) Sources of polonium-210 in atmosphere. Environ Sci Technol 10:586–591

Moore HE, Poet SE, Martell EA (1977) Vertical profiles of ^{222}Rn and its long-lived daughters over the eastern Pacific. Environ Sci Technol 11:1207–1210

Nho E-Y, Ramonet M, Ardouin B, Le Cloarec MF (1996) Origins of ^{210}Po in the atmosphere at Lamto, Ivory Coast: Biomass burning and Saharan dusts. Atmos Environ 30:3705–3714

Nho E-Y, Ardouin B, Ramonet M (1997) ^{210}Po, an atmospheric tracer of long-range transport of volcanic plumes. Tellus B 49:429–438

Nevissi A (1984) Pb-210 and Po-210 in Mount St. Helen's ash. J Geophys Res 89:6326–6328

Nevissi A (1985) Measurement of ^{210}Pb atmospheric flux in the Pacific Northwest. Health Phys 48:169–175

Olsen CR, Larsen IL, Lowry PD, Cutshall NH, Todd JF, Wong GTF, Casey WH (1985) Atmospheric fluxes and marsh-soil inventories of ^{7}Be and ^{210}Pb. J Geophys Res 90 (D6):10,487–10,495

Paatero J, Hatakka J, Mattsson R, Viisanen Y (1998) Analysis of daily ^{210}Pb air concentrations in Finland. Radiat Prot Dosimetry 77:191–198

Papastefanou C (2009) Radon decay product aerosols in ambient air. Aerosol Air Qual Res 9:385–393

Papastefanou C, Bondietti EA (1991) Mean residence times of atmospheric aerosols in the boundary layer as determined from ^{210}Bi/^{210}Po activity ratios. J Aerosol Sci 22:927–931

Pham MK, Povinex PP, Nies H, Betti M (2013) Dry and wet deposition of ^{7}Be, ^{210}Pb and ^{137}Cs in Monaco air during 1998-2010: Seasonal variation of depositional fluxes. J Environ Radioact 120:45–57

Poet SE, Moore HE, Martell EA (1972) Lead 210, bismuth 210 and polonium 210 in the atmosphere: Accurate ratio measurement and application to aerosol residence time determination. J Geophys Res 77:6515–6527

Prospero JM (1999) Long-range transport of mineral dust in the global atmosphere: impact of African dust on the environment of the southeastern United States. Proc Natl Acad Sci 96:3396–3403

Preiss N, Genthon C (1997) Use of a new database of lead 210 for global aerosol model validation. J Geophys Res 102:25347–25357

Rangarajan C, Gopalakrishnan S, Eapen DC (1976) Global variation of ^{210}Pb in surface air and precipitation. In: Hardy EP (ed) Health and safety laboratory environmental quarterly, Sept. 1–Dec. 1 1975, U.S. E.R.D.A., New York, HASL-298, pp 163–182

Rastogi N, Sarin MM (2008) Atmospheric ^{210}Pb and ^{7}Be in ambient aerosols over low and high latitude sites in semi-arid region: Temporal variability and transport processes. J Geophys Res 113:D11103. doi:10.1029/2007JD009298

Renfro AA, Cochran JK, Colle BA (2013) Atmospheric fluxes of Be-7 and Pb-210 on monthly time-scales and during rainfall at Stony Brook, New York (USA). J Environ Radioact 116:114–123

Robbins JA (1978) Geochemical and geophysical applications of radioactive lead. In: Triage JO (ed) The biogeochemistry of lead in the environment, pp 285–393

Saari H-K, Schmidt S, Castaing P, Blanc G, Sautour B, Masson O, Chochran JK (2010) The particulate ^{7}Be/^{210}Pbxs and ^{234}Th/^{210}Pbxs activity ratios as tracers for tidal-to-seasonal particle dynamics in the Gironde estuary (France): implications for the budget of particle-association contaminants. Sci Total Environ 408(20):4784–4794

Sato J, Doi T, Segawa T, Sugawara SI (1994) Seasonal variation of atmospheric concentrations of ^{210}Pb and ^{7}Be at Tsukuba, Japan, with a possible observation of ^{210}Pb originating from the 1991 eruption of Pinatubo volcano, Philippines. Geochem J 28:123–129

Schuler C et al (1991) A multitracer study of radionuclides in Lake Zurich, Switzerland. 1. Comparison of atmospheric and sedimentary fluxes of [7]Be, [10]Be, ^{210}Pb, [210]Po and [137]Cs. J Geophys Res 96(C9):17,051–17,065

Simkin T, Unger JD, Tilling RI, Vogt PR, Spall H (1994) This dynamic planet. http://cmase.uark.edu/teacher/workshops/GEMS-lessons. Accessed 5 May 2010

Sheng Z, Kuroda PK (1985) Atmospheric injections of Po-210 from the recent volcanic eruptions. Geochem J 19:1–10

Su CC, Huh CA (2002) Atmospheric [210]Po anomaly as a precursor of volcanic eruptions. Geophys Res Lett 29(5):1070. doi:10.1029/2001GL013856

Su CC, Huh CA, Lin FJ (2003) Factors controlling atmospheric fluxes of [7]Be and ^{210}Pb in northern Taiwan. Geophys Res Lett 30(19), 2018. doi:10.1029/2003GL018221

Szegvary T, Conen F, Ciais P (2009) European [222]Rn inventory for applied atmospheric studies. Atmos Envion 43:1536–1539

Talbot RW, Andren AW (1983) Relationships between Pb and ^{210}Pb in aerosol and precipitation at a semiremote site in northern Wisconsin. J Geophys Res 88:6752–6760

Tateda Y, Iwao K (2008) High Po-210 atmospheric deposition flux in the subtropical coastal area of Japan. J Environ Radioact 99(1):98–108

Trumbore SE, Keller M, Bosky SC, Costa Ad (1990) Measurements of soil and canopy exchange rates in the Amazon rain forest using [222]Rn. J Geophys Res 95:16865–16873

Turekian KK, Graustein WC (2003) Natural radionuclides in the atmosphere. In: Treatise in geochemistry, 4.10, pp 261–279

Turekian KK, Nozaki Y, Benninger LK (1977) Geochemistry of atmospheric radon and radon products. Annu Rev Earth Planet Sci 5:227–255

Turekian KK, Benninger LK, Dion EP (1983) [7]Be and ^{210}Pb total deposition fluxes at New Haven, Connecticut and Bermuda. J Geophys Res 88:5411–5415

Turekian KK, Graustein WC, Cochran JK (1989) Lead-210 in the SEAREX Program: an aerosol tracer across the Pacific. In: Duce RA (ed) Chemical oceanography, vol 10. Academic Press, pp 51–80

Vecchi R, Marcazzan G, Valli G (2005) Seasonal variation of ^{210}Pb activity concentration in outdoor air of Milan (Italy). J Environ Radioact 82:251–266

Vogler S, Jung M, Mangini A (1996) Scavenging of [234]Th and [7]Be in Lake Constance. Limnol Oceanogr 41(7):1384–1393

Wallner G, Berner A, Irlweck K (2002) Aerosols: unexpected disequilibrium phenomena between airborne radio activities of lead-210 and its progenies bismuth-210 and polonium-210. Naturwissenschaften 89:569–574

Wilkening MH, Clements WE (1975) Radon-222 from the ocean surface. J Geophys Res 80:3828–3830

Wilkening MH, Clements WE, Stanley D (1975) Radon-222 flux measurements in widely separated regions. In: Adams JAS (ed) The natural radiation environment II, vol 2, pp 717–730, USERDA CONF-720805, 959 pp

Wilkniss PE, Larson RE (1984) Atmospheric radon measurements in the Arctic: Fronts, seasonal observations, and transport of continental air to polar regions. J Atmos Sci 41:2347–2358

Winkler R, Rosner G (2000) Seasonal and long-term variation of ^{210}Pb concentration in air, atmospheric deposition rate and total deposition velocity in south Germany. Sci Total Environ 263:57–68

Yamamoto M, Sakaguchi A, Sasaki K, Hirose K, Igarashi Y, Kim CK (2006) Seasonal and spatial variation of atmospheric ^{210}Pb and [7]Be deposition: Features of the Japan Sea side of Japan. J Environ Radioact 86(1):110–131

Yan G, Cho HM, Lee I, Kim G (2012) Significant emissions of Po-210 by local burning into the urban atmosphere of Seoul, Korea. Atmos Environ 54:80–85. doi:10.106/j.atmosenv.2012.02.090

Yi Y, Bai J, Liu G, Yang W, Yi Q, Huang Y, Chen H (2005) Measurements of the atmospheric depositional fluxes of [7]Be, ^{210}Pb, and [210]Po (in Chinese with English abstract). Mar Sci 29 (12):20–24

Chapter 6
Radon: A Geochemical and Geophysical Tracer in Marine System

6.1 Introduction

Radon concentration gradients at key interfaces such as sediment-water and air-water in aqueous systems (oceans, rivers and lakes) have been widely utilized to determine exchange rates of gases across these interfaces. Such exchange rates are required for understanding a variety of environmental problems, such as reaeration rates of rivers and estuaries, nutrient dynamics in coastal systems, and the role of the oceans in controlling the atmospheric concentrations of potentially harmful gases such as CO_2, N_2O, and SO_2 (Hartman and Hammond 1984). Although ^{222}Rn and other noble gases (argon, neon, helium, krypton and xenon) do not have any impact on the biological processes in marine system, other major constituent gases such O_2, CO_2, and N_2O are produced and consumed in large amounts by bio-geochemical processes. The exchange of O_2 at air-sea interface is vital for the continued sustenance of life at the surface oceans and lakes. Deforestation and fossil fuel burning has resulted in continuous increase of atmospheric CO_2 since the first direct measurements of CO_2 in air in 1958. Anthropogenically released CO_2 and NO_2 (mainly as a byproduct of the oxidation of organic nitrogen) are the key gases that play an important role in controlling the surface temperature of the Earth by trapping long-wave radiation emitted from the surface (Greenhouse effect). The factors and processes that control the air-sea flux of these gases are important as these studies have direct bearing on the long-term climate variations.

The observed disequilibrium between ^{222}Rn and ^{226}Ra in aqueous systems serves as one of the most powerful tools among all the parent-daughter disequilibria in the ^{238}U-^{235}U-^{232}Th-series. It is utilized at the air-sea (quantification of rates of air-sea exchange) and sediment-water (chemical exchange) interfaces. The differing solubility and the ability of radon to partition into a gas phase and contrasting geochemical properties compared to its progenitor, enables it to serve as a tracer. In this chapter, the key applications of the disequilibrium between ^{222}Rn and ^{226}Ra in aqueous system is reviewed and presented.

6.2 Solubility of Radon in Seawater

The solubility of radon, along with all other noble gases, is given in Table 6.1. The solubility of noble gases increases from lower atomic mass to higher atomic mass (He to Rn; Table 6.1). The solubility expressed as volume partition coefficients are also given in Table 6.1. The partitioning of radon between air and water (volume partitioning coefficients) can also be understood from a simple experiment: we place one liter of seawater in contact with 1 L of air, and some radon is injected into this system, and allowed to equilibrate between the water and gas phases at 24 °C. For every 10 atoms of radon that go into the water, 54 atoms of radon would reside in the air (assuming air-water partitioning coefficient at 24 °C to be 5.4). In other words, ~ 16 % of the total radon will be found in the solution phase and ~ 84 % will be found in the air space (note that for He, for every atom that goes into water, 135 atoms will be found in the air, as the volume distribution coefficient of helium is 135 at 24 °C or only 0.7 % will be found in the solution phase and 99.3 % will be found in the air space). Radon, similar to other noble gases, is more soluble in water as the temperature is decreased (406 cm^3/L at 0 °C compared to 186 cm^3/L at 24 °C, 54 % decrease). Such a percent decrease is much higher for lighter noble gases (only 5 % decrease for helium). The equilibrium concentrations of radon in surface ocean water can be calculated by multiplying the partial pressure of radon in dry air (atm) and the solubility of radon (cm^3 L^{-1} or moles kg^{-1}).

Oceanographers have argued that all the deep ocean water was once at the surface, with the abundant gases in surface water nearly in equilibrium with their corresponding atmospheric gases. Some gases are produced or consumed by reactions in the ocean, largely catalyzed by biological reactions, causing disequilibria. The extent of the disequilibrium is defined by the relative rates of reaction and physical exchange of the gas across the air-water interface. As an inert radioactive gas, the reactions governing the radon behavior are only production from its parent and radioactive decay, allowing a mass balance to be easily

Table 6.1 Solubilities (S) of various gases in seawater per atmospheric pressure (compiled data taken from Broecker and Peng 1982)

Gas	Molecular Weight g/mole	S at 0 °C (cm^3/L)	S at 24 °C (cm^3/L)	[a]S at 0 °C (10^{-3} mol kg^{-1})	[a]S at 24 °C (10^{-3} mol kg^{-1})	S at 0 °C/S at 24 °C	Air partition coeff. (air/water) at 0 °C
He	4	7.8	7.4	0.34	0.32	1.1	135
Ne	20	10.1	8.6	0.44	0.37	1.2	116
N$_2$	28	18.3	11.8	0.80	0.51	1.6	85
O$_2$	32	38.7	23.7	1.69	1.03	1.6	42
Ar	40	42.1	26.0	1.83	1.13	1.6	39
Kr	84	85.6	46.2	3.8	2.1	1.8	22
Xe	131	192	99	8.4	4.3	1.9	10
Rn	222	406	186	17.8	8.1	2.2	5.4

[a]Average density of sea water is assumed to be 1025 kg m^{-3}

developed and utilized for the determination of the air-sea exchange rate. The difference in the partial pressure of radon in surface seawater and the atmosphere above is useful for its utility as a tracer of gas exchange rates at air-sea interface (Sect. 3.7).
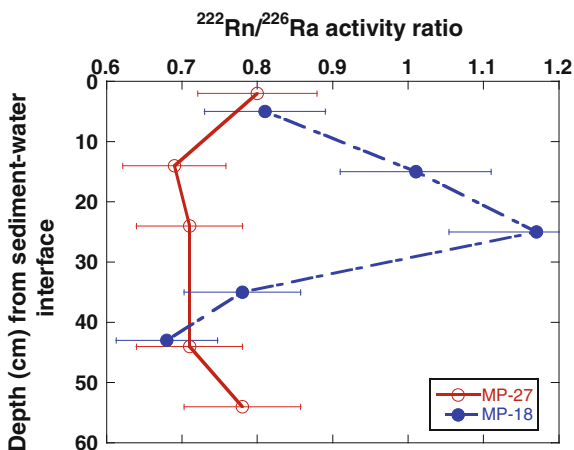
6.3 ^{222}Rn as a Tracer in Rivers and Estuaries

Radon concentrations in surface water and subsurface ground water differ widely. This difference reflects two factors. The first factor is that high concentrations of the radium parent are associated with solids. As ^{226}Ra undergoes alpha decay inside a mineral grain, a fraction of the daughter ^{222}Rn produced is recoiled into the surrounding media (radon emanation). Due to the high host matrix surface area/fluid volume ratio in groundwater, they acquire high concentrations of radon. Some of this radon may be transferred from groundwater and pore fluids before it decays. The second factor leading to low surface water ^{222}Rn concentrations is that some of this radon in surface water may escape to the atmosphere before it can decay. The kinetics of radon production from solids and from dissolved radium can be precisely determined, offering the potential to deduce exchange rates across interfaces by constructing a budget for radon.

Radon concentrations in rivers vary both spatially and temporally, depending upon the volume of discharge, flow rate, amount of base flow, and exchange rates across both the sediment-water and air-water interfaces, etc. Excess ^{222}Rn concentration (excess ^{222}Rn (Bq m^{-3}) = measured ^{222}Rn (Bq m^{-3}) – ^{226}Ra (Bq m^{-3})) was found to decrease downstream in the fresh water section of the Pee Dee River in South Carolina, USA and the primary source of excess ^{222}Rn was attributed to the groundwater discharge (Elsinger and Moore 1983). While ^{226}Ra concentration in Pee Dee River was found to vary between 0.5 and 1.0 Bq m^{-3}, ^{222}Rn concentration varied between 33 and 233 Bq m^{-3}, with the highest and lowest ^{222}Rn concentrations in March and June–July, respectively. Excess ^{222}Rn concentrations at all times suggest there is a significant groundwater component in the Pee Dee River (Elsinger and Moore 1983). However, groundwater inputs are not the sole source of all excess radon. Inputs from the molecular diffusion from pore waters, irrigation of pore waters through physical processes that induce flow through pore waters or organisms that irrigate their burrows are also important mechanisms governing input. An example where benthic exchange, rather than groundwater flow, dominated the input is found in San Francisco Bay where benthic flux chambers and pore water disequilibria indicated similar inputs to the overlying waters, with irrigation by fauna playing a major role in exchange (Hartman and Hammond 1984).

Concentrations of ^{222}Rn in small streams entering the Hudson River estuary have been reported to have 5–10 times higher compared to that of the estuary (Hammond et al. 1977), and this was attributed to the shallowness and contribution of ^{222}Rn

from groundwater flow. Note that the ^{222}Rn/^{226}Ra ratios in pore water profiles from two sediment cores in Hudson River indicate diffusion of ^{222}Rn to the water column in one profile while in the other, ^{222}Rn/^{226}Ra activity ratio ~ 1 for two depths (Fig. 6.1). Concentrations of radon measured in the Hudson River estuary in the summer season (mean: 23–25 mBq/L, with standard deviations 18–25 %, number of samples, n = 106) had slightly higher values than those in winter (mean: 18–24 mBq/L, with standard deviations 12–40 %, n = 17), although they are not statistically very different. Using a simple mass balance approach of ^{222}Rn in the Hudson River estuary, with input terms of: (i) diffusion of ^{222}Rn from bottom sediments; (ii) production in the water column, (iii) stream inflow and (iv) groundwater discharge and sink terms of: (i) decay and (ii) evasion to the atmosphere, Hammond et al. (1977) estimated a mean residence time (τ) of radon in the estuary to be ~ 3 days. With an effective horizontal diffusivity (K) of ~ 700 m^2 s^{-1}, the spatial distance (L) that a ^{222}Rn atom can move can be estimated as follows:

$$L \sim \sqrt{(K\tau)} \sim 15 \, \text{km}$$

Thus, the radon is expected to be uniformly mixed in this estuary (Hammond et al. 1977). However, it is important to note that the submarine groundwater discharge (SGD) is likely highly variable within an estuary, both spatially and temporally, and its effect could result in concentration gradients across the estuary. For the Hudson River estuary, the sink terms from the water column was estimated to be 40–65 % of the total radon by radioactive decay and 35–60 % of the total radon is lost by evasion to the atmosphere and the relative percentages of these two depended on mean depth of the water column. Input terms from ^{226}Ra decay in the water column, stream runoff, and groundwater are relatively small compared to inputs from sediments. Note that the source terms from production in the water column and stream inflow can be quantified easily, while quantification of groundwater discharge requires more systematic, spatial and temporal sampling (Cable et al. 1996;

Burnett et al. 2006). The source term diffusion from bottom sediments depends on a number of factors that include effective diffusivity in sediments which in turn depends on the porosity. From a mass balance, the rate of change of the concentration of ^{222}Rn can be written (Broecker 1965; Hammond et al. 1977) as:

$$dC/dt = \lambda C_{eq} - \lambda C + (d/dx)\left[D_s(dC/dx)\right] \qquad (6.1)$$

where C: concentration of ^{222}Rn per wet sediment volume at x; C_{eq}: concentration of ^{222}Rn supported by emanation at depth 'x'; λ: decay constant of ^{222}Rn; D_s: effective diffusivity of ^{222}Rn in sediments; and 'x' depth in sediment.

If we assume the porosity, C_{eq} and D_s are independent of depth, then, Eq. (6.1) can be solved for ^{222}Rn flux across the sediment-water interface per unit area (J_0):

$$J_0 = \sqrt{(D_s\lambda)}\left(C_{eq} - C_0\right) \qquad (6.2)$$

where C_o is the concentration at x = 0 (i.e., at the sediment-water interface). The diffusion fluxes could change with changes in the biological (including bio-irrigation) and/or physical mixing of sediments. In sediments, the molecular diffusivity, D_m, is related to the effective diffusivity of radon in sediments, D_s, as: $D_s = (D_m/\theta^2)$, where θ is the effect of tortuosity on diffusive path length. Hammond et al. (1977) estimated θ to be 1.2 for sediments in Hudson River having a porosity of 60–80 %. Radon flux calculated from Eq. (6.2) accounted for only 40 % of the total input required. They proposed additional input derived from stirring of the surface layer of the sediments, is mainly due to currents.

6.4   Activities of ^{222}Rn in Coastal, Continental Margins and in Surface Mixed Layers in the Open Ocean

The concentrations of ^{222}Rn in the coastal waters vary widely, mainly from the variable fractions of riverine discharge, benthic exchange and submarine groundwater discharge. The range of concentrations reported in literature for coastal waters are given in Table 6.2.

The activities of ^{222}Rn in surface waters in the open ocean also vary widely. Extensive measurements of ^{222}Rn in the surface mixed layers (depth at which the gradient in water temperature and salinity change from the small values characterizing the mixed layer to the much larger values characterizing the upper thermocline) from 90 stations (covering from 72.0° N to 66.1° S), collected during the GEOSECs global ocean expeditions indicate that the activities varied between 0.65 and 2.1 Bq m^{-3} (Table 6.2; Peng et al. 1979). In all of the stations, the activities of ^{222}Rn are less than that of ^{226}Ra in the mixed layer of the surface ocean, indicating loss of ^{222}Rn from the mixed layer to the atmosphere. A plot of ^{222}Rn in the mixed layer versus ^{226}Ra yield a slope value of 0.77 ± 0.03, indicating that on an average 23 % of the ^{222}Rn escapes from the mixed layer to the atmosphere (Fig. 6.2). The

Table 6.2 [222]Rn Concentrations riverine, coastal, shelf-slope and mixed-layer waters in the open ocean

Location	Range and median (Bq m^{-3})	N	References	[226]Ra conc (Bq m^{-3})
Hudson River estuary	23.8 ± 4.2	106 (summer)	Hammond et al. (1977)	–
	21.7 ± 5.8	17 (winter)		
Pee Dee River	33–233	–	Elsinger and Moore (1983)	0.05–0.10
Bering sea shelf waters	0.7–8.3	–	Glover and Reeburgh (1987)	1.3–2.0
Global ocean mixed layer	0.65–2.1	90	Peng et al. (1979b)	–

Fig. 6.2 Activity of [222]Rn is plotted against [222]Ra in mixed layer samples collected during GEOSECS. The standard errors associated with the measurements is ±7 % (Peng et al. 1979). The slope value, [222]Rn/[226]Ra = 0.77 ± 0.03 indicates that an average of 23 % of the [222]Rn undergoes escape to the atmosphere
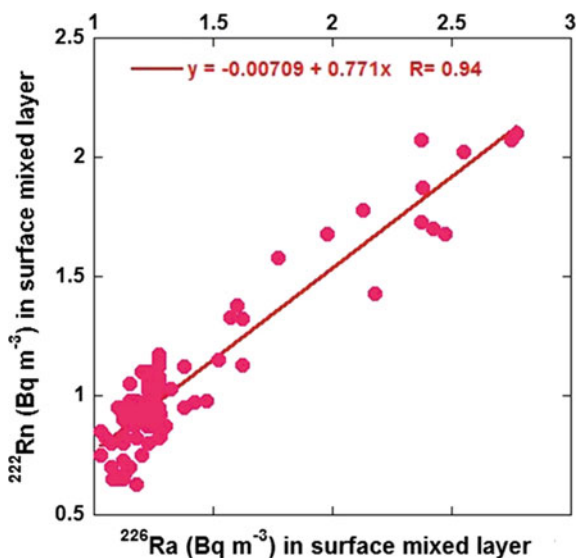
surface water [226]Ra concentrations in the Atlantic, Indian and Pacific Oceans are relatively constant (Fig. 6.3), but significantly higher concentrations were found south of the Antarctic Convergence compared to the north of the convergence and this was attributed to much higher upwelling of the deeper water with a higher radium concentration. The large differences in the activity of [222]Rn in deeper waters of the Pacific and Atlantic Oceans will likely exist due to large concentration differences of [226]Ra their water column (Fig. 6.3). For example, the [226]Ra activities in the deep waters of the Equatorial and Northwest Pacific Ocean is about 2–3 times higher than that of the Northwest Atlantic (Fig. 6.3). The concentrations of [226]Ra in

Fig. 6.3 Vertical profiles of ^{226}Ra in Northwest Atlantic, Eastern Equatorial Pacific, Northwest Pacific and Indian Ocean (47° 38′ S; 128° 04′ E, data from Ku et al. 1970). The deep water concentrations in the Pacific is ∼3 times higher than that of the Atlantic
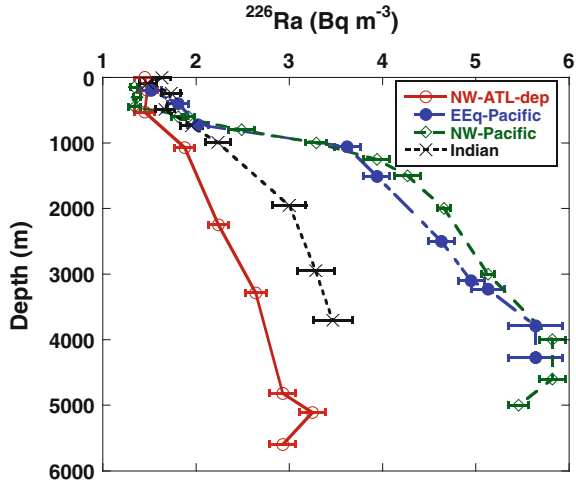
Fig. 6.4 The most recent ^{226}Ra vertical profile from North Atlantic (Nov. 2011, Aug. 35.4° N; 66.7° W; Charette et al. 2015) is compared to the data obtained in the North Atlantic test station 41 years ago (Aug. 1970; 35.8° N; 68° W; Trier et al. 1972) and 20 years ago at Transient Tracers in the Ocean (TTO) station 6 (April 1981; 34.7° N; 67.4° W; Key et al. 1992)
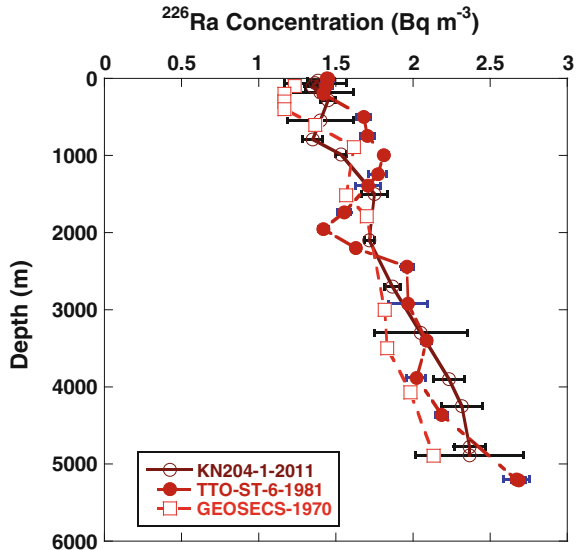
the deeper waters follow this trend: NW Atlantic < Indian < SW Pacific < NE Pacific (Fig. 6.3, Chung 1974a, b). The variations in the surface water ^{226}Ra concentration is attributed to the amount of Si present that limits further depletion of radium in the surface waters (Ku et al. 1970). However, ^{226}Ra data collected at three different times over a span of ∼40 years in almost the same site in the Atlantic Ocean (KN-204 in 2011; TTO cruise in 1981 and GEOSECS cruise 1970) yielded the same ^{226}Ra activity within ∼± 10 % (Fig. 6.4; Charette et al. 2015) and thus, it is quite likely that the radon inventory for a given specific site remain constant over longer periods of time.

6.5 Vertical Profiles of ^{222}Rn concentration in the Oceanic Water Column

The distribution of ^{222}Rn in the oceanic water column provides important information on key processes taking place at oceanic boundaries. Those include: (i) gas exchange rates across the air-sea interface and (ii) vertical mixing rates of water near the surface and near the bottom of the ocean. The utility of radon as a tracer for exchange of gases across air-sea interface was first proposed by Broecker (1965) and subsequently ^{222}Rn deficiencies relative to ^{226}Ra in the surface mixed layer was confirmed by Broecker et al. (1967) in the northwest Pacific. The existing concentration gradients of ^{222}Rn at these interfaces make these applications possible (Table 6.3).

There are three contrasting concentration regimes between ^{222}Rn and ^{226}Ra in the oceanic water column: (i) disequilibrium between ^{222}Rn and ^{226}Ra in the upper 50–100 m, with ^{222}Rn/^{226}Ra activity ratio of <1.0 (Fig. 6.5). Radon in the upper ocean has been lost to the atmosphere, although it has not reached equilibrium with the air above. As discussed in Sect. 6.2, at equilibrium (at 24 °C) between air and water, only ∼16 % of the total radon (=radon in air + radon in water) is expected to be in water. However, the ^{222}Rn activity in the mixed layer is reported to vary between 0.65 and 2.1 Bq m^{-3}, while in air above the deep ocean surface it is ∼0.07 Bq m^{-3} of air at STP; (ii) below the euphotic zone into the thermocline all the way to ∼50–200 m above the sediment-water interface, ^{222}Rn is in equilibrium with ^{226}Ra, with ^{222}Rn/^{226}Ra activity ratio of ∼1.0. When a parcel of water is isolated from the atmosphere and from sediments in about a month, ^{222}Rn will be in secular equilibrium with its parent, ^{226}Ra; and (iii) in the bottom 200 m from the sediment-water interface, there is significant excess ^{222}Rn, with ^{222}Rn/^{226}Ra activity ratio of ≫1.0, and this excess ^{222}Rn can be used as a tracer to determine the vertical mixing rates in the deep-sea.

Table 6.3 Inventory of excess ^{222}Rn from the GEOSECS water column data and sedimentation rates (modified from Sarmiento and Broecker 1980)

Location	Sedimentation rate (mm/kyr)	Number of stations	Geometric mean —Σ^{222}Rn (Bq m^{-2})	95 % confidence limits of mean (Bq m^{-2})
Atlantic Ocean	>100	7	80	50–128
	30–100	19	267	217–350
	10–30	16	283	200–400
Pacific Ocean	10–30	9	350	233–517
	3–10 (W. Pacific)	21	567	400–800
	1–3 (E. Pacific)	8	1500	117–3330
	<1	15	267	2170–3330

The geometric of the ^{222}Rn standing crops were normalized to a depth of 4000 m

Fig. 6.5 Plot of the average salinity normalized radon content for various depths below the surface. The departure between the equilibrium curve and the measured ^{222}Rn curve represent the radon lost to the atmosphere (data taken from Broecker and Peng 1971)
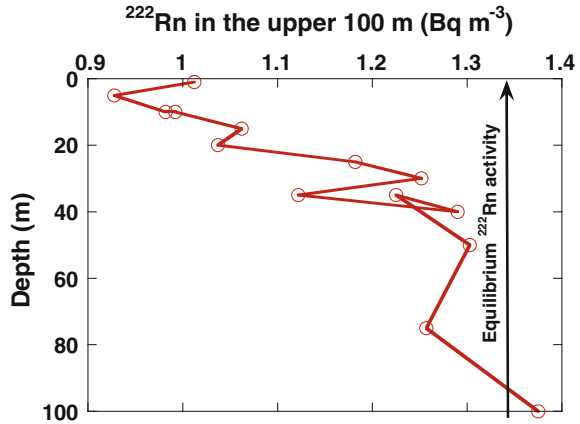
In the open ocean, roughly ~ 10 % of the ^{226}Ra in sediment diffuses into the water column (Key et al. 1979), with the ^{226}Ra and ^{222}Rn generally to be in secular equilibrium between the bottom of the euphotic zone and about ~ 100–200 m above the sediment-water interface. Through most of the water column, radon distribution generally reflects that of its ^{226}Ra parent. Consequently, deep Atlantic waters have less radon than deep Pacific and deep Indian Ocean waters. This follows the general enrichment of deep ocean waters in ^{226}Ra (Fig. 6.3) as they "age" during the journey to the N. Pacific (Broecker and Peng 1982; Ku and Luo 1994).

6.6 Applications of Radon at Interfaces

6.6.1 ^{222}Rn as a Tracer of Gas Exchange Rates at Air-Sea Interface

There is a constant exchange of atmospheric gases between ocean surface and atmosphere, but the spatial and temporal exchanges of different gases vary. Quantification of the amount of gas exchange requires the gas exchange coefficient. For example, for an understanding of carbon dioxide or oxygen budgets in the upper ocean, we need to know the coefficient of air-sea exchange. Several factors that affect the exchange rates of gases include temperature, wind velocity, solubility of the gas, diffusion rate, surface effects such as the formation of bubbles by breaking waves at moderate to high wind velocity and chemical nature of the water (Wanninkhof et al. 2009).

Evidence for the loss of radon from the upper mixed layer comes from the vertical profile of ^{222}Rn in the upper 100 m, which indicates that there is loss of ^{222}Rn to the atmosphere from <80 m, where the ^{222}Rn/^{226}Ra activity ratio of <1.0 (Fig. 6.5). Similar profiles have also been reported from other places, including tropical Pacific Ocean (Broecker and Peng 1974); Peng et al. 1979; Cochran 1992). In the thermocline, below the euphotic zone, ^{222}Rn is expected to rapidly approach equilibrium with ^{226}Ra. This observation of disequilibrium between ^{222}Rn and ^{226}Ra in the upper waters is useful to obtain the rates of ^{222}Rn emanation to the atmosphere.

Two models have been utilized to determine the gas exchange efficient at the air-sea interface: (i) stagnant thin film model (Fig. 6.6) and (ii) surface renewal model. Radon-222 has been used to estimate gas exchange rates between atmosphere and surface-ocean using thin-film model (Broecker 1965; Broecker et al. 1967; Broecker and Peng 1971; Peng et al. 1974; Glover and Reeburgh 1987; Bender et al. 2011; Yeung et al. 2015), estuaries (Hammond et al. 1977; Hammond and Fuller 1979), Lakes (Emerson et al. 1973; Emerson 1975) and River (Elsinger
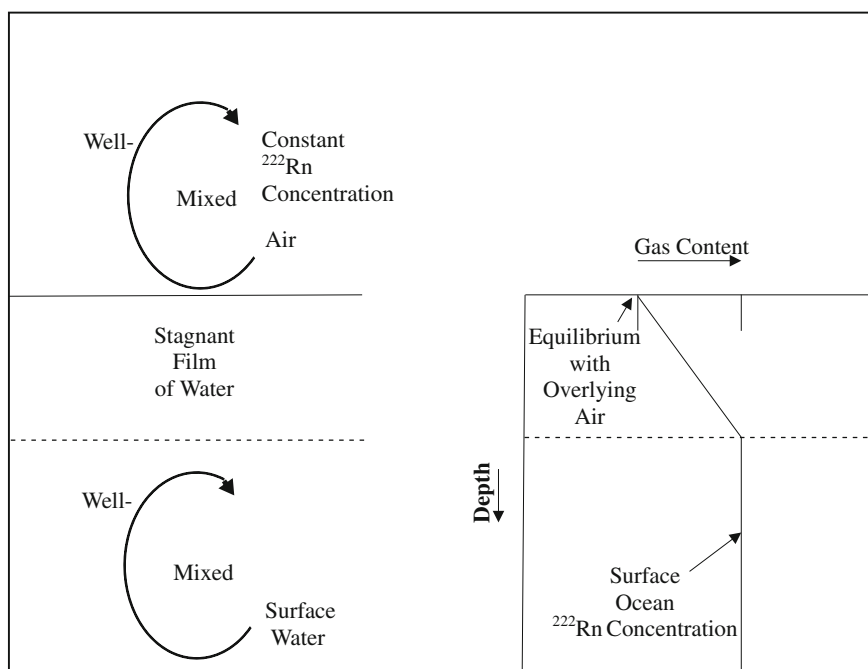
Fig. 6.6 Thin-film gas exchange model for ^{222}Rn. A thin stagnant film separates the well mixed overlying air from the well mixed underlying surface water. Radon is transferred between air and water only by molecular diffusion through this film. The film thickness decreases with the degree of agitation at the air-sea interface. The global average film thickness is 40 μm (Figure modified from Broecker and Peng 1982)

and Moore 1983). From several laboratory experiments, it has been shown that 'physical' gas exchange rate (mass transfer coefficient) of various gases varies as a function of wind velocity (summarized in Emerson 1975; Winninkhof 1992, Winninkhof and McGillis 1999). A statistically significant correlation between averaged wind speed and ^{222}Rn transfer coefficient was reported in Southeastern Bering Sea shelf waters (Glover and Reeburgh 1987). However, theoretical studies postulate various relationships between wind speed and transfer coefficient. According to Smethie et al. (1985) radon method is the only method capable of establishing the relationship between average wind speed and transfer coefficient obtained from field studies in the ocean. Details of these studies in the estimation of gas exchange coefficient are given below.

When a liquid water–gas (atmosphere) system is not in equilibrium, the escape of gas (radon) takes place so as to reach equilibrium. The transfer has often been described by assuming that two boundary layers straddle the air-sea interface, and that transport across the interface is limited by diffusion through these layers. For non-reactive gases of low solubility, like radon, transport through the aqueous phase will be limiting, while the atmospheric boundary layer has little impedance. At the interface, gas and liquid phases are assumed to be in equilibrium. In the aqueous phase, there is a thin surface layer of the liquid side which is also practically free from mixing by convection. This assumption of existence of stationary films of gas and liquid, respectively on the two sides of the interface, known in literature as 'thin film model', was proposed by Lewis and Whitman in 1924. In the main body of water and air, the mixing by convection was assumed to be rapid which implies that the concentration of ^{222}Rn in water and air are uniform. Gases cross this boundary film only by molecular diffusion. Although the diffusive processes are chaotic, if there is a concentration gradient, then, there will be net transfer of material from the zone of high concentration to the zone of low concentration. If the radon concentration in the water is not in equilibrium with the concentration of radon in the air, there will be a net flow of radon through the stagnant film. The rate at which radon is transferred across the air-sea interface will depend on:

  (i) Thickness of the film (thicker the film, larger resistance to the radon atom to wander through it);
 (ii) Rate at which radon diffuse through sea water (more rapid molecular motion with higher temperature) and
(iii) The magnitude of the disequilibrium between radon concentration in the air and that in the water (higher concentration gradient, the more rapid diffusive transfer).

An alternative description of transport assumes that the aqueous phase is continuously renewed (surface renewal model). In both cases, gas exchange rates are defined by a piston velocity, and empirical observations have allowed the exchange rates of radon to be related to those for other gases (see review by Wanninkhof et al. 2009). Broecker and Peng (1974) used radon (Fig. 6.6) to determine the piston velocity [k = λh $(C_E - C_x)/(C_S - \propto P^{atm})$]. By equating the diffusive flux across

the air-sea boundary layer to the flux that is required to support the integrated ^{222}Rn deficiency in the mixed layer, we get:

$$D_m \frac{(C_S - \propto P^{atm})}{z} = \lambda \int_0^\infty (C_E - C_x) dx \qquad (6.3)$$

where D_m is the molecular diffusion coefficient (m^2 s^{-1}) of radon in sea water, α is the solubility of radon in surface sea water, P_{atm} is the partial pressure (atm) of radon in air, z is the thickness (m) of the stagnant film, C_s is radon activity (Bq m^{-3}) at the base of the boundary layer, C_E is radon activity (Bq m^{-3}) in equilibrium with dissolved ^{226}Ra, and C_x (Bq m^{-3}) is radon activity at depth x (m) in the surface ocean. Rearranging equation (6.3), we get:

$$\int_0^\infty (C_E - C_x) dx = (C_E - C_S)\hbar \qquad (6.4)$$

$$z = \frac{D}{\lambda \hbar} \frac{1}{(C_E/C_S - 1)} \qquad (6.5)$$

Values of piston velocity and stagnant film thickness for world oceans and Canadian Lake reported in literature are summarized in Table 6.4. The gas transfer coefficient using ^{222}Rn obtained during the GEOSECS program in the Atlantic and Pacific oceans range from 0.5 to 6.8 m/d with most values falling between 1.0 and 4.0 m/d, with a global average radon-based gas transfer coefficient value of 2.8 m/d (Peng et al. 1979). The mean gas transfer coefficient in the Antarctic zone (4.1 m/d in south of 40° S) is higher than that reported for the southern temperate zone (2.9 m/s, 15° S–45° S). The equatorial zone (15° S–15° N) has the lowest gas exchange rate. Glover and Reeburgh (1987) reported a range of values, 0.2–4.9 m/d (mean: 2.2 m/d) from the Bering Sea shelf waters (Table 6.4). Note that the gas exchange rate is faster in the Antarctic (mean gas exchange coefficient = 3.7 m/d).

There are certain limitations on the utility of radon as a tracer for gas exchange studies (Kromer and Roether 1978; Roether 1983; Smethie et al. 1985). The inherent assumptions include: (i) the method implicitly assumes lateral homogeneity, invariant of mixed layer depths, and steady state of the radon deficit in the mixed layer; (ii) the wind speed parameterization was largely unconstrained due to local wind speed history prior to radon sampling; and (iii) 'snapshots' studies were conducted; however, the mixed layer ^{222}Rn deficiency reflects gas transfer velocity over the ~ 2 weeks prior to sampling, weighted toward the present (Bender et al. 2011). Reevaluation of radon data from GEOSECS results using wind speed products, derived from reanalyses of historical meteorological data utilizing numerical weather models, to estimate the evolution of the ^{222}Rn in the mixed layer at historical sampling locations was conducted by Bender et al. (2011). They also assumed a constant mixed layer depth during ~ 2 weeks prior to sampling as there is no robust way to reconstruct the time history of mixed layers. Furthermore,

Table 6.4 Mass transfer coefficients for oceans and lakes derived from radon

Location	Mass transfer coefficient Mean (range) m/day	Film thickness range (μm)	Reference
Oceans			
Tropical N. Atlantic	1.9		Broecker and Peng (1982)
N. Atlantic	1.8	9–56	Peng (1973)
N. Pacific	3.9 (1.8–6.8)	–	Peng (1973), Peng et al. (1974)
S. Pacific	1.9	16–400	Peng (1973)
Eastern Tropical	1.0–3.0		Yeung et al. (2015)
Antarctic zone	4.1		Peng (1973)
Southeastern Bering	2.2 (0.2–4.9)		Glover and Reeburgh (1987)
Sea shelf			
Global Ocean	2.9–6.5		Bender et al. (2011)
Lakes (*ELA)			
ELA-227	0.4 (0.2–0.6)		Emerson et al. (1973)
ELA-227	0.16	400–1000	Emerson (1975)
ELA-261	0.16	mean: 600	Emerson (1975)
ELA-304	0.20 (0.16–0.25)		Emerson (1975)
River			
Pee Dee River	2.1–4.1	19–48	Elsinger and Moore (1983b)
Daly River	1.0		Cook et al. (2003)
San Francisco Bay	0.4–1.8		Hartman and Hammond (1984)

*ELA: Experimental Lakes Area in small Canadian Shield lakes area

presence of internal waves affecting the measured depth of the mixed layer to differ from the average depth assumed and lateral processes affecting the measured ^{222}Rn profiles resulting in inaccurate piston velocities were also not taken into account.

Using the gas transfer coefficient and thickness of the mixed layer, the residence time of radon, τ, in the mixed layer can be calculated as follows:

$$\tau = \text{depth of the mixed layer (m)} / \text{gas transfer coefficient (m/s)}$$

The calculated residence times in the 90 mixed layer samples from the GEOSECS global ocean data set fall in the range of 5–63 days, with most values in the range of 10 and 35 days (average: 22 days; Peng et al. 1979). The mean residence time in the Antarctic waters is 13 days, significantly lower compared to the global average. Other non-reactive gases have similar residence times, although the piston velocities will depend on their molecular diffusivities (Wanninkhof et al. 2009).

6.6.2 ^{222}Rn as a Tracer of Diapycnal and Isopycnal Mixing

Radon, along with ^{228}Ra and ^{3}He, have been utilized to determine the coefficients of isopycnal and diapcynal mixing coefficients in the upper ocean. Radon is produced in sea floor sediments in much larger amounts compared to the oceanic water column, as the total inventory of ^{226}Ra in the bottom sediments for a water column depth of 3600 m water is expected to be 9.9×10^{6} Bq m^{-2}, assuming that residence time of ^{230}Th is less than 100 years in the water column and there is no boundary scavenging effect or sediment focusing. The inventory of ^{226}Ra in the water column is expected to be <10 % of this value and hence the production rate of ^{222}Rn in the sediment column is expected to be much higher compared to radon production rate in the water column. The distribution of this ^{222}Rn excess above the sea floor carries the information about the rate of vertical mixing of the seawater.

In order to estimate diapycnal mixing (mixing perpendicular to the local surfaces of constant density, known as isopycnals) coefficient, the following assumptions are commonly made (Broecker and Peng 1982): (i) the role of vertical advection is small compared to that of the vertical diffusion. In fact, an estimate on the vertical advection term can be obtained as follows: the rate of upward advection based on ^{14}C-based ventilation rate is ~4 m/year. During the mean life of ^{222}Rn (5.5 d), the vertical movement of ^{222}Rn thus is only 6 cm; and (ii) the distribution in the vertical direction is governed entirely by diapycnal processes. Under these two assumptions, one-dimensional mass balance involves the balance between diffusion and radioactive decay. The concentration of ^{222}Rn at any depth above the sediment-water interface can be obtained by solving the equation:

$$K_Z \frac{\partial^2 C_z}{\partial z^2} - \lambda C_z = 0 \qquad (6.6)$$

where C_z is concentration of excess ^{222}Rn activity (=activity of total ^{222}Rn—activity of ^{226}Ra; all activities in Bq m^{-3}) at some height 'z' above the sediment-water interface; K_Z is the diffusion coefficient and λ is decay constant (i.e., = 0.693/3.82 d) of ^{222}Rn. If K_z is constant, the vertical profile of ^{222}Rn is governed by the equation:

$$C_z = C_0 \exp\left[-z * (\sqrt{(\lambda/K_Z)})\right] \qquad (6.7)$$

where C_0 is concentration of excess ^{222}Rn activity at sediment-water interface. The concentration of ^{222}Rn from the sediment-water interface upward decreases exponentially. One can calculate the depth at which the activity decreases to 50 % of what is found at the sediment-water interface:

$$\begin{aligned}
0.5 &= \exp\left[-z_{1/2} * (\sqrt{(\lambda/K_Z)})\right] \\
K_Z &= \left(1.443\, z_{1/2}\right)^2 \lambda
\end{aligned} \qquad (6.8)$$

The vertical profiles of excess ^{222}Rn from sediment-water interface into the ~ 200 m depth in the water column from 3 stations in the Western and Southern Indian Ocean are given in Fig. 6.7 (data and K_z values given in Fig. 6.7 are taken from Chung and Kim 1980) for data from western and southern Indian Ocean, Young and Kim (1980). Of the three profiles shown in Fig. 6.7, K_z values could be calculated for only two: for ST-417 (0.10 m^2 s^{-1}, Arabian Sea) and ST-435 (0.0012 m^2 s^{-1}, South Australian Basin of the Indian Ocean). The eddy diffusivity in GEOSECS-I stations ranged between 0.0020 m^2 s^{-1}– 0.013 m^2 s^{-1}, by a factor of approximately six. Although the eddy diffusivity calculation assumes a simplified version of diffusion (one dimension, and other perturbations to the vertical profiles are ignored), it remains unknown how this model reflects the actual vertical mixing process. Furthermore, the perturbation in vertical profiles of ^{222}Rn profiles could be due to turbidity flow or any transient advective process (Fig. 6.7c, Chung 1974a, b). It is likely an oversimplification, as many near bottom profiles show evidence that eddy diffusivity decreases with increasing distance from the bottom.

In some of the vertical profiles, there is no exponential decrease of excess ^{222}Rn in ST-430 (Antarctic Indian Basin) and it is attributed to the transient characteristics of the bottom water. Similar observations of constant ^{222}Rn profiles over 30–200 m above bottom in several Atlantic and Pacific ^{222}Rn profiles collected in GEOSECS stations have been reported and in those places lower limits on the diffusivity in the benthic mixed layer have been estimated (Broecker and Peng 1982). The calculated diffusion coefficient for ^{222}Rn in the northwestern Atlantic (5400–5900 m) and southwestern Pacific (5400–5700 m) were 0.04 m^2 s^{-1} and 0.012 m^{2}s^{-1}, respectively (Broecker and Peng 1982). From the measurements of ^{222}Rn profiles at the GEOSECS-I station in the northeast Pacific at varying intervals over a period of 2.5 years, Chung (1974a, b) showed that the profiles varied considerably in ^{222}Rn concentration indicating transient characteristics of the bottom water in the deep Pacific. Radon profiles measured on April 27 and April 28, 1972, indicated transient characteristics of the bottom water in the deep Pacific while ^{226}Ra concentrations are fairly uniform, within the errors of measurements. Chung (1974a, b) attributed this to possible non-steady state produced by a turbidity flow or any transient advective process causing such drastic change in the vertical ^{222}Rn profiles near the sediment-water interface.

From the vertical transport rates of ^{222}Rn, one can, in principle, deduce the transport rates of other tracers. For example, ^{222}Rn in the abyssal boundary layer, discussed above, can be used to estimate the buoyancy fluxes or heat flux rates, assuming that local mixing are similar to all (Sarmiento et al. 1976). Sarmiento and Rooth (1980) attempted to show that the distribution of excess ^{222}Rn in the bottom waters of the deep sea might reflect horizontal as well as vertical mixing processes. Significantly higher standing crops of excess ^{222}Rn in the deep ocean passages in the southwest Atlantic Ocean (Vema Channel) and in the Pacific Ocean (Samoan, Clarion, and Wake Island passages) were observed. The sediment floors under these passages contain high abundance of manganese nodules that contain very high concentrations of ^{230}Th$_{xs}$ and ^{226}Ra, and radon diffusion from these manganese

Fig. 6.7 Near bottom excess-radon profile in three stations: **a** ST-417—Arabian Sea (12° 58.3′ N; 64° 28.8′ E, total water depth: 4115 m, K_z value is calculated for the benthic boundary layer; ^{226}Ra = 3.73 Bq m^{-3}); **b** ST-435—South Australian Basin (39° 57.2′ S; 109° 58.3′ E, total water depth: 4638 m, K_z value is calculated for the upper layer; ^{226}Ra = 3.73 Bq m^{-3}); and **c** ST-430—Antarctic Indian Ocean (59° 59.1′ S; 60° 58.6′ E, total water depth: 4737 m, K_z value could not be calculated; ^{226}Ra = 3.73 Bq m^{-3}). Data are taken from Chung and Kim (1980)
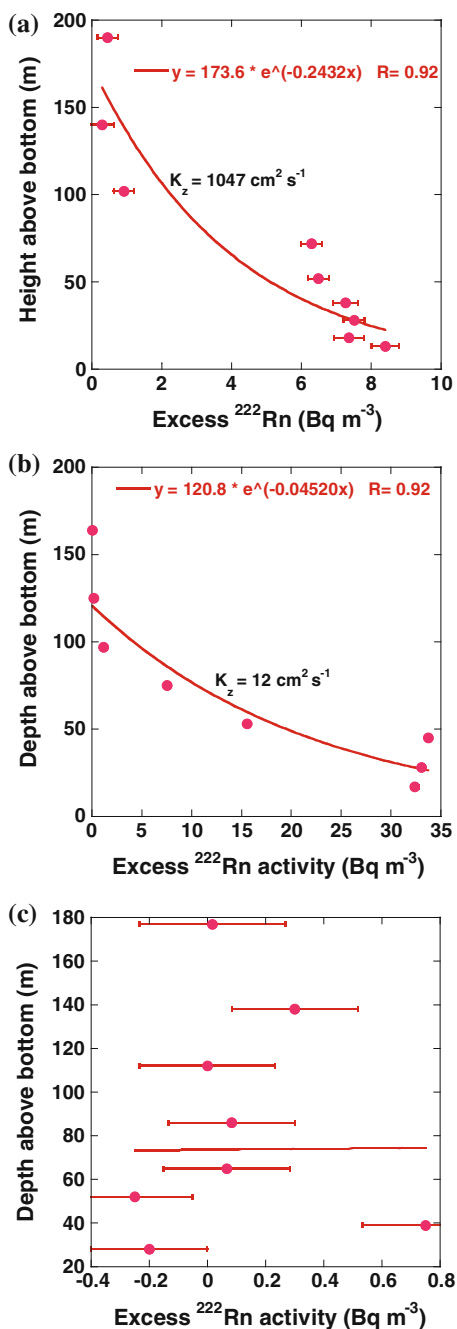
nodules and encrustations and walls of the passages leads to higher standing crops of excess ^{222}Rn. The great heights at which excess ^{222}Rn found was attributed to the exceptionally high apparent vertical mixing in the passages, as bottom topography of the ocean floor plays an important role in determining the nature of deep water circulation and hydrography (Sarmiento et al. 1978).

6.6.3 Inventories and Fluxes of Radon-222 in the Oceanic Water and Sediment Column

Broecker et al. (1968) first reported an interesting observation that there is considerable variations in the standing crops of excess radon (radon activity exceeding that of the ^{226}Ra parent) in the deep water column, and they suggested that the variation should be inversely related to the sedimentation rate because of the direct effect of the sedimentation rate on the ^{230}Th concentration in the sediments. ^{230}Th produces ^{226}Ra, the radon parent, and high concentrations of ^{226}Ra in near-surface sediment should lead to substantial fluxes of radon into the overlying water. A key factor controlling this relation is that the total amount of ^{230}Th produced in a finite depth of water column remains constant (i.e., the total production of ^{230}Th (Bq m^{-2} y^{-1}) over a depth of 4000 m remains constant within <1 %, whether it is Atlantic or Pacific or Indian Ocean, and this is due to conservative nature of U, with a very long residence time, $\sim$500 kyr, in the ocean). The standing inventory of excess ^{222}Rn (normalized to a depth of 4000 m) is significantly higher in the Pacific (mean: 1120 Bq m^{-2}, with 95 % confidence limits of: 880–1400 Bq m^{-2}, calculated from 57 profiles) than the Atlantic (mean: 230 Bq m^{-2}, with 95 % confidence limits of: 180–300 Bq m^{-2}, calculated from 52 profiles) and this is attributed to higher activities of ^{230}Th and ^{226}Ra per g of dry sediments, due to low sedimentation rates in the Pacific compared to Atlantic (Sarmiento and Broecker 1980). A comparison of the sedimentation rates in the Pacific and Atlantic and the corresponding inventories of excess ^{222}Rn is given in Table 6.3. Note that the boundary scavenging of ^{230}Th may also affect the inventories of excess ^{230}Th and thereby ^{226}Ra inventories and thus, in areas where there is active boundary scavenging, we expect higher excess inventories of ^{222}Rn as well. Such fine scale variations can be seen in Table 6.3 of the data reported reported in Sarmiento and Broecker (1980) where the inventories of ^{222}Rn in the 30°–40° N latitude belt in the West Pacific (570 Bq m^{-2}) and East Pacific (1500 Bq m^{-2}) differ by a factor of 2.6. In summary, the excess inventory of ^{222}Rn in the water column provides direct information on the rates of sedimentation, including possible information on the boundary scavenging.

Measured concentrations of ^{222}Rn in deep-sea sediment pore waters are 10^4–10^5 times higher than that of the oceanic water lying above the sediment-water interface. Due to this concentration gradient, radon diffuses from the sediment into the water column. Broecker (1965) suggested that the diffusion of ^{222}Rn from the

sediment column into to the overlying water column is expected to result in deficiency of ^{222}Rn (i.e., inventory of ^{226}Ra > inventory of ^{222}Rn) in the sediment column and excess ^{222}Rn in the overlying water above the sediment-water interface. The rate of change of ^{222}Rn concentration, C (Bq m^{-3}) with time at any point equals the diffusional input – decay + production of ^{222}Rn supported by ^{226}Ra in secular equilibrium.

$$\frac{dC}{\partial t} = D_s \frac{\partial^2 C}{\partial z^2} - \lambda C + \lambda C_{eq} \tag{6.9}$$

where D_s is the molecular diffusion coefficient of ^{222}Rn in sediments. At steady state, dC/dt = 0 and Eq. 3.9 can be solved using the boundary conditions C = C$_0$ in overlying water at the sediment-water interface and C = C$_{eq}$ at infinite depth. The steady-state solution to Eq. 3.9 is:

$$C = C_{eq}^{\infty} \left\{ 1 - \exp\left[-\left(\frac{\lambda}{D_s}\right)^{\frac{1}{2}} z \right] \right\} + C_0 \left\{ \exp\left[-\left(\frac{\lambda}{D_s}\right)^{\frac{1}{2}} z \right] \right\} \tag{6.10}$$

From Fick's law, the radon flux across the sediment-water interface is given by

$$F = -D_s \frac{\partial C}{\partial z^{z=0}} = -(\lambda D_s)^{\frac{1}{2}} (C_{cq} - C_0) \tag{6.11}$$

The ^{222}Rn flux from bottom sediments can thus be calculated as follows:

$$F = \lambda \int_0^{\infty} (C_{cq} - C_0) dz \tag{6.12}$$

where F is the radon flux (Bq m^{-2} s^{-1}), and λ is the ^{222}Rn radioactive decay constant.

One simple way of determining the radon flux involves collection of sediment core and placing distilled water on top of the sediment cores which are then sealed and stored for about 2 weeks. Then the radon standing crop in the water overlying the sediment is measured. However, in field conditions other factors such as bio-turbation, physical mixing, bio-irrigation, physical irrigation in addition to the molecular diffusion and chemical processes will affect the radon flux.

A comparison of the integrated radon deficit in the sediment column to the integrated surplus in the overlying water column indicated that both agree reasonably well in the deep sea (Key et al. 1979b). Berelson et al. (1987) reported reasonable agreements between the ^{222}Rn deficit in the water column and the ^{222}Rn flux measured by benthic chamber experiments. There are distinct differences in the bottom water surplus of ^{222}Rn in the Pacific (300–3300 Bq m^{-2}; Broecker et al. 1968; Berelson et al. 1987; Chung 1974a, b) and Atlantic (30–700 Bq m^{-2}; Sarmiento et al. 1978; Key et al. 1979b). The mean benthic fluxes of ^{222}Rn also

differ widely, with 15×10^4 Bq m^{-2} y^{-1} in the Pacific and 1.7×10^4 Bq m^{-2} y^{-1} in the Atlantic, while the mean for the global ocean is estimated to be 10×10^4 Bq m^{-2} y^{-1} (Huh and Kadko 1992). Chung (1974a, b) observed that the radon flux across the sediment-water interface varied by a factor of 2 between GEOSECS Pacific stations bottom waters. He also suggested that the excess-radon profile in Pacific bottom water may be variable in time. As mentioned before, since the ^{222}Rn benthic flux is directly related to the concentrations of ^{226}Ra in sediments, the variations of ^{222}Rn fluxes mainly reflect the variations in ^{230}Th fluxes from the water column to the sediment, which in turn depends on the sedimentation rates. Furthermore, the ^{226}Ra concentrations in the Pacific Ocean water column are significantly higher than that of the Atlantic Ocean (Fig. 6.3). The contrasting different sedimentation rates between the Atlantic and Pacific Oceans, are due to varying of sediment discharge loads from rivers, and is the reason for the differences in the ^{230}Th flux to the sediments. The specific activity (Bq g^{-1}) of ^{230}Th (and ^{226}Ra) in manganese nodules are much higher than those in the bottom sediments and hence the diffusion of ^{222}Rn from the Mn-nodule will result in elevated levels of ^{222}Rn in the overlying sea water as well as in the underlying sediments (Krishnaswami and Cochran 1978; Huh and Ku 1984). In surficial sediments of coastal and estuarine areas, enhanced activities of the benthic fauna (such as burrow irrigation and particle mixing) and the effects of bottom currents lead to elevated fluxes of ^{222}Rn compared to those expected from molecular diffusion alone (Hammond et al. 1977, 1985; Hartman and Hammond 1984; Colbert et al. 2008; Martin and Banta 1992).

6.6.4   Concentrations of ^{222}Rn in Hydrothermal Vent

Studies on the chemistry of the submarine hydrothermal fluids indicate that ^{222}Rn and other inert gases such as ^{3}He, ^{4}He are enriched at the TAG and Snakepit hydrothermal vent fields in the Mid-Atlantic Ridge system. Concentrations of ^{222}Rn and ^{226}Ra in the TAG vent fluids, (TAG buoyant plume) and Snakepit vent fluids ranged between 260 and 2950 Bq m^{-3} (compared to 5.5 Bq m^{-3} in seawater) and 17 and 277 Bq m^{-3} (compared to 6.0 Bq m^{-3} in seawater), respectively (Rudnicki and Elderfield 1992). It has been suggested that the enrichment of bottom waters through low-temperature venting could be a possible source of ^{222}Rn enrichment of plumes above the Juan de Fuca Ridge (e.g., Kadko et al. 1990). Relationship between ^{222}Rn concentration and helium isotopic ratio (^{3}He/^{4}He) can potentially provide information on the origin of radon in the neutrally buoyant plume (such as TAG). From the measured radon/ΔT ratio in the near-field plume and the standing crop of hydrothermally injected radon, Rosenberg et al. (1988) estimated the heat flux $1 - 5 \times 10^9$ W into the overlying plume of the Endeavor segment of the Juan de Fuca Ridge.

6.7 Quantification of Submarine Groundwater Discharge Using ^{222}Rn as a Tracer

A mass balance approach can be utilized to quantify the amount of submarine groundwater discharge for an aqueous system (e.g. river, coastal area of a lake) using radon as a tracer. The sources of radon for an aqueous system include production from its parent (^{226}Ra), benthic fluxes due to molecular diffusion and irrigation of sediments, additional input from submarine groundwater discharge in the coastal/estuarine waters and physical transport processes in the water column (including transport of offshore surface waters into the coastal areas). For sinks, since there is no biological or abiological removal of radon from aqueous system, most radon loss from surface waters is from degassing and radioactive decay. Radon concentration in groundwater is significantly enriched (often 3–4 orders of magnitude) relative to coastal marine waters, and thus a mass balance approach for ^{222}Rn can be utilized to quantify the amount of groundwater discharge if other source/sink terms can be quantified. If radon sources are localized, lateral mixing will dilute the inputs. Due to the short half-life, the lateral advection contribution from the open ocean should be negligible. Advective transport of groundwater (pore water) through sediments is often reported to be a dominant source term for ^{222}Rn (Burnett et al. 2006). Elsinger and Moore (1983) observed excess ^{222}Rn concentration in Pee Dee River and ^{222}Rn concentrations were reported to vary between 22 and 233 Bq m-3 while the ^{226}Ra concentrations varied between 0.5 and 1.0 Bq m-3, clearly indicating 1 to 2 orders of magnitude higher ^{222}Rn. From the measurements of ^{222}Rn flux using a benthic flux chamber deployed near a submarine spring in the northeastern Gulf of Mexico, Cable et al. (1996) showed that the total advective-diffusive flux of ^{222}Rn (87 ± 30 Bq m-2 d-1) is much higher that of the diffusive flux (3 ± 1 Bq m-2 d-1). From the measurement of ^{222}Rn in the advecting fluids, the ^{222}Rn fluxes could be easily converted in water fluxes. Furthermore, from the measurements of nutrients and other key trace metals in the advecting fluids, the fluxes of these species can also be quantified.

One of the main advantages of ^{222}Rn is that it integrates the signal over its mean life. As a result, smaller scale variations which may be unimportant for larger scale studies will be smoothed out and this approach may be optimal in environments where especially large spatial variation is expected. One of the disadvantages of ^{222}Rn method is that radon escape to the atmosphere may be difficult to model under certain circumstances such as large sudden changes in wind speeds, and waves breaking along a shoreline. It has been shown that, overall the submarine groundwater discharge estimated from ^{222}Rn method compares reasonably well (at least in some cases) well with other methods (Table 6.5); examples include: estimated integrated SGD ranges (daily averages) via four different approaches for Cockburn, Sound, Australia (November 25–December 6, 2000), and Shelter Island, New York (Table 6.5). Radon has been utilized to quantify rates of groundwater inflow to a river, in conjunction with other gas tracers such as SF_6 (Cook et al. 2003). Since gas exchange process is usually modeled as a diffusive process

Table 6.5 Estimated integrated groundwater discharge (daily averages, m^3/m day) via four different approaches for Cockburn Sound, Australia and Shelter Island, NY (from Burnett et al. 2006)

Location	Seepage meters	Ra isotopes	Radon	Modeling
Cockburn Sound, Australia	2.5–3.7	3.2	2.0–2.7	2.5–4.8
Shelter Island, New York	0.4–17.5	–	16–26[a]	0.23–10[b]
			18–20[c]	

The seepage meter, Ra isotopes, and Rn measurements were all made during the same period. The modeling was performed for average conditions

[a]Mixing losses of Rn are based inspection of calculated Rn fluxes

[b]Using an estimate of mean freshwater discharge, based on water budget estimate and MODFLOW (details given in Burnett et al. 2006)

[c]Mixing losses of Rn based on short-lived Ra isotopes

through a thin film, the gas transfer velocities of two gases A (K$_A$) and B (K$_B$) are related to their diffusion constants as follows:

$$K_A/K_B = (D_A/D_B)^{1/2} \qquad (6.13)$$

From Eq. 6.13, one can calculate the piston velocity of an unknown gas, B, if the piston velocity of A (^{222}Rn) and the diffusion coefficients of the unknown gas and ^{222}Rn are known.

6.8 ^{222}Rn Concentrations and its Utility as a Tracer in Lakes

Determination of mass transfer coefficients from surface waters is given in sect. 6.6. Investigation on the recycling of nutrients and particular matter from the euphotic zone to the hypolimnion and vertical component of the transport to the understanding of mass flux and mass balance requires reliable estimate of the vertical diffusion coefficient. While one-dimensional transport equation is often adequate in the open ocean, bottom geometry in near-shore regions and in most lakes cannot be neglected and thus, the one-dimensional problem becomes two- or three-dimensional in limnology. The vertical diffusivity calculated for lakes with one-dimensional vertical model developed for tracer distribution in the deep sea (Eq. 3.6) often leads to a significant overestimation of vertical diffusivity in lakes (Imboden and Joller 1984). Although traditionally the vertical diffusion coefficient is determined by the temperature method, the limitation of this method is that there exists only very small changes in the temperature near the bottom of many lakes. Furthermore, the heat is also transmitted into the water column by other means (Imboden and Emerson 1978) which leads to less reliable estimate of the vertical diffusion coefficient. The advantage of ^{222}Rn is that its relatively short mean-life creates measurable horizontal and vertical gradients near the lake bottom, allowing

the determination of multidimensional eddy diffusion coefficients from a single set of profiles (Imboden and Emerson 1978). Furthermore, the effect of horizontal transport on the apparent vertical eddy diffusion coefficient can also be evaluated. A solution to the 2-D problem in lakes has been presented by Colman and Armstrong (1987).

Radon-222 concentrations are generally expected to be significantly higher in lake water than that of ^{226}Ra (^{222}Rn/^{226}Ra > 1.0), due to inflow of radon-rich groundwater in the lake as well as discharge of streams/rivers that also have higher groundwater-derived ^{222}Rn (unlike deep ocean where the contributions from groundwater is assumed to be negligible). Thus, the amount of ^{222}Rn produced from the decay of ^{226}Ra often is insignificant. In streams that discharge into the Experimental Lakes Area-Canadian Shield lakes, ^{226}Ra concentration was reported to be less than 17 mBq L^{-1} while ^{222}Rn concentrations were reported to be 100–500 times higher (1.7–8.3 Bq L^{-1}; Emerson 1975). For an average mass transfer coefficient of 0.2 ± 0.1 m day^{-1} for the three lakes in the Experimental Lakes Area (ELA) in the Canadian Shield area, the corresponding stagnant boundary layer thickness was calculated to be 600 μm (Table 6.4, Emerson 1975).

From the monthly measurements of ^{222}Rn at different stations in Greifensee, Switzerland, Imboden and Emerson (1978) reported the hypolimnetic vertical and horizontal eddy diffusion coefficients of (0.5–2.0) × 10^{-5} m^2 s^{-1} and (1,000–10,000) × 10^{-5} m^2 s^{-1}, respectively, in 1975. Imboden and Joller (1984) reported for Baldeggersee Lake in the central plain of Switzerland (47° 12′ N; 8° 16′ E) a decrease in the horizontal diffusivity from 5.8 × 10^{-2} m^2 s^{-1} in June to 1.2 × 10^{-2} m^2 s^{-1} in October; the vertical diffusivity varied between 1.2 × 10^{-5} m^2 s^{-1} and 12 × 10^{-5} m^2 s^{-1}. The ^{222}Rn flux from sediment-water interface was reported to be 6.5 ± 1.2 Bq m^{-2} d^{-1}, which is orders of magnitude lower than that in the deep ocean primarily due to differences in the inventories of ^{226}Ra in their sedimentary columns.

6.9 Conclusion and Future Research Direction

The disequilibrium between ^{222}Rn and ^{226}Ra is one of the most successful and powerful applications of U-Th-series radionuclides in marine system. Applications of this pair as a tracer to investigate the following include: (i) estimation of piston velocities for determining air-sea gas exchange rates in the ocean, estuaries, and lakes; (ii) determination of vertical eddy diffusion coefficient in the ocean and other aqueous bodies; (iii) quantification of amount of groundwater discharge; and (iv) and characterization of transport coefficients for chemical exchange between pore waters and overlying waters. Furthermore, the contrasting differences in the inventories of ^{222}Rn in the whole water column between Atlantic and Pacific Oceans is attributed to the differences in the sedimentation rates between these two oceans and hence the depth-normalized inventory yield information on the sedimentation rates and possibly the effects of boundary scavenging. Presence

of ferromanganese nodules at the bottom of the ocean floor also is another important source of radon and under ideal conditions, one could possibly use radon as a tracer for the estimation of ferromanganese nodule density at the ocean floor.

Recent advances in instrumentation (the Rad-7) that allow spatial surveys of radon distribution with high resolution which have allowed identification of localized inputs of radon that are useful for characterizing groundwater sources. Additional work needs to be done relating amounts of groundwater and sediment irrigation inputs to corresponding inputs of nutrients, by characterizing the relation between nutrients and radon in the transported fluid. It is particularly important in developing such budgets to find the subsurface zone that may be deficient in radon but may act as a source for the radon excess observed in the overlying water.

There is generally an exponential decrease in the activity of excess ^{222}Rn from the sediment-water interface to 50–200 m in the water column, in many places such profiles were not observed and thus radon could serve as a tracer to understand some of the less-known or unknown short-time-scale processes that take place at benthic boundary layers. So far no field data seem to have documented the equilibrium between ^{222}Rn and ^{226}Ra (i.e., ^{222}Rn/^{226}Ra activity ratio = 1.0, within experimental error) from thermocline to $\sim$200 m above sediment-water interface (although it is always assumed); presence of disequilibrium, if exists, could provide information on processes which remains elusive and that take place in short time-scales (days to couple of weeks). Under global warming scenario, the values of mass transfer coefficient and surface film thickness could change resulting in changes in the exchange rates of greenhouse gases between the ocean and atmosphere and monitoring these parameters periodically at selected sites such as Bermuda Atlantic Time Series (BATS) may be useful.

References

Bender M, Kinter S, Cassar N, Wanninkhof R (2011) Evaluating gas transfer velocity parametrizations using upper ocean radon distributions. J Geophys Res 116:C02010. doi:10.1029/2009JC005805

Berelson WM, Buchholtz MR, Hammond DE, Santschi PH (1987) Radon fluxes measured with the MANOP Bottom Lander. Deep-Sea Res 34:1209–28 [13.2.4]

Broecker WS (1965) An application of natural radon to problems in oceanic circulation. In: Ichiye DT (ed) Symposium on diffusion in ocean and fresh waters, pp 116–145. Lamont-Doherty Geol. Observatory, Palisades, NY. [5.5.3, 10.4.2, 10.5, 10.5.1, 11.5]

Broecker WS, Peng T-H (1971) The vertical distribution of radon in the BOMEX area. Earth Planet Sci Lett 11:99–108 [10.5.1]

Broecker WS, Peng T-H (1974) Gas exchange rates between air and sea. Tellus 26:21–35

Broecker WS, Peng T-H (1982). Tracers in the sea, Eldigo press

Broecker WS, Li YH, Cromwell J (1967) Radium-226 and radon-222: concentration in Atlantic and Pacific Oceans. Science 158:1307–1310

Broecker WS, Cromwell J, Li YH (1968) Rates of vertical eddy diffusion near the ocean floor based on measurements of the distribution of excess Rn-222. Earth Planet Sci Lett 5:101–105

Burnett WC et al (2006) Quantifying submarine groundwater discharge in the coastal zone via multiple methods. Sci Total Environ 367:498–543

Cable JE, Bugna GC, Burnett WC, Chanton JP (1996) Application of Rn-222 and CH_4 for assessment of groundwater discharge to the coastal ocean. Limnol Oceanogr 41:1347–1353

Charette M, Morris P, Henderson P, Moore WS (2015) Radium isotope distributions during the US GEOTRACES North Atlantic Cruises. Mar. Chem. 177:184–195

Chung Y-C (1974a) Radium-226 and Ra-Ba relationships in Antarctic and Pacific waters. Earth Planet Sci Lett 23:125–135

Chung Y-C (1974b) Transient excess radón profiles in Pacific bottom wáter. Earth Planet Sci Lett 21:295–300

Chung Y, Kim K (1980) Excess Rn-222 and the benthic boundary layer in the western and southern Indian Ocean. Earth Planet Sci Lett 49(2):351–359

Colbert SL, Berelson WM, Hammond DE (2008) Radon-222 budget in Catalina Harbo, CA 2: Flow dynamics and residence time in a tidal beach. Limnol Oceanogr 53:659–665

Colman JA, Armstrong DE (1987) Verticale eddy diffusivity determined with Rn-222 in the benthic boundary-layer of ice-covered lakes. Limnol Oceanogr 32(3):577–590

Cochran JK (1992) The oceanic chemistry of the uranium- and thorium-series nuclides. In: Ivanovich M, Harmon RS (eds) Uranium-series disequilibrium, 2nd edn. Publications, Oxford Science, pp 334–395

Cook PG, Favreau G, Dighton JC, Tickell S (2003) Determining natural groundwater influx to a tropical river using radon, chloroflurocarbons and ionic environmental tracers. J Hydrol 277:74–88

Elsinger RJ, Moore WS (1983) Gas exchange in the Pee Dee River based on Rn-222 evasion. Geophys Res Lett 10:443–446

Emerson S (1975) Gas exchange rates in small Canadian Shield lakes. Limnol Oceanogr 20(5):754–761

Emerson S, Broecker WS, Schindler DW (1973) Gas exchange rates in a small lake as determined by the radon method. J Fish Res Bd Can 30:1475–1484

Glover DM, Reeburgh WS (1987) Radon-222 and radium-226 in southeastern Bering Sea shelf waters and sediment. Cont Shelf Res 7(5):433–456

Hammond DE, Fuller C (1979) The use of Rn-22 to estimate benthic exchange and atmospheric exchange rates in San Francisco Bay. In: San Francisco Bay: the urbanized estuary, pp 213–30. California Academy of Science, San Francisco

Hammond DE, Simpson HJ, Mathieu G (1977) Radon 222 distribution and transport across the sediment-water interface in the Hudson River estuary. J Geophys Res 82(27):3913–3920

Hammond DE, Fuller CC, Harmon D et al (1985) Benthic fluxes in San Francisco Bay. Hydrobiologica 129:69–90

Hartman B, Hammond DE (1984) Gas exchange rates across the sediment-water interfaces in south San Francisco Bay. J Geophys Res 89:3593–3603

Huh C-A, Kadko DC (1992) Marine sediments and sedimentation processes. In: Ivanovich M, Harmon RS (eds) Uranium-series disequilibrium, 2nd edn. Publications, Oxford Science, pp 460–486

Huh C-A, Ku TL (1984). Radiochemical observations on manganese nodules from three sedimentary environments in the north Pacific. Geochim Cosmochim Acta 48:951–63

Imboden DM, Emerson S (1978) Natural radon and phosphorus as limnologic tracers: horizontal and vertical eddy diffusion in Greifensee. Limnol Oceanogr 23:77–90

Imboden DM, Joller Th (1984) Turbulent mixing in the hypolimnion of Baldeggersee (Switzerland) traced by natural radon-222. Limnol Oceanogr 29(4):831–844

Kadko DC, Rosenberg ND, Lupton JE, Collier RW, Lilley MD (1990) Chemical reaction rates and entrainment within the Endeavour Ridge hydrothermal plume. Earth Planet Sci Lett 99:315–335

Key RM, Guinasso NL, Schink DR (1979) Emanation of radon-222 from marine sediments. Mar Chem 7:221–250

Key RM, Moore WS, Sarmiento JL (1992) Transient tracers in the Ocean North Atlantic study final data report for 228Ra and 226Ra. Technical Report No. 92–2, Ocean Tracer Laboratory, Princeton University, Princeton, NJ

Krishnaswami S, Cochran JK (1978) Uranium and thorium series nuclides in oriented ferromanganese nodules: growth rates, turn over times and nuclide behavior. Earth Planet Sci Lett 40:45–62

Ku T-L, Luo SD (1994) New appraisal of Ra-226 as a large-scale oceanic mixing tracer. J Geophys Res 99:10255–10273

Ku T-L, Li YH, Mathieu GG, Wong HK (1970) Radium in the Indian-Antarctic Ocean south of Australia. J Geophys Res 75(27):5286–5292

Lewis WK, Whitman WC (1924) Principles of gas absorption. Ind Eng Chem 17:1215–1220

Martin WR, Banta GT (1992) The measurement of sediment irrigation rates: a comparison of the Br-tracer and ^{222}Rn/^{226}Ra disequilibrium techniques. J Mar Res 50:125–154

Peng T-H (1973) Determination of gas exchange rates across sea-air interface by the radon method. PhD thesis, Columbia Univ

Peng T-H, Takahashi T, Broecker WS (1974) Surface radon measurements in the North Pacific Ocean station Papa. J Geophys Res 79:1772–1780

Peng T-H, Broecker WS, Mathieu GG, Li Y-H, Brainbridge AE (1979) Radon evasion rates in the Atlantic and Pacific Oceans as determined during the GEOSECS Program. J Geophys Res 84:2471–2486

Roether W (1983) Field measurement of air-sea gas transfer–methodical search. Bound-Layer Meteoro 27(1):97–103

Roether W, Kromer B (1978) Field determination of air-sea gas-exchange by continuous measurement of Rn-222. Pure Appl Phys 116(2–3):476–485

Rosenberg ND, Lupton JE, Kadko D, Collier R, Lilley MD, Pak H (1988) Estimation of heat and chemical fluxes from a seafloor hydrothermal vent field using radon measurements. Nature 334:604–607

Rudnicki MD, Elderfield H (1992) Helium, radon and manganese at the TAG and Snakepit hydrothermal vent fields, 26° and 23° N Mid-Atlantic Ridge. Earth Planet Sci Lett 113:307–321

Sarmiento JL, Broecker WS (1980) Ocean floor Rn-222 standing crops in the Atlantic and Pacific Oceans. Earth Planet Sci Lett 49:341–350

Sarmiento JL, Rooth CGH (1980) A comparison of vertical and isopycnal mixing models in the deep sea based on radon 222 measurements. J Geophys Res 85(C3):1515–1518

Sarmiento JL, Feely WH, Moore WS, Bainfridge AE, Broecker WS (1976) The relationship between vertical eddy diffusion and buoyancy gradient in the deep sea. Earth Planet Sci Lett 32:357–370

Sarmiento JL, Broecker WS, Biscaye PE (1978) Excess bottom radon 222 distribution in deep ocean passages. J Geophys Res 83(10):5068–5076

Smethie WM Jr, Takahashi T, Chipman DW, Ledwell JR (1985) Gas exchange and CO_2 flux in the tropical Atlantic Ocean determined from ^{222}Rn and pCO_2 measurements. J Geophys Res 90:7005–7022

Trier RM, Broecker WS, Feely HW (1972) Ra-228 profile at second GEOSECS Intercalibration Station, 1970, in North Atlantic. Earth Planet Sci Lett 16(1):141. doi:10.1016/0012-821X(72)90249-X

Wanninkhof R (1992) Relationship between gas exchange and wind speed over the ocean. J Geophys Res 97(C5):7373–7381. doi:10.1029/92JC00188

Wanninkhof R, McGillis W (1999) A cubic relationship between air-sea CO_2 exchange and wind speed. Geophys Res Lett 26(13):201–291. doi:10.1029/1999GL900363

Wanninkhof R, Asherm WE, Ho DT et al (2009) Advances in quantifying air-sea gas exchange and environmental forcing. Ann Rev Mar Sci 1(1):213–244

Yeung LY, Berelson WM, Hammond DE, Prokopenko MG, Wolfe C, Rollins N (2015) Upper-ocean gas dynamics from radon profiles in the Eastern Tropical South Pacific. Deep-Sea Res I 99:35–45. doi:10.1016/j.dsr.2015.01.008

Young Y, Kim K (1980) Excess ^{222}Rn and the benthic boundary layer in the western and southern Indian Ocean. Earth Planet Sci Lett 49:351–359

Chapter 7
Progeny of Radon (^{210}Pb) as a Tracer and Chronometer in Continents and Aqueous Systems

7.1 Introduction

One of the most widely used progeny of radon is ^{210}Pb, which is utilized as both a chronometer and a tracer. Most of the aspects pertaining to the applications of radon as a tracer in the earth's sub-systems are discussed in several other chapters, and application of ^{210}Pb as a tracer and chronometer is discussed in this chapter. Its particle-reactive nature in both freshwater and marine systems, as well as its suitable half-life for chronological reconstruction of contaminants and other environmental changes in both freshwater and coastal marine systems (over a time scale of 100–120 years) makes ^{210}Pb an extremely powerful chronometer. Recent search in Scopus (www.scopus.com) with the key words "sediment" AND "^{210}Pb" yielded 2,616 results which include 2,273 articles, 155 conference papers and 33 review articles. This can be compared to a search on key words "^{14}C dating," which yielded 10,977 results (search was conducted on 11 December 2015). Thus, ^{210}Pb is the most-widely utilized isotope after ^{14}C as a chronometer. (Note that these two radioisotopes cover different time scales—^{14}C is utilized as a chronometer in different branches of studies that include archaeology, anthropology, dating of sediments in lakes, oceans, etc for the past $\sim$ 50 ky while ^{210}Pb is primarily used as chronometer confined to the last 100–120 years).

In the decay chain of ^{238}U, the longest-lived isotope between ^{226}Ra (half-life: 1,600 years) and ^{210}Pb (half-life: 22.3 years), is ^{222}Rn (half-life: 3.82 days). In rocks and minerals, ^{226}Ra and ^{210}Pb are expected to be in secular equilibrium, but the diffusional behavior of noble gas daughter ^{222}Rn could result in disequilibrium between ^{222}Rn and ^{210}Pb. A fraction of the radon produced in surface oils, rocks, minerals and surface waters escapes to the atmosphere where it undergoes radioactive decay and eventually becomes ^{210}Pb. The short-lived decay products of radon (^{218}Po: $T_{1/2}$ = 3.10 min; ^{214}Pb: $T_{1/2}$ = 26.8 min; ^{214}Bi: $T_{1/2}$ = 19.7 min; ^{214}Po: $T_{1/2}$ = 0.164 ms) are all heavy metal atoms and are charged, and hence they quickly (compared to the mean-lives of these nuclides) attach to the surfaces

of aerosols and dust particles. During precipitation (rain, snow, etc.), the ^{210}Pb is removed by rainout and washout from the atmosphere, reaches the Earth's surface, and accumulates in surface soils or in accreting media such as glaciers, peat bogs, and eventually in lake and marine sediments (Fig. 7.1). Simply stated, the diffusion of radon out of the Earth's crust results in horizontal redistribution of its decay products. As a result of this process, the surface layers of land, oceanic water column and snow/ice fields contain higher activities of ^{210}Pb than that expected from equilibrium with ^{226}Ra (or ^{222}Rn in surface ocean). The atmospherically-delivered ^{210}Pb in the surface waters of lakes and coastal ocean are quantitatively removed by scavenging onto particulate matter in the water column where the residence time of dissolved ^{210}Pb is of the order of a month or less (e.g., Baskaran and Santschi 1993; Jweda et al. 2008). Under such circumstances, ^{210}Pb-laden particulate matter settles down on the surficial sedimentary layer. The succeeding layers of ^{210}Pb-laden sedimentary layers of material are buried by later deposits, and the rate of exponential decay is used to obtain chronology.

There are two sources of ^{210}Pb to the recently deposited (<120–150 years) sediments. The fraction of the total ^{210}Pb which is in equilibrium with ^{226}Ra activity is known as "supported ^{210}Pb," and will remain essentially constant in the time scale of ^{210}Pb's utility. The activity of ^{210}Pb in excess of the equilibrium activity is known as 'unsupported' (not supported by parent ^{226}Ra in the time scale of ^{210}Pb) or also known as "excess," (^{210}Pb$_{xs}$) which undergoes radioactive decay with its half-life. It is this excess ^{210}Pb component (sometimes referred as fallout ^{210}Pb, as there is very little supported ^{210}Pb falling from the atmosphere compared to atmospheric ^{222}Rn-derived ^{210}Pb) that provides the basis for major tracer and chronometer applications. Although the ^{210}Pb atmospheric depositional flux is essentially continuous, (mainly in areas where there is year-around precipitation) because of the continuous exhalation of ^{222}Rn from the earth's surface reaching the atmosphere, weekly, monthly and seasonal variations of atmospheric depositional fluxes have been widely reported (Chap. 5, Baskaran et al. 1993; Du et al. 2015) (Table 7.1).

Applications of ^{210}Pb as a chronometer are useful for a large spectrum of researchers that include biologists, paleoecologists, limnologists, geochemists, speleologists, atmospheric chemists, etc. The initial geochronological work with

Table 7.1 Summary of the main excess ^{210}Pb-based models for sediment radiometric dating

Model	Analytical solutions	Some references
CRS: Constant Rate of Supply	$\Sigma(m) = \Sigma_0 \exp(-\lambda t)$	Appleby and Oldfield (1978)
CIC: Constant Initial Concentration	$A(m) = A_0 \exp(-\lambda t)$	Robbins and Edgington (1975), Robbins (1978)
CF-CSR: Constant flux and Constant Sedimentation Rate	$A(m) = A_0 \exp(-\lambda m/w); t = m/w$	Krishnaswamy et al. (1971), Smith and Walton (1980)
CF-CS-Constant Diffusion	$A(m) = \frac{\phi}{w - k_m \beta} \exp(\beta m); \beta = \frac{w - \sqrt{w^2 + 4\lambda k_m}}{2k_m}$	Robbins (1978), Laissaoui et al. (2008)

[210]Pb on permanent snowfields was reported by Goldberg (1963). He reported that the results obtained using ^{210}Pb were found to be in agreement with those derived from stratigraphic evidence. Subsequently, this method was applied successfully to the dating of Antarctic ice sheets (Crozaz et al. 1964; Crozaz and Langway 1966). Applications of ^{210}Pb as a dating tool for the dating of recently deposited sediments started in the early 1970s (Krishnaswamy et al. 1971; Koide et al. 1972) and have been utilized to date sedimentary deposits from a range of environments including lakes, rivers, reservoirs, flood plains, wetlands, estuaries and coastal marine environments, permitting sedimentation rate determination over the past 100–120 years. Disequilibrium between ^{210}Pb and [226]Ra has also been extensively utilized to date both biogenic and inorganic carbonates including corals (Baskaran and Krishnamurthy 1993), mollusk shells, otoliths, fish bones, speleothems, inorganic carbonates formed under concrete bridges and whale falls (see in-depth review paper by Baskaran 2011a). These materials hold signatures of the history of climatological, environmental and chemical changes that have taken place in various earth systems such as lakes, rivers, oceans, karsts and other terrestrial environments from which the materials form (Baskaran and Iliffe 1993; Krishnamurthy et al. 2003; Baskaran et al. 2005; Baskaran 2011a). In particular, recently grown deep-sea corals could be used for understanding the penetration of anthropogenic substances into the ocean including transient tracers (such as Pu), as well as paleo-circulation changes in the deep sea on decadal and sub-decadal time scales (Druffel et al. 1990). Surface water corals could be utilized as archives to retrieve seasonal and inter-annual variations of temperature and salinity. Molluskan shells are ubiquitous and are common in freshwater and marine systems. Reliable dating of these shells coupled with measurements of geochemical parameters (e.g., stable isotopes, concentrations of minor and trace elements) will aid in the reconstruction of paleo-environmental changes and pollution histories over the past 100–120 years. Cave deposits are also ubiquitous and have been widely utilized as proxies for reconstructing paleoclimate and paleo-environmental changes. Recent cave deposits (<150 years) have the potential to reconstruct elements of climate such as temperature and amount of precipitation (Baskaran and Krishnamurthy 1993; Tanahara et al. 1997; Ku and Li 1998; Woo et al. 2005). Retrieval of these paleo-records requires precise chronology.

Applications of ^{210}Pb as a tracer to assess rates and patterns of soil redistribution and for tracing sediment movement in terrestrial and aquatic environment were started in mid-1990s (Walling and He 1999; Wallbrink and Murray 1996). A recent review on the use of ^{210}Pb as a tracer of soil and sediment movement in terrestrial environment, including both the land surface and surface waters, are given in Mabit et al. (2014).

In this chapter, ^{210}Pb as a tracer for soil erosion studies and as a chronometer in freshwater (lakes, reservoirs and rivers) and coastal marine systems are discussed. Furthermore, use of ^{210}Pb as a tracer of sediment focusing and sediment mixing in aqueous systems along with importance of scavenging in marine environment is also presented (Fig. 7.1).
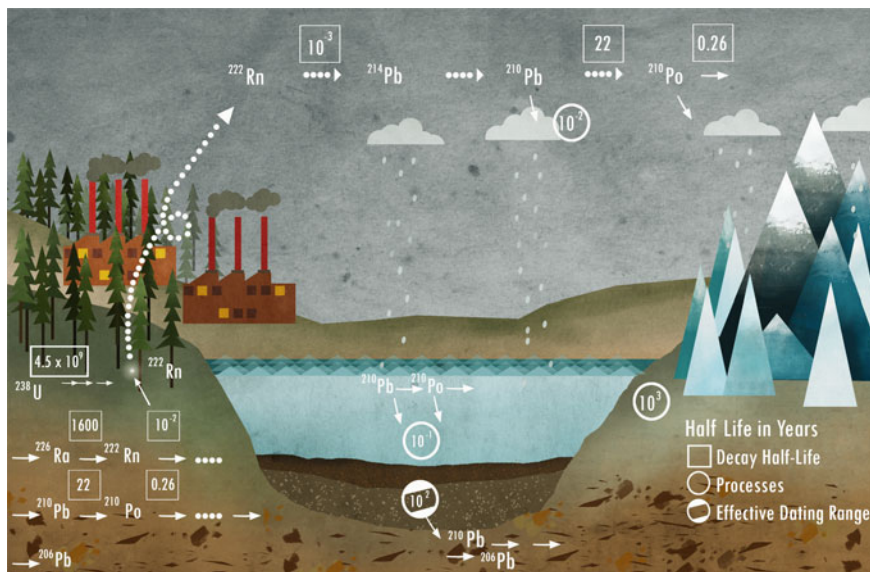
Fig. 7.1 Radon released from earth surface embarks on its journey in the atmosphere and undergoing radioactive decay through four short-lived radionuclides (^{218}Po, ^{214}Pb, ^{214}Bi, ^{214}Po) before the production of ^{210}Pb

7.2 Geochemical Behavior of ^{210}Pb in the Environment

To utilize ^{210}Pb as a soil erosion tracer, the major requirement is that it is highly particle-reactive with $K_d \geq 10^5$ cm^3 g^{-1}, and soil redistribution is tagged by the associated soil-particle-bound ^{210}Pb. This behavior of soil Pb (strong binding to soil particles, both mineral particles and soil organic matter) is the founding principle upon which this method relies. The major processes that redistribute the soil particles in a landscape are mechanical processes such as movement of water, wind and tillage erosion. Lead has the highest K_d values (=concentration in solid phase/concentration in solution phase) compared to alkaline and transition elements (Mg, Sr, Co, Zn, Ni, Cd, Cr(III), and Cu; Welp 1999). The sorption of Pb increases with increasing pH. Relative to ^{137}Cs sorption, generally ^{210}Pb has stronger affinity on to soil particles, although Cs has higher affinity for inter-layered clay minerals such as illite (e.g., Klaminder et al. 2006). ^{210}Pb also binds strongly with oxy-hydroxides of Fe and Mn and has strong affinity with organic matter at acidic pH (Dorr 1995; Gustafsson et al. 2011). Because of the geochemical behavior of Pb in the environment, the post-depositional redistribution of ^{210}Pb in a landscape is due to soil/sediment erosion and disturbance as well as transport processes.

7.3 Variations in the Source Term of Unsupported ^{210}Pb in the Environment: Inter-annual Atmospheric Depositional Fluxes of ^{210}Pb

The major source of unsupported ^{210}Pb in the environment is the atmospheric deposition. It has been well documented that the atmospheric deposition of ^{210}Pb in any region is primarily governed by meteorological parameters and is generally constant when averaged over several years (expected to be less than ±5 % averaged over the mean-life of ^{210}Pb, 32 years; summarized in Baskaran 2011b). However, the inter-annual variations of depositional flux at any given site are much less compared to sub-annual time-scale variations. Such inter-annual variations are primarily caused by the changes in the amounts of precipitation (Chap. 5). While short-term variations such as monthly or seasonal variations will likely be smoothed out in sedimentary records, annual variations could be preserved at least in some of the accreting environment. Due to temporal variabilities in the atmospheric deposition of ^{210}Pb, soil erosion rates and changes in ^{210}Pb fluxes require averaging over time intervals of one to a few years (perhaps 4–6 years, as the average fallout over 6 years is reported to be <±10 %) and hence all erosion studies can only yield a time resolution of 6 years or more.

7.4 Applications of ^{210}Pb

7.4.1 ^{210}Pb as a Tracer for Soil Erosion Studies

The principle behind the application of ^{210}Pb as a soil erosion tracer is the comparison of the measured total inventory in an area to the inventory of an undisturbed site or 'reference site.' The erosional index, ε, is given by:

$$\varepsilon = I_{Pb-M}/I_{Pb-B} \tag{7.1}$$

where I_{Pb-M} is the measured total ^{210}Pb$_{xs}$ inventory over a region (Bq m^{-2}) and I_{Pb-B} is the cumulative inventory of atmospheric fallout in the region (=average annual fallout (Bq m^{-2} y^{-1}) * mean-life of ^{210}Pb, 32.2 years (=22.3 year/0.693)).

The measured inventory of ^{210}Pb$_{xs}$ (I, in units of Bq m^{-2}) at a point on earth can be expressed as:

$$I = \int_{-z}^{0} C\rho dz \tag{7.2}$$

where z is the depth in the soil to which atmospherically-delivered ^{210}Pb has penetrated (from the surface), 0 is the soil surface, C is the activity of ^{210}Pb$_{xs}$ derived from atmospheric fallout (in Bq kg^{-1}) in the ith layer, and ρ is the soil

density (kg m^{-3}). In practice, this is measured by collecting samples with sampling depth resolution (dz) on the order of 20–30 cm. The inventory I at a location is governed by ^{210}Pb deposition, which is a function of the amount of precipitation and location of the site (latitude, longitude and altitude), particulate losses, and solute losses. Inventories can be used to find if the sampling location is stable with non-eroding surfaces over a period of ~100 years. With combined measurements of ^{210}Pb and ^{10}Be, one can cover a much longer time-scale.

In Eq. 7.1, if ε is less than 1, then it is likely that erosion could have occurred in <~100 years and if ε is greater than 1 then, net soil accumulation could have taken place in less than the past ~100 years. Since ^{210}Pb is useful as a tracer for a time period of 4–5 times the length of its half-life (~100 years), use of an appropriate conversion estimation method will aid in the quantification of soil erosion or deposition rate (in tons per hectare per year, t ha^{-1} y^{-1}). Similar methods have been utilized with other fallout radionuclides, ^{137}Cs, ^{239,240}Pu and ^{10}Be (^{137}Cs: Ritchie and McHenry 1990; ^{10}Be: Pavich et al. 1986; and ^{239,240}Pu: Everett et al. 2008; Xu et al. 2013). A comparison of ^{137}Cs-based erosion rates are plotted against ^{210}Pb$_{xs}$-based erosion rates in Fig. 7.2 (Mabit et al. 2014)."

Since the basic approach of estimating soil erosions rates obtained using ^{210}Pb$_{xs}$ and other particle-reactive radionuclides (^{137}Cs, ^{239,240}Pu, ^{7}Be and ^{10}Be) is similar (basically comparing the measured inventory to the expected fallout inventory), the combined use of other nuclides offers considerable potential to investigate the erosional history of a study site and increases the confidence in the results obtained. For example, the measurement of ^{210}Pb in conjunction with another short-lived particle-reactive radionuclide, such as ^{7}Be, on hillslopes after a significant storm can be used to trace event-scale soil sediment redistribution (Kaste and Baskaran 2011). If ^{210}Pb as a sediment tracer is used to track longer timescales and compared to ^{7}Be distribution from a single, intense storm, the soil movement can be put into perspective with processes operating over the course of years to decades (Walling et al. 1999). Meteoric ^{10}Be (T$_{1/2}$ = 1.4 ma) has great potential for quantifying soil and sediment transport processes and authigenic mineral formation rates on soil-mantled hillslopes (e.g. Willenbring and von Blanckenburg 2010a, b). Investigations on the loss and accumulation of ^{10}Be combined with ^{210}Pb over different points of a landform can be used to study how sediment transport processes control the fate and storage of carbon on a hillslope (Harden et al. 2002).

7.4.2 Sediment Focusing and Erosion Using ^{210}Pb as a Tracer

Integrated ^{210}Pb$_{xs}$ inventories from sediment cores can be used to determine sediment focusing factors (F_f^i) by comparing the measured and expected radionuclide inventories in each core:

$$F_f^i = \frac{I_m^i}{I_{ex}^i} \tag{7.3}$$

where (I_{ex}^i) is the expected inventory (from fallout + production from ^{226}Ra in the water column) of ^{210}Pb$_{xs}$ (Bq m^{-2}). Focusing factors of >1 are indicative of sediment focusing, which can be due to the movement of fine-grained sediments as a result of local currents and/or bottom sediment movements (e.g., Blais and Kalff 1995; Wong et al. 1995). From a recent study on seven sediment cores from Lake St. Clair and Clinton River in southeast Michigan, it has been reported that the focusing factors ranged from 0.73 to 8.37 (GM: 1.99) for ^{210}Pb$_{xs}$ and typically higher values were found in the river relative to the lake (Jweda and Baskaran 2011). In ocean margin sediments, the ^{210}Pb inventories were found to be higher than those expected from the direct atmospheric deposition + production from ^{226}Ra [measured inventory/(production of ^{210}Pb from atmospheric decay + production from ^{226}Ra) ratio of 0.69–1.63] and were attributed to boundary scavenging and sediment focusing due to local bottom currents (e.g., higher inventories of ^{210}Pb in bottom sediments in the Gulf of Mexico Baskaran and Santschi 2002). Advective transport of dissolved nuclides to regions of high productivity waters in the margins resulted in higher suspended particle concentrations and fluxes, which result in enhanced scavenging of ^{210}Pb (and other particle-reactive nuclides). Furthermore, particle composition (such as opal Si, Fe–Mn oxides, carbonate and terrigenous material such as clays) also plays a significant role on the scavenging of dissolved ^{210}Pb.

7.4.3 ^{210}Pb as a Tracer of Ice Rafted Sediments (IRS) in the Arctic Ocean

Activities of ^{210}Pb in ice-rafted sediments (IRS) in the seasonal ice-cover of the Arctic Ocean have been reported to be relatively high (Baskaran 2005; Masque et al. 2007). When sea ice is formed (mostly in shallow waters in the marginal seas of the Arctic Ocean such as Siberian margins of the Laptev, Kara and Barents Seas), large amounts of fine-grained sediments get incorporated into the sea ice during formation of new ice mainly through suspension freezing of bottom sediments and river-borne sediments. This ice is subsequently transported to different parts of the Arctic. During its transit, atmospherically-delivered ^{210}Pb is intercepted by the ice cover and the ^{210}Pb is added to the IRS during freezing-thawing cycles. The activities of ^{210}Pb in IRS have been reported to be highly variable, with values ranging between 13 and 212 Bq kg^{-1}, which is 1–2 orders of magnitude higher than those reported in the coastal sediments (average: 31.7 Bq kg^{-1}, n = 134, Baskaran 2005). Although there is no published data for melt ponds, the activities are expected to be higher compared to the surface ocean waters. During summer, the snow and upper 0.3 to 0.7 m of the ice melt off of the ice surface. Tracer studies

indicate that meltwaters disperse over distances of tens of meters on the time scale of days, with much of the meltwater pooling in depressions at the surface (Cooper et al. 1991; Eicken et al. 2002). IRS accumulates at the surface and in melt pools and are subjected to meltwater flushing (Eicken et al. 2002). During this process, the IRS released from melting comes in contact with seawater in melt ponds and additional scavenging may take place. Based on controlled experiments, it has been estimated that ∼ 15 % of the total sediment load is released to the water column during melt (Eicken et al. 2002). During multiple freezing-thawing cycles, the IRS is often pelletized and thus, can undergo sinking very quickly. Cooper et al. (2005) reported presence of ^{7}Be in benthic surface sediments collected from as deep as 945 m in Barrow Canyon in the Arctic, but it has not been reported from any other ocean basins. It is likely that the pelletized sediments enriched in ^{210}Pb are released sporadically during freezing-thawing cycles and can result in variations in the ^{210}Pb depositional flux at the sediment-water interface, although no studies have been conducted to document this speculation.

7.4.4 ^{210}Pb as a Geochronometer

Reconstruction of environmental changes such as sedimentation and erosion rates, surface water acidification, eutrophication and trace-metal/radionuclide/organic pollutant contamination requires a reliable chronology. The use of ^{210}Pb to determine modern sedimentation rates began with the study of dating of lake sediments by Krishnaswamy et al. (1971) and coastal marine sediments by Koide et al. (1972).

When sedimentary particulate matter undergoes settling from the water column after scavenging of dissolved ^{210}Pb, it becomes part of the sedimentary record, although a large portion of the sedimentary material can undergo remineralization before their eventual burial. When succeeding layers of sedimentary material are buried by later deposits, the fallout ^{210}Pb incorporated in a given layer decreases exponentially with time following the radioactive decay law. When the annual deposition of the mass of sedimentary particulate matter and activity of ^{210}Pb remain constant, then, the exponential decrease of excess ^{210}Pb activity with depth can be utilized to determine the mass accumulation rate and this method is commonly known as the "constant flux: constant sedimentation" (CFCS) method. We get one value for the mass accumulation rate for the whole core covering a time scale of ∼ 120 years. This is also the widely used methodology to obtain the mass accumulation rate (usually the mass depth is plotted against the natural logarithm of the excess ^{210}Pb; the slope * decay constant = mass accumulation rate (g cm^{-2} y^{-1}); or linear sedimentation rate is obtained from the slope of the linear best-fit-line when linear depth is plotted against the natural logarithm of the excess ^{210}Pb (=the slope * decay constant = linear sedimentation rate (cm y^{-1})). This method generally works well in lakes where there is no major post-depositional movement of sedimentary material, there is no major current to redistribute the sedimentary material near sediment-water interface and there is no temporal variations of sediment flux

from anthropogenic activity. Note that there is compaction of sediments in a core and hence it is highly recommended to determine the mass accumulation rates rather than the linear sedimentation rates. There could be a finite amount of mixing in surficial sediments, as observed from the activities of ^{210}Pb$_{xs}$ in the upper ~ 4 cm (Jweda and Baskaran 2011) and hence the mass accumulation rates refer to apparent mass accumulation rates, as apparent rates do not delineate sediment accumulation rates from mixing rates.

In reality, a typical vertical profile of ^{210}Pb$_{xs}$ in a sediment core is result of a number of factors and processes. The primary factors include variations in the mass flux of sediment particles and variations in the atmospheric flux of ^{210}Pb (mainly due to variations in the amount of annual precipitation and in some cases, sources of air masses). The secondary factors include variations in the extent of remineralization of particles downcore and variations in the additional input of ^{210}Pb derived from ^{222}Rn (and ^{226}Ra) decay during submarine groundwater discharge.

The exponential decrease in ^{210}Pb$_{xs}$ activity can be due to radioactive decay plus sedimentation alone, or uniform diffusive mixing alone or some combination of these two (e.g., Baskaran et al. 2014—replot of ^{210}Pb from a deep-sea sediment core shows that the apparent ^{210}Pb sedimentation rate can be 24–80 times higher than that of long-term sedimentation rate obtained using ^{14}C). Therefore, it is mandatory to have independent validation of ^{210}Pb-based chronology (Smith 2001; Baskaran et al. 2014). Such independent methods include peak of ^{137}Cs corresponding to 1963 from the global fallout or 1986 peak fallout from the Chernobyl accident in certain parts of Europe; varves, known contaminant inputs (e.g., mercury mining impact in a watershed, Baskaran et al. 2014) or record of known natural episodic events), or penetration depths (and peak) of ^{239,240}Pu (or ^{137}Cs) in sedimentary layer corresponding to 1952 (e.g., Ravichandran et al. 1995). Note that 86 % of the ^{137}Cs introduced to the environment in 1952 has decayed away by year 2016 and hence the detection of ^{137}Cs corresponding to 1952 is becoming more challenging. Diffusion of ^{137}Cs in freshwater sedimentary systems has also been widely reported e.g., (Evans et al. 1983; Davis et al. 1984; Comans et al. 1989) and post-depositional downward migration of ^{137}Cs in sedimentary layers will result in an overestimation of sedimentation rates based on the introduction of ^{137}Cs in the environment in 1952.

There are a number of model-dependent methods available for the ^{210}Pb$_{xs}$ dating (Sanchez-Cabeza and Ruiz-Fernandez 2012; Mabit et al. 2014). In the CFCS model, it is assumed that the system is in steady state with a constant accumulation of sediments and a constant supply of ^{210}Pb$_{xs}$. The ^{210}Pb$_{xs}$ activity (A_x) at depth 'x' can be calculated from the equation:

$$A_x = A_o e^{-\lambda_{Pb} t} \tag{7.4}$$

where A_x and A_o are the activities of ^{210}Pb$_{xs}$ in a sediment layer at depth 'x' (cm) and at the surface layer (initial activity), respectively, and t is the age (year) of the sediment layer at depth 'x.' The mass accumulation and linear sedimentation rates can be determined using this method. Sediment layer ages (year) based on the CFCS model can be determined from the equation:

$$t_{CFCS} = M/w_{Pb} \tag{7.5}$$

where M is the cumulative mass depth at a given sedimentary layer (g cm^{-2}) and ω_{Pb} is the mass accumulation rate (g cm^{-2} y^{-1}).

A large number of studies over the past 4 decades on the dating of lacustrine sediments have been conducted. Results on the consistency check of ^{210}Pb-based chronology with another independent geochronological marker are mixed. While it is not the scope of this book to review all the literature on ^{210}Pb dating of sediments, it is relevant to show case studies where ^{210}Pb chronology agree and do not agree with other independent methods (e.g. ^{137}Cs-based method or historical marker such as metal contamination history). For example, the sediment mass accumulation rate (MAR) obtained for the CFCS model (0.66 g cm^{-2} y^{-1}) is in close agreement with the ^{137}Cs-peak based mass accumulation rate (0.65 g cm^{-2} y^{-1}) in Weber Dam, Michigan (Fig. 7.3). In the case of ^{137}Cs, it is assumed to correspond to the peak fallout year of 1963 and the accumulation rates are assumed to be constant over the whole core (or at least up to the penetration depth of ^{137}Cs), similar to the assumption with CFCS model on the vertical profiles of ^{210}Pb$_{xs}$ (Fig. 7.3).

An inter-comparison of ^{210}Pb$_{xs}$-based MAR to that of ^{137}Cs-peak corresponding to 1986 Chernobyl event in a sediment core from Lake Middle Marviken, Sweden
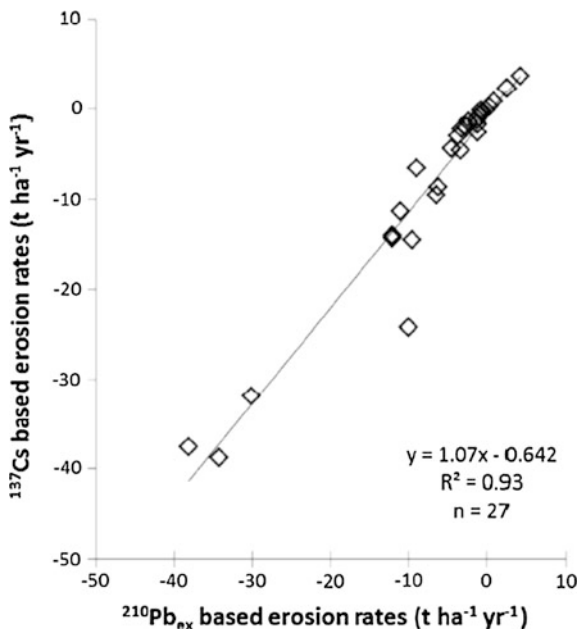
Fig. 7.2 Comparison of soil redistribution (erosion) rates obtained using ^{137}Cs and ^{210}Pb$_{xs}$-based methods (Figure is taken from Mabit et al. 2014—with permission from Elsevier Scientific Publishing Company, Amsterdam)
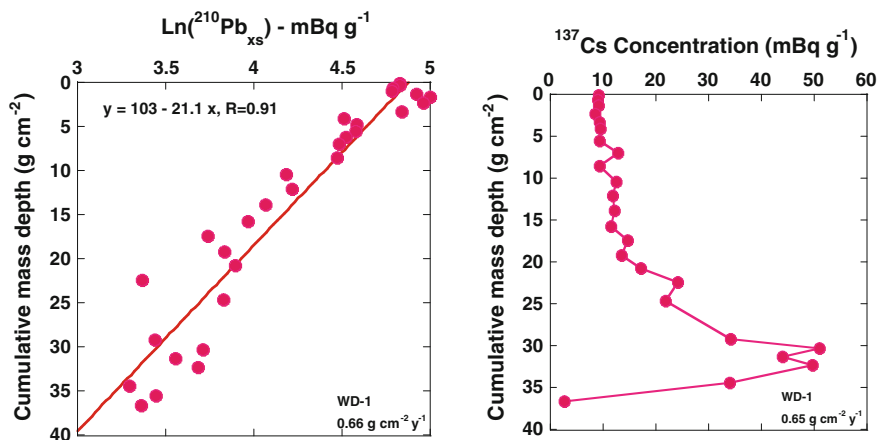
Fig. 7.3 Vertical profiles of Ln(^{210}Pb$_{xs}$) and ^{137}Cs activities in WD-1 (data from Kumar et al. 2016). The sediment accumulation rates obtaining ^{210}Pb$_{xs}$ and ^{137}Cs methods in Weber Dam in Michigan agree quite well

shows that the MARS obtained by these two methods differ by factor of 2 (Fig. 7.4). This discordancy was attributed to 2–4 times higher than the expected total inventory of ^{210}Pb$_{xs}$ in the dated sediment core. This higher inventory of ^{210}Pb$_{xs}$ was attributed to sediment focusing and possible production of ^{210}Pb from ^{222}Rn and ^{226}Ra-enriched submarine groundwater-discharge (Routo et al. 2007). Elevated levels of excess ^{210}Pb at bottom of cores in several reservoirs from the Midwestern United States have been observed (Baskaran, unpublished data). Another investigation from a highly-impacted watershed in southwestern Arkansas, USA indicates
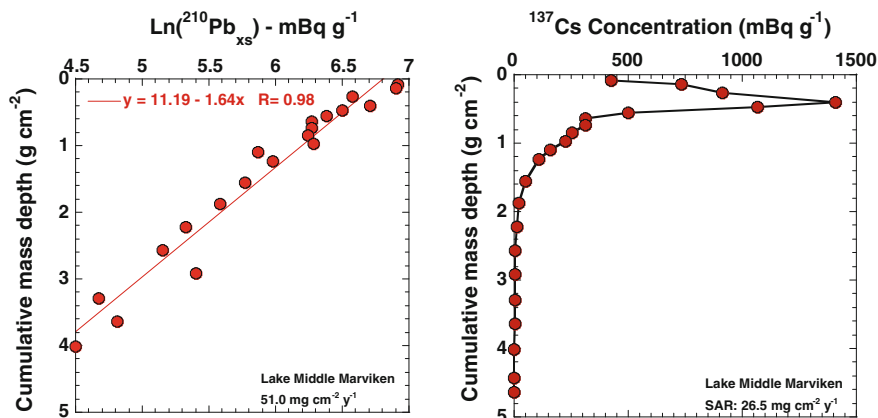
Fig. 7.4 Vertical profiles of Ln(^{210}Pb$_{xs}$) and ^{137}Cs activities of a sediment core Lake Middle Marviken, Sweden. ^{210}Pb$_{xs}$-based sediment accumulation rate is about 2 times higher that of ^{137}Cs-peak fallout from Chernobyl

Fig. 7.5a *Filled circle* vertical profile of measured ^{210}Pb$_{xs}$; *Open circle* calculated ^{210}Pb$_{xs}$ activity assuming constant initial ^{210}Pb$_{xs}$ concentration of 47.4 mBq g^{-1} at deposition and using ^{137}Cs-peak based sediment accumulation rate: *Open square* calculated ^{210}Pb$_{xs}$ activity at deposition using ^{137}Cs-based sediment accumulation rate of a core from Hendrix Lake, SE Arkansas, USA (from Baskaran et al. 2014)
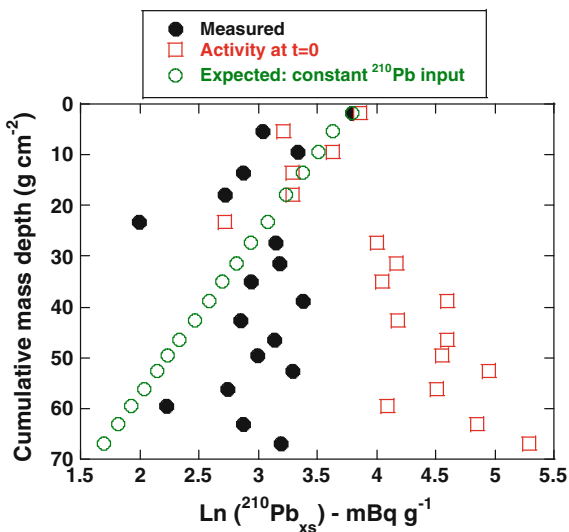
that there is no decrease in excess ^{210}Pb activity with depth while the ^{137}Cs vertical profile indicated sharp peak corresponding to 1963 and the ^{137}Cs penetration depth of ^{137}Cs corresponds to 1952 (Figs. 7.5a and 7.5b). Four independent evidences (two time marker events based on ^{137}Cs (peak corresponding to 1963 and penetration depth corresponding to 1952, Fig. 7.5) and two marker-events based on Hg mining activity Baskaran et al. 2014) result in about the same sedimentation rates, although ^{210}Pb$_{xs}$ does not decrease with depth. This sediment core could not be dated with any of the existing ^{210}Pb$_{xs}$ models.

If mass accumulation rates are variable (Appleby and Oldfield 1992), then sediment ages can be calculated using either: (i) the constant rate of supply (CRS) of the ^{210}Pb model or (iii) the constant initial concentration (CIC) model (Robbins and Edgington 1975; Oldfield et al. 1978; Robbins 1978; Appleby et al. 1979; Jweda and Baskaran 2011; Sanchez-Cabeza and Ruiz-Fernandez 2012;

Fig. 7.5b Vertical profile of ^{137}Cs in Hendrix Lake, southwestern Arkansas, USA (from Baskaran et al. 2014)
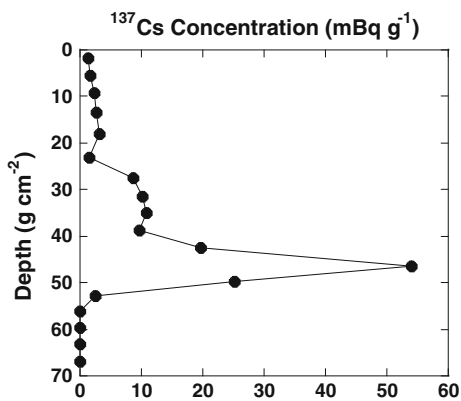
Bonotto and Garcia-Tenorio 2014). The CRS model assumes that there is a constant flux and efficient transfer of ^{210}Pb$_{xs}$ from the water to surficial sediments. In coastal areas and shallow freshwater systems where suspended particle concentrations and fluxes are high, the transfer of ^{210}Pb from the water column to the sediments is very efficient. This results in a constant rate of supply to the accreting sedimentary layer even if the sediment accumulation rate varies over time. In the CRS model, the initial ^{210}Pb$_{xs}$ activity varies inversely with the sediment accumulation rate and is given by:

$$\sum A_m = \left(\sum A_\infty\right)\left(1 - e^{-\lambda_{Pb}t}\right) \tag{7.6}$$

where $\sum A_m$ is measured ^{210}Pb$_{xs}$ inventory to mass depth m_i (Bq m^{-2}) and $\sum A_\infty$ is the total ^{210}Pb$_{xs}$ inventory of the sediment core. The age (year) of the sediment layer is calculated from the following equation:

$$t_{CRS} = -\frac{\ln\left(1 - \dfrac{\sum A_m}{\sum A_\infty}\right)}{\lambda_{Pb}} \tag{7.7}$$

The CIC model assumes a constant initial activity at the sediment-water interface regardless of changes in net accumulation. Since the ^{210}Pb$_{xs}$ transfer function is directly proportional to the mass flux, the CIC model should be better suited than the CRS model for systems dominated by erosional input (e.g., Jweda and Baskaran 2011). Sediment layer ages (year) based on the CIC model can be calculated from:

$$t_{CIC} = -\frac{\ln\left(\dfrac{A_M}{A_0}\right)}{\lambda_{Pb}} \tag{7.8}$$

where A_0 is the initial ^{210}Pb$_{xs}$ activity at the sediment-water interface (mBq g^{-1}) and A_M is the measured ^{210}Pb$_{xs}$ activity at the cumulative mass depth 'M'.

A comparison of ^{210}Pb$_{xs}$-based ages calculated using Eqs. (7.5), (7.7) and (7.8) are given on a sediment core from Weber Dam in Michigan, USA is illustrated in Fig. 7.6. The CFCS-based ^{210}Pb$_{xs}$ chronology agrees with the ^{137}Cs-peak based chronology (Figs. 7.3 and 7.6); however, there are large differences between the ages obtained based on CRS and CIC models compared to ^{137}Cs-peak based ages, indicating not all three models are useful for a given environmental setting. In areas where there are changes in sediment accumulation rates that have taken place, the CRS and CIC-based ages often differ, with CIC model-based ages almost always younger than dates calculated using the CRS model (Blais et al. 1995). There are often discrepancies between ^{210}Pb$_{xs}$-based ages and ^{137}Cs-based ages and such discrepancies were attributed to diffusion of Cs downward in soft water sediments, whereas hard water sediments act to effectively immobilize Cs (Blais et al. 1995). However, this observation is not consistently reported by other researchers. For example, Jweda and Baskaran (2011) reported agreement between ^{137}Cs-based

Fig. 7.6 Vertical profile of model ages of sediment layers obtained from ^{210}Pb$_{xs}$ (CF: CS, CIC, and CRS) and ^{137}Cs activities Weber Dam core WD-1
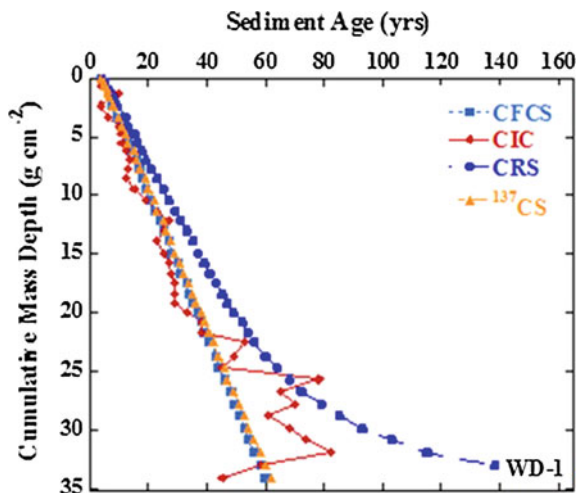
chronology and ^{210}Pb$_{xs}$-CFCS-model-based chronology in four out of five sediment cores from Lake St. Clair and Clinton River in southeast Michigan, USA, with less reliability using the CRS and CIC age models. More recent studies in two reservoirs from the Midwestern United States indicate that more than one ^{210}Pb$_{xs}$-based model may have to be applied to obtain chronology from multiple cores collected within one reservoir that agrees with the ^{137}Cs method and most post-depositional migration of ^{137}Cs has taken place in one core, but not in all cores (Kumar et al. 2016). More studies are needed to address under what conditions post-depositional mobility of Cs takes place and what ^{210}Pb$_{xs}$-based model is suitable under what conditions.

Utility of ^{137}Cs and ^{239,240}Pu peak method yields one curve fitting or mapping date assignment, although assignment of age from the ^{137}Cs or ^{239,240}Pu horizon (deepest level where activity can be detected) is possible. Plutonium (^{239,240}Pu) is more particle-reactive than ^{137}Cs in freshwater and marine setting and hence its mobility is restricted. There is virtually no decay of ^{239}Pu (half-life = 24,110 year) or ^{240}Pu (half-life = 6563 year) over the past 64 years ($\ll$1 %), since its first deposition in 1952. The peak of ^{239,240}Pu in undisturbed sedimentary column is well-preserved compared to ^{137}Cs, due to post-depositional diffusion of ^{137}Cs, and hence it is a preferable candidate (Ravichandran et al. 1995). However, the utility of all three, ^{210}Pb, ^{137}Cs and ^{239240}Pu to delineate sediment mixing and sediment accumulation rates would be preferable (Krishnaswami et al. 1980; Wan et al. 1987; Ravichandran et al. 1995).

7.4.5   Numerical Sediment Mixing Model

The upper portions of the sediment cores in many shallow water lakes (e.g., Lake St. Clair in southeast Michigan), often exhibit sediment-mixing features such as

subsurface ^{210}Pb$_{xs}$ activity peaks and smeared distributions of ^{210}Pb$_{xs}$ (and ^{137}Cs). It was pointed out that most sediment regimes in freshwater systems undergo mixing or bioturbation in the upper 4 cm, mainly as a result of the foraging and physiological activities of benthic organisms (Robbins and Edgington 1975). Mixed layers indicate possible post-depositional mobility of ^{210}Pb$_{xs}$ or active sediment mixing by physical or biological processes. The near-exponential decay of ^{210}Pb$_{xs}$ combined with sharp ^{137}Cs peaks in a large number of sediment cores indicate that although mixing processes were occurring, mixing rates were not significant enough to completely homogenize sediment deposits. Nevertheless, it may be necessary to evaluate the degree of mixing because variations in depths and rates of sediment mixing have been found to significantly influence trace metal concentration profiles and calculated contaminant accumulation rates (e.g., Ravichandran et al. 1995).

Mixing models have been utilized to incorporate post-depositional redistribution processes neglected by simple dating models. Those processes include: (i) physical mixing by sediment stirring, slumping or resuspension, (ii) bioturbation and biological mixing by burrowing organisms, (iii) post-depositional diffusive chemical mobility, and (iv) selective particle mixing based on particle composition or size (Baskaran and Naidu 1995; Benninger et al. 1979; Benoit and Hemond 1991; Crusius and Anderson 1991). The overall effect of these processes can be assessed by assuming that the distribution of ^{210}Pb$_{xs}$ was due to incomplete dynamic mixing analogous to eddy diffusion and that the vertical distribution of ^{210}Pb$_{xs}$ was given by the advection-diffusion equation (Benninger et al. 1979; Guinasso and Schink 1975; Krishnaswami et al. 1980; Robbins et al. 1977):

$$\frac{\partial A}{\partial t} = \frac{\partial}{\partial x}\left(K_b \frac{\partial A}{\partial x}\right) - s_{Pb}\frac{\partial A}{\partial x} - \lambda_{Pb}A_{Pb} \tag{7.9}$$

where K_b is the eddy-diffusive mixing coefficient (cm^2 year^{-1}), s_{Pb} is the linear sedimentation rate (cm year^{-1}), and A_{Pb} is the ^{210}Pb$_{xs}$ specific activity in a given sediment layer. The steady state solution to Eq. (7.9) with boundary conditions $A'(x) = A'_0$, $x = 0$ and $A' = 0$, $x = \infty$ is given by the equation:

$$A'(x) = A'_0 e^{\alpha x} \tag{7.10}$$

where A'_0 is the ^{210}Pb$_{xs}$ surficial activity, $A'(x)$ is the ^{210}Pb$_{xs}$ activity at depth 'x', and

$$\alpha = \frac{s_{Pb} \pm \sqrt{s_{Pb}^2 + 4\lambda K_b}}{2K_b} \tag{7.11}$$

where α is the slope of the line representing the decrease of ln(^{210}Pb$_{xs}$) with respect to cumulative mass depth.

The decadal time-scale average mixing coefficient (K_b) using ^{210}Pb$_{xs}$ for sediments can be determined assuming the following: (i) K_b has remained constant with depth; (ii) the ^{210}Pb$_{xs}$ activity profiles were in steady-state; and (iii) that $s_{Pb}^2 \ll 4\lambda K_b$

(Krishnaswami et al. 1980). With these assumptions, Eq. 7.11 can be simplified and then re-arranged to calculate K_b from the equation:

$$K_b = -\lambda/\alpha^2 \tag{7.12}$$

The mixing coefficient calculated using Eq. 7.12 in a freshwater lake is reported to vary widely. For example, the calculated mixing coefficients in Lake St. Clair has been reported to vary between 0.1 to 4.6 (Robbins et al. 1990; Jweda and Baskaran 2011) and can be compared to the values reported for other high energy environments such as the San Francisco Bay and the Yangtze River Estuary, which had mixing coefficients (calculated from excess ^{234}Th) up to 170 and 260 cm^2 year^{-1}, respectively (Fuller et al. 1999; McKee et al. 1984). The average values of K_b in the riverine sediments were reported to be generally higher than those for the lacustrine sediments. The higher mixing coefficients in the river were likely caused by highly frequent resuspension and physical stirring events that incrementally redistributed sediment grains along the river bottom. A potential constraint on K_b values based on the ^{210}Pb$_{xs}$ mixing model is the utilization of the cosmogenic radionuclide ^{7}Be. The presence of ^{7}Be to subsurface depths is a consequence of either very rapid sediment accumulation or mixing processes because of the short-lived (T$_{1/2}$ = 53.3 d) nature of the nuclide.

In the case of open-ocean sediments where the sedimentation rates are very low (1–10 cm ky^{-1}), most of the ^{210}Pb$_{xs}$ is expected to be confined to the upper <1 cm or so. However, a nice exponential decay of ^{210}Pb$_{xs}$ going to ∼10 cm or more is commonly found. For example, the long-term sedimentation rates in two cores collected from the deep-ocean in South Atlantic—Antarctic yielded 0.5–1.5 cm ky^{-1} while the calculated apparent ^{210}Pb$_{xs}$-based sediment rates (36–40 cm ky^{-1}) is more than an order of magnitude higher than that of long-term sedimentation rates. Thus, uniform sediment mixing or any combination of mixing and sedimentation could produce pseudo-exponential decay (DeMaster and Cochran 1982; Baskaran et al. 2014).

7.4.6 Residence Time Pb in the Oceanic Water Column

A number of studies have been reported for the distribution of ^{210}Pb in the oceanic water column (Craig et al. 1973; Cochran 1992). The residence time of total ^{210}Pb in the water column can be calculated based on a box-model approach. The major inputs to the box are: (i) atmospheric fallout (I_A^o) and (ii) the production from its grandparent, ^{226}Ra (λ_{Pb} A$_{Ra}$). The major outputs from the box are: (i) decay of ^{210}Pb (λ_{Pb} A$_{Pb}^T$) and (ii) its removal by scavenging (ψ_c^0 A$_{Pb}^T$). In this simple approach, additional sources/sinks (such as the advection, diffusion, etc.) have been assumed to be negligible. Supporting evidence for this assumption can be inferred from the measured sediment inventory of ^{210}Pb from a suite of sediment cores collected from the Gulf of Mexico. For example, Baskaran and Santschi (2002)

showed that the measured inventory in major fraction of the analyzed sediment cores is about the same as that expected from the production rate in the overlying water column + atmospheric deposition (more discussion is presented later) (Fig. 7.6).

The mass balance can be written as follows:

For total ^{210}Pb:

$$\lambda_{Pb}A_{Ra} + I_A^0 = \lambda_{Pb}A_{Pb}^T + \psi_c^0 A_{Pb}^T \tag{7.13}$$

where, λ_{Pb} is the decay constant of ^{210}Pb (0.03136 year^{-1}), I_A^0 is the measured atmospheric input of ^{210}Pb (=1.00 Bq m^{-2} y^{-1}), A_{Ra} = ^{226}Ra activity (Bq m^{-2}) in the water column; A_{Pb}^T is the total ^{210}Pb (Bq m^{-2}; dissolved + particulate), ψ_c^0 is the first-order rate constant for removal from the water column (year^{-1}).

From Eq. (7.13), the residence times (τ_c = $1/\psi_c^0$ for total ^{210}Pb) can be calculated as follows:

$$\tau_c = 1/\psi_c^0 = A_{Pb}^T/[\lambda_{Pb}(A_{Ra} + (I_A^0/\lambda_{Pb}) - A_{Pb}^T)] \tag{7.14}$$

In order to determine the residence time of ^{210}Pb in the entire water column, Eq. (7.14) can be rewritten in terms of inventories of ^{210}Pb as:

$$\tau_c = I_{Pb}^T\lambda_{Pb}/\{\lambda_{Pb}[(\lambda_{Pb}I_{Ra} + (I_A^0) - \lambda_{Pb}I_{Pb}^T)]\} \tag{7.15}$$

where I_{Pb}^T and I_{Ra} are the measured inventories of total ^{210}Pb and ^{226}Ra, respectively; the term $[I_{Ra} + (I_A^0/\lambda_{Pb})]$ is the total supply of ^{210}Pb. From the mass balance considerations,

$$\begin{aligned} \text{Total supply } (\lambda_{Pb}I_{Ra} + I_A^0) - \text{Measured inventory } (I_{Pb}^T\lambda_{Pb}) \\ = \text{Deficiency}(\lambda_{Pb}I_{Ra} + I_A^0 - \lambda_{Pb}I_{Pb}^T) \end{aligned} \tag{7.16}$$

Equation (7.15) thus reduces to:

$$\tau_c = (\text{Total supply} - \text{Deficiency})/(\lambda_{Pb} \times \text{Deficiency}) \tag{7.17}$$

The 'scavenging effectiveness (SE)' is defined as (Cochran et al. 1990; Baskaran and Santschi 2002):

$$SE = \text{Deficiency}/\text{Total supply} \tag{7.18}$$

$$\tau_c = [(1/SE - 1) \times 1/\lambda_{Pb}] \tag{7.19}$$

Using Eqs. (7.18) and (7.19), the residence times and scavenging effectiveness for ^{210}Pb for the entire water column can be determined. As a case study, the residence times calculated for 14 whole water columns in the shelf and slope stations in the Gulf of Mexico using Eq. (7.17) varied between 0.06 to 4.4 years,

$$y = 0.2301 + 0.002731x \quad R = 0.97447$$
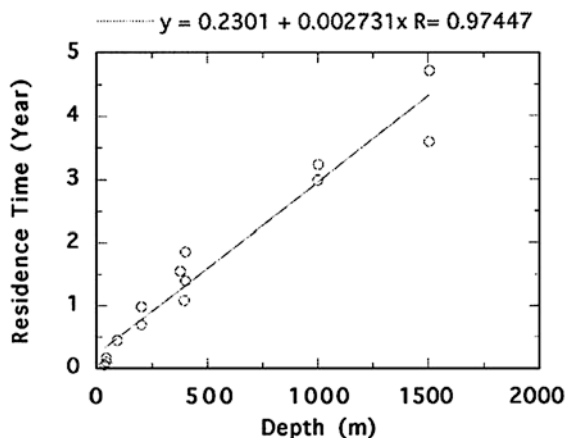
with a linear increase in residence time with depth of the water column (Fig. 7.7;
Baskaran and Santschi 2002). Similar approaches can be made to determine the
residence time of ^{210}Pb for any other discretely-defined water depths.

7.5 Summary and Future Research Direction

Applications of Pb-210 as a chronometer and tracer extends from terrestrial to
aquatic systems. In the case of soil erosion studies, multiple radionuclide tracers
with different half-lives (^{239,240}Pu, ^{7}Be and ^{10}Be) will yield information on different
time scales (1 month time scale for ^{7}Be, 10–60 year time scale for ^{239,240}Pu; up to
100 year time scale for ^{210}Pb and up to 7 million year time scale for ^{10}Be). In a
highly human-impacted watershed, all three commonly used ^{210}Pb$_{xs}$-based models
sometime do not yield reliable chronology. To validate ^{210}Pb$_{xs}$-based chronology,
^{137}Cs (both peak and initial introduction in the environment) has been widely used.
The nature of biogeochemical cycling that affects the post-depositional migration of
Cs remains less understood.

A thorough investigation of the factors that cause variations of ^{210}Pb inputs will
help to quantify the relative importance of these inputs in affecting the vertical
profiles of ^{210}Pb$_{xs}$. Such input sources of ^{210}Pb need to be incorporated into the
^{210}Pb dating models to extend the utility of ^{210}Pb even in highly disturbed sediment
columns. Quantification of SGD discharge and its impact on the vertical profiles of
^{210}Pb needs to be assessed and incorporated into the ^{210}Pb dating models.
Normalizing the temporal variations of atmospheric depositional flux of ^{210}Pb with
the annual amount of precipitation will aid in characterizing the variations in the
atmospheric delivery of ^{210}Pb. There are very limited studies on the utility of Pu,
both as a chronometer and as a tracer for erosion study, primarily due to the need
for a licensed Pu isotope (^{242}Pu) in the Pu analysis, which prevents many labora-
tories in pursuing Pu for tracer and chronometer studies. Plutonium in conjunction

with ^{137}Cs and ^{210}Pb will help to delineate sediment mixing from sedimentation. For soil erosion studies in the time scale of <100 years, the combined use of ^{210}Pb and [239,240]Pu along with a short-lived radionuclide ([7]Be), will likely provide a robust tool to identify and quantify short (few months) and relatively long-term (<100 year) time scale soil erosion rates in different environments.

References

Appleby PG, Oldfield F (1992) Application of lead-210 to sedimentation studies. In: Ivanovich M, Harmon RS (eds) Uranium-series disequilibrium: applications to earth, marine and environmental sciences. Clarendon Press, Oxford, pp 731–778

Appleby P, Oldfield F, Thompson R, Huttennen P, Tolonen K (1979) ^{210}Pb dating of annually laminated lake sediments from Finland. Nature (Lond) 280:53–55

Baskaran M (2005) Interaction of sea ice sediments and surface water in the Arctic Ocean: evidence from excess [210]Pb. Geophys Res Lett 32:L12601. doi:10.1029/2004GL022191

Baskaran M (2011a) Po-210 and Pb-210 as atmospheric tracers and global atmospheric Pb-210 fallout: a review. J Environ Radioact 102:500–513. doi:10.1016/j.jenvrad.2010.10.007

Baskaran M (2011b) Environmental isotope geochemisry—past, present and future. In: Baskaran M (ed) Handbook of environmental isotope geochemistry. Springer, pp 3–10 (ISBN: 978-3-642-10636-1)

Baskaran M, Iliffe TM (1993) Age determination of recent cave deposits using excess [210]Pb- a new technique. Geophys Res Lett 20(7):603–606

Baskaran M, Krishnamurthy RV (1993) The δ13C of cave deposits: a potential indicator of the $\delta^{13}C$ of atmospheric CO2. Geophys Res Lett 20:2905–2908

Baskaran M, Naidu AS (1995) ^{210}Pb-derived chronology and the fluxes of ^{210}Pb and ^{137}Cs isotopes into continental shelf sediments, East Chukchi Sea, Alaskan Arctic. Geochim Cosmochim Acta 59:4435–4448

Baskaran M, Santschi PH (1993) The role of particles and colloids in the transport of radionuclides in coastal environments of Texas. Mar Chem 43:95–114

Baskaran M, Santschi PH (2002) Particulate and dissolved ^{210}Pb activities in the shelf and slope regions of the Gulf of Mexico waters. Continent Shelf Res 22:1493–1510

Baskaran M, Coleman CH, Santschi PH (1993) Atmospheric depositional fluxes of [7]Be and ^{210}Pb at galveston and college station, Texas. J Geophys Res 98:20555–20571

Baskaran M, Hong G-H, Kim S-H, Wardle WJ (2005) Reconstructing seawater column ^{90}Sr based upon ^{210}Pb/[226]Ra disequilibrium dating of mollusk shells. Appl Geochem 20:1965–1973

Baskaran M, Nix J, Kuyper C, Karunakara N (2014) Problems with the dating of sediment core using excess ^{210}Pb in a freshwater system impacted by large scale watershed changes. J Environ Radioact 1–9

Benninger LK, Aller RC, Cochran JK, Turekian KK (1979) Effects of biological sediment mixing on the ^{210}Pb chronology and trace metal distribution in a Long Island Sound sediment core. Earth Planet Sci Lett 43:241–259

Benoit G, Hemond HF (1991) Evidence for diffusive redistribution of ^{210}Pb in lake sediments. Geochim Cosmochim Acta 55:1963–1975

Blais JM, Kalff J (1995) The influence of lake morphometry on sediment focusing. Limnol Oceanogr 40:582–588

Blais JM, Kalff J, Cornett RJ, Evans RD (1995) Evaluation of ^{210}Pb dating in lake sediments using stable Pb, Ambrosia pollen, and [137]Cs. J Paleolimnol 13:167–178

Bonotto DM, Garcia-Tenorio R (2014) A comparative evaluation of the CF:CS and CRS models in Pb-210 chronological studies applied to hydrodynamic basins in Brazil. Appl Radiat Isot 92:58–72

Cochran JK (1992) The oceanic chemistry of the uranium- and thorium-series nuclides. In: Ivanovich M, Harmon RS Uranium-series disequilibrium, 2nd ed, Oxford Science Publications, p 334–395

Cochran JK, McKibbinvaughan T, Dornblaser MM et al (1990) Pb-210 scavenging in the North-Atlantic Oceans. Earth Planet Sci Lett 97(3–4):332–352

Comans RNJ, Middelburg JJ, Zonderhuis J, Woitteiz JRW, De Lange GJ, Das HA, Van Der Weijden CH (1989) Mobilization of radiocaesium in pore water of lake sediments. Nature 339 (6223):367–369

Cooper LW, Olsen CR, Solomon DK et al (1991) Stable isotopes of oxygen and natural and fallout radionuclides used for tracing runoff during nowmelt in an arctic watershed. Water Resour Res 27:2171–2179

Cooper LW, Larsen IL, Grebmeier JM et al (2005) Detection of rapid deposition of ice-rafted material to the Arctic Ocean benthos using the cosmogenic tracer Be-7. Deep Sea Res. 52:3452–3461

Craig H, Krishnaswami S, Somayajulu BLK (1973) Pb-210, Ra-226: radioactive disequilibrium in the deep sea. Earth Planet Sci Lett 17:295–305

Crozaz G, Langway CC (1966) Dating Greenland firn-ice cores with ^{210}Pb. Earth Planet Sci Lett 1:194–196

Crozaz G, Debreuck W, Picciotto E (1964) Antarctic snow chronology with Pb-210. J Geophys Res 69(12):2597–2604

Crusius J, Anderson RF (1991) Immobility of ^{210}Pb in Black Sea sediments. Geochim Cosmochim Acta 55:327–333

Davis RB, Hess CT, Norton SA, Hanson DW, Hoagland KD, Anderson DS (1984) ^{137}Cs and ^{210}Pb dating of sediments from soft-water lakes in New England (U.S.A.) and Scandinavia, a failure of ^{137}Cs dating. Chem Geol 44:151–185

DeMaster DJ, Cochran JK (1982) Particle mixing rates in deep-sea sediments determined from excess ^{210}Pb and ^{32}Si profiles. Earth Planet Sci Lett 61:257–271

Dörr H (1995) Application of ^{210}Pb in soils. Paleolimnology 13:157–168

Druffel ERM, King LL, Belastock RA, Buesseler KO (1990) Growth rate of a deep-sea coral using ^{210}Pb and other isotopes. Geochim Cosmochim Acta 54:1493–1500

Du J, Du J, Baskaran M, Bi Q, Huang D, Jiang Y (2015) Temporal variations of atmospheric depositional fluxes of ^{7}Be and ^{210}Pb over 8 years (2006–2013) at Shanghai, China and Synthesis of global fallout data. J Geophys Res 120. doi:10.1002/2014JD022807

Eicken H, Krouse HR, Kadko D et al (2002) Tracer studies of pathways and rates of meltwater transport through Arctic summer sea ice. J Geophys Res Oceans 107:20

Evans DW, Alberts JL, Clark RA (1983) Reversible ion-exchange fixation of cesium-137 leading to mobilization from reservoir sediments. Geochim Cosmochium Acta 47:1041–1049

Everett SE, Tims SG, Hancock GJ, Bartley R, Fifield LK (2008) Comparison of Pu and ^{137}Cs as tracers of sediment transport in terrestrial environment. J Environ Radioact 99(2):383–393

Fuller CC, vanGeen A, Baskaran M, Anima R (1999) Sediment chronology in San Francisco Bay, California, defined by ^{210}Pb, ^{234}Th, ^{137}Cs, and $^{239,\ 240}$Pu. Mar Chem 64:7–27

Goldberg ED (1963) Geochronology with Lead-210. Radioactive dating. I.A.E.A, Vienna, pp 121–131

Guinasso NL, Schink DR (1975) Quantitative estimates of biological mixing rates in abyssal sediments. J Geophys Res 80:3032

Gustafsson JP, Tiberg C, Edkymish A, Kleja DB (2011) Modelling lead (II) sorption to ferrihydrite and soil organic matter. Environ Chem 8(5):485–492

Harden JW, Fries TL, Pavich MJ (2002) Cycling of beryllium and carbon through hillslope soils in Iowa. Biogeochemistry 60:317–335

Jweda J, Baskaran M (2011) Interconnected riverine-lacustrine systems as sedimentary repositories: Case study in southeast Michigan using ^{210}Pb and ^{137}Cs-based sediment accumulation and mixing models. J Great Lakes Res 37:432–446

Jweda J, Baskaran M, Van Hees E, Schweitzer L (2008) Short-lived radionuclides ([7]Be and ^{210}Pb) as tracers of particle dynamics in a river system in southeast Michigan. Limnol Oceanogr 53:1934–1944

Kaste JM, Baskaran M (2011) Meteoric [7]Be and [10]Be as process tracers in the environment. In: Baskaran M (ed) Handbook of environmental isotope geochemistry. Springer, pp 61–86 (ISBN: 978-3-642-10636-1)

Klaminder J, Renberg I, Bindler R, Appleby P, Emteryd O, Grip H (2006) Estimating the mean residence time of lead in the organic horizon of boreal forest soils using 210-Pb, stable lead and a soil chronosequence. Biogeochemistry 78:31–49

Koide M, Soutar A, Goldberg ED (1972) Marine geochronology with [210]Pb. Earth Planet Sci Lett 14:442–446

Krishnamurthy RV, Schmitt D, Atekwana EA, Baskaran M (2003) Isotopic investigations of carbonate growth on concrete structures. Appl Geochem 18:435–444

Krishnaswami S, Benninger LK, Aller RC, von Damm KL (1980) Atmospherically-derived radionuclides as tracers of sediment mixing and accumulation in near-shore marine and lake sediments: evidence from [7]Be, ^{210}Pb, and [239,240]Pu. Earth Planet Sci Lett 47:307–318

Krishnaswamy S et al (1971) Geochronology of Lake Sediments. Earth Planet Sci Lett 11:407–414

Ku T-L, Li HC (1998) Speleothems as high-resolution paleoenvironmental archives: records from northeastern China. Proc Indian Acad Sci (Earth Planet Sci) 107(4):321–330

Kumar A, Hage-Hassan J, Baskaran M et al (2016) Multiple sediment cores from reservoirs are needed to reconstruct recent watershed changes from stable isotopes (δ^{13}C and δ^{15}N) and C/N ratios: case studies from the midwestern United States. J Paleolimnology. doi:10.1007/s10933-016-9888-0

Laissaoui A, Benmansour M, Ziad N et al (2008) Anthropogenic radionuclides in the water column and a sediment core from the Alboran Sea: application to radiometric dating and reconstruction of historical water column radionuclide concentrations. J Paleolim 40(3):822–833

Mabit L, Benmansour M, Abril JM (2014) Fallout ^{210}Pb as soil and sediment tracer in catchment sediment budget investigations: a review. Earth Sci Rev 138:335–351

Masque P, Cochran JK, Hirschberg DJ et al (2007) Radionuclides in Arctic sea ice: tracers of sources, fates and ice transit time scales. Deep Sea Res Part I 54:1289–1310

McKee BA, Nittrouer CA, DeMaster DJ (1984) The use of [234]Th/[238]U disequilibrium to examine the fate of particle reactive species on the Yangtze continental shelf. Earth Planet Sci Lett 68:431–442

Oldfield F, Appleby PG, Battarbee RW (1978) Alternative ^{210}Pb dating: results from the New Guinea Highlands and Lough Erne. Nature 271:339–342

Pavich M, Brown L, Harden JW et al (1986) [10]Be distribution in soils from Merced river sediment terraces, California. Geology 50:1727–1735

Ravichandran M, Baskaran M, Sanstschi PH, Bianchi TS (1995) Geochronology of sediments in the Sabine-Neches estuary, Texas, U.S.A. Chem Geol 125:291–306

Ritchie JC, McHenry JR (1990) Application of radioactive fallout Cesium-137 for measuring soil erosion and sediment accumulation rates and patterns: a review. J Environ Qual 19:215–233

Robbins JS (1978) Geochemical and geophysical applications of radioactive lead isotopes. In: Nriagu JO (ed) Biogeochemistry of lead. Elsevier, New York, pp 285–393

Robbins JA, Edgington DN (1975) Determination of recent sedimentation rates in Lake Michigan using Pb-210 and Cs-137. Geochim Cosmochim Acta 39:285–304

Robbins JA, Krezoski JR, Mozley SC (1977) Radioactivity in sediments of the Great Lakes: post-depositional redistribution by deposit-feeding organisms. Earth Planet Sci Lett 36:325–333

Robbins JA, Mudroch A, Oliver BG (1990) Transport and storage of ^{137}Cs and ^{210}Pb in sediments of Lake St. Clair Can J Fish Aquat Sci 47:572–587

Routo J, Meyers PA, Hjorth T, Baskaran M, Hallberg R (2007) Sedimentary geochemical record of recent environmental changes around Lake Middle Marviken, Sweden. J Paleolimnol 37:529–545

Sanchez-Cabeza JA, Ruiz-Fernandez AG (2012) ^{210}Pb sediment radiochronology: an integrated formulation and classification of dating tools. Geochim Cosmochim Acta 82:183–200

Smith JN (2001) Why should we believe ^{210}Pb geochronologies. J Environ Radioact 55:121–123

Smith JN, Walton A (1980) sediment accumulation rates and geochronologies measured in the Saguenay Fjord using the Pb-210 dating method. Geochim Cosmochim Acta 44(2):225–240

Tanahara A, Taira H, Takemura M (1997) Radon distribution and the ventilation of a limestone cave in Okinawa. Geochem J 31:49–56

Wallbrink PJ, Murray AS (1996) Determining soil loss using the inventory ratio of excess lead-210 to cesium-137. Soil Sci Soc Am J 60(4):1201–1208

Walling DE, He Q (1999) Using fallout lead-210 measurements to estimate soil erosion on cultivated land. Soil Sci Soc Am J 63:1404–1412

Walling DE, Owens PN, Leeks GJL (1999) Fingerprinting suspended sediment sources in the catchment of the River Ouse, Yorkshire, UK. Hydrol Process 13:955–975

Wan GJ, Santschi PH, Sturm M, Farrenkothen K, Lueck A, Werth E, Schuler C (1987) Natural (^{210}Pb, ^{7}Be) and fallout (^{137}Cs, ^{239,240}Pu, ^{90}Sr) radionuclides as geochemical tracers of sedimentation in Greifensee, Switzerland. Chem Geol 63:181–196

Welp G (1999) Inhibitory effects of the total and water-soluble concentrations of nine different metals on the dehydrogenase activity of a loess soil. Biol Fertil Soils 30(1–2):132–139

Willenbring JK, von Blanckenburg F (2010a) Meteoric cosmogenic Beryllium-10 adsorbed to river sediment and soil: applications for earth-surface dynamics. Earth Sci Rev 98:105–122

Willenbring JK, von Blanckenburg F (2010b) Long-term stability of global erosion rates and weathering during late-Cenozoic cooling. Nature 465:211–214

Wong CS, Sanders G, Engstrom DR, Long DT, Swackhamer DL, Eisenreich SJ (1995) Accumulation, inventory, and diagenesis of chlorinated hydrocarbons in Lake Ontario sediments. Environ Sci Technol 29:2661–2672

Woo KS, Hong G-H, Choi DW, Jo KN et al (2005) A reconnaissance on the use of the speleothems in Korean limestone caves to retrospective study on the regional climate change for the recent and geologic past. Geosci J 9:243–247

Xu YH, Qiao JX, Hou XL, Pan SM (2013) Plutonium in soils from northeast China and its potential application for evaluation of soil erosion. Scientific Reports 3:3506. doi:10.1038/srep03506

Chapter 8
Radon in Groundwater System

8.1 Introduction

Radon, along with other daughter products in ^{238}U-, ^{235}U- and ^{232}Th-decay series, have been widely utilized in groundwater systems as powerful tracers to infer physico-chemical transport reactions of these nuclides (and their chemical analogs), to identify and trace water movement using ratios of radionuclides such as ^{234}U/^{238}U, ^{226}Ra/^{228}Ra, and to determine groundwater ages. The eleven elements that are produced from the decay of ^{238}U-^{235}U-^{232}Th to their ultimate stable Pb isotope (^{238}U $\rightarrow$ ^{206}Pb; ^{235}U $\rightarrow$ ^{207}Pb and ^{232}Th $\rightarrow$ ^{208}Pb) exhibit very strong relative fractionations within the surrounding groundwater due to their contrasting geochemical behavior during and after their release into the water and their subsequent interaction with the surrounding host aquifer rocks. The release of U-Th series radionuclides to the groundwater depend on the concentration and location of the parent nuclides (^{238}U, ^{235}U and ^{232}Th) within the host rocks, the physical and chemical properties of the host rocks (e.g., density, melting temperature of the minerals associated with the host rock, type of bonding of minerals, etc.), and the chemistry of the groundwater surrounding the host rocks. It has been shown that of all the U-Th daughter nuclides, ^{222}Rn specific activity is found to be the highest in groundwater systems because of the least reactive nature of radon, and remains in groundwater without any removal by precipitation or sorption. Since radon is a noble gas and does not react with solids, near 100 % of the radon released into the groundwater remains as dissolved phase (Fig. 8.1, IAEA 2014).

Although the activity of ^{222}Rn in groundwater is very high compared to is parent, ^{226}Ra, the molar abundance is very low (e.g. 1 Bq/L = 8.05×10^{-19} mol/L; typically 1.0×10^{-19} to 10×10^{-19} mol/L, although values up to two orders of magnitude higher values have also been reported) and thus, radon does not form a separate gas phase, but it will partition into any existing volatile phase.

It is known that noble gases have high solubility in organic liquids and hence this property can be utilized to investigate the partitioning of radon between organic

Fig. 8.1 Systematics of decay products all ^{238}U-series radionuclides. The major and minor fluxes to each nuclide can be readily seen from the arrows shown. Nuclides in the decay series within the host rock minerals supply atoms at the surface and in the groundwater by recoil during a decay. Of all the nuclides shown, ^{222}Rn undergoes without removal on the surface of mineral grains (adapted from Porcelli and Swarzenski, 2003, with permission from American Mineralogical Society)
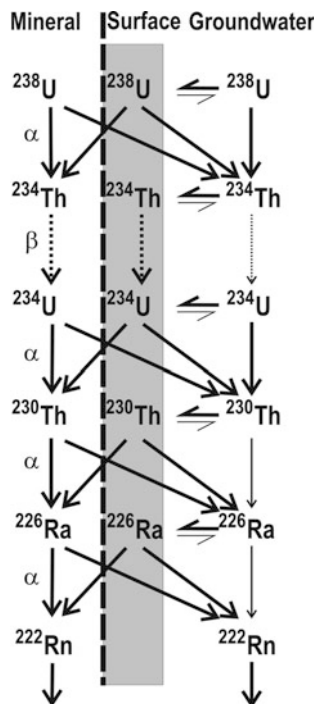
solvents and water. This, in conjunction with ^{4}He, the ^{222}Rn/^{4}He ratio is useful to estimate the age of the groundwater. Due to relatively high abundance of ^{222}Rn in groundwater compared to surface waters, it is a useful tracer for quantifying the infiltration of meteoric water. In this chapter, the source and sink terms of radon in groundwater and its utility as a tracer and possibly as a chronometer in subsurface waters is presented.

8.2 Activities of ^{222}Rn and Ra Isotopes in Groundwater

8.2.1 Sources and Sinks of ^{222}Rn in Groundwater

Radon concentrations in groundwater often vary by up to 5 orders of magnitude. The major sources and sinks of ^{222}Rn in groundwater include: (i) production from dissolved ^{226}Ra; (ii) input from weathering resulting in congruent dissolution of U-bearing host rocks, although leaching and incongruent breakdown of host rocks also could contribute ^{222}Rn to the surrounding waters; (iii) input by recoil; (iv) inputs from desorption—this term is negligible because there is no adsorption of ^{222}Rn from the waters onto host rock matrix; (v) input from production of sorbed ^{226}Ra— when ^{230}Th in host rock undergoes alpha decay, some of the ^{226}Ra is released to the

surrounding fluid and the residence time of ^{226}Ra in freshwater is often considered to be short. Thus, the dissolved ^{226}Ra atom in groundwater is often removed onto the surface of the host solid matrix. The fractional amount of ^{222}Rn resulting from the decay of sorbed ^{226}Ra atoms on the host rock matrix depend on the geometry of the host rock mineral grain and the location of the ^{226}Ra atom on the mineral grain. Some of the ^{222}Rn may be released into alpha recoil track or fission track which could also eventually diffuse out reaching the surrounding water. Assigning a value for the fractional amount of ^{222}Rn released from the sorbed ^{226}Ra to the surrounding groundwater is difficult and no experimental data exist to provide a finite value; (vi) removal by precipitation—radon does not undergo precipitation and there is no removal by this mechanism; (vii) removal by sorption—there is no removal of radon by sorption onto mineral grains. As mentioned in Chap. 1, isolated sorption of radon on soil and rock grains have been reported, although sorption at room temperature and humidity conditions common at Earth's surface is not significant. In addition to the seven possible sources listed above, there is likely a diffusion source from the surrounding rocks near the groundwater, although this is not well documented; and (viii) radioactive decay.

The mass balance of radon in groundwater can be summarized as follows:

Rate of change of molar concentration of ^{222}Rn in a groundwater system = advectional   input + weathering   input + recoil   input + desorption   (=0 because there will not be any adsorbed ^{222}Rn on host matrix) + production from ^{226}Ra—radioactive decay—precipitation (=0 because ^{222}Rn does not undergo precipitation)—adsorption (=0 as radon does not undergo sorption).

8.2.2   Equilibrium Radon Concentration in an Aquifer

The aquifer specific equilibrium radon concentration in groundwater (C^∞) is governed by the radium activity concentration of the aquifer matrix (A_{Ra}, Bq per kg of aquifer matrix), the radon emanation coefficient (ε, dimensionless) that quantifies the share of the produced ^{222}Rn atoms that emanate into the pore space, the porosity (n, m^3/m^3) of the aquifer matrix and bulk density (ρ_b, mass of dry sediment (kg)/volume of wet sediment, m^{-3}) of the aquifer matrix. The higher porosity for a given density will result in lower radon concentration in the pore space (Tanner 1964). The equilibrium ^{222}Rn concentration is given by the equation (Andrews and Wood 1972):

$$C^\infty \left(\mathrm{Bq\,m^{-3}} \right) = \varepsilon\, A_{Ra}\, \rho_b / n \qquad (8.1)$$

Andrews and Wood (1972) proposed that diffusion along fracture planes was a significant source of ^{222}Rn to solution; note that the source of the diffusing ^{222}Rn is derived from alpha recoil. Since there is no loss of ^{222}Rn by sorption, at steady state

which is established in ~ 6 half-lives, (~ 23 days, ~ 98 %), the ^{222}Rn concentration in the water (Bq L^{-1}) at equilibrium will be equal to its recoil supply (atoms s^{-1} L^{-1}).

Equilibrium radon concentration in groundwater normally range between 10,000 and 100,000 Bq m^{-3} (10 and 100 Bq L^{-1}) and is expected to remain constant, unless other subsurface activities (e.g., seismic) affect the release rates and movement of subsurface radon. However, if organic solvents such as NAPL are present in groundwater, then, radon concentration in groundwater will decrease due to radon partitioning between NAPL and water. Usually, neither advection nor diffusion or dispersion play any significant role in radon distribution patterns in saturated aquifers (Schubert et al. 2000).

8.2.3   Case Study: Temporal and Spatial Variations of ^{222}Rn Concentration in Groundwater in a Regional Scale

Temporal variations of radon concentrations (note: concentrations and activity concentrations and activities are synonymously used in this book, as in a majority of the published literature) in soil and groundwater have been utilized to predict subsurface seismic activities (Chap. 10). There is a large body of data on the concentrations of ^{222}Rn in groundwater. Most of these data indicate both temporal and spatial variations in the activity of ^{222}Rn at any given location. For example, radon concentrations from groundwater in Southern California have been reported to vary from 1.0×10^3 to 7.8×10^5 Bq m^{-3}, with ^{222}Rn/^{226}Ra activity ratios ranging from 10 to 10^5 (Chung 1981). The range of values also varied in different fault zones in Southern California (Chung 1981): Elsinore fault: 1.6×10^3 to 5.7×10^4 Bq m^{-3}; San Jacinto Fault: 6.5×10^3 to 1.8×10^5 Bq m^{-3}; and San Andreas Fault: 1.0×10^3 to 7.8×10^5 Bq m^{-3}. In one well that punctured the San Andreas fault, the ^{222}Ra measured over a period of 4 years (total 5 samples) varied by a factor of ~ 2, from 2×10^5 to 4×10^5 Bq m^{-3}, with less variations in conductivity and <35 % change in ^{226}Ra activity. Such large spatial variations in the concentrations of ^{222}Rn are common, as shown in Table 8.1. Concentrations of radon in thermal spring waters are considerably lower, as radon often degasses from the gaseous phase. For example, radon concentrations in Syabru-Bensi hot springs located at the front of the High Himalaya in Central Nepal had ^{222}Rn concentration of less than 2.5 kBq m^{-3} (=2.5 Bq L^{-1}), with exponentially decreasing ^{222}Rn concentration with increase in water temperature. In contrast, the ^{222}Rn activity in gas bubbles collected in the water or in the dry gas discharges varied from 16 to 41 kBq m^{-3} (Perrier et al. 2009). Spatial variations in the activity concentration of ^{222}Rn in the United States for different lithologies are shown in Table 8.2. From the measured ^{222}Rn concentrations in groundwater samples analyzed from Guarani aquifer in S. America that spreads around 10^6 km^2 within four countries (Brazil, Argentina, Uruguay and Paraguay), Bonotto (2004) reported that the activity concentrations are log-normally distributed.

Table 8.1 Activity concentration of ^{222}Rn and ^{222}Rn/^{226}Ra activity ratio in selected groundwater samples

Location	Nature of the water	^{222}Rn ($\times 10^4$ Bq m^{-3})	^{222}Rn/^{226}Ra activity ratio ($\times 10^3$)	Reference
New Zealand	Geothermal waters	0.067–500		Whitehead (1980)
S. Finland	Well waters	3–1700		Asikainen (1981)
Gujarat, India	Groundwater	0.33–1.5	0.1–10	Hussain and Krishnaswami (1982)
S. California, USA	Groundwater	0.1–78	0.01–100	Chung (1981)
Connecticut, USA	Groundwater	1.4–19.8	1.2–30.0	Krishnaswami et al. (1982)
Kharagoda brines, India	Shallow subsurface brine	0.44–1.07	13.2–237	Krishnaswami et al. (1991)
Coastal California aquifer, USA	Groundwater	0.27–0.70	0.57–14.3	Swarzenski et al. (2013)

8.3   Major Sources of ^{222}Rn to Groundwater

The three major possible sources of radon to groundwater are: (i) supply from dissolved ^{226}Ra; (ii) supply from source rock weathering reactions, and (iii) supply from alpha recoil processes. The relative importance of each of these three sources are discussed below.

8.3.1   Supply of ^{222}Rn from Its Dissolved Parent ^{226}Ra in Groundwater

If the groundwater system is in steady state with respect to ^{222}Rn and ^{226}Ra, the total activity of ^{222}Rn and ^{226}Ra will remain constant in time. In this case, the total supply of ^{222}Rn from the decay of ^{226}Ra = radioactive decay of ^{222}Rn. Radium-226 activity in groundwater around the globe varies widely. From a total of 1270 groundwater samples collected from 15 major principal and other major aquifer systems used for drinking from 45 states in all major physiographic provinces of the USA, Szabo et al. (2012) showed that the activity of ^{226}Ra varied over 2 orders of magnitude, from 0.5 to 550 Bq m^{-3} (Table 8.2). Anoxic groundwater seeping through sinkhole vents in Lake Huron was found to have very high ^{226}Ra activities (up to 72 Bq m^{-3}), which is about 2 orders of magnitude higher than that in Lake Huron surface waters (Baskaran et al. 2016). The activity of ^{226}Ra in groundwater depends on a number of factors that include the concentration and distribution of ^{238}U in the rock matrix, solubility of uranium, solubility of radium, rate of release

Table 8.2 General lithologic and radiologic characteristics of the 15 principal aquifer systems in the USA evaluated during 1985–2005 and distribution of the 1270 sampled well by water use (PS: Public supply; D: Domestic; O: Observation) (Data taken from Szabo et al. 2012)

Principal aquifer system name	States with samples	Predominant lithologies	Radon-222, median^2, and maximum (Bq/L)	Number and type of wells (PS/D^4/O^5)
Coastal Plain sands; commonly quartzose, Coastal Plain: North Atlantic	DE, MD, NC, NJ, VA	Sand and clay, some mixed w. gravel or silt	6.3, 24.8	24/25/36
Coastal Plain: Southeastern	AL, MS	Sand and clay, some mixed w. gravel	7.8, 23.0	0/27/3
Coastal Plain: Texas Uplands, Gulf Lowlands, Mississippi Embayment	AR, LA, MO, MS, TN, TX	Sand and clay, some mixed w. gravel; some silt and clayey silt	11.8, 321	19/75/30
Basin-fill, alluvial, or fluvial sands and gravels; commonly arkosic or lithic-gragment rich, High Plains, Tertiary alluvium	KS, NE, OK, TX	Sand and gravel; some sand and clay, sand or clay	12.5, 38.8	17/19/27
Mountain West: alluvium, valley fill	CO, ID, MT, WA, WY	Gravel, poorly sorted, mixed w. sand, silt; or sand, poorly sorted, mixed w. gravel and clay; cobbles; some silt, clay	20.6, 50.3	1/1/44
Pacific Coastal, (Central Valley, Williamette Basin) alluvium, fill	CA, OR	Gravel, mixed w. sand, silt; or some sand, mixed w. silt	22.2, 88.8	1/24/30
Rio Grande and Basin and Range basin fill	AZ, CO, NV, UT	Sand and gravel, mixed w. clay; or gravel and sand, mixed w. silt; cobbles; or sand, silt, clay	26.7, 181	11/9/21
Glacial sands and gravels; commonly lithic-gragment rich, Glacial sand and gravel	17 states	Sand; or gravel; or sand and gravel, some mixed w. silt or clay; some silt or clay	13.3, 317	42/196/179
Sandstones and shales, Appalachian Piedmont: Mesozoic Basins	NJ, PA	Shal, mudstone; or shale and sandstone; or some conglomerate; or argillite	67.3, 185	1/27/02

Table 8.2   (continued)

Mountain West Foreland/Tertiary/Cretaceous sandstones	CO, MN, MT, ND, WY	Sandstone, some arkosic; some interbedded w. shale; some mostly shaley; or shale	22.2, 164	0/24/16
Intermixed sandstones and carbonate rocks, Appalacian Plateau: Valley and Ridge and Mississipian Limestones	AL, PA, TN	Shale; some interbedded w. sandstone, siltstone; or limestone, some w. chert; or residuum; or rare sandstone	33.1, 223	4/35/20
Carbonate rocks, Floridan, and Surficial	FL, GA, NC, SC	Limestone; or limey sand	15.9, 199	4/71/27
Carbonate rocks, Mid-continent and Ozark Plateau Cambro-Ordovician dolostones	AR, IA, KS, MO, OK	Dolomite; or sandstone; or interbedded dolomite and sandstone	5.9, 50.7	48/0/1
Crystalline (felsice to intermediate) igneous and metamorphic rock and basalt, Crystalline (felsic) rock: New England	CT, MA, ME, NH, RI, VT	Metamorphic or igneous rocks: schist, granite-gneiss, tonalite, granite, syenite	**81.4, 7955**	0/87/2
Basalt	CT, HI, ID WA	Basalt	4.1, 174	30/1/5

of ^{226}Ra by weathering (or leaching), extent of recoil relative to the rate of geo-chemical reactions (adsorption-desorption, precipitation-dissolution onto/from mineral surfaces), and the residence time of water.

The geochemical behavior of ^{226}Ra in groundwater has direct bearing on the supply of ^{222}Rn. In aqueous systems, radium behaves similar to other divalent alkaline-earth cations such as Sr, Ca and is most similar to Ba. Its geochemical behavior depends also on the abundance of other divalent cations in the water. For example, the concentrations of Ca and Sr in open ocean seawater are 10.56 mM and 0.0928 mM, respectively (Broecker and Peng 1982), while ^{226}Ra concentration in open ocean is $\sim 1.62 \times 10^{-13}$ mM (~ 80 dpm m^{-3} or 1.3 mBq L^{-1}) making the Ra soluble and hence traces the water mass, as Ra is unable to compete with other divalent cations that is $>10^{14}$ times higher in concentration ('competing ion effect', e.g., Sturchio et al. 2001). However, in groundwater where Ca or Sr concentrations are much lower, Ra can be relatively easily removed from the solution to solid surfaces. The K_d of Ra is lower than that of Th which would explain why ^{226}Ra activity in groundwater is significantly higher than ^{234}Th which is also produced in

the same ^{238}U decay chain (Krishnaswami et al. 1982; Tricca et al. 2001; Reynolds et al. 2003). At a pH of ~ 10, Ra can form neutral or anionic (mainly SO_4^{2-}) complexes (Langmuir and Riese 1985). Radium concentration at 1.62×10^{-16} M (given above), is $>10^{14}$ orders of magnitude lower than that of Ca or Sr and hence if the concentrations of Ba or Sr are large enough exceeding the solubility of their salts (such as $BaSO_4$ or $BaCO_3$ or $SrSO_4$), then Ra could precipitate with $BaSO_4$ (barite) or $BaCO_3$ (witherite) or $SrCO_3$ (celestite) as well as Ra sulfate which is insoluble (Langmuir and Melchoir 1985; Martin and Akber 1999).

In low ionic strength groundwater and surface waters, radium is often considered to be particle-reactive, with partition coefficient values ranging between 10^3 and 10^4 have been reported for a range of lithologies (e.g., Baskaran et al. 2016). This implies that under natural conditions, radium will migrate at rates of 10^{-3}–10^{-4} times that of the groundwater and hence the production rate will differ compared to radon production in salt water (Krishnaswami et al. 1991). Once ^{226}Ra is produced from the decay of dissolved ^{230}Th or injected into the solution phase by recoil, ^{226}Ra is likely to be more efficiently removed on to host mineral surface.

8.3.2   Supply of ^{226}Ra and ^{222}Rn by Weathering

Generally, as discussed earlier, in most groundwater systems, the activity of ^{222}Rn is about 10^3–10^5 times higher than ^{226}Ra or any other nuclide in the ^{238}U-decay chain, but the ^{222}Rn activity per unit volume of groundwater is generally of the same order of magnitude as the ^{222}Rn activity per volume of aquifer solids. If dissolution of aquifer solids is taking place and contributing all of the ^{222}Rn to the groundwater, then, one needs a dissolution rate of the order of 10 kg y^{-1} L^{-1} and it is not possible to have this high dissolution rate (Krishnaswami et al. 1982). Thus, ^{222}Rn supplied to groundwater is predominantly by recoil and its recoil supply rate is orders of magnitude higher than its supply rate from in situ decay of dissolved ^{226}Ra and congruent dissolution. In the case of weathering, it is assumed that all the nuclides from the weathered material are released together (congruent weathering). The weathering term input, b = BWI and B is given by:

$$B = (1 - \text{porosity}(n))\, \rho_R / n\rho_W \qquad (8.2)$$

where ρ_R and ρ_W are the densities of host rock and groundwater, respectively; W: first order rate constant for weathering release of radon and I is the host rock molar concentration of ^{226}Ra. From a comparison of the recoil and weathering terms in a one-dimensional advective transport equation with terms for water-rock interaction incorporated, Porcelli and Swarzenski (2003) estimated the mean time scale for chemical weathering to be 10^7 years, and therefore any nuclide with a half-life of $<10^5$ year would be supplied primarily by recoil.

8.3.3 Supply from Recoil

Direct recoil of ^{222}Rn atom, into aqueous phase can occur when a ^{226}Ra atom located within the recoil distance from the grain boundary, undergoes radioactive decay (see Chap. 3). It has been shown that daughter nuclides that are generated with high recoil energies are propelled across the mineral surface and are stopped within the aqueous phase (Kigoshi 1971; Fleischer and Raabe 1978) and the rate of ejection of ^{222}Rn into groundwater is determined only by the fraction of ^{226}Ra within recoil distance of mineral surfaces or channels. The energy associated with recoil mechanism during alpha decay is about 10^4–10^6 times larger than that of the typical bond energies ($\sim$ few eV). The recoil distance of daughter ^{222}Rn atom when parent ^{226}Ra atom undergoes alpha decay will vary depending on the nature of the mineral in which the decay takes place. This physical supply process can be quantified (Porcelli and Swarzenski 2003) as:

$$\text{The recoil input term is} = B \lambda_P P_R \varepsilon_i \tag{8.3}$$

where B is the mass ratio of rock to water [B = $(1-n)$ $\rho_R/n\rho_W$; where n is the porosity of the host rock, ρ_R and ρ_w are the densities of the host rock and groundwater, respectively]; λ_P is the decay constant of the parent (^{226}Ra for ^{222}Rn); P_R is the host rock parent activity concentration; and ε_i is the recoil fraction for ^{222}Rn.

The recoil supply of the ^{238}U-series nuclide located near the surface of a mineral grain results in depletion for the next nuclides in the decay chain. For example, Krishnaswami et al. (1982) calculated that the recoil supply of ^{222}Rn (4th alpha recoil product) is only 48 % as that of ^{234}Th (1st alpha recoil product). Furthermore, the value of ε_{Rn} depends upon the size of the ^{226}Ra-bearing mineral grains, with smaller grains having a larger proportion of the contained ^{226}Ra within recoil distance from the surface. As one would expect, the fractional escape of ^{222}Rn would depend upon the geometry of the grains. Assuming spherical grains, the relationship between the recoil rate and the radius of the grains with uniformly distributed ^{226}Ra for a recoil distance of 20 nm is shown in Fig. 8.2 (Porcelli 2008). For a typical aquifer grain size of 1 mm, the fraction of ^{222}Rn released is $\sim 6 \times 10^{-5}$. However, Krishnaswami et al. (1982) reported that the measured ^{222}Rn in groundwater activities correspond to up to ~ 10 % of the amount being produced in the aquifer host matrix and a number of possible causes have been suggested to explain this high release rates (Porcelli 2008). Those include: (i) ^{226}Ra concentrated in small primary grains. From Fig. 8.2, for a release of 3 % of recoiled radon into solution, the required grain size should be several microns in diameter which is generally below the typical size of U-bearing minerals, but is possible locally (Porcelli 2008); (ii) a dominant portion of the ^{226}Ra is present in accessory minerals or secondary phases. In freshwater system, residence time of radium is relatively short and removed radium sorbs onto grain surfaces (Baskaran et al. 2016). The emanation rates of radon from these Ra-enriched surface coating could contribute significantly to the

total radon measured in the groundwater; and (iii) enhanced release of radon due to crystal lattice damage resulting from alpha and recoil tracks. It was shown that U-bearing minerals released less ^{222}Rn into air after heating, likely due to annealing of lattice damage (Garver and Baskaran 2004; Eakin et al. 2016).

8.3.4 Calculations of Retardation Factors

If the rate of transport of a groundwater ^{222}Rn is decreased by the factor R_{Rn} relative to the groundwater flow rate due to interaction with the host rock surfaces, then the retardation factor is

$$R_{Rn} = 1 + K_{Rn} \tag{8.4}$$

where K_{Rn} is the ratio of the inventory atoms absorbed on surfaces to the inventory in the surrounding groundwater. If 5 % of Rn is on surfaces, then, it will migrate at a rate of 1/0.95 (=1.05). Modeling the transport range of some of these nuclides (e.g., U, Th, Ra, Rn, and Pb radioisotopes) in groundwater enables one to calculate their retardation factors which are useful to predict their mobility in subsurface environment.

8.4 Applications of Radon as a Tracer and Chronometer

8.4.1 Radon as a Tool to Date Groundwater

Combined use of radon and helium as an earthquake predictor is presented in Chap. 10 (Earthquake chapter). Efforts have been made to date groundwater by combining ^{222}Rn and ^{4}He. In the ^{238}U, ^{235}U and ^{232}Th series, there are a total of 21 alphas (8 from ^{238}U-series, 7 from ^{235}U-series and 6 from ^{232}Th-series) and when an alpha particle picks-up 2 electrons, it becomes a ^{4}He atom. Similar to radon, He is not subject to removal from groundwater by water-rock interactions, and does not undergo precipitation. Since ^{4}He is stable, it will accumulate with time. Measured ^{222}Rn in groundwater reflects the time scale over its mean life (=5.51 days) while for ^{4}He, it reflects the accumulation over the residence time of the groundwater. If the accumulation rate of ^{4}He in groundwater is constant, then, relative ages of groundwater can be determined from the measurements of ^{4}He. If the recoil rate of ^{222}Rn is used to determine the release rates of ^{4}He from the aquifer matrix, then, ^{4}He/^{222}Rn ratio can be utilized to determine absolute ages (Torgersen 1980). The ^{222}Rn/^{4}He (amu) ratio is 55.5 and hence the recoil distance of ^{4}He will be much higher than that of ^{222}Rn ($\sim$20 nm). Note that a number of factors can affect the distribution of ^{226}Ra in mineral grains and thereby the release rates of ^{222}Rn, but the same factors may not affect ^{4}He release into the groundwater. Although there are

Fig. 8.2 The fraction of ^{222}Rn produced within a mineral grain that is released by direct recoil from a spherical grain. For a hypothetical grain size of 1 mm, the fraction of ^{222}Rn released is ~ 0.2 % (adapted from Porcelli 2008, with permission from Elsevier Ltd.)
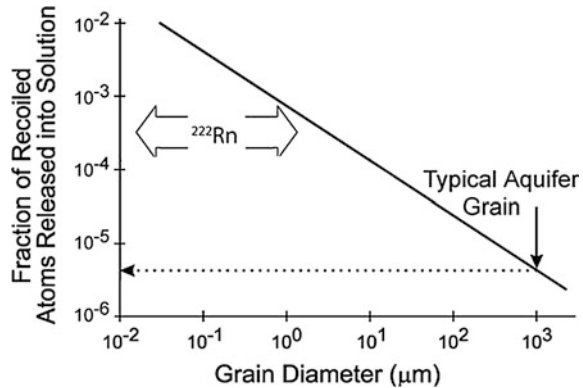
significant short-term variations of ^{222}Rn activities in groundwater (more details discussed in Chap. 10; for example, radon is a useful tracer to predict earthquakes), if one assumes ^{222}Rn activities remain constant, one could use the ^{222}Rn/^{4}He ratios to calculate an apparent groundwater age. The equation to calculate the age is given by Agarwal et al. (2006):

$$\text{Age(year)} = (R_{Rn}/R_{He}) * (A_{Rn}/A_{He}) * (C_4/A_{222}) \qquad (8.5)$$

where (R_{Rn}/R_{He}) is release factor ratio for radon and helium from the aquifer matrix to groundwater, A_{Rn}/A_{He} is accumulation rate ratio of ^{4}He and ^{222}Rn, C_4 is concentration of ^{4}He (atoms L^{-1}), and A_{222} is activity (atoms L^{-1} year^{-1}) of ^{222}Rn in groundwater. Agarwal et al. (2006) showed that generally ^{4}He/^{222}Rn estimated ages of groundwater samples collected from North Gujarat-Cambay region in western India are in reasonable agreement with ^{14}C age estimates for helium release factor (R_{He}) value of 0.4 ± 0.3, although some pockets of anomalously high ^{4}He concentrations, not accompanied by high ^{222}Rn activities, have been observed along some deep-seated faults in the study area.

8.4.2 Radon as a Tracer for Quantifying the Infiltration of Meteoric Water

When meteoric water seeps through the ground, some of the radon migrating through the soil pores come in contact with the infiltrating water through the soil. The radon activity in the infiltrating water increases until a steady state between emanation and radioactive decay is attained (Hoehn and von Gunten 1989, 1992). Using the ingrowth of ^{222}Rn, Hoehn and von Gunten (1989) assessed the residence times of bank infiltration. Since radon does not sorb on to aquifer matrix, radon is transported without any retardation. Savoy et al. (2011) investigated the dynamics of groundwater recharge of karst aquifer using ^{222}Rn and CO_2 in an underground

stream of the Milandre test site in Switzerland. From the measured temporal variations of radon and CO_2, using a conceptual model, they investigated different hydrological conditions under which soil or meteoric water transited through the vadose zone to the saturated zone. Radon is also used as a tracer to investigate stream water-groundwater interaction (Stellato et al. 2013).

8.4.3   Radon as a Recoil Flux Monitor for the Determination of Adsorption/Desorption Rate Constants and Retardation Factor for Radium

As discussed earlier, the main supply of radon to groundwater is by recoil and the recoil release fraction, ε_{Rn}, could be used to determine the recoil supply rate of other members of the U-Th series radionuclides. The differences in specific activities between ^{234}Th-^{234}U-^{226}Ra-^{222}Rn-^{210}Pb-^{210}Po of the ^{238}U-series are attributed to the differences in their residence times (or removal rate constants) in the aqueous phase of the groundwater system. For example, in five groundwater samples from Connecticut, USA ^{222}Rn activity was found to vary from 1.4×10^4 to 19.8×10^4 Bq m^{-3}, while the corresponding values of ^{226}Ra varied between 2.6 and 6.5 Bq m^{-3}. The ^{234}Th/^{222}Rn activity ratios varied between 0.4×10^{-6} and 13.0×10^{-5} (Krishnaswami et al. 1982). The concentrations of U-Th series radionuclides in groundwater system is governed by the rates of dissolution-precipitation of minerals, adsorption/desorption rates of parent and daughter nuclides, degree of retardation in nuclide mobility, the distribution of ^{238}U, ^{235}U and ^{232}Th in mineral grains, dispersive and diffusion transport of fluid and other physicochemical properties of interest in the rock-water system (Krishnaswami et al. 1982; Ku et al. 1992; Copenhaver et al. 1993; Porcelli and Swarzenski 2003). Krishnaswami et al. (1982) assumed that the diffusion and dispersion of U-Th radionuclides to be small and considered cases where dissolution and precipitation reactions were not important. The major source of short-lived radionuclides in solution is from recoil, both from the aquifer solids (lattice-bound) as well as from the adsorbed parent isotopes. Note that all four naturally-occurring radium isotopes (^{226}Ra ($T_{1/2} = 1,600$ y) from ^{230}Th, ^{223}Ra ($T_{1/2} = 11.4$ d) from ^{227}Th, ^{224}Ra ($T_{1/2} = 3.66$ d) from ^{228}Th, and ^{228}Ra ($T_{1/2} = 5.75$ y) from ^{232}Th) are directly derived from the alpha decay of insoluble Th parents. These isotopes occur in subsurface fluids at concentration levels that are an order of magnitude higher than their immediate parent thorium isotopes, as a result of continuing supply through alpha decay.

In anthropogenically unperturbed subsurface environments, the radionuclides in host matrix are derived from two pools: dissolved nuclides sorbed onto solid matrix, and lattice-bound. The exchange of radionuclides (sorption-desorption) taking place between dissolved and sorbed phases occurs primarily by dissolution, precipitation, and/or recoil (Ku et al. 1992; Luo et al. 2000; Porcelli and Swarzenski 2003).

If P is the supply rate (Bq m^{-3}) of a nuclide to solution by dissolution, in situ production and recoil (atoms s^{-1} volume^{-1}), k_1 and k_2 are first-order adsorption and desorption rate constants, respectively, and N_d and N_s are the concentration of the nuclide in dissolved phase (atoms/volume of H_2O) and adsorbed on aquifer matrix (atoms/volume of H_2O), then, from mass balance consideration one can write the following equations (Krishnaswami et al. 1982; Swarzenski et al. 2013):

$$\text{Solution phase:}\quad P + k_2 N_s = \lambda N_d + k_1 N_d \qquad (8.6)$$

$$\text{Solid matrix phase:}\quad k_1 N_d = \lambda N_s + k_2 N_s \qquad (8.7)$$

The ratio of the activity ($=\lambda N_d$) of a nuclide to its production (P) in solution can be calculated from Eqs. (8.6) and (8.7):

$$\Omega = \lambda N_d/P = (k_2 + 1)/(k_1 + k_2 + \lambda) \qquad (8.8)$$

The adsorption and desorption rate constants are expected to be the same for two isotopes of the same element, assuming that isotopic fractionation is negligible. If 'i' and 'j' refer to two isotopes of an element, then, using mass balance equations of each of these nuclides can be combined and solved for k_1 and k_2 (Krishnaswami et al. 1982):

$$k_1 = [(\lambda_i - \lambda_j)(1 - \Omega_i)(1 - \Omega_j)]/(\Omega_i - \Omega_j) \qquad (8.9)$$

and

$$k_2 = [\Omega_i \Omega_j(\lambda_j - \lambda_i) + \lambda_i \Omega_j - \lambda_j \Omega_i)]/(\Omega_i - \Omega_j) \qquad (8.10)$$

The retardation factor (R_f) is related to k_1, k_2 and decay constant λ as follows:

$$R_f = (k_1 + k_2 + 1)/(k_2 + \lambda) \qquad (8.11)$$

From the measured activities of ^{222}Rn, ^{224}Ra and ^{228}Ra in the solution phase, and the specific activities of ^{230}Th, ^{228}Th, ^{228}Th in the solid phase, the values of k_1 and k_2 can be determined using Eqs. (8.9) and (8.10).

From the measurement of ^{224}Ra/^{222}Rn activity ratios, radium retardation factor (R_f, the migration rate of the groundwater constituent relative to the groundwater flow rate) have been determined. These studies showed that the activity concentrations of short-lived nuclides are considerably less than those expected from their supply by recoil from the aquifer solids following their production from alpha decay. This deficiency is attributed to adsorption of these nuclides from solution onto adjoining solid surfaces. Using the equations of (8.9) and (8.10), the time scale involved with the removal is estimated to be rapid, of the order of minutes or less (Krishnaswami et al. 1982). From the distribution of thorium isotopes (^{234}Th-^{228}Th) and Ra (^{224}Ra-^{228}Ra), the adsorption is reported to be reversible. The retardation

factor calculated using Eq. (8.11), reported to vary from 4.5×10^3 to 2.0×10^5 for various nuclides in different aquifers (Krishnaswami et al. 1982, 1991; Swarzenski et al. 2013). However, the retardation factors in subsurface shallow brines for Ra in is found to be 3–4 orders of magnitude lower than that in potable ground waters and the residence time of Ra was reported to be ~ 1 day, as opposed to less than a few minutes in potable waters. These observations suggest that Ra is considerably less 'particle-reactive' in saline waters compared to potable groundwater (Krishnaswami et al. 1991).

8.4.4   Radon as a Tracer for Monitoring NAPL Contamination in Groundwater

One of the key properties of radon is that it has a high solubility in organic liquids and hence this property can be utilized to investigate the partitioning of radon between organic solvents and water. Being ubiquitous in subsurface environment, radon has been utilized for three related applications: (i) residual NAPL contamination in soils; (ii) residual NAPL contamination in aquifers and (iii) monitoring the effectiveness of remediation of dissolved NAPL in groundwater (e.g., Schubert 2015). Subsurface contamination with non-aqueous phase liquid (NAPL) is a common problem in sites such as gas stations, military bases, airports and industrial plants among others. Often the contamination arises from leaking pipelines, pumps or storage tanks and the NAPL not only enters the vadose zone of the soil but also it enters the saturated zone or the aquifer. Although the light NAPL (LNAPL, density is less than water, $\rho_{NAPL} < 1.0$ g cm^{-3}) often occupy some of the capillary fringe as well remain on the top of the aquifer, the relative amount in each phase could gradually change with depth. Quantitative estimation of residual NAPL saturation of the aquifer pore space at any particular site is difficult to estimate. Preferential partitioning of radon into NAPL can therefore be applied for the quantitative determination of residual NAPL in an aquifer (Hunkeler et al. 1997; Semprini et al. 2000; Schubert et al. 2001, 2007a, b; Davis et al. 2005).

It was demonstrated that in areas contaminated with residual NAPL, the preferential dissolution of radon in the residual organic phase results in a local radon deficit in the groundwater with regard to its natural aquifer-specific background concentration (Schubert et al. 2007a). A thermodynamic explanation for radon partitioning in NAPL is given in Schubert et al. (2007b).

Radon solubility in pure NAPLs is often expressed in terms of the Ostwald coefficient (L), which is the ratio of the equilibrium radon concentrations in NAPL (C_{NAPL}) to air (C_{air}). Note that L is independent of the partial pressure of ^{222}Rn (which is very small in the environment) if ideal gas behavior and Henry's Law are applicable (Schubert et al. 2007a). The NAPL-specific partition coefficient, $K_{NAPL/W}$ is given as:

$$K_{NAPL/W} = C_{NAPL}/C_W = (C_{NAPL}/C_{air}) * (C_{air}/C_W) \qquad (8.12)$$

where C_w is concentration of ^{222}Rn in water.

A summary of radon partition coefficients, $K_{NAPL/W}$, for commonly occurring NAPL and DNAPL are given in Table 8.3. The $K_{NAPL/W}$ values vary between 19 and 60 while for $K_{DNAPL/W}$ for chloroform and CS2 are 53 and 81, respectively (Table 8.3).

8.4.5   Partition Coefficients of Commonly Occurring NAPL and DNAPL

Partitioning of radon into residual organic phase causes its retardation compared to the movement of a conservative tracer (e.g., chloride). The degree of radon deficit in groundwater in a NAPL-contaminated aquifer section depends on the pore space saturated with residual NAPL and on the radon partition coefficient specific for the NAPL present. The degree of retardation is utilized to obtain quantitative information on the residual NAPL saturation of the pore space (Jin et al. 1995).

Table 8.3 Radon partition coefficients $K_{NAPL/W}$ for commonly occurring NAPL and DNAPL mixtures at 23 °C (unless the temperatures are explicitly stated)

Substance[a]	$K_{NAPL/W}$	Reference
Gasoline	38.9	Schubert et al. (2007b)
Diesel	60.0 40 ± 2.3 @ 12 °C	Schubert et al. (2007b), Hunkeler et al. (1997)
Kerosene	47.4	Schubert et al. (2007b)
Ethanol	27.9	Schubert et al. (2007b)
Hexane	57.2 ± 3.1	Schubert et al. (2007b)
Benzene	40.8 ± 5.7	Schubert et al. (2007b)
Toluene	46.8 ± 0.4 42 @ 10 °C	Schubert et al. (2007b), Hunkeler et al. (1997)
Trichloroethylene	32 ± 1	Hunkeler et al. 1997
Trichloromethane	24 ± 1	Hunkeler et al. (1997)
o-dichlorobenzene	45 ± 2	Hunkeler et al. (1997)
Xylene	54	Semprini et al. (2000)
Di-ethyl-ether	53	Semprini et al. (2000)
1-Pentanol	37	Semprini et al. (2000)
2-Butanol	26	Semprini et al. (2000)
Methanol	19	Semprini et al. (2000)
SF$_6$	32 ± 1	Hunkeler et al. (1997)
Substance	$K_{DNAPL/W}$	Reference
Chloroform	53	Semprini et al. (2000)
CS$_2$	81	Semprini et al. (2000)

[a]NAPL mixtures are Gasoline, Diesel and Kerosene

When NAPL is also present in the pore space, the radon will be present in both the water and the NAPL phases and Eq. (8.11) can be modified as follows (Semprini et al. 2000):

$$C_n S_n + C_w S_w = \frac{C_{Ra} E_p \rho_b}{\phi}.$$
(8.13)

where C_n and C_w are the concentrations of ^{222}Rn in the NAPL and water phases, respectively, and S_n and S_w are the NAPL and water phase saturations, respectively; C_{Ra} is concentration of ^{226}Ra in aquifer solids (Bq kg^{-1}), E_p is emanating power, ρ_b is aquifer solids bulk density (kg m^{-3}) and ϕ is porosity.

Assuming linear partitioning of radon between water and NAPL:

$$C_n = K_c C_w$$
(8.14)

where K_c is the water/NAPL partition coefficient, and C_w is the steady-state concentration of radon in water in the presence of NAPL. Substituting Eq. (8.14) into Eq. (8.13) and rearranging,

$$C_w = \frac{C_{Ra} E_p \rho_b / \phi}{1 + S_n(K - 1)}.$$
(8.15)

Equation (8.15) can be rearranged to obtain the deficit in radon concentration in the presence of NAPL:

$$\frac{C_{w(NAPL)}}{C_{w(background)}} = \frac{1}{1 + S_{NAPL}(K_c - 1)},$$
(8.16)

where $C_{w(\text{NAPL})}$ is radon concentration (Bq m^{-3}) in a groundwater sample from the NAPL contaminated zone, and $C_{w(\text{background})}$ is radon concentration (Bq m^{-3}) in a 'background' groundwater sample from outside the NAPL contaminated zone as given in Eq. (8.11). Radon deficit determination requires radon NAPL/water partition coefficient. A summary of partition coefficient for commonly-occurring NAPL and DNAPL (Table 8.3) shows that the NAPL partition coefficient varies between 19 and 60 while those for DNAPLs (CHCl$_3$ and CS$_2$) have K_c values of 53 and 81, respectively. The equilibrium partition model predictions based on Eq. (8.16) indicate that the radon deficit is extremely sensitive to the presence of small residual NAPL saturations (Semprini et al. 2000). For a K_c value of 50, the estimated value for a chlorinated solvent, a residual saturation of only 1 %, results in a 33 % reduction in the aqueous radon concentration (Fig. 8.3, Semprini et al. 2000). The model Eq. (8.16) assumes that the radon emanation rate remains constant in both the background area as well as in areas with NAPL contamination.
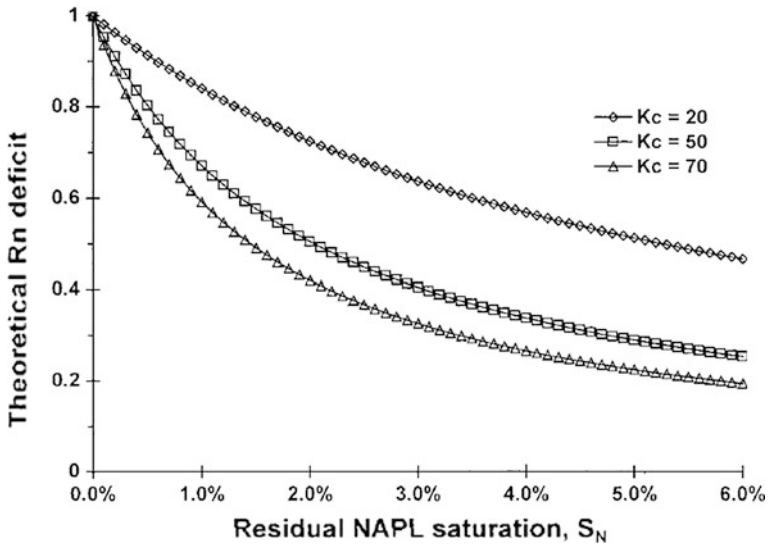
Fig. 8.3 Equilibrium partitioning model-predicted (based on Eq. 8.16) radon deficit for several values of the NAPL/water radon partition coefficient, K_c. The radon deficit is extremely sensitive to the presence of small residual NAPL saturations. For a K_c value of 50, a residual saturation of ~1 %, results in 33 % reduction in the aqueous ^{222}Rn concentration (figure taken from Semprini et al. 2000; permission from Kluwer Academic Publishers)

8.4.6 Subsurface Horizontal Transport of Radon with NAPL Partitioning

In order to identify and quantify the residual NAPL saturations in subsurface, a one-dimensional flow and transport model for radon has been used that simulates the distributions of radon (Hunkeler et al. 1997; Samprini et al. 2000). This model includes dispersive ($\frac{D\phi\partial^2 C}{\partial x^2}$) and advective ($\frac{\partial(VC)}{\partial x}$) transport of ^{222}Rn by groundwater flow, radioactive decay of ^{222}Rn ($\lambda\phi C$), and ^{222}Rn emanation from aquifer solids ($E\rho_b\lambda$) and equilibrium partitioning between the stationary residual NAPL phase and the mobile groundwater phase.

$$\frac{\partial(\phi C)}{\partial t} = \frac{D\phi\partial^2 C}{\partial x^2} - \frac{\partial(VC)}{\partial x} - \lambda\phi C + E\rho_b\lambda, \qquad (8.17)$$

where D is the dispersion coefficient (m^2/d), V is the Darcy velocity (m/d), and λ is the first-order decay constant for radon (0.00754 h^{-1}) and E represents radon emanation factor radium concentration of the aquifer solids times the emanation power ($C_{Ra} \times E_p$). It is assumed that the radon emanation, E, is constant and independent of the radon concentration in the pore fluid (Tanner 1978; Fleischer 1983). The two-phase radon transport (aqueous phase ^{222}Rn and NAPL phase

^{222}Rn) includes properties of radon's NAPL/water partitioning and is accomplishing by treating these phases separately. This model assumes that radon emanation is independent of the pore fluid saturation.

$$\frac{\phi\partial(C_wS_w + C_nS_n)}{\partial t} = \frac{D\phi S_w\partial^2 C_w}{\partial x^2} + \frac{D\phi S_n\partial^2 C_n}{\partial x^2} - \frac{\partial(C_wV_w)}{\partial x} - \frac{\partial(C_nV_n)}{\partial x} - \lambda\phi C_wS_w$$
$$- \lambda\phi C_nS_n + E\rho_b\lambda.$$

(8.18)

Most of the NAPL is highly particle-reactive and so it is reasonable to assume it is immobile. The two-phase radon transport Eq. (8.18) reduces to

$$\frac{\phi\partial(C_wS_w + C_nS_n)}{\partial t} = \frac{D\phi S_w\partial^2 C_w}{\partial x^2} - \frac{\partial(C_wV_w)}{\partial x} - \lambda\phi C_wS_w - \lambda\phi C_nS_n + E\rho_b\lambda$$

(8.19)

Note that each of the term is defined earlier.

If we assume that equilibrium partitioning is achieved, and the local equilibrium assumption applies, and substituting Eq. (8.14) into (8.19) and after rearrangement, the two-phase radon transport equation becomes:

$$\left(1 + \frac{K_cS_n}{S_w}\right)\frac{\partial C_w}{\partial t} = \frac{1}{S_w\phi}\left[\frac{D\phi S_w\partial^2 C_w}{\partial x^2} - \frac{\partial(C_wV_w)}{\partial x} + E\lambda\rho_b\right] - \lambda C_w\left(1 + \frac{K_cS_n}{S_w}\right)$$

(8.20)

The inherent assumption in Eq. (8.20) is that the residual NAPL saturation does not change (i.e. the NAPL is not slowly dissolving) in the time-scale comparable to the mean-life of ^{222}Rn and in the typical time scale simulations of ~ 1 month (or less) to achieve steady-state spatial distribution. The retardation factor is given by

$$R = 1 + \frac{K_cS_n}{S_w}.$$

(8.21)

After substitution of Eq. (8.21) into Eq. (8.20) and rearranging the Eq. (8.20), the aqueous phase radon transport in saturated soil equation is expressed as

$$\frac{\partial C_w}{\partial t} = \frac{1}{S_w\phi R}\left[\frac{D\phi S_w\partial^2 C_w}{\partial x^2} - \frac{\partial(C_wV_w)}{\partial x} + E\lambda\rho_b\right]\lambda C_w$$

(8.22)

Note that under the assumptions of steady-state conditions and no flow, Eq. (8.16) can be obtained from Eq. (8.21). Equation (8.22) can be solved numerically using the finite difference method. A number of analytical solutions to a set of equations and formulations (e.g. dispersion equation, steady-state radon transport equation with advection, etc.) have been reported and the details are given in Semprini et al. (2000).

Some of the advantages in using radon are that radon is a ubiquitous and natural constituent of groundwater and the determination of groundwater production rates is fairly straight forward. The limitations of using radon as naturally occurring partitioning tracer for the assessment of residual NAPL contamination of aquifers include: (i) possible inhomogeneity in the aquifer matrix and radium affecting the assumption of uniform production of radon uniformly throughout the investigated aquifer portion; (ii) local changes in the permeability of the aquifer associated with preferential groundwater paths bypassing isolated sub-domains of the aquifer; and (iii) considerable alterations in the composition of a complex NAPL mixture (mole fractions) may occur as a result of NAPL ageing as some more soluble or volatile components eventually result in significant change of the radon partition coefficient of the remaining residual NAPL (Schubert et al. 2007b).

Other methods utilized to trace the movement of NAPL contaminants have their limitation as well. Tracers such as SF_6 or alcohols have to be injected into the aquifer which results in additional expenditure and may cause technical or even legal problems (Schubert et al. 2000). Conventional techniques such as drilling and core-sampling the vadose zone and by installing wells to collect groundwater samples and subsequent laboratory analysis of aquifer samples are time consuming and expensive. Overall, accurate localization and quantitative estimation of the residual NAPL (or NAPL source zone) is challenging due to usually erratic and patchy shape of the contamination (Schubert et al. 2007a, b).

8.4.7   Other Applications of Radon in Groundwater

Radon-222 has been used as a tracer to investigate movement of formation waters derived from granitic rocks surrounding the Cajor Pass borehole (Hammond et al. 1988). From the measured gradient in ^{222}Rn activity in the borehole, Hammond et al. inferred that the inputs of radon to water are localized and occurs primarily in several, localized, discrete fracture zones. Using a simple recoil model and using permeability data, they reported limiting estimates for fracture size, density and porosity. Refinement of such studies requires detailed studies of fracture distribution and radium distribution along fracture walls and grain boundaries.

Another application of radon as a tracer is to quantify the amounts of submarine groundwater discharge which is discussed in Sect. 6.7 (also a review paper by Burnett et al. 2006). Uncertainties resulting from the use of ^{222}Rn as a tracer for quantitative submarine groundwater discharge discussed in Burnett et al. (2007). Radon-220 (known as thoron, a decay product in the ^{232}Th-series) has the same chemical properties as ^{222}Rn, but has a much shorter half-life ($T_{1/2}$: 56 s) compared to ^{222}Rn ($T_{1/2}$: 3.82 d). Detection of thoron in the environment indicates the source of radon is nearby. In natural waters, sources of thoron should indicate the points of groundwater discharges more precisely than ^{222}Rn. From the spatial variability of thoron in canals of Bangkok, Thailand, it was shown that the seepage of water into canals is not uniform (Chanyotha et al. 2014; Swarzenski et al. 2015).

8.5   Future Research

There is a large spatial (even within a small scale of 10–100 m in aquifers) and temporal variations in the concentrations of radon and the factors and processes that control these variations need further investigations. Radon serves as a powerful tracer in locating and quantifying the amount of non-aqueous phase liquids present in subsurface contaminated waste or industrial site. Radon not only has the potential of having spatial resolution on the sub-decameter level that enables it as a suitable in situ monitoring tool to locate free-phase plumes of LNAPLs, but also to determine the surface trace of their boundaries with enough accuracy needed for the purposes of site assessment and site remediation. This radon method is low-cost, noninvasive and nondestructive method for quantifying NAPL contamination. For the radon method to work more effectively other factors that can affect radon emanation rates will have to be better understood. The heterogeneities in porosity and radon emanation rates will have direct bearing on the measured ^{222}Rn activity concentrations and thus, the effect of potential geological variability on radon emanation rates within contaminated zones needs a thorough investigation. The possibility of dating groundwater using ^{4}He/^{222}Rn ratio has not been utilized widely. The factors that affect the release rates of ^{4}He needs further investigation. The retardation factors calculated for Ra isotopes from the radioactive daughters of naturally-occurring ^{238}U and ^{232}Th series isotopes vary widely depending on the ionic strength of the solution. More studies are needed to identify the in situ parameters that control the sorption characteristics of radium from the measurements of naturally occurring U-Th series radionuclides. Thoron has the potential to investigate the uniformity of seepage of groundwater at the sediment-water interface in rivers, canals and coastal areas and thus can serve as an excellent prospecting tool.

References

Agarwal M, Gupta SK, Deshpande RD, Yadava MG (2006) Helium, radon and radiocarbon studies on a regional aquifer system of the North Gujarat-Cambay region, India. Chem Geol 228:209–232

Andrews JN, Wood DF (1972) Mechanism of radon release in rock matrices and entry into groundwaters. Trans Inst Mining Metall B81:198–209

Asikainen K (1981) State of disequilibrium between ^{238}U, ^{234}U, ^{226}Ra and ^{222}Rn in groundwater from bedrock. Geochim Cosmochim Acta 45:201–206

Baskaran M, Novell T, Nash K, Ruberg SA, Johengen T, Hawley N, Klump JV, Biddanda BA (2016) Tracing the seepage of surface sinkhole vent waters into Lake Huron using radium and stable isotopes of oxygen and hydrogen. Aquat Geochem. doi:10.1007/s10498-015-9286-7

Bonotto DM (2004) Doses from Rn-222, Ra-226 and Ra-228 in groundwater from Guarani aquifer, South America. J Environ Radioact 76:319–335

Broecker WS, Peng TH (1982) Traces in the Sea. Eldigo Press, pp 690

Burnett WC et al (2006) Quantifying submarine groundwater discharge in the coastal zone via multiple methods. Sci Total Environ 367:498–543

Burnett WC et al (2007) Remaining uncertainties in the use of Rn-222 as a quantitative tracer of submarine groundwater discharge. In: Sanford W, Langevin C, Polemio M, Povinec P (eds) A new focus on groundwater–seawater interactions. International Association of Hydrological Sciences Publication, vol 312, pp 109–118

Chanyotha S, Kranrod C, Burnett WC, Lane-Smith D, Simko J (2014) Prospecting for groundwater discharge in the canals of Bangkok via natural radon and thoron. J Hydrol 519:1485–1492

Chung Y-C (1981) Radium-226 and radon-222 in Southern California groundwater: spatial variations and correlations. Geophys Res Lett 8(5):457–460

Copenhaver SA, Krishnaswami S, Turekian KK et al (1993) Retardation of ^{238}U and ^{232}Th decay chain radionuclides in long island and Connecticut aquifers. Geochim Cosmochim Acta 57:597–603

Davis BM, Istok JD, Semprini L (2005) Numerical simulations of radon as an in-situ partitioning tracer for quantifying NAPL contamination using push-pull tests. J Contam Hydrol 78:87–103

Eakin M, Brownlee SJ, Baskaran M, Barbero L (2016) Mechanisms of radon loss from zircon: Microstructural controls on emanation and diffusion. Geochim Cosmochim Acta 184:212–226

Fleischer RL (1983) Theory of alpha-recoil effects on radon release and isotopic disequilibrium. Geochim Cosmochim Acta 47(4):779–784

Fleischer RL, Raabe RO (1978) Recoiling alpha-emitting nuclei: mechanisms for uranium-series disequilbrium. Geochim Cosmochim Acta 42:973–978

Garver E, Baskaran M (2004) Effects of heating on the emanation rates of radon 222 from a suite of natural minerals. Appl Radiat Isot 61:1477–1485

Hammond DE, Leslie BW, Ku T-L, Torgersen T (1988) ^{222}Rn concentrations in deep formation waters and the geohydrology of the Cajon Pass borehole. Geophys Res Lett 15(9):1045–1048

Hoehn E, von Gunten HR (1989) Radon in groundwater—a tool to assess infiltration from surface waters in aquifers. Water Resour Res 25(8):1795–1803

Hoehn E, von Gunten HR (1992) Radon-222 as a groundwater tracer– a laboratory study. Environ Sci Technol 26(4):734–738

Hunkeler D, Hoehn E, Hohener P, Zeyer J (1997) ^{222}Rn as a partitioning tracer to detect diesel fuel contamination in aquifer: laboratory study and field observations. Environ Sci Technol 31 (11):3180–3187

Hussain N, Krishnaswami S (1982) U-238 series radioactive disequilibrium in groundwaters: implications to the origin of excess U-234 and fate of reactive pollutants. Geochim Cosmochim Acta 44:1287–1291

IAEA (2014) The environmental behaviour of radium: revised edition http://www-pub.iaea.org/MTCD/Publications/PDF/trs476_web.pdf

Jin M, Delshad M, Dwarakanath V, McKinney DC, Pope GA, Sepehrnoori K, Tilburg CE (1995) Partitioning tracer test for detection, estimation, and monitoring the remediation performance assessment of subsurface nonaqueous phase liquids. Water Resour Res 31(5):1201–1211

Kighoshi K (1971) Alpha recoil ^{234}Th: dissolution in water and the ^{234}U/^{238}U disequilibrium in nature. Science 173:47–48

Krishnaswami S, Graustein WC, Turekian KK, Dowd JF (1982) Radium, thorium, and radioactive isotopes in ground waters: application to the in situ determination of adsorption-desorption rate constants and retardation factors. Water Resour Res 18:1633–1645

Krishnaswami S, Bhushan R, Baskaran M (1991) Radium isotopes and 222Rn in shallow brines, Kharagoda (India). Chem Geology 87:125–136

Ku T-L, Luo S, Leslie BW, Hammond DE (1992) Decay-series disequilibria applied to the study of rock-water interaction and geothermal systems. In: Ivanovich M, Harmon RS (eds) Uranium-series disequilibrium-application to earth, marine and environmental sciences. Clarendon Press, Oxford, pp 631–668

Langmuir D, Riese AC (1985) The thermodynamic properties of radium. Geochim Cosmochim Acta 49:1593–1601

Langmuir D, Melchior D (1985) The geochemistry of Ca, Sr, Ba and Ra sulfates in some deep brines from the Palo Duro Basin. Texas Geochim Cosmochim Acta 49:2423–2432

Luo SD, Ku T-L, Roback R et al (2000) In-situ radionuclide transport and preferential groundwater flows at INELL (Idaho): decay-series disequilibrium studies. Geochim Cosmochim Acta 64:867–881

Martin P, Akber RA (1999) Radium isotopes as indicators of adsorption-desorption interactions and barite formation in groundwater. J Environ Radioact 46(3):271–286

Perrier F, Richon P, Byrdina S et al (2009) A direct evidence for high carbon dioxide and radon-222 discharge in Central Nepal. Earth Planet Sci Lett 278(3–4):198–207

Porcelli D (2008) Investigating groundwater processes using U- and Th-series nuclides. In: Krishnaswami S, Cochran JK (eds) Radioactivity in the environment, vol 13. doi:10.1016/S1569-4860(07)00004-6

Porcelli D, Swarzenski PW (2003) The behavior of U- and Th-series nuclides in groundwater. Rev Mineral Geochem 52(1):317–361

Reynolds BC, Wasserburg GJ, Baskaran M (2003) The transport of U- and Th-series radionuclides in sandy confined aquifers. Geochim Cosmochim Acta 67:1955–1972

Savoy L, Surbeck H, Hunkeler D (2011) Radon and CO_2 as natural tracers to investigate the recharge dynamics of karst aquifers. J Hydrol 406:148–157

Schubert M (2015) Using radon as environmental tracer for the assessment of subsurface non-aqueous phase liquid (NAPL) contamination—a review. Eur Phys J Special Topics 224 (4):717–730

Schubert M, Fryer K, Treutler HC et al (2000) Radon-222 as an indicator of subsurface NAPL contamination. In: Bjerg PL, Engesgaard P, Krom TD (eds) International Conference on Groundwater Research, Copenhagen, Denmark, June 6–8 2000

Schubert M, Paschke A, Lau S et al (2007a) Radon as a naturally occurring tracer for the assessment of residual NAPL contamination of aquifers. Environ Pollut 145:920–927

Schubert M, Lehmann K, Paschke A (2007b) Determination of radon partition coefficients between water and organic liquids and their utilization for the assessment of subsurface NAPL contamination. Sci Total Environ 376:306–316

Semprini L, Hopkins OS, Tasker BR (2000) Laboratory, field and modeling studies of Radon-222 as a natural tracer for monitoring NAPL contamination. Transp Porous Media 38:223–240

Stellato L, Terrasi F, Marzaioli F, Belli M, Sansone U, Celico F (2013) Is ^{222}Rn a suitable tracer of stream-groundwater interactions? A case study from Italy. Appl Geochem 32:108–117

Sturchio NC, Banner JL, Binz CM, Heraty LB, Musgrove M (2001) Radium geochemistry of ground waters in Paleozoic carbonate aquifers, midcontinents USA. Appl Geochem 16:109–122

Swarzenski PW, Baskaran M, Rosenbauer RJ, Edwards BD, Land M (2013) A combined radio- and stable-isotopic study of a California coastal aquifer system. Water 5(2):480–504. doi:10.3390/w5020480

Swarzenski PW et al (2015) Observations of nearshore groundwater discharge: Kahekili Beach Park submarine springs, Maui, Hawaii. J Hydrol Reg Stud. 10.1016/j.erjh.2015.12.056

Szabo Z, DePaul VT, Fischer JM, Kraemer TF, Jacobsen E (2012) Occurrence and geochemistry of radium in water from principal drinking-water aquifer systems of the United States. Appl Geochem 27:729–752

Tanner AB (1964) Radon migration in the ground: a review. In: Adams JAS, Lowder WM (eds) The natural radiation environment. Univ. of Chicago Press, Chicago, Illinois, p 161

Tanner AB (1978) Radon migration in the ground: a supplementary review. In: Gessel T, Lowder W (eds) The natural radiation environment III. Department of Energy, Oak Ridge, TN, pp 5–56

Torgersen T (1980). Controls on pore-fluid concentration of He-4 and Rn-222 and the calculation of He-4-Rn-222 ages. J Geochem Exploration 13(1):57–75

Tricca A, Wasserburg GJ, Porcelli D, Baskaran M (2001) The transport of U- and Th-series nuclides in a sandy unconfined aquifer. Geochim Cosmochim Acta 65:1187–1210

Whitehead NE (1980) Radon measurements at three New Zealand and geothermal areas. Geothermics 9:279–286

Chapter 9
Radon: A Tracer for Geochemical Exploration

9.1 Introduction

Radon is a unique element in the radioactive decay of ^{238}U that has properties quite different from the other elements in the ^{238}U-decay chain. Because ^{222}Rn is radioactive and has a short half-life, it can be detected at extremely low activity levels and thus provide a basis for a very sensitive geochemical exploration method. For example, a typical 1 pCi ^{222}Rn activity (=2.22 disintegrations per minute (dpm) = 37 mBq) has a total number 17,262 atoms which corresponds to 2.93×10^{-20} mol of radon which can be easily detected by a suitable method (Chap. 2). Variations in radon activity on earth surface has been extensively studied as it provides a clue to the locations of uranium ore, hydrocarbon deposits, geothermal resources and impending earthquakes and/or volcanic eruptions. Aerial surveys have been conducted to detect the uranium sources. Identification of these resources or prediction of the earthquakes or volcanic eruptions is often made with the measurements of radon in soil gas generally within the upper 1 m from Earth's surface. To get a better understanding of the variations of soil gas radon activity requires that a thorough investigation of the subsurface vertical motion of the radon gas be made.

The activity of ^{222}Rn in soil gas is usually an expression of how much ^{226}Ra is present locally (with in <2 m from earth surface) and how easily ^{222}Rn can escape from the soil grains that contain the radium. The three factors that determine the soil ^{222}Rn activity are the diffusion, advective transport of radon with other gases (or gas flows caused by advective transport; e.g. hydrocarbon gases from micro-seepage) and radioactive decay. If diffusion and radioactive decay are the only two deciding factors, then, the mean diffusion distance, L, is given by: $L \sim \sqrt{D\tau} \sim 1.2$ m, where D is the molecular diffusion coefficient of ^{222}Rn in air and τ is its mean life (=4.766×10^5 s). The characteristic distance traveled by an atom of ^{220}Rn or ^{219}Rn is too small because both are too short-lived and hence move very little distance (<2 cm for ^{220}Rn (half-life = 55.6 s) and <0.5 cm for ^{219}Rn (half-life = 3.96 s)) during their life-time and hence they are not of any

consequence. Radon escape to the atmosphere from earth surface results in ^{222}Rn concentration very close to zero at the surface and a vertical plot of ^{222}Rn with depth subsurface has the characteristic of an exponential variation with depth, depending on the effects of upward ^{222}Rn flow and diffusion (Grammakov 1936).

9.2 Attenuation of Gamma-Rays Emitted from Radon Daughter Nuclides

Gamma-rays emitted from the daughter products of ^{222}Rn (^{214}Pb, ^{214}Bi, Chap. 1, Table 1.6a) at earth's surface do not loose energy continuously along their paths as do charged particles such as electrons and alpha particles. The photons interact with matter via three fundamental processes: photoelectric effect, Compton Effect and pair production. In photoelectric effect and pair production, the entire energy of the photon is transferred to the medium in a single interaction while in Compton Effect, the photon may transfer only a part of its energy to an electron and the photon is degraded in energy. Thus the absorption of the gamma-ray in matter is exponential with a half-thickness greater than the range of beta particles of the same energy. The average specific ionization of a gamma ray is about 1–10 % of that caused by an electron of the same energy. The ionization observed for gamma rays is almost entirely secondary in nature. The average gamma-ray energy loss per ion pair formed is about 35 keV in air, similar to beta rays.

If I_0 is the incident intensity of the gamma rays, the intensity transmitted through a thickness d is given by

$$I_d = I_0 e^{-\mu d} \tag{9.1}$$

where μ is the absorption coefficient (note that this is the total absorption coefficient which is the sum of the absorption coefficients for photoelectric effect, Compton scattering, and pair production). The half-thickness, $d_{1/2}$, is defined as the thickness which makes $I_d = \frac{1}{2} I_0$; $d_{1/2} = 0.693/\mu$. The absorber thickness is often given in terms of surface density, ρd (in grams cm^{-2}). In terms of mass absorption coefficient, μ/ρ, Eq. (9.1) is given by:

$$I_d = I_0 e^{-(\mu/\rho)\rho d} \tag{9.2}$$

As can be seen in Eq. (9.2), the intensity at any depth is a function of the density of host matrix. High density minerals have high attenuation coefficient for lower gamma-ray energies (e.g., 46.5 keV of ^{210}Pb in the decay chain of ^{222}Rn has much higher attenuation for high-density (and high-temperature) minerals such as zircon, monazite, apatite compared to low density (and low-temperature) minerals such as feldspars, although the attenuation is not significant at 352 keV (^{214}Pb gamma-energy). Typically, gamma energy will be absorbed by $\sim$100 m of air column.

9.3   Transport of Radon in Subsurface Environment

9.3.1   Radon Transport Processes Below Earth's Surface

The normal radon concentration of soil gas is typically in the range of 10–1,000 pCi/L (370 Bq m^{-3} to 3.7×10^4 Bq m^{-3}) which is equivalent to 5×10^{-15} to 5×10^{-17} parts of Rn per part of soil gas on a weight basis (Gingrich 1984, Ramola et al. 1989). Since the mass concentration of Rn is only a very small fraction of the total gases, radon does not act as an independent constituent, but it is always found mixed with all the other soil gases which are mainly air (comprised primarily of CO_2, O_2, N_2, and water vapor). The two major modes of transport of subsurface radon is by diffusion and advection. Diffusion can sufficiently explain the movement of radon atoms out of the rocks and minerals and short distance into open or water-filled pores between particles followed by other transport processes leading to considerably larger distances, up to a few meters. These transport mechanisms are grouped into two major categories: earth-mechanical and fluid convection (Fleischer and Mogro-Campero 1979; Gingrich 1984).

9.3.1.1   Earth-Mechanical Transport Mechanisms

The earth-mechanical transport category includes the following (Gingrich 1984):

- (i)   Barometric pressure changes
- (ii)   Soil- and air-temperature gradients
- (iii)   Wind-turbulence effects on the surface
- (iv)   Earth tidal pumping effects
- (v)   Pore-pressure changes due to seismic stress and
- (vi)   Sweep by other gases, including volatile organic compounds from soil hydrocarbon

It is widely recognized that the atmospheric pressure change causes a pumping effect, bringing radon from buried sources to the surface. However, the impact of pump effect at a depth of 2 m and above are negligible. The transport of ^{222}Rn from where it is produced subsurface to earth's surface takes place through underground channels, fissures and cracks. Transport of radon in some cases is caused by thermal gradients and pressure differentials having various natural origins. Previous research studies have shown that the high wind velocity present for a number of hours will reduce the radon content in the top soil layer. Strong winds reduce the surface pressure enabling the mixing of upper soil air that has high ^{222}Rn concentration with the free atmosphere where the activities are 1–3 orders of magnitude lower (see atmospheric chapter section). Furthermore, short-term ^{222}Rn concentration measurements in the soil gas have exhibited long-term constant variations (6–12 h) and this was attributed to earth tidal effects. The earth tides cause a pumping action by the opening and closing of fractures and pore spaces thus driving

subsurface ^{222}Rn to the surface. Subsurface seismic activities also have been found to result in significant changes in the ^{222}Rn activities in soil gas and groundwater (more details in Chap. 8).

9.3.1.2 Fluid Convection Mechanism for the Transport of Radon

The most common mode of transport of energy in fluids (both air and water) is by convection. Similar to the transport of water vapor from earth surface to the atmosphere, radon that is generated underneath is brought to the surface by fluid convection within the earth. In this process, a convection cell is generated either by water or soil gas by subsurface temperature gradients which cause the lighter, warmer fluids to move upward and cooler fluids to move downward (Fig. 9.1). Uranium orebody is anticipated to generate high heat, due to radioactive decay (both ^{238}U and ^{235}U decay chain), which act as a heat source for the upwelling convection. In areas of high permeability or fracturing, the convection is more effective in the transfer of radon. It has been estimated that the advectional velocities are in the range of ~3 m per day in soil (which implies Rn released at ~15 m subsurface could reach within the mean-life of ^{222}Rn). The temperature gradient subsurface (at average thermal gradient of 30°C/km, for 10–15 m depth, temperature difference is only 0.30°–0.45°C) could change due to changing seasons which would cause changes in the convection cells. When upper layers of the soil are heated during the summer months, an inversion could result (i.e., low density air mass at the surface and colder air mass subsurface) resulting in a barrier that will prevent the rising soil gas reaching the surface resulting in lower radon concentration at the surface. Results from a number of studies have shown that radon activities over known uranium deposits tend to support the convection cell theory, with higher surface air radon activities in the winter and lower values in the summer, as shown in Fig. 9.1 (Mogro-Campero and Fleischer 1977).

The convective fluid mechanism involves fluid flow within the earth caused by the buoyancy induced in either water or air by the geothermal gradient, dT/dz, which could lead to convection cells within the earth. The stability conditions for such a convective flow in a subsurface porous medium depends upon the a number of parameters including hydraulic permeability (K), vertical dimension of the convective region (h), change of fluid density with temperature (dρ/dT), thermal diffusivity of the fluid-filled medium (D), and viscosity of the fluid (η). It has been reported that convection can occur when the following condition is met:

$$Kgh^2(dT/dz)_{net}(d\rho/dT) > 4\pi^2 D\eta \tag{9.3}$$

where g is the gravitational acceleration (9.8 m s^{-2}) and $(dT/dz)_{net}$ is the excess of dT/dz over the adiabatic value. Equation (9.3) predicts for vertical dimension of the convective region of 100 m, and $(dT/dz)_{net}$ = 30 °C/km, convection will occur
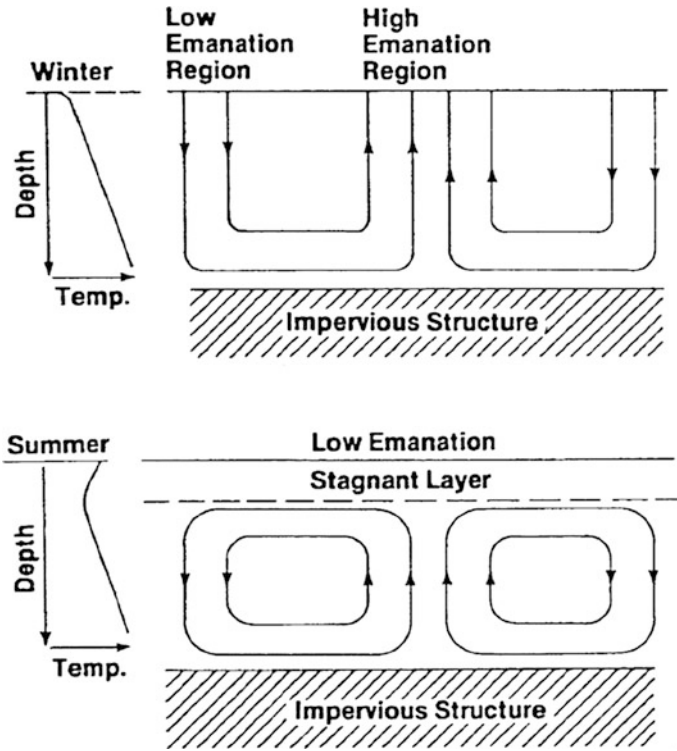
Fig. 9.1 Subsurface fluid convection patterns (Mogro-Campero and Fleischer 1977)—permission from Elsevier Scientific Publishing Company, Amsterdam

(either air or water) in sand ($K > 3 \times 10^{-7}$ cm^2) (Mogro-Campero and Fleischer 1977). On the other hand, for vertical dimension of the convective region of 300 m, convection would occur for K values of $>3 \times 10^{-8}$ cm^2 (corresponding to sand, soil and sandstone of high permeability) and thus, in regions of high permeability, thermally induced sub-terrestrial fluid convection is a potential transport mechanism which could transport radon from up to 300 m from earth surface (Mogro-Campero and Fleischer 1977). Permeabilities of core samples of typical sandstones and mudstones are lower than 1 darcy ($=10^{-8}$ cm^2) whereas model calculation of atmospheric pumping require greater than ~ 500 darcy for the successful transport of radon over distances of ~ 100 m (Fleischer et al. 1980). Note that one can expect the signals from 300 m deep-buried U ore only during fraction of the time when upward convective motion occurs through the near surface ore. Kristiansson and Malmqvist (1982) considered the possibility of long-distance transport of radon to be a result of general upward flow of other gases acting as a carrier for radon. Radon measurements at 60 cm downwards from earth surface showed background patterns that are reproducible over time, but readings taken

over a 13-month period for a set of 55 positions at a site in New Mexico gave nearly constant monthly readings, but there were three periods where the radon data increased by a factor of 2 or more. The source for the increase in sporadic puffs of upflowing radon originating at unknown depths was attributed to possible convective flow (Mogro-Campero and Fleischer 1977).

9.3.2 The Effect of Meteorological Parameters on the Release of Radon from Subsurface

The meteorological parameters such as pressure, temperature, wind speed, both frequency and amount of precipitation can affect the transport time scale of radon from subsurface to surface. When large pressure gradient exists as a result of variations in atmospheric conditions, radon can be transported vertically upward much faster when heterogeneous soils contain large amounts of cracks and channels through which radon could escape (Schery and Siegel 1986). However, if radon were to come from ∼100 m from surface, it is unlikely that atmospheric pressure variation will impact at that depth. Also, from long-term radon measurements from holes at <1 m from the surface, two of the high radon emissions were observed during decreasing pressure, one during increasing pressure and one at a time of constant long-term pressure. The intermittent pressure changes such as those that are associated with frontal passage or with wind effects are short events relative to the monitoring periods and hence it is unlikely to be the cause. Another important factor is the temperature inversion in the planetary boundary layer which will affect the vertical movement of radon from soil to the free atmosphere.

When temperature inversion exists, radon can be trapped close to the surface of the earth, as colder (which is denser) air mass lies above the ground. An estimate on the radon present in the air under temperature inversion condition can be estimated as follows: for a typical radon emanation rate of 1 atom $cm^{-2} s^{-1}$ (21 mBq $m^{-2} s^{-1}$), it is estimated that aerial concentration of radon will range from 0.9 to 74 mBq m^{-3} at 1 m above ground with strong mixing and with inversion, at 100 m above ground will be 15 mBq m^{-3} (Beck 1974). The corresponding gamma-ray dose at 100 m will range from 0.1 to 1.4 mR h^{-1}. This can be compared to the dose rate, from uranium concentration of 2 ppm (∼1.5 dpm g^{-1} or 25 mBq g^{-1}) distributed evenly in the soil, of 0.54 mR h^{-1}. Thus, when temperature inversion exists, radon in air can contribute a major proportion of the total uranium-daughter-derived dose rate. Grasty (1979) reported atmospheric radon contributing between 60 and 80 % of the uranium channel count in one survey. One of the most promising measurements of atmospheric radon is the 352 keV gamma-ray peak of ^{214}Pb (branching ratio: 35.9 %).

9.3.3 Vertical Transport of Radon in Subsurface Soil

Using the conservation of radon mass in subsurface soil and a simple continuity equation, one can derive an equation that describes the vertical transport of radon. This equation was utilized by a number of researchers (e.g., Clements and Wilkening 1974; King 1978; Pinault and Baubron 1996). The two major mechanism by which radon is transported vertically upward from subsurface soil are the advective and diffusional transport. The advective and convective flux density (F_a), which is the mass of radon transported per unit of bulk cross-sectional area per unit time, is given by:

$$F_a = vC \tag{9.4}$$

where C is the concentration of radon in soil gas (=mass of radon per unit volume of air) and v is the Darcy's velocity of soil air (or the volume of air flowing per unit area of bulk cross-sectional area of soil per unit time in the direction z, which is vertically upward towards Earth's surface). The diffusive flux density in soil (F_d), which is the mass of radon transported per unit of bulk cross-sectional area of soil per unit time by diffusion, is defined by Fick's law for molecular diffusion:

$$F_d = D_z \partial(nC)/\partial z \tag{9.5}$$

where D_z is the diffusion coefficient of radon in soil in the direction z, n is the effective gas porosity, and nC is the mass of radon in soil/bulk volume of soil. The diffusion coefficient for radon in soil (D_z) is related to the diffusion coefficient for radon in pure air (D_a) as follows:

$$D_z = D_a \tau_z \tag{9.6}$$

where τ_Z is the coefficient of tortuosity of moist soil.

The conservation of mass of radon results in the following continuity equation:

$$\partial(nC)/\partial t = -\partial F/\partial z - \lambda nC + n\Phi \tag{9.7}$$

where t is time, F is the total flux density (=$F_d + F_a$) in direction z, λ is the ^{222}Rn decay constant, and Φ is the source term (=production rate of radon per unit volume of moist soil pore space). Substituting Eq. (9.5) for F_d and (9.4) for F_a in Eq. (9.7), we get the transport equation:

$$\partial C/\partial t = \partial(D_z \partial C/\partial z)/\partial z - \partial(vC/n)/\partial z - \lambda C + \Phi \tag{9.8}$$

Since diffusion constant along the vertical (upward) is constant, and advectional transport term ($v\,\partial C/\partial z$) is much larger than that of $C\frac{\partial C}{\partial z}$, Eq. (9.8) reduces to:

$$\partial C / \partial t \approx D_z \partial^2 C / \partial z^2 - (v/n) \partial C / \partial z - \lambda C + \Phi \qquad (9.9)$$

The first term in the right hand side of the transport Eq. (9.9) is the diffusion term, the second term is the advective flow term, and the third term is the decay of ^{222}Rn term and the fourth term is the production term. The first term in the right hand side of the transport equation (9.9) is the diffusion term, the second term is the advective flow term, the third term is the decay of ^{222}Rn term and the fourth term is the production term. Using the boundary conditions: $C(0, t) = 0$ and $C(-\infty, t) = \Phi/\lambda$ ^{222}Rn concentration in the soil gas is assumed to be at steady state governed by molecular diffusion alone. The steady state solution for Eq. (9.9) is given by C as a function of z in Clements and Wilkening (1974).

9.4   Radon as Geochemical Exploration Tracer

Measurement of natural radiation arising from the daughter products of radon has found applications in exploration geology. Changes in the activities of radon in soil gas and groundwater are often used as tool in the identification of subsurface uranium ore and hydrocarbon reservoir. Furthermore, radon activity in lake water has been used with some success in exploring hidden uranium deposits located beneath the lake or in adjacent areas draining into the lake (Gingrich 1984). Aerial gamma-ray mapping has been used as a guide for geological mapping, whereas gamma-ray methods have been extensively employed for quantitative determination of uranium (and thorium) in ore-body evaluation.

9.4.1   Radon as a Tool in Uranium Exploration

The major interest in uranium exploration arose in the late 1940s and surface and aerial radioactivity methods for exploration were developed. From long-term measurements of radon, cases have been described in which strong enhancements in radon close to the earth's surface over uranium deposits were observed. In some cases, these uranium deposits were previously known, and in others these deposits were only found after drilling that was guided by the measurements of radon. Note that the concentration of uranium in surface soils varies widely. For example, ^{238}U concentration in surface soils in the United States range between <1 and >5 ppm (Fig. 9.2). A large scale effort on uranium exploration was undertaken by the U.S. Department of Energy's National Uranium Resource Evaluation (NURE) program, started in 1977 and completed in 1982. This five year airborne investigation encompassed measurements of gamma radiation over the entire U.S., from altitudes normalized to 122 m (400 ft.) along flight lines approximately 3–10 km (2–6 miles) apart.
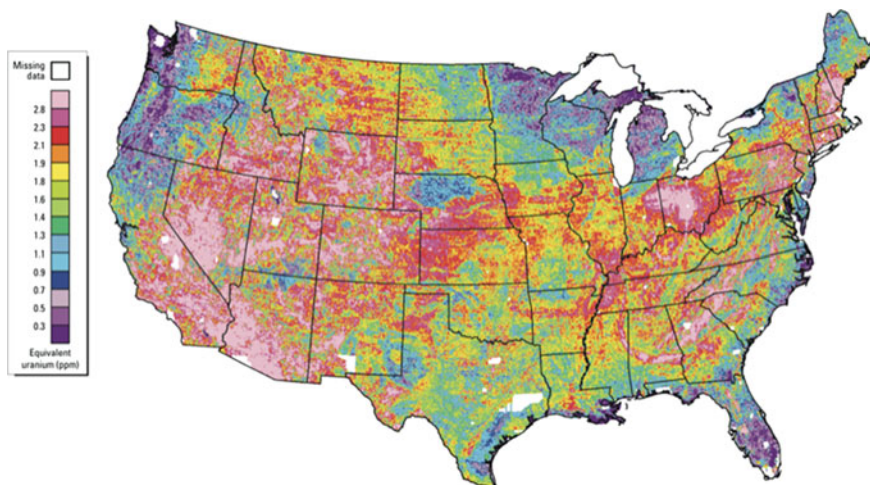
Fig. 9.2 Equivalent uranium concentration in surface soils and rocks of the conterminous United States. Adapted from Duval et al. (2005). Terrestrial Radioactivity and Gamma-ray Exposure in the United States and Canada. Open-file Report 2005-1413. Reston, VA:U.S. Geological Survey

The intensity of gamma radiation from a point source decreases inversely with the square of the distance from the source. Thus, even at 122 m above ground, large detector systems with sufficiently high count rates will be able to register 'hot-spots' of uranium at and near the surface. The gamma rays detected in an aerial survey are commonly emitted from the upper 30 cm of the natural surface material as well as vegetation. Aerial gamma-ray surveys measure gamma rays from the decay of ^{214}Bi (daughter product in the decay chain of ^{222}Rn) and ^{208}Tl (daughter product in the decay chain of ^{220}Rn). The single gamma ray of ^{214}Bi (1.76 MeV) was found to be the most suitable from many major uranium deposit discoveries (Dickson and Wheller 1992). Note the gamma ray from ^{40}K is used to measure the concentration of potassium. Aerial surveys were made using 20–50 l Na(I) detectors mounted in aircraft or helicopters that flew at altitudes between 60 and 200 m at flight-line spacing of 120–1500 m (Bristow 1983; Smith 1985). Emanation of ^{220}Rn from soil and accumulation in the air will have very little effect on aerial surveys, with its diffusion path length of ~ 20 cm in porous soil. However, ^{222}Rn emanation rate from porous soils is 5–50 % and thus, significant amounts of ^{222}Rn produced from the decay of ^{226}Ra in surface materials are therefore lost to the atmosphere. Hence the detector mounted in an aircraft measures both radiation from the ground and atmosphere, with the atmospheric radon resulting in significant background activity. The inherent uncertainties in airborne measurements need to be taken into consideration in the data analysis. However, these data analysis provides us with an important and readily accessible screening tool for a qualitative assessment of uranium potentials in large exploratory areas. The advantage of NURE analysis mentioned earlier is a cost effective starting point for evaluation of large areas.

Radon-222 integrated over several weeks in shallow holes in the earth had also been used in uranium exploration work and also in searching for premonitory earthquake signals (Fleischer and Mogro-Campero 1982; Chap. 8). Many of the uranium ores are located in or along faults from where radon can relatively easily escape through and hence can serve as effective tracer in the identification of the uranium source. For example, uranium deposits in the Athabasca Basin of Canada and the Alligator River area of Australia's Northern Territory (note Australia has 29 % of the global recoverable U as of 2013, with 1.706 million tons (total global recoverable U estimate: 5.9 million tons); compare this to the total amount of estimated U in the world ocean of 4.2 billion tons (average U activity of 3.2 ppb in seawater)), (http://www.world-nuclear.org/info/Nuclear-Fuel-Cycle/Uranium-Resources/Supply-of-Uranium/) are fault-controlled, and radon was used in both areas for exploration of these hidden deposits. Solid state track detectors placed in inverted cups in the ground recorded high radon readings at points that were more than 100 m above uranium deposits and subsequent drilling led to the discovery of significant uranium ore bodies (Gingrich 1975).

If radon is capable of moving from deep inside the ground, then, locally enhanced concentration of radon near the surface is expected to provide signals for the location of subsurface uranium. Due to its mean life of 5.0 days and its diffusion coefficient in soil gas, it has been demonstrated that ^{222}Rn concentration is reduced by a factor of ~ 2 at distances of about 1 m (Tanner 1964). From a knowledge of the mean diffusion distances of radon in the ground, it is estimated that uranium-enriched rocks and minerals, (10^4 fold higher than the average concentration), lying at ~ 10 m from the surface would be perceptible and certainly no more than ~ 20 m, if radon moves only by diffusion (Fleischer 1988). Diffusion theory in conjunction with the half-life of ^{222}Rn implies that measurable amounts of radon will not arrive from distances of more than 10–15 m from earth surface. Migration of radon from deep inside ($\gg$10 m) to the surface requires a separate transport mechanism. If a mineral ore is located at 100 m from surface, the average velocity required for the signal to reach the surface should be >0.02 cm/s. Of the several study sites where high concentration of radon were reported on earth's surface, one of the most striking sites is the Grants mineral belt area of New Mexico, USA, a site located at 16 km north of Thoreau, Western Nuclear Inc. Uranium ore at a depth of 89 m, which is 40 m above the water table was solely guided by the location of highest ^{222}Rn readings (Mogro-Campero and Fleischer 1977). A more systematic transport mechanism than diffusion was proposed to be likely operative. Geothermally induced convection was proposed as a possible mechanism of transport from deep underground (>100 m). For an ore at 100 m, upward sustained gas motion speed (gas motion speed = flow speed (cm^3/cm^2 s)/porosity) of 3×10^{-3} cm/s are required. While there is no experimental observations that prove that long-distance transport (>10^1–10^2 m) of radon occurs underground, the answer to the question on how faster transport of radon takes place within the earth remains less known.

In subsurface, presence of hydrocarbons produces a reducing environment around the area where they accumulate. This reducing environment causes the

uranyl ion (UO_2^{2+}) dissolved in groundwater to reduce from hexavalent (+VI) to tetravalent (+IV) oxidation state and to precipitate as UO_2 around the pool of hydrocarbons. The chemical reactions for this process is given as:

$$3UO_2^{2+} + CH_4 + H_2O \rightarrow CO + 3UO_2 + 6H^+$$
$$4UO_2^{2+} + CH_4 + 2H_2O \rightarrow CO_2 + 4UO_2 + 8H^+$$
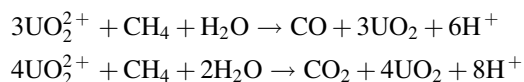
A halo U precipitate could form around the hydrocarbon pool can undergo disintegration and could become a source of radon gas. This radon could migrate upward perhaps jointly with other hydrocarbon vapor through the cracks and faults and could even signal that mark the contour of the subsurface NAPL accumulation (Garcia-Gonzalez et al. 2008).

9.4.2   Limitations in Using ^{222}Rn as a Prospecting Tool

There are limitations on the utility of radon as prospecting tool. In particular, if radon concentration in soil gas are affected by changes in the seasonal temperature variations, barometric pressure and soil moisture content, the migration range of radon could be affected which in turn will add complexity to the interpretation of radon signal in the air. Deposition of ^{226}Ra (either by sorption or precipitation) closer to the surface soil from the flowing groundwater could result in higher amounts of radon release which could also be transported vertically upward due to prevailing atmospheric conditions. Radon escape variability from shallow groundwater aquifers (^{222}Rn/^{226}Ra activity ratios varied from 200 to >10,000, King et al 1982; Asikainen 1981) also could be a possibility in areas where the soils are highly heterogeneous and cracks and channels are present.

9.4.3   Radon as a Tool for Hydrocarbon Exploration

Geochemical measurements in soils have been utilized as indicators of deeper petroleum and natural gas. These measurements include concentration of hydrocarbons such as methane, ethane, propane, and butane in soils (Horvitz 1939), fluorescence (heavy ringed hydrocarbons such as naphthalene, phenanthrene, anthracene in soils indicate possible presence of oil in the subsurface structure), elemental ratios in soils (e.g. Mn/K, Sr/Ca, Fe/S), stable carbon isotopic measurements, radon and other radioactivity (Donovan 1974).

The application of airborne and surface gamma-ray surveys to petroleum exploration has been proposed and has been applied for a long period of time. In most known oil or gas fields in west Texas, USA, Saunders et al. (1987) observed gamma-ray anomalies, with positive equivalent-uranium and negative potassium
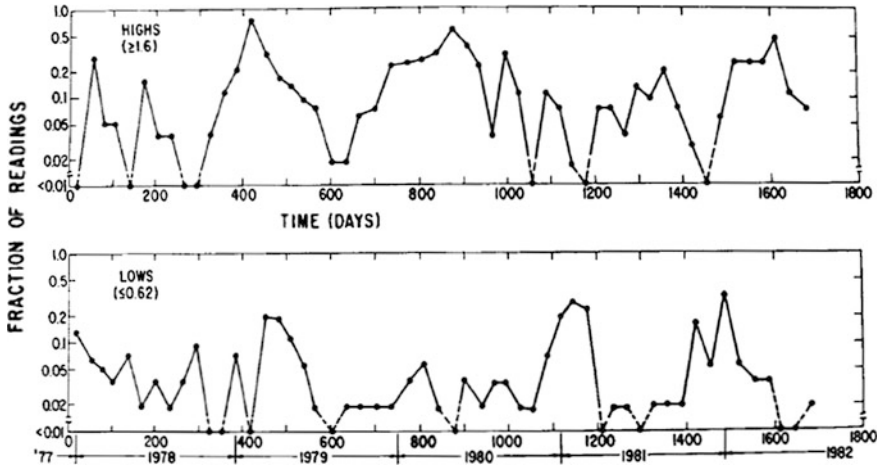
Fig. 9.3 Fraction of radon-monitoring sites that reported meaningfully higher (≥1.6 times the usual value at each individual site) and unusually low readings (≤0.62 times the usual value) at Thoreau, New Mexico, U.S.A. Figure is taken from Fleischer (1988). Courtesy of Elsevier Publications Inc

anomalies in west Texas, likely reflecting trapping of uranium in reduced alteration zones affected by petroleum microseepage and bacterial action. Radiation measurements are made with airborne and truck-mounted total count and spectrometer systems for gamma radiation and solid state detectors deployed in the near surface for alpha daughter products from the decay of radon.

The possible accumulation of uranium (or Ra) around soil reservoirs has resulted in the application of radon or helium methods for petroleum exploration (Philp and Crisp 1982). From a comparison between location of petroleum and the field ^{222}Rn values over a 2-month period at Cement, Oklahoma, U.S.A., Fleischer (1988) reported that the oil and gas were concentrated in a West-Northwest: East-Southeast belt of a 13 km × 16 km and radon map also showed that there were three highest readings over the hydrocarbon-rich region (Fig. 9.3). Radon monitoring data from 54 sites over a period of 4.6 year interval show variations with time of unusually high readings and unusually low readings at Thoreau, New Mexico, U.S.A (Fig. 9.3). Long-term breathing of the earth is also evident in Fig. 9.3 and hence more caution needs to be exercised in interpreting the temporal variations of soil gas radon.

It is speculated that radon can aid in the exploration of hydrocarbon by detecting the micro-seepage from a reservoir. Radon measurements can detect if vertical flow velocities are $>3 \times 10^{-4}$ cm/s (1.08 m/h or 25.9 m/d or 143 m over ^{222}Rn mean-life). A simplified hydrocarbon reservoir in which gases from the edge of a trap create a doughnut-shaped region of upward flow is shown (Fig. 9.4). Due to high pressure gradients caused by release of gases, radon could complex with hydrocarbon gases and travel much faster than the distance traveled by molecular diffusion over ^{222}Rn mean-life. Although hydrocarbon deposits are located at much deeper depths from earth's surface, tracers of residual organic material such as
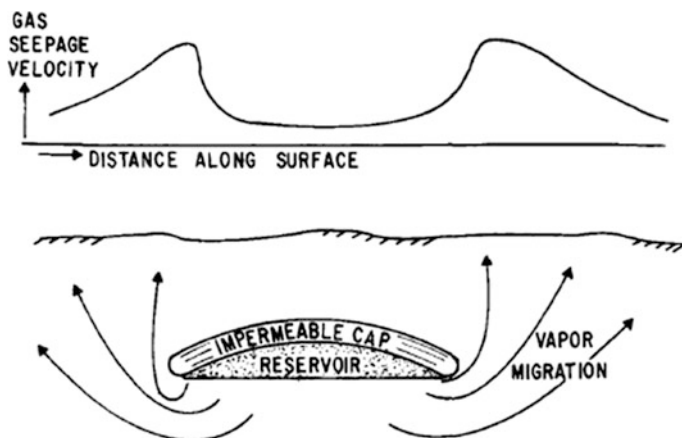
Fig. 9.4 Model gas seepage from a simplified hydrocarbon reservoir. Hydrocarbon or volcanic gases could create pressure gradients that would cause upward flow of radon along with these gass (figure taken from Fleischer 1988. Courtesy of Elsevier Inc.)

benzene, toluene, ethylbenzene and xylenes (BTEX, commonly found in petroleum derivatives such as petrol) are frequently found in soil above the hydrocarbon deposits. Such hydrocarbon residue in soils is attributed to the microseepage mechanism of transport in which vertical ascent of colloidal size gas bubbles migrate through a network of interconnected groundwater-filled 'microfractures.' The bubble buoyancy drives it toward the surface in a near vertical pathway as much as possible. It is likely transported through a large number of networks of joints and bedding planes which provide a highly permeable route through the rock mass. Application of radon and helium in conjunction with measurement of organics in soil gases could serve as a powerful tool for oil and gas exploration.

9.4.4 Detection of Natural Gamma Radiation in Petroleum Exploration Boreholes

Subsurface application of gamma radiation involves conventional downhole logging to measure gamma radiation intensity which is a measure of potassium, uranium and thorium (and their daughter products, i.e. daughter products of ^{238}U-, ^{235}U- and ^{232}Th series radionuclides) and it provides information on lithology, variations of organic carbon, clay typing, permeability and potential recognition of fracture systems. The measurements of the intensity of natural gamma rays in boreholes were initiated in 1935 in the U.S.A. and former U.S.S.R. using either ionization chambers or Geiger-Muller counters. Presence and distribution of radioactive elements in the earth's crust, mainly ^{40}K and U-Th series radionuclides, result in gamma radiation being emitted continuously. A major portion of the gamma-radiation in the

U-Th-series radionuclides is derived from the decay chains of radon (^{214}Bi, ^{214}Pb, ^{212}Pb; Porcelli and Baskaran 2011). There are significant variations of the concentration of gamma-emitting radionuclides, with usually high γ-ray-emitting radionuclides in shales, intermediate in sand and low activities in dense carbonates and anhydrites, although exceptions to this general rule are frequently encountered. The advantages of the gamma-ray logging include: (i) detected easily through steel casing and cement, and the type of fluid in the hole, whether it be liquid or gas, making very little difference; and (ii) the ability to distinguish shales from non-shales, particularly under conditions in which other types of logging tools are useless, making the γ-ray log very useful for lithology determination. Although the counting rate was improved by a factor of 2–3 from the introduction of scintillation detectors using sodium iodide crystals in the early 1950s, its use in commercial logging of natural γ-rays has been limited to the recording of the gross intensity of the γrays. In the assessment of remaining oil reserves in old drill holes, presence of $BaSO_4$ and $RaSO_4$ often occurs on well casings. The Ra can be mobilized by the saline, reducing brines of the formation waters and in cases like this, the gamma emissions from Ra and its daughter products (e.g. ^{214}Pb, ^{214}Bi) could obscure the uranium signal (Krishnaswami et al. 1991; Dickson and Wheller 1992).

9.5 Future Directions

Radon is useful to locate natural resources such as uranium deposits, oil and natural gas fields, and geothermally useful regions. Many of these exploration technique involves measurements of radon in near surface soil and air. There are other meteorological parameters that affect the radon concentration in soils. Combining radon with other noble gases (e.g., He) will likely yield better results and may make radon as a more robust geochemical exploration tracer for uranium and hydrocarbon. The importance of volatile organic compounds such as BTEX in the vertical transport of radon from deep subsurface (>100 m) has been speculated and needs further investigation. Although several mechanisms have been proposed on the radon flow inside the earth, no single mechanism has been firmly established and more work needs to be done to get better understanding of radon flow inside earth.

References

Asikainen M (1981) State of disequilibrium between ^{238}U, ^{234}U, ^{226}Ra and ^{222}Rn in groundwater from bedrock. Geochim Cosmochim Acta 45:201–206

Beck HL (1974) Gamma-radiation from radon daughters in atmosphere. J Geophys Res 79:2215–2221

Bristow Q (1983) Airborne g-ray spectrometry in uranium exploration. Principles and current practice. Int J Appl Radiat Isot 34:199–229

Clements WE, Wilkening MH (1974) Atmospheric pressure effects on [222]Rn transport across the earth-air interface. J Geophys Res 79:5025–5029

Dickson BL, Wheller GE (1992) Uranium-series disequilibrium in exploration geology. In: Ivanovich M, Harmon RS (eds) Uranium-series disequilibrium. Clarendon Press, Oxford, pp 704–730

Donovan TJ (1974) Petroleum microseepage at Cement, Oklahoma: evidence and mechanism. Bull Am Assoc Petrol Geol 58:429–446

Duval JS, Carson JM, Holman PB, Darnley AG (2005) Terrestrial radioactivity and gamma-ray exposure in the United States and Canada. Open-file Report 2005-1413, U.S. Geological Survey, Reston, VA

Fleischer RL (1988) Radon in the environment—opportunities and hazards. Nucl Tracks Radiat Meas 14:421–435

Fleischer RL, Mogro-Campero A (1979) Radon enhancements in the Earth: evidence for intermittent upflows. Geophys Res Lett 6:361–364

Fleischer RL, Mogro-Campero A (1982) Radon transport in the earth: a tool for uranium exploration and earthquake prediction. In: Fowler PH, Clapham VM (eds) Solid state nuclear track detectors (Prof. 11th international SSNTD conference, 7–12 September 1981), pp 501–512, Pergamon Press, Oxford

Fleischer RL, Hart HR, Mogro-Campero A (1980) Radon emanation over an ore body: search for long-distance transport of radon. Nucl Instrum Method 173:169–181

Garcia-Gonzalez JE, Ortega MF, Chocon E et al (2008) Field validation of radon monitoring as a screening methodology for NAPL-contaminated sites. Appl Geochem 23:2753–2758

Gingrich JE (1975) Results from a new uranium exploration method: Trans. AIME 258:61–64

Gingrich JE (1984) Radon as a geochemical exploration tool. J Geochem Explor 21:19–30

Grammakov AG (1936) On the influence of some factors in the spreading of radioactive emanations under natural conditions. Zh Geofiz 6:123–148

Grasty RL (1979) Gamma-ray spectrometric methods in uranium exploration—theory and operational procedures. In: Hood PJ (ed) Geophysics and geochemistry in the search for metallic ores, pp 147–159. Economic Geology Report 31, Geological Survey of Canada

Horvitz L (1939) On geochemical prospecting. J Geophys Res 10:487–493

King C-Y (1978) Radon emanation on San Andreas fault. Nature 271:515–519

King PT, Michel J, Moore WS (1982) Groundwater geochemistry of [228]Ra, [226]Ra and [222]Rn. Geochim Cosmochim Acta 46:1173–1182

Krishnaswami S, Bhushan R, Baskaran M (1991) Radium Isotopes and 222Rn in Shallow Brines, Kharagoda (India). Chem Geol (Isotope Geoscience Section) 87:125–136

Kristiansson K, Malmqvist L (1982) Evidence for nondiffusive transport of Rn-86(222) in the ground and a new physical model for the transport. Geophys 47:1444–1452

Mogro-Campero A, Fleischer RL (1977) Subterrestrial fluid convection: a hypothesis for long-distance migration of radon within the Earth. Earth Planet Sci Lett 34:321–325

Philp RP, Crisp PT (1982) Surface geochemical methods used for oil and gas prospecting—a review. J Geochem Explor 17:1–34

Pinault JL, Baubron JC (1996) Signal processing of soil gas radon, atmospheric pressure, moisture, and soil temperature data: A new approach for radon activity modeling. J Geophys Res 101:3157–3171. doi:10.1029/95JB03121

Porcelli D, Baskaran M (2011) An overview of Isotope Geochemistry in Environmental Studies. In: Baskaran M (ed) Handbook of environmental isotope geochemistry, pp 11–32, Springer. ISBN: 978-3-642-10636-1

Ramola RC, Sandhu AS, Singh M et al (1989) Geochemical-exploration of uranium and using radon measurement techniques. Nucl Gelphys 3(1):57–69

Saunder DF, Terry SA, Thompson CK (1987) Test of National Uranium Resources Evaluation gamma-ray spectral data in petroleum reconnaissance. Geophysics 52:1547–1556

Scherry SD, Siegel D (1986) The role of channels in the transport of radon from the soil.
    J Geophys Res 91B:12366–12374
Smith RJ (1985) Geophysics in Australian mineral exploration. Geophysics 50:2637–2665
Tanner AB (1964) Radon migration in the ground: a review. In: Adams JAS, Lowder WM
    (eds) The natural radiation environment, p 161. Universit of Chicago Press, Chicago, Illinois

Chapter 10
Radon as a Tracer for Earthquake Studies

10.1 Introduction

Radon is one of the most powerful tracers as a precursor to predicting earthquakes. Because of its unique chemical properties (virtually no adsorption, dissolution or precipitation), its movement in subsurface environments is primarily controlled by radioactive decay, diffusion and sometimes by advection (possibly with other gases). Changes in radon activities in soil gas and ground water can provide valuable information on subsurface seismic activity in the earth's crust and provide insights on the earthquake formation process (e.g., Talwani et al. 1980; Silver and Wakita 1996; Wakita 1996). Zones showing a greater than usual outgassing of radon, as observed by ^{222}Rn concentration in soil-gas and ground water, have also shown the presence of subsurface areas with anomalous subsurface heat and increased permeability.

Radon emanation rates from rocks and minerals vary widely, as discussed in Chap. 3. Radon emanation rates have been reported to be higher from seismically active areas including subsurface active faults, as they provide major conduit paths for radon and other gases (such as CO_2, CH_4, N_2, H_2, He, Cl, and F) to escape. The escape rates of gases from subsurface faults are not uniform and they depend on a number of factors that include subsurface porosity, permeability, conductivity of the underlying material, etc. If there is no seismic or volcanic activity in the subsurface environment, then the radon release rates are expected to be relatively constant. However, due to subsurface seismic activities, the rupturing energy released could alter the porosity and permeability of subsurface material affecting the conduit pathways of radon. Due to variations in the stress-strain relationships of the subsurface material, the radon and other noble gases escape could also be heterogeneous, affecting the precursor signal.

The changes in geochemical (chemical composition, radon, tritium, and ^{14}C in groundwater, water temperature), geophysical (geomagnetic field intensity and resistivity) and hydrological parameters (water level, extent of ground upheaval, crustal deformation measurement) preceding significant earthquakes have been reported since the 1960s (a summary of progress of the earthquake prediction program over the first $\sim$30 years in Japan is given in Wakita 1996). The first evidence of a correlation between ^{222}Rn and an earthquake came from highly elevated activity of ^{222}Rn in water from a deep Russian well prior to the Tashkent earthquake of April 26, 1966 (Ulomov and Mahashev 1971; Sadovksy et al. 1972). They reported that radon activities in several deep wells with depths of 1200–2400 m in Tashkent and its vicinity rose progressively and then dropped at the time of a major earthquake to normal level of approximately 19 Bq L^{-1}. This work stimulated much additional research and subsequently played a prominent role in the successful prediction of the Haicheng earthquake (7.3 Richter Scale or M$_s$, on February 4, 1975 in Haicheng, Liaoning, China, a city with a population of approximately 1 million at the time). It is noteworthy that radon measurements played a critical role in the successful prediction of this earthquake (Chinese Seismology Delegation 1976). This was the most successful evacuation before a devastating major earthquake in history. Subsequent to this, a large number of studies in this area with claims reporting correlations between soil gas, ground water radon concentration and earthquakes resulted in a large number of publications as a result of three symposia. This research appeared in the 10th June 1980 *Journal of Geophysical Research*, the May 1981 *Geophysical Research Letters* and the 1984–1985 *Pure and Applied Geophysics* 122, Nos. 2–4 and reader is referred to these special volumes.

In this chapter, mechanisms of vertical transport of radon and the variations of radon concentration in soil gas and groundwater from seismically active regions (both earthquakes and volcanic eruption) are summarized, based on a large number of observations reported in published literature. A summary of our current understanding on how effective soil-gas and groundwater radon levels are in predicting earthquakes and volcanic eruption is given and the potential future areas of research investigation are summarized.

10.2   Mechanism of Vertical Transport of ^{222}Rn in Seismically-Active Areas

Radon emanates into the pore space of rock grains and soils principally by the process of nuclear recoil during its formation from the alpha decay of radium (Tanner 1964; Ishimori et al. 2014). Generally about 10–30 % of radon escapes from grain matrices to pore space for moisture contents above about 20 %. Subsequently, subsurface radon is brought to the surface by molecular diffusion governed by Fick's law and by advection flow governed by Darcy's law. As discussed in Chap. 9, three factors that affect the flow of ^{222}Rn inside the earth are:

(i) geothermally-induced convection; (ii) pre-seismic stresses in the earth and (iii) underground gas emanation. The geothermal gradient inside the earth ($\sim$30 °C/km) induces buoyancy of the fluid which results in fluid flow leading to convection within the earth. As discussed in Chap. 9, thermally induced sub-terrestrial fluid convection is a potential transport mechanism for ^{222}Rn in regions of higher than usual permeability. In areas where many active faults and fracture zones exist, radon and other terrestrial gases can easily escape from underneath and hence ^{222}Rn activities in soil gas and ground water near the earth's surface are generally expected to be higher.

It is well-documented that regions having many active faults are also generally highly impermeable. Prior to major earthquakes, rupturing and energy release will result in significant alteration of the porosity and permeability of the surrounding rocks near the epicenter of the earthquake. As discussed in Chap. 9, any long-distance transport of ^{222}Rn from uranium-ore body to the overlying earth surface depends on the effective permeability in a vertical direction. Laboratory measurements of the permeability of core samples, comprised of typical sandstones and mudstones, yield permeability values generally lower than 1 darcy (10^{-8} cm^2), but model calculations for typical convection requires greater than $\sim$500 darcy for successful transport of radon over distances of $\sim$100 m. During seismic activities, the change in permeability is not routinely measured and hence it is not known how much the permeability changes before, during and after major earthquakes. It is anticipated that excessive seismic stresses over a longer period of time would result in highly fractured material subsurface and under such circumstances radon and other gases can easily escape through cracks and crevices.

Release of intense stresses in a relatively small local region (10^0–10^2 km^2) that can cause earthquakes to have strain fields that are expected to extend to long distances, assuming that the earth acts as an elastic medium. In such a medium, when an area of the ground is squeezed, the pore spaces are narrowed non-linearly and the gas will be extruded. The changes in the porosity and permeability in these areas where seismic activity is intense will result in changes in the ^{222}Rn release rates. Igarashi et al. (1995a, b) attributed the observed anomalous increase in radon concentration in groundwater to the formation of micro-cracks in the aquifer system; sudden reduction in radon concentration one week before the earthquake was attributed to sealing some of the micro-cracks.

Mineral deposits including hydrocarbon deposits that occur subsurface can emit gas which could cause pressure gradients resulting in an upward flow of gases (including radon). The gases can come either from hydrocarbons (such as petroleum or natural gas deposits), noble gases from the decay of uranium, thorium or other volatiles that are derived from minerals. For example, micro-seepage of hydrocarbons results in organic residues in soils. Testing of near-surface soil samples from places where subsurface hydrocarbon deposits are present has shown the presence of benzene, toluene, ethylbenzene and xylenes (commonly known as BTEX), volatile organic compounds (VOCs) that are commonly found in petroleum derivatives such as petrol. The average pressure of the gas (P) generated in a homogenous permeable medium which obeys Darcy's law can be calculated as follows:

$$P = D\,\varepsilon\eta/k \tag{10.1}$$

where ε is porosity, k is permeability, η is viscosity of the gas and D is the pressure diffusivity. Determination of the pressure requires the viscosity of the gas as well as porosity of the permeable medium which cannot be readily calculated. Large scale breakdown of hydrocarbon deposits subsurface in the form of soil residue can generate sufficient pressure in gas which could release CO_2 that can carry radon and other gases including CO_2, CH_4, N_2, H_2, He, Cl and F.

To quantify the effect of vertical flow of soil gas on radon concentration, a one dimensional model has been used. In this model, the soil layer is considered to be a homogenous medium for the upper >10 m with uniform radon production. The vertical transport of radon is regulated by two processes: (i) molecular diffusion governed by Fick's law and (ii) gas flow governed by Darcy's law. Using a standard continuity equation for radon and applying the standard boundary condition that radon concentration is negligible at ground surface, the steady-state result for radon concentration (C, atom m^{-3}) as a function of depth ($-z$) is given by the equation (given in William Clements Ph.D. thesis as cited in King 1978):

$$C = \frac{\varphi}{\lambda}\left\{1 - \exp\left[\gamma\left(\frac{\varepsilon\lambda}{D}\right)^{1/2}Z\right]\right\} \tag{10.2}$$

Fig. 10.1 Radon concentration of subsurface soil-gas as a function of depth for theoretical model. This figure is adapted from King (1978)—with permission from Nature, Macmillan Journals Ltd. (1978)
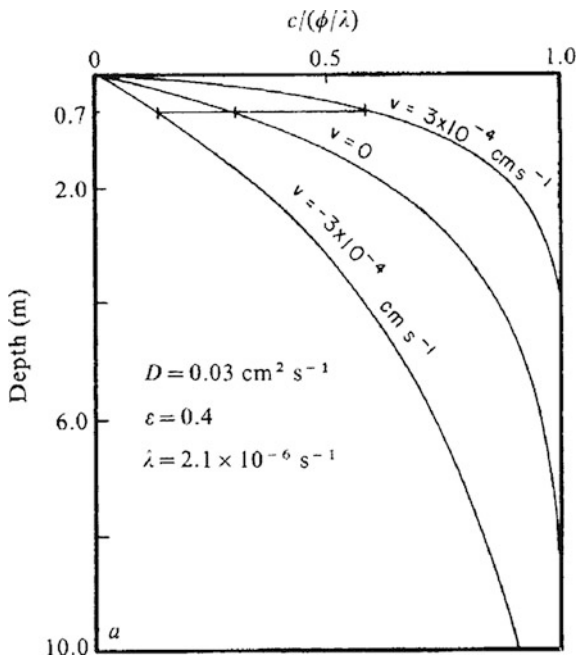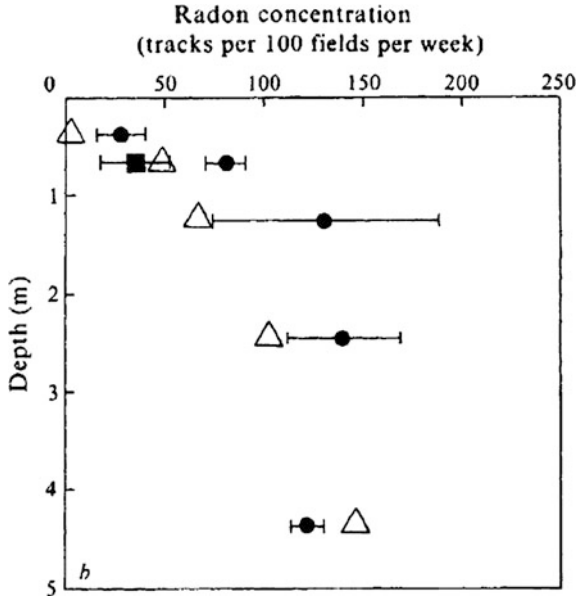
Fig. 10.2 Radon activity of subsurface soil gas as a function of depth at site 20 in radon monitoring station in central California (King 1978). X-axis is in units of number of particle tracks per 100 fields of view per week; each unit is equivalent to 100 mBq L^{-1} (or 2.7 pCi L^{-1}); Area of 100 fields = 5.75 mm^2; *Square* indicates a long-term average value at the usual monitoring depth of 0.7 m. The *filled circle* indicates the result for an anomalous period (weeks 96–98) and the *triangle* indicates the result for a nearly normal period (weeks 99–100, monitoring started on 7 May 1975). Error bars indicate 1 σ. Figure is taken from King (1978) with permission from Nature Publishing Group

where

$$\gamma = \frac{v}{2(\varepsilon\lambda D)^{1/2}} + \left(\frac{v^2}{4\,\varepsilon\lambda\,D_{eff}} + 1\right)^{1/2} \tag{10.3}$$

where φ is volumetric radon emanation rate (or radon source term, atoms m^{-3} s^{-1}), λ is the decay constant of ^{222}Rn, ε is soil porosity, D_{eff} is the effective diffusion coefficient of radon in soil, and v is the apparent soil gas flow velocity (volume flow per unit area per unit time). Note that the relationship between the effective diffusion coefficient and molecular diffusion coefficient (D_0) is given by Schery et al. (1984):

$$D_{eff} = \varepsilon\tau\,D_o \tag{10.4}$$

For an effective diffusion coefficient value of 3×10^{-6} m^2 s^{-1}, 40 % soil porosity ($\varepsilon = 0.4$), and for three different apparent velocities (-3×10^{-6} m s^{-1}, 0 and 3×10^{-6} m s^{-1}), the theoretical radon activities calculated using Eq. (10.2) are plotted in Fig. 10.1 and can be compared to the measured values at different depths separated by several meters (Fig. 10.2, King 1978). It appears that during anomalous

periods radon concentration increased at the shallower depths only, in agreement with the model. Note that a small vertical flow of soil gas (3×10^{-6} m s^{-1}) can perturb significantly the subsurface radon concentration profile at shallower depths (<10 m) such that the concentration at the monitoring depth (0.7 m) is changed by a factor of 2.

10.3   Variations in the Activities of Radon in Groundwater and Soil

10.3.1   Long Term Monitoring of Radon Activities

Continuous monitoring of radon activities in groundwater and soil gas is essential in predicting earthquakes. Many countries that are located on plate boundaries such as China, India, Japan, Russia, Turkey and the United States have ongoing long-term monitoring programs. In some other countries, the area is too vast to monitor (such as hundreds of small islands in Indonesia where 5 of the 17 largest earthquakes took place in the last 106 years (1906–2012) with magnitudes ranging from 8.5 to 9.5). In other areas, government agencies simply do not have adequate resources to monitor (e.g. Chile where 3 of 17 largest earthquakes took place during 1906–2012). Although long-term monitoring of soil-air and groundwater activities is critical in predicting earthquakes, a thorough understanding of other factors that affect the concentrations of radon near earth surface is essential. For example, 5 years of high resolution radon data obtained from sampling in 15 min intervals at 10 m depth in a 68 m deep borehole of a monitoring station in the Northwest Himalayan region showed a complex pattern with strong seasonal and diurnal trends (Kamra et al. 2013). Results from a large number of monitoring wells in Southern California indicate that the largest spatial variations, by four orders of magnitude, are observed along the San Andreas fault zone, with no systematic spatial trend (Chung 1981). Such variations were not found to be related to the subsurface seismic activities. However, major geophysical events, such as earthquakes and volcanic eruptions, have often been shown to generate significant variations of ^{222}Rn concentration in the soil. Radon measurements in soil air between 2007 and 2011 at Tuzla fault line in the Izmir-Seferihisar region (38° 07′ 29.24″ N; 26° 54′ 43.42″ E, about 80 km SW of the city of Izmir) of Western Turkey, with an average concentration of 338 ± 38 kBq m^{-3}, are shown in Fig. 10.3 (Tarakci et al. 2014). The data from this monitoring station clearly exhibited many perturbations due to the high seismic activity of this area and the fault lines in its proximity (Tarakci et al. 2014).

Efforts have been continuously made to increase the accuracy of long-term predictions, in particular in regions where large earthquakes are occurring along plate boundaries and in inland areas. Historical records of earthquakes' geodetic survey data accumulated over 100 years and data from the trench study of active faults provide evidence for repetition of large earthquakes in several areas.
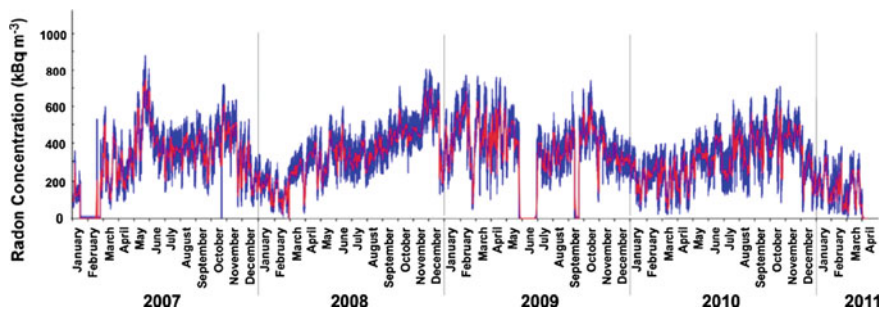
Fig. 10.3 Radon in soil gas measurements data recorded at Tuzla fault line in the Izmir-Seferihisar region (38° 07′ 29.24″ N; 26° 54′ 43.42″ E (about 80 km SW of the city of Izmir, Western Turkey) between 2007 and 2011. This data exhibited many perturbations due to the seismic activity of this area and the fault lines in its proximity. Details on statistical analysis of data are given in Tarakci et al. (2014). With permission from Elsevier Scientific Publishing Company, Amsterdam

Table 10.1 The comparison of ^{222}Rn activities (This data is taken from Tabar et al. (2013)) in soil-gas from different Tectonic regimes

Country	Radon activity (Bq m^{-3})	Study
India	1,657–1,855	Chaudhuri et al. (2010)
India	1,500–15,900	Choubey et al. (2007)
Jordan	800–26,700	Abumurad and Al-Tamimi (2005)
Russia	1,700–24,000	Iakovleva and Ryzhamova. (2003)
Ghana	9,910–42,100	Amponsah et al. (2008)
Cameroon	5,500–8,700	Ngachin et al. (2008)
Canada	6,800–74,700	Chen et al. (2008)
Turkey	209–7,389	Erees et al. (2006)
Turkey	4,300–9,800	Inceoz et al. (2006)
Turkey	98–8,594	Tabar et al. (2013)

Continuous monitoring provides real-time data from over 300 sites and this data gives insight on crustal deformation. Possible relationships between the micro-seismic events and the observed ^{222}Rn anomalies are commonly explored in order to link anomalous radon concentration to seismic events (Table 10.1).

10.4 Use of Helium/Radon Ratio as a Precursor for Predicting Earthquakes

Due to its short half-life, most of the ^{222}Rn found at earth's surface is likely derived from the upper few meters of the upper crust. In contrast, helium (^{4}He) is stable and mainly produced from the alpha decay (an alpha particle comprises of two protons

and two neutrons and when the alpha particle picks up two electrons, it is a ^{4}He atom) in the U-Th series (8 alpha particles are emitted from the decay of ^{238}U to the eventual stable ^{206}Pb; 7 alpha particles are emitted from the decay of ^{235}U to ^{207}Pb and 6 alpha particles are emitted from the decay of ^{232}Th to ^{208}Pb; Table 1.6a, b, c). Since ^{4}He is stable and its mass is only 1.80 % of the mass of ^{222}Rn, its diffusional and advectional transport is expected to be much higher compared to ^{222}Rn (note: advectional transport does not depend on the mass). The diffusion coefficient is inversely proportional to the square root of its atomic mass and thus the relationship between the ratio of diffusion coefficient of radon (D_{Rn}) to that of He (D_{He}) and their atomic masses (M_{He} and M_{Rn}) is given by:

$$D_{Rn}/D_{He} = (M_{He}/M_{Rn})^{1/2} \qquad (10.5)$$

Or, the diffusion coefficient of helium, D_{He}, is $\sim$7 times higher than that of radon, D_{Rn}. As a result, helium is expected to be derived from much deeper layers than radon (note: it is not clear whether it is because of higher diffusion coefficient or its infinitely long half-life (stable) or a combination of both, compared to radon's short mean-life). Elevated levels of helium is utilized as a 'pathfinder' of fault systems and a precursor to some earthquakes (Quattrocchi et al. 1999). Virk et al. (2001) proposed that the helium/radon ratio can be used as a predictor of earthquakes. They proposed a conceptual model to describe the mobility of helium and radon that comprised of four stages:

(a) Under normal stress/strain conditions, the amount of radon and helium (and the ratio between the two elements) is relatively constant in a given site (segment AB, Fig. 10.4);

(b) In segment BC, the stress builds up around the hypocenter leading to faults and cracks subsurface through which helium from much deeper depths can escape and thus, emanation rates of helium increases much higher than that of radon, resulting in increase in He/Rn ratios (segment BC, Fig. 10.4). The stress at the end of this segment reaches the elastic limit;

Fig. 10.4 A conceptual He/Rn ratio model as a predictive tool for earthquakes. The figure is taken from Virk et al. (2001), with permission from Elsevier Science Ltd

A-B : He/Rn ratio under normal condition
B-C : Rise in He/Rn ratio as stresses accumulate at depth
C-D : Drop in He/Rn ratio prior to triggering of the shock
D-E : Drop back in He/Rn ratio after the shock
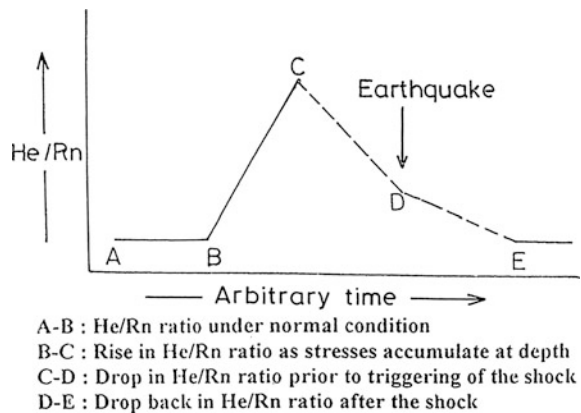
(c) Just before the rupture, the surrounding crustal rocks are under excessive strain resulting in higher amount of radon escape and hence the He/Rn ratio falls suddenly (segment CD) signaling the impending earthquake; and

(d) The segment DE could represent the period of after-shock where relatively higher amount of radon will escape compared to helium. After the point E, both Rn and He drop to normal values after relaxation of strain and the ground conditions stabilize.

The support for the above conceptual model comes from the temporal variations of radon and helium in soil air at Palampur (32.10° N, 76.51° E) which is located 393 km from the Chamoli earthquake epicenter (32.20° N, 79.5° E), with a focal depth of 21 km, as reported by the Indian Meteorological Department (Virk et al. 2001). Helium concentration in soils started increasing on 18th March and reached its peak value on 24th March (5 days before earthquake) while radon concentration attained its minimum value on 20 March and peak value on 27th March (Fig. 10.5). This observation suggests that helium is influenced by the strain build-up prior to radon as is evidenced in the He/Rn ratio (Figs. 10.5 and 10.6). The peak value of
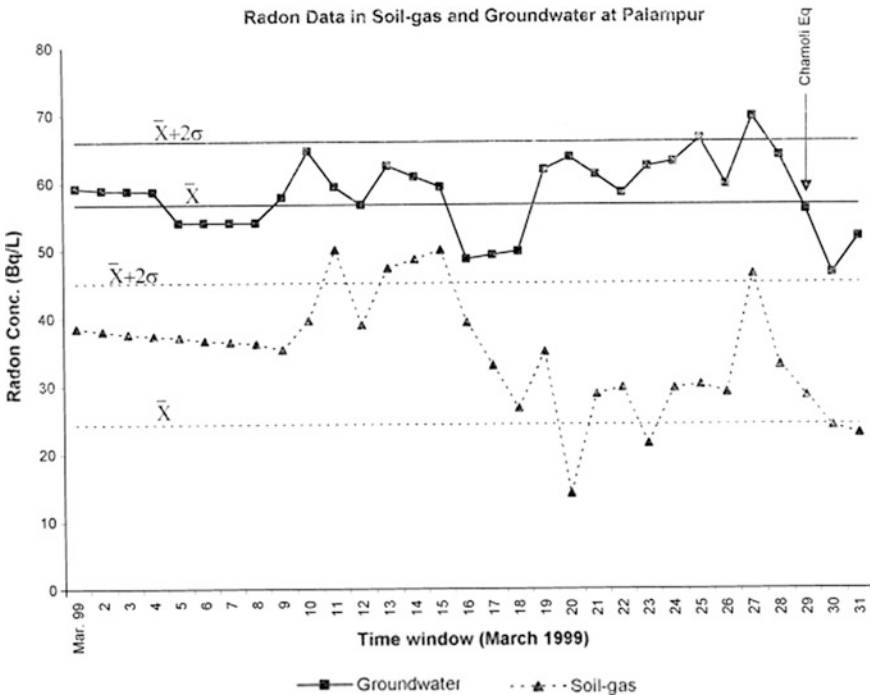
Fig. 10.5 Radon anomalies in soil-gas and groundwater at Palampur, India (3110° N, 76. 51° E), as a precursor to Chamoli earthquake (magnitude 6.5 Ms occurred on 29th March 1999, with epicenter at 30.2° N, 79.5° E (focal depth 21 km). The figure is adapted from Virk et al. (2001), with permission from Elsevier Science Ltd
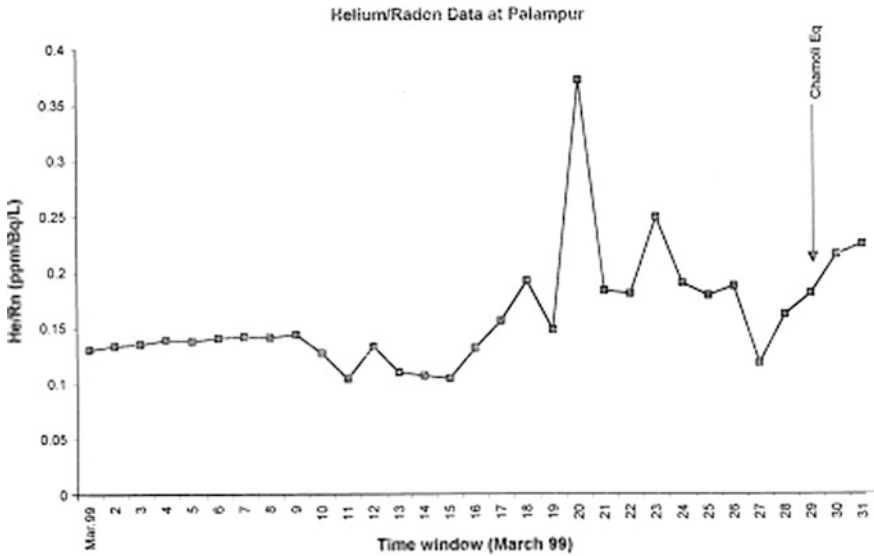
Fig. 10.6 Helium/radon ratio anomaly in soil-gas at Palampur (32.10° N, 76.51° E) which is at 393 km from the Chamoli earthquake epicenter, in N–W Garhwal Himalaya in N–W Himalayas (from Virk et al. 2001)—with permission from Elsevier Science Ltd

He/Rn ratio is found on 19th March and the minimum value was found on 27th March (2 days before earthquake). Virk et al. (2001) attributed this sudden rise and then fall of He/Rn ratio to be a precursory signal for the impending earthquake. Note that He/Rn ratios are not sensitive to micro-earthquakes (helium responds to seismic events of M = 5 or higher and no response for M = 2–4), including aftershocks in Chamoli. Although Virk et al. (2001) have reported results from two earthquake events, more studies are needed to validate the use of He/Rn ratio as a robust predictor of earthquake.

10.5 Case Studies

10.5.1 Kobe Earthquake (17 January 1995, Magnitude M = 7.2) and Other Earthquake Studies in Japan

Japan is located along the Pacific "ring of fire," which is an area of high seismic and volcanic activity from New Zealand, through Japan, across to Alaska, and down the west coasts of North and South America. Japan is on the edges of several continental and oceanic tectonic plates. At 5:45 a.m. (local time) on 17 January 1995, an earthquake of magnitude 7.2 on the Richter scale struck the Kobe region of south central Japan. This region is the second most populated and industrialized area in

Japan after Tokyo, with a total population of about 10 million people. Although the ground shaking lasted for only about 20 s, more than 5,000 people died and over 300,000 people lost their homes. The financial loss from the earthquake was estimated to be USD $150 billion ($\sim$3 % of total GDP of Japan in 1995) due to damage to roads, houses, factories and infrastructure (electric, gas, water, sewage, phone cables, etc.). Pre-seismic signals in groundwater discharge, radon and chloride concentration and strain were observed at three locations, all within the ultimate aftershock zones, beginning 3 months before the event (Fig. 10.7). The main shock (larger arrowhead in Fig. 10.7 top) produced co-seismic discontinuous change in all indicators. Radon concentration in the 17 m deep observation-well located about 30 km northeast of the hypocenter of the earthquake at the end of 1993 was reported to be stable at 20 Bq L^{-1}, but started to increase gradually from the beginning of the observation in October 1994, and by the end of November 1994, radon concentration reached about 60 Bq L^{-1}, which was about 3 times the level of the same period 1 year before. A sudden increase was seen on 8 January 1995 (>10 times higher than that observed at the beginning of observation), 9 days before the earthquake, but a sudden decrease was observed on 10 January, 7 days before the earthquake (Igrashi et al. 1995b). By 22 January 1995, the radon concentration was reported to have returned to the pre-October 1994 level. The precursory anomalies began about 3 months before the major earthquake event (smaller arrowhead in Fig. 10.7 top). The changes in the signals of radon, strain and water level in Uzu-Ohima earthquake in 1978 (M = 7.0, 14 January 1978) are remarkably similar to Kobe earthquake (Fig. 10.7; note that the monitoring began about 1 month before the main shock), clearly indicating that the precursory signals can predict the forthcoming major earthquake.

The long-term (over 18 years) variations of radon concentrations in groundwater at the Suokoen site (SKE) shows precursory radon changes accompanying the 1978 Izu-Oshima-kinkai earthquake (M 7.0), and are highlighted in Figs. 10.8 and 10.9. There is a clear change in the radon count rate (in cpm) at the time of the 1978 earthquake, but no other comparative change is reported in that record, which coincides with the absence of other earthquakes of comparative size in the Izu region (Wakita 1996). Note that there are several changes associated with local events including seismic and volcanic activities such as those of 1980, 1984, 1988, 1989 and 1990 (Fig. 10.8). Precursory changes of radon, water level, water temperature, strainmeter readings and foreshocks from the 1978 earthquake in the Izu-Oshima-Kinkai earthquake (M 7.0) are given in Fig. 10.9. Anomalous changes such as groundwater level, crustal movement and foreshocks occurred simultaneously and there is similarity in these changes (Fig. 10.9). Based on the studies conducted in several other places in Japan, it appears that the radon anomaly in tectonically-active region is not uniform in all stations. Indeed, the 1978 radon anomaly was observed only at a single station and there was no anomalous change with the preceding earthquake of M 6.7 (June 29, 1980). At the Kashima site (KSM) in northeast Japan, the radon concentration in a well that was drilled on the

Fig. 10.7 Comparison of precursory anomalies associated with two earthquakes (*Top* M = 7.2 Kobe earthquake of 17 January 1995; *Bottom* Izu-Ohima earthquake of 1978) (adapted from Wakita 1996, with permission from the National Science Academy, USA)
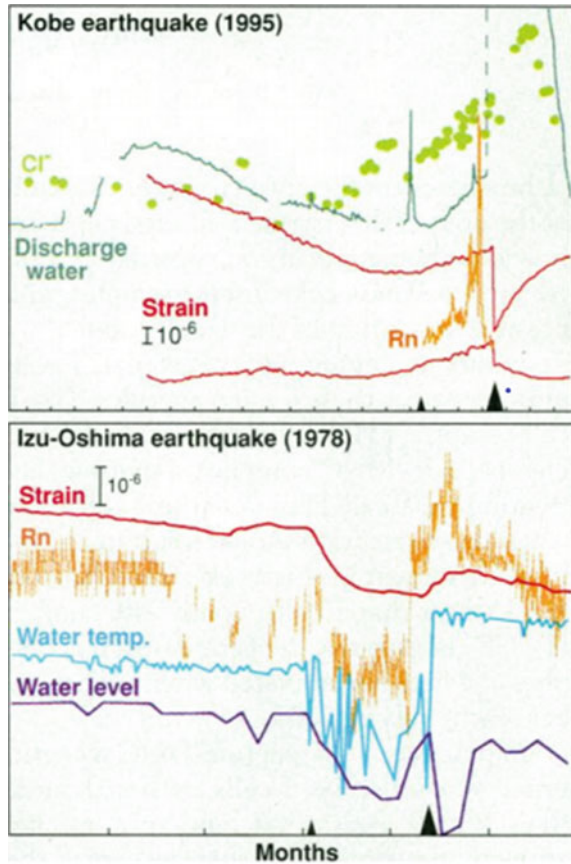
Futaba fault decreased after the occurrences of earthquakes nearby. Changes in radon concentration has also been supported by data from a M = 7.3 earthquake (11 July 1995) in the Burma-China border region.

10.5.2 Earthquake Studies in Southern California, Alaska and Hawaii in the United States

10.5.2.1 San Andreas Fault, California, USA

In seismically-active areas with a dense population such as southern California in the United States, continuous monitoring of soil gas and monitoring wells for radon levels will help to minimize human and financial loss, if the precursor signals are effective in predicting the forthcoming earthquake. A considerable amount of monitoring has been conducted on the inland San Andreas fault system,
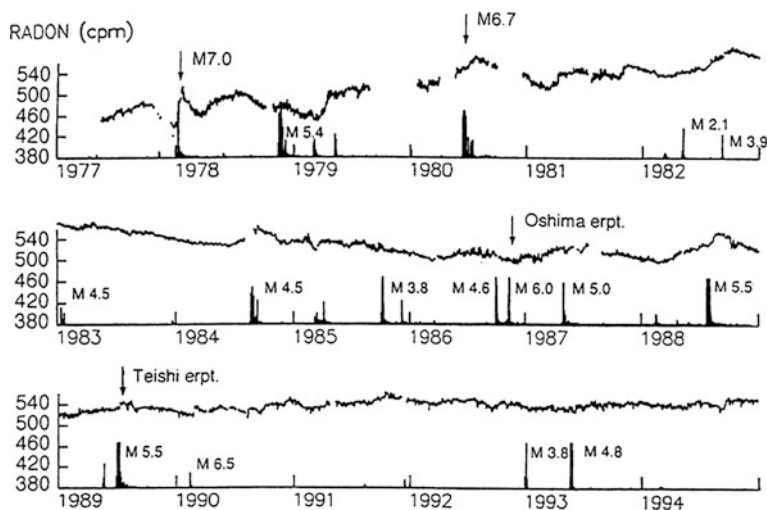
Fig. 10.8 Long-term variations of radon activity in monitoring wells at Suokoen site (SKE) in Izu Peninsula together with relative seismic activity in and around Izu Peninsula. The figure is taken from Wakita (1996), with permission from the National Science Academy, USA)

1000 km × 200 km plate boundary zone. This zone of 200,000 km^2 area is only sparely instrumented in terms of hydro-geochemical and related strain. From the monitoring of subsurface radon emanation in 20 shallow dry holes along an active 60-km segment of the San Andreas and Calaveras faults in central California, USA, starting from 7 May 1975 for period of about 2 years, King (1978) reported weekly average values of activities of soil gas to vary between 0.19 and 85 Bq L^{-1} (5 and 2,300 pCi L^{-1}). The measured radon concentration showed large temporal variations that are spatially coherent over ≥60-km long fault segment (King 1978). The two medium-sized earthquakes (magnitude 4.3 and 4.0) occurred closer to the times when the radon concentration in the soil at 0.7 m below surface reached its peak. It was also reported that the radon emanation began to increase rapidly several weeks before the magnitude 4.3 quake and this was attributed to strain build up. As discussed in Chap. 3, it is unlikely that radon comes from the focal depth that lies several kilometers subsurface. However, it could be derived from the increase in crustal compression that squeezes out the soil gas in the deep reaching fault gouge zone. Such perturbations due to higher outgassing rate may perturb the vertical subsurface radon concentration profile (King 1978). The radon concentration profile indicates that it increases rapidly with depth by ∼2–3 orders of magnitude (Fig. 10.2, King 1978) and the deeper soil gas containing high radon is brought up to the surface. Figure 10.11 indicates that the radon activities were anomalously high even a few months after the earthquake (week 96–98), but for a 2-week period (week 99, 100), the radon concentration was nearly back to the average level.
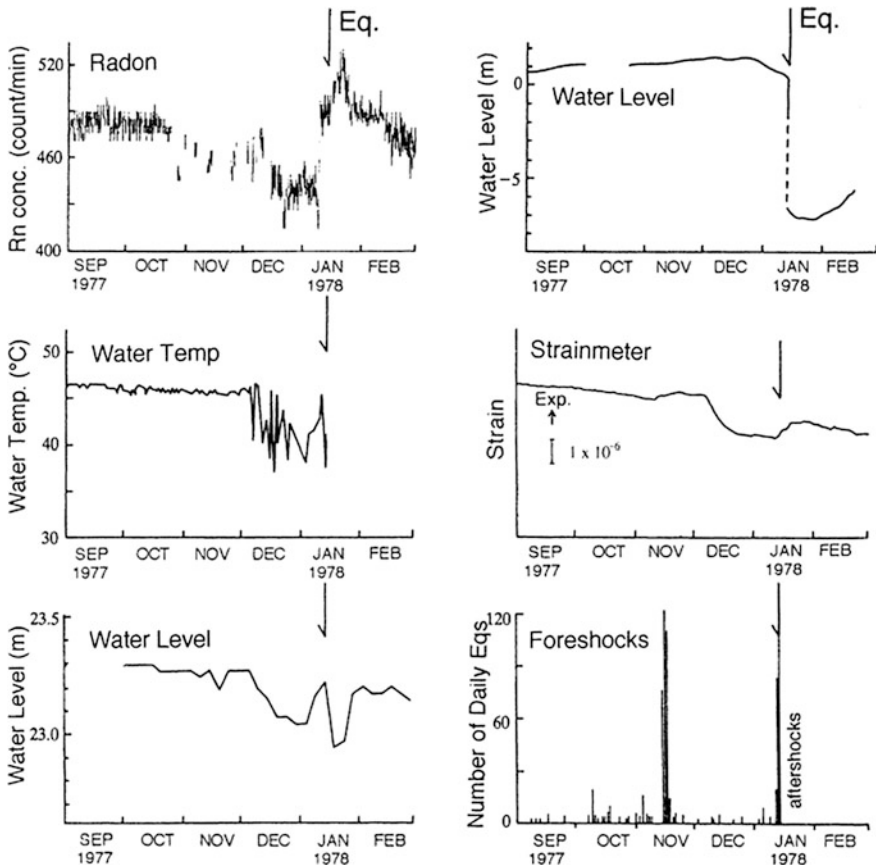
Fig. 10.9 Precursory changes of the Izu-Oshima-kinkai earthquake (M7.0) on January 14, 1978. Eq: earthquake This figure is adapted from Wakita (1996), with permission from the National Science Academy, USA

10.5.2.2   Alaskan Earthquake Study

In Alaska, three of the seventeen largest earthquakes (magnitude scale of 8.5–9.5) that occurred in the world since 1900 took place. In this region, the Pacific Plate moves steadily northward at a rate of ∼5 cm/year and subducts beneath the North American Plate. Radon readings from August 1982 to June 1983 at Sand Point, Alaska, U.S.A. (which is 178 km from the epicenter of an earthquake of magnitude scale 6.3), indicated variability observed over a period of 6 weeks prior to the earthquake (Fleischer 1988). The magnitude of variability of radon readings differed widely, although all four stations are nearly equidistant from the earthquake (Fig. 10.12). Premonitory increases in radon readings were observed in 1, 3 and 4, but decreases in stations 1 and 3 afterwards. A factor of 2 decline was found in

Fig. 10.10 Co-seismic radon drops observed at the KSM site. Eq: earthquake. The figure is adapted from Wakita (1996), with permission from the National Science Academy, USA
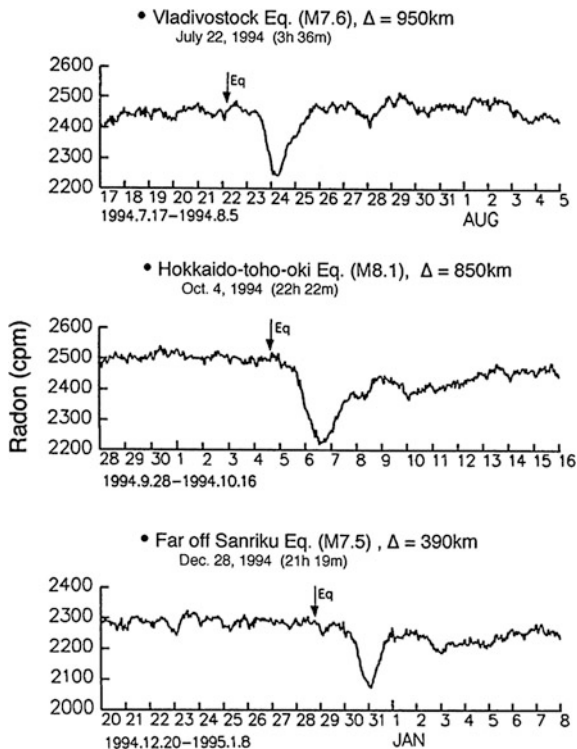
station 2 after the earthquake, although no premonitory effect was observed in this station. It is clear that there is need to assess each monitoring site and the selection of site is also critical, as all stations do not behave similarly.

10.5.2.3 Kilauea Volcano Site in Hawaii

Most volcanoes are created at tectonic plate boundaries. The Hawaii hotspot which is a volcanic hotspot, is located near the Hawaiian Islands. Radon activities from hot spring waters and gases have been reported to vary widely and are commonly attributed to erupting or about to erupt volcanoes and volcanically-induced earthquakes (e.g., Cox et al. 1980). Radon activities measured near the surface of the earth (<1.0 m from surface) often show large fluctuations that cannot always be correlated with variations in volcanic or seismic activity (Chap. 4). From soil-air radon data obtained from August 1978 – May 1980 in Kilauea volcano, Hawaii, Cox et al. (1980) observed an increase in radon concentrations (in seven of the nine stations) up to ∼21 times the background level (during August-September 1978) for the months up to and including November 1979 volcanic eruption. The drastic increase was attributed to outgassing of gas including radon with the eruption and the seismic events and to various causes related to the movement of magma towards
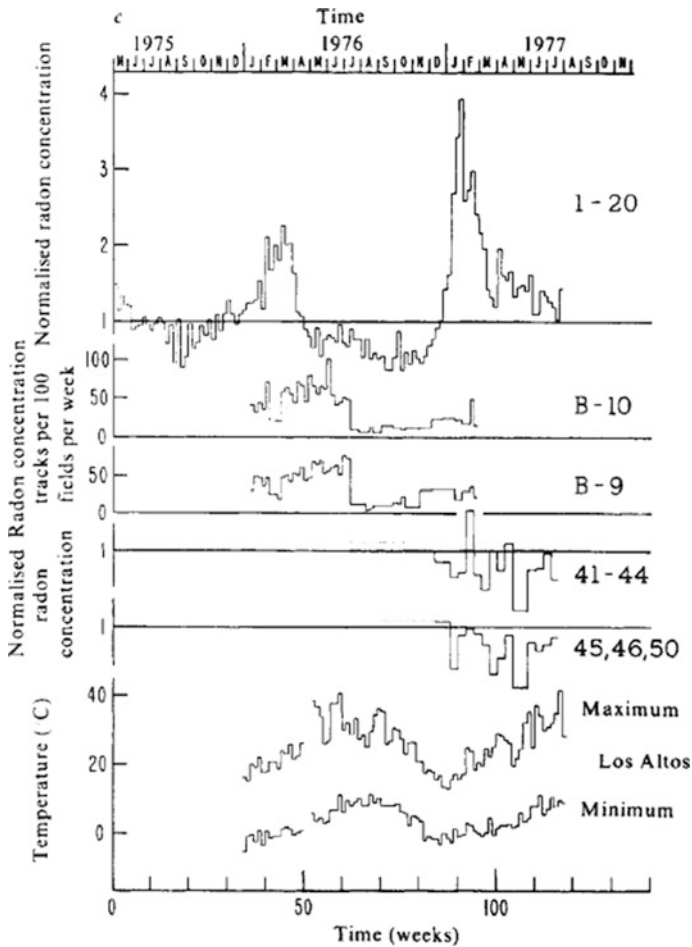
Fig. 10.11 Radon emanation recorded by the array of 20 stations, 4 stations along the San Andreas fault (41–44) in San Francisco Bay area, three stations in Hayward fault (45, 46, 50) and two control stations in Los Altos; area of 100 fields = 5.75 mm^2; each unit is equivalent to 100 mBq L^{-1} (or 2.7 pCi L^{-1}). The dashed lines indicate that some stations in the arrays were not yet in operation. The atmospheric temperature were recorded in Los Altos, CA. Figure is adapted from King (1978), with permission from Nature Publishing Group

the surface and the associated deformation of the country rock. The rise of magma causes local temperatures to rise and increases the fracture permeability of the surrounding material. The escaping steam and other gases in the volcano are thermally stimulated and thus serve as agents for transporting other available radon encountered during migration towards the surface. Secondary mineralization of minerals such as CaSO$_4$ deposited on fracture surfaces in zones where hydrothermal activity has occurred also could release a large amount of radon produced from the co-precipitated RaSO$_4$ on mineral surfaces. There is some consensus on the

Fig. 10.12 Radon readings (in pCi L^{-1}; 1 pCi L^{-1} = 37 mBq L^{-1}) at Sand Point, Alaska, U.S.A. which is 178 km from the epicenter of an earthquake of magnitude scale 6.3 (taken from Fleischer 1988; with permission from Elsevier Science Ltd.)
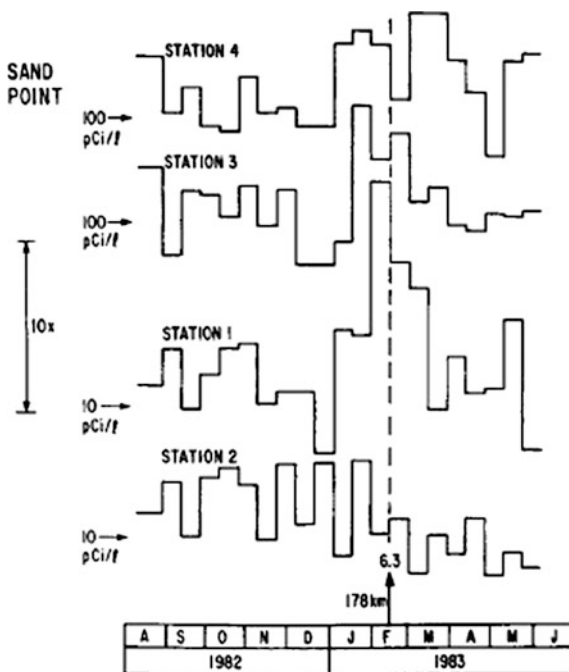
observation that radon concentration increases before and during seismic events (caused by either intrusive, extrusive or earthquake activity). The overall obser-vation on the decrease of radon following the eruption seems to be caused by the depletion of radon available in rock fractures and pores from flushing by increased outgassing before and during volcanic eruptions (and earthquakes). Similar post-eruptive Rn depletion was reported in thermal springs of Karymsky volcano on the Kamchatka Peninsula, Russia (Fig. 10.13).

10.5.3   Earthquake Studies in North-Western Himalaya

The Himalayan mountain range of 2,400 km has been undergoing extensive crustal shortening and a number of major thrust planes have been formed as a result of intensive tectonic activities. In particular, Bhagirthi and Alaknanda valleys of Garhwal Himalaya in the northwestern Himalayas have suffered a number of major and minor earthquakes of magnitude >6.0 that include: Badrinath earthquake (1803), Gangotri earthquake (1816), Mussoorie earthquake (1865), Uttarkashi earthquake (20 October 1991, M_s = 7.0) and Chamoli earthquake (29 March 1999, M_s = 6.5). It has been reported, based on the time series radon data in soil air and groundwater during 1992–1999 in the grid between 30–34° N, and 74–78° E in N–W Himalaya, that there is a positive correlation in about half of the cases
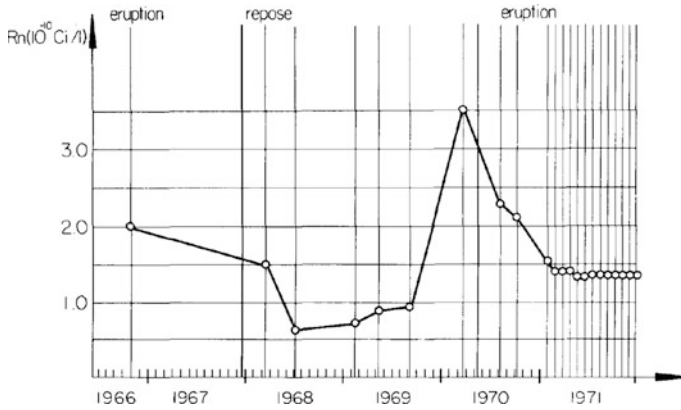
Fig. 10.13 ^{222}Rn activity in thermal waters of Karymsky volcano, Kamchatka (Russia), during one cycle of activity. Adapted from Gasparini et al. (1978) (with permission from Elsevier Scientific Publishing Company, Amsterdam)

between total radon emission and the micro-seismicity in the area under investigation (Walia et al. 2002). The earthquake magnitude was found to have a moderate positive correlation with distance from the epicenter and weak positive correlation between amplitude of radon precursory signal (Walia et al. 2002). When radon activities in groundwater (including thermal waters) or soil-air exceed the average activity by two standard deviations (2σ), then, the activity is considered to exhibit radon anomalies. Radon concentration in soil air at the Palampur site increased from a background level of 24 ± 10 Bq L^{-1} to 47 Bq L^{-1}, exceeding mean $\pm 2\sigma$ value at the peak level (Fig. 10.5). The corresponding values in the groundwater samples increased from a background level of 57 ± 5 Bq L^{-1} to 70 Bq L^{-1}, exceeding mean $\pm 2\sigma$ value at the peak level (Fig. 10.5; Virk et al. 2001). Thus, the increase of ^{222}Rn concentration both in soil-gas and groundwater are clearly evident in the northwestern Himalayan regional study. Virk et al. (1998) also reported radon and helium anomalies in geothermal springs of N–W Himalaya. Radon activities in soil gas or springs near thermal springs were found to be very high (1657–1855 Bq m^{-3}; Chaudhuri et al. 2010). Continuous monitoring of soil gas was carried out in Garhwal Himalaya by Ramola et al. (2008). Radon anomalies along with meteorological parameters were found to be statistically significant for the seismic events with magnitudes M 2.0–6.0 and epicenter distances of 16–250 km from the monitoring stations.

10.5.4 Earthquake Studies in Turkey

Turkey is one of the world's most active earthquake and volcano regions. Turkey is a part of the great Alpine belt that extends from the Atlantic Ocean to the Himalayas

Mountains, which was formed when the Arabian, African and Indian continental plates began to collide with the Eurasian Plate. The Anatolian Plate moves towards the west and southwest along strike-slip faults (East and North Anatolian Fault Zones). Continuous time-series radon activities in soil-gas provide important information on the seismic activity. Southern and Western parts of Turkey have experienced intense earthquake activity in the last few thousand years. One of the most striking examples of this is the destruction of the Biblical churches in Asia Minor (Church of: Ephesus, Smyrna (now known as Izmir), Pergamos, Thyatira, Sardis, Philadelphia and Laodicea—referenced in the Biblical book of Revelation) that are over 1900 years old. Four of these churches in Asia Minor were almost completely destroyed by major earthquake activities since their construction in the first century (about 1900 years ago), while the other three are largely destroyed due to intense seismic activities. Radon data recorded at 15 min intervals, with the detector unit placed 1 m inside the soil, from a monitoring station (38° 07′ 29.24″ N; 26° 54′ 43.42″ W, about 80 km SW of the city of Izmir) located at Tuzla fault line in the Izmir-Seferihisar region of Western Turkey (Fig. 10.14), indicated many perturbations due to seismic activity in this area (Tarakci et al. 2014). Erees et al. (2007) reported monthly radon activities in thermal waters collected from 7 monitoring sites in the Denizli Basin in Western Turkey from May to December 2000 to vary from 0.67 to 25.9 Bq L^{-1}, with an average value of 4.8 Bq L^{-1} (1σ = 5.6 Bq L^{-1}). Monthly measurements of ^{222}Rn from 7 stations of thermal waters along faults in the Denizli Basin in Western Turkey indicated a correlation between ^{222}Rn activities and magnitudes of earthquakes in certain times in some basins and in other times, no correlation was found (3 typical stations, viz., Kizildere, Klzilsu, and Yenice, are shown in Fig. 10.14, adapted form Erees et al. 2007). Inan et al. (2008) reported soil gas radon concentration and spring waters were responsive to the seismic activity and to earthquakes of M > 4 in the Marmara Region of Turkey. Sac et al. (2011) reported peak value of ^{222}Rn concentration 10 days before the Seferihisar earthquake. They also found a significant decrease in ^{222}Rn concentration a few days after the earthquake. Although an overall correlation between earthquake and radon anomaly in soil air and water have been frequently observed, the relationship between radon anomaly and specific earthquake parameters such as magnitude, the epicenter position and the time of the earthquake are complex and so far no such relationships have been established between these parameters and precursory signals.

10.5.5 Earthquake and Volcanic Eruption Studies from Other Regions of the World

In addition to the specific examples given above, there are other areas in the world where radon has been utilized as a tracer for precursor studies. Most of the radon anomalies in soil air and water in the vicinity of Eastern Japan were associated with
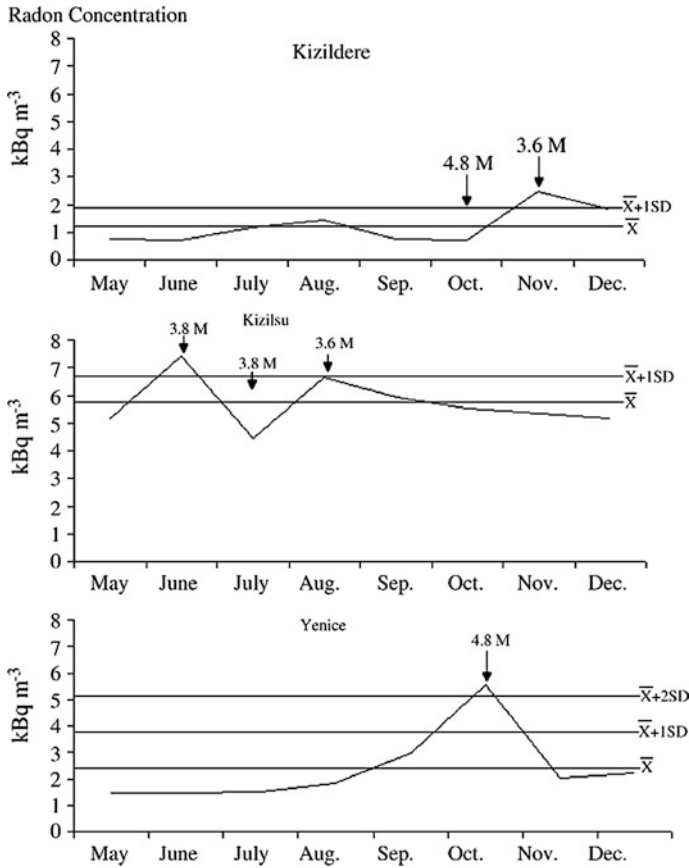
Fig. 10.14 Variations of radon concentration in three thermal water monitoring stations (Kizildere, KIzilsu, and Yenice) and magnitudes of earthquakes in the Denizli Basin, Western Turkey (figure taken from Erees et al. 2007; with permission from Elsevier Scientific Publishing Company, Amsterdam—Radiation Measurements 42 (2007, 80–86)

large earthquakes (Igarashi and Wakita 1990). Fleischer (1988) reported an increase of radon levels by a factor of 500 over an interval of 5 weeks at Blue Mountain Lake, New York, U.S.A. Data obtained from a time-series analysis showed a positive correlation between radon concentration and earthquake activity for the Dudley earthquake (M 5.0) in England (Crockett et al. 2006). A set of discrete ^{222}Rn measurements between July 2002 and May 2003 in the Santa Venerina area of Mt. Etna revealed well-defined linear anomalies and was interpreted as being caused by active faults. Based on this data, Burton et al. (2004) hypothesized that the positive anomalies are attributable to active faults that were strengthened by the concentrated damage during the earthquakes that struck this area in late October 2003. From radon measurements in soils from a seismically active area and time, Nikolopoulos et al. (2012) observed that strong radon disturbances may be linked to

the strong earthquake on 8th June 2008 (M = 6.5), occurred at 29 km from the instrument site. One of the recent monitoring (May 18, 2000 to June 17, 2011) studies of ^{220}Rn and ^{222}Rn in Seongryu limestone cave in Seonyu Mountain in the eastern part of S. Korea indicated anomalous peaks of ^{222}Rn and ^{220}Rn observed in February 2011 which were considered to be precursory signals prior to the Tohoku-Oki Earthquake that took place approximately 1 month later (Oh and Kim 2015). Note that this monitoring site is ∼1200 km distance from the epicenter of the Tohoku-Oki Earthquake. Prior to this earthquake, changes in water level, temperature and conductivity were also observed in 14 % of the 320 monitoring wells in S. Korea. Due to short half-life of ^{220}Rn (55.6 s), ^{220}Rn levels at >1.0 m above cave floor was found to be below detection level, similar to observations reported elsewhere since 1970s (Chap. 11) and hence the sampling inlet needs to be positioned close to the cave floor and farther away from cave entrance to minimize the impact of air ventilation with the outside air (Oh and Kim 2015).

10.6 Conclusion and Future Research Direction

A large number of studies have been attempted to link the temporal variations of the activities of ^{222}Rn in soil-air and groundwater to earthquake prediction. In a stricter sense, "prediction" implies the stipulation of the time when an earthquake can take place, its location and magnitude, with estimates of the uncertainties around each of these parameters. The field has not come close to this level of rigor in prediction. When societies prioritize the allocation of scarce resources, it behooves to ask whether further efforts and more resources should be devoted to the search for prediction methods. There are cases where some of the earthquakes in tectonic regimes were predicted with useful accuracy of time and space (such as Haicheng earthquake in China).

There is a general consensus that radon activities in surface soil air, gas and groundwater vary prior to, during and post- earthquake activity. Research conducted so far has shown that pre-seismic signals are known to be highly variable in space and time (known as "response heterogeniety"). Wells that are only meters apart have been reported to yield very different co-seismic or pre-seismic anomalies. Furthermore, many pre-seismic signals have been reported far from the impending earthquake's epicenter, making it difficult to come-up with a physical mechanism to explain such an observation. The distinct difference in the half-life of the radon-thoron pair (^{222}Rn-^{220}Rn) has the potential to obtain additional insights on using radon as a precursor for earthquake prediction.

There are several factors and processes that remain either poorly known or entirely unknown (among the 'known unknown'). Questions such as: (i) How does the stress accumulation and release change the physical properties of the subsurface rocks which manifests in the form of co-seismic change in levels of radon, helium and other gases? (ii) How do we quantify the effects of the opening and closing of micro-cracks of the sub-surface rocks in the release rates of radon when earthquake

activities start at focal depth? (iii) While long-range transport of atmospheric transport of gases takes place at >150 km/day, in subsurface environments, is it possible that radon can travel at much higher velocities (possibly with other gases) due to the presence of fractures resulting from seismic activities, although the densities of air and subsurface material differ by 3 orders of magnitude? (iv) What is (are) the mechanism(s) that dominates the vertical movement of radon subsurface where seismic activities are intense? Note that several mechanisms have been suggested with respect to radon flow inside the earth, but no single mechanism has been firmly established and more work needs to be done for a better understanding of the radon flow in the upper crust of the earth. Due to short mean life of ^{222}Rn, most of the radon to earth's surface is expected to come from the upper few meters, while ^{4}He being stable, could come from much deeper layers and hence ^{4}He could serve as a 'pathfinder' of fault systems and precursor. The ratio of ^{4}He/^{222}Rn seem to hold much higher promise and need to be pursued as a powerful precursor tool in predicting earthquakes.

References

Abumurad KM, Al-Tamimi MH (2005) Natural radioactivity due to radon in Soum region, Jordon. Radiat Meas 39(1):77–80

Amponsah P, Banoeng-Yakubo B, Andam A et al (2008) Soil radon concentration along fault systems in parts of south eastern Ghana. J Afr Earth Sci 51(1):39–48

Burton M, Neri M, Condarelli D (2004) High spatial resolution radon measurements reveal hidden active faults on Mt. Etna. Geophys Res Lett 31(7):L07618. doi:10.1029/203GL019181

Chaudhuri H, Das NK, Bhandari RK, Sen P, Sinha B (2010) Radon activity measurements around Bakreswar thermal springs. Radiat Meas 45:143–146

Chen J, Falcomer R, Ly J et al. (2008) Long-term monitoring of soil gas radon and permeability at two reference sites. Radiat Prot Dosim 131(4):503–508

Chinese Seismology Delegation (1976) In: Proceedings of the lectures by the seismological delegation of the people's Republic of China. Seismology Society of Japan, Earthquake Research Institute, Tokyo University, Tokyo, Japan

Choubey VM, Mukherjee PK, Bajwa BS et al (2007) Geological and tectonic influence of water-soil-radon relationship in Mandi-Manali area, Himachal Himalaya. Environ Geol 52(6):1163–1171

Chung Y-C (1981) Radium-226 and radon-222 in Southern California groundwater: spatial variations and correlations. Geophys Res Lett 8(5):457–460

Crockett RGM, Gillmore GK, Phillips PS et al (2006) Tidal synchronicity of built-environment radon levels in the UK. Geophys Res Lett 33(L05308):2006. doi:10.1029/2005GL024950

Cox ME, Cuff KE, Thomas DM (1980) Variations of ground radon concentrations with activity of Kilauea Volcano, Hawaii. Nature 288:74–76

Erees S, Aytas S, Sac MM et al (2006) Radon concentrations in thermal waters related to seismic events along faults in Denizli Basin, Western Turkey. Radiat Meas 42:80–86

Erees FS, Aytas S, Sac MM, Yener G, Salk M (2007) Radon concentrations in thermal waters related to seismic events along faults in the Denizli Basin, Western Turkey. Radiat Meas 42:80–86

Fleischer RL (1988) Radon in the environment—opportunities and hazards. Nucl Tracks Radiat Meas 14:421–435, Int J Radiat Appl. Instrum Part D

Gasparini P, Silvia M, Mantovani MSM (1978) Radon anomalies and volcanic eruptions. J Volcanology Geothermal Res 3:325–341

Iakovleva VS, Ryzhamova NK (2003) Spatial and temporal variations of radon concentration in soil air. Radiat Meas 36:385–388

Igarashi G, Wikita H (1990) Groundwater radon anomalies associated with earthquakes. Tectonophysics 180:2–4

Inan S, Akgul T, Seyis C et al (2008) Geochemical monitoring in the Marmara region (NW Turkey): a search for precursors of seismic activity. J Geophys Res 113:1–4

Inceoz M, Baykara O, Aksov E et al (2006) Measurements of soil gas radon in active fault systems: a case study along the North and East Anatolian fault systems in Turkey. Radiat Meas 41(3):349–353

Igarashi G, Saeki N, Takahata K et al (1995a) Ground-water radon anomaly before the Kobe earthquake in Japan. Science 269:60–61

Igarashi G, Saeki S, Takahara N et al (1995b) Ground-water radon anomaly before the Kobe earthquake in Japan. Nature 269:60–61

Ishimori Y, Lange K, Martin P, Mayya YS, Phaneuf M (2014) Measurement and calculation of Radon releases from NORM residues. IAEA Technical Report Series 474

Kamra L, Choubey VM, Kumar N et al (2013) Radon variability in borehole from multi-parametric geophysical observatory of NW Himalaya in relation to meteorological parameters. Appl Radiat Isot 72:137–144

King C-Y (1978) Radon emanation on San Andreas Fault. Nature 271:516–519

Ngachin M, Garavaglia M, Giovani C et al (2008) Radioactivity level and soil radon measurement of volcanic area in Cameroon. J Environm Radioact 99(7):1056–1060

Nikolopoulos D, Petraki E, Marousaki A et al (2012) Environmental monitoring of radon in soil during a very seismically active period occurred in South West Greece. J Environ Monit 14:564–578

Oh Y, Kim G (2015) A radon-thoron isotope pair as a reliable earthquake precursor. Sci Rep 5(13084):2015. doi:10.1038/srep13084

Quattrocchi F, Guerra M, Pizzino L, Lombardi S (1999) Radon and helium as pathfinders of fault systems and groundwater evolution in different Italian areas. In: Proceedings IV international conference on rare gas geochemistry, vol 22C. Rome, 8–10 Oct 1997, Nuovo Cimento, pp 309–316

Ramola RC, Prasad Y, Prasad G, Kumar S, Choubey VM (2008) Soil-gas radon as seismotectonic indicator in Garhwal Himalaya. Appl Radiat Isot 66:1523–1530

Sac MM, Harmansah C, Camgoz B (2011) Radon monitoring as the earthquake precursor in fault line in Western Turkey. Ekoloji 20(79):93–98

Sadovsky MA, Nersesov IL, Nigmatullaev SK et al (1972) The processes preceding strong earthquakes in some regions of Middle Asia. Tectonophysics 14:295

Schery SD, Gaeddert DH, Wilkening MH (1984) Factors affecting exhalation of radon from gravelly sandy loam. J Geophys Res 89:7299–7309

Silver PG, Wakita H (1996) A search for earthquake precursors. Science 273:77–78

Tabar E, Kumru MN, Ichedef M et al (2013) Radioactivity level and the measurement of soil gas radon concentration in Dikili geothermal area, Turkey. Int J Rad Res 11(4):253–261

Talwani P, Moore WS, Chiang J (1980) Radon anomalies and microearthquakes at Lake Jocassee, South Carolina. J Geophys Res 85:3079–3088

Tanner AB (1964) Radon migration in the ground: a review. In: Adams JAS, Lowder WM (eds) Natural radiation environment. University of Chicago Press, Chicago, pp 161–190

Tarakci M, Harmansah C, Sac MM, Ichedef M (2014) Investigation of the relationship between seismic activities and radon level in Western Turkey. Appl Radiat Isot 83:12–17

Ulomov VI, Mahashev BZ (1971) The Tashkent earthquake of 26 April 1966. Akad, Nauk Uzbek SSR FAN 188

Virk HS, Kumar N, Sharma AK (1998) Radon/helium survey of thermal springs of Parbati, Beas and Sutlej valleys in Himachal Himalaya. J Geol Soc India 52:523–528

Virk HS, Walia V, Kumar N (2001) Helium/radon precursory anomalies of Chamoli earthquake Garhwal Himalaya, India. J Geodyn 31:201–210

Wakita H (1996) Geochemical challenge to earthquake prediction. Proc Natl Acad Sci USA 93:3781–3786

Walia V, Virk HS, Kumar P (2002) Empirical scaling relationships between earthquake magnitudes, epicentral distances and amplitudes of radon anomalies in N–W Himalaya. Indian J Pure Appl Phys 40:743–749

Chapter 11
Radon: A Human Health Hazard in the Environment

11.1 Introduction

Radon-222 and its decay products are ubiquitous in the environment, including in the air we breathe. When radon, the heaviest naturally-occurring radioactive noble gas, undergoes radioactive decay, its daughter products emit high-energy alpha particles and associated gamma-rays. It is estimated that about half of the total natural radiation exposure for human being comes from radon (UNSCEAR 2000). The relative doses from natural and man-made sources of radiation are given in Fig. 11.1. It is widely known that radon is the single major contributor to the ionizing radiation dose received by the general population and is the second most frequent cause of lung cancer after smoking. Most of the radon-induced lung cancer cases were reported to occur among smokers due to a strong combined effect of smoking and radon. Radon was classified as a human carcinogen (in the same carcinogen group as tobacco smoke, asbestos and benzene) in 1988 by the International Commission on Radiation Protection (IARC), a cancer research agency under the World Health Organization.

A large number of studies on indoor radon and lung cancer around the globe provide strong evidence that radon causes a substantial number of cases of lung cancer in the general public. It has been estimated that the percentage of lung cancer cases attributable to radon range from 3 to 14 %, depending on the average radon concentration and the assumptions involved in the risk calculations (WHO 2009).

When radon gas is inhaled, high-energy ionizing alpha particles are produced from the decay of ^{222}Rn (alpha particles produced during the decay of ^{222}Rn, ^{218}Po
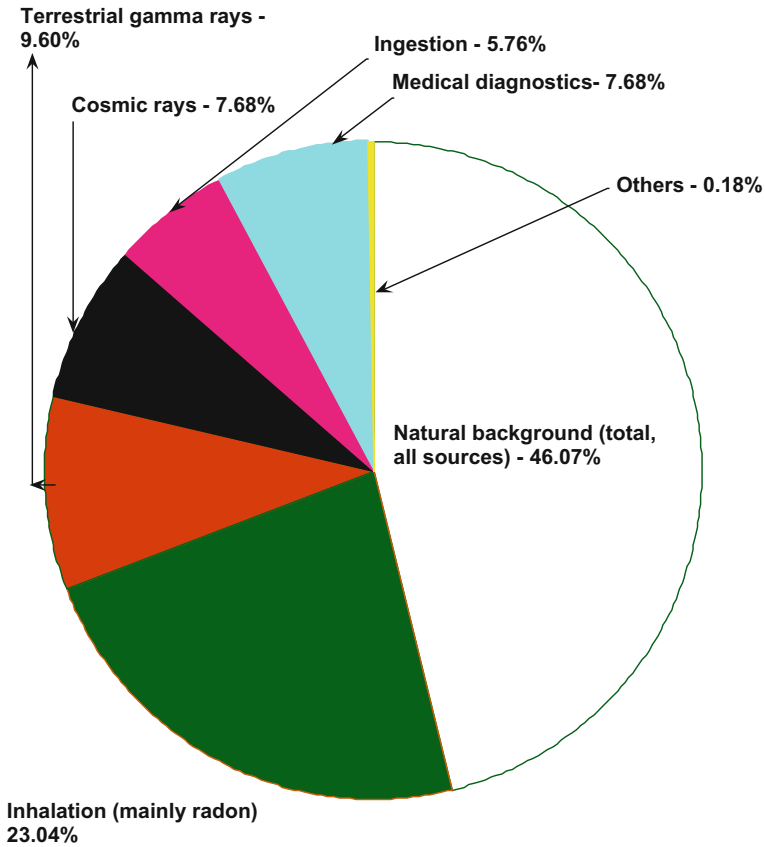
Fig. 11.1 Pie chart showing relative doses from natural and man-made sources of radiation (data from WHO 2009)

and ^{214}Po, Chap. 1), and each of the alpha particles can interact with biological tissue in the lungs leading to major damage to the DNA of a cell. Such DNA damage can, in principle, occur at any level of ^{222}Rn exposure. It is generally accepted that there should be at least one mutation and proliferation of intermediate cells that have sustained some degree of DNA damage which can greatly increase the pool of cells available for the development of cancer (WHO 2009). Since it is possible that radon-related damage can occur at any level of exposure, it seems unlikely that there is a threshold concentration below which radon does not have the potential to cause lung cancer. However, the probability of mutation occurring is higher when the number of alpha particles produced from higher ^{222}Rn activities increase, and hence the chances of getting cancer increase with higher levels of indoor radon.

11.2   Historical Development of Studies Related to Indoor Radon as Health Hazard

Evidence of increased mortality among certain groups of underground uranium miners resulting from respiratory diseases date back to the 16th century in central Europe. A high incidence rate of fatal respiratory disease was reported among eastern European miners as early as the 16th century, although radon was not discovered at that time. Early epidemiological studies of miners provided a wealth of information for assessing the health risks associated with radon exposure on miners (Committee on the Biological Effects of Ionizing Radiation, 1988). Only in the 19th century the respiratory disease was attributed to lung cancer (WHO 2009). In the twentieth century, radon was suspected to be the primary cause of lung cancer in radon-exposed miners. The causal role of radon in lung cancer was firmly established in the 1950s (BEIR IV 1988). Radon exposure, along with other natural and anthropogenic radiation, started drawing public attention at the beginning of nuclear testing in 1952. Initially, concern about radon focused on health effects from drinking groundwater. Subsequently, inhalation of radon released to the indoor air from the consumption of groundwater was suspected to be the primary source of exposure. In the mid-1970s, radon emanation from building material in some regions of the country due to the use of alum shale (a variety of shale or clay slate used to produce a particular type of light concrete, WHO 2009) containing high activities of ^{226}Ra was suspected to be the primary source of indoor radon. By 1978, several homes were found to have high indoor ^{222}Rn levels, but they were not
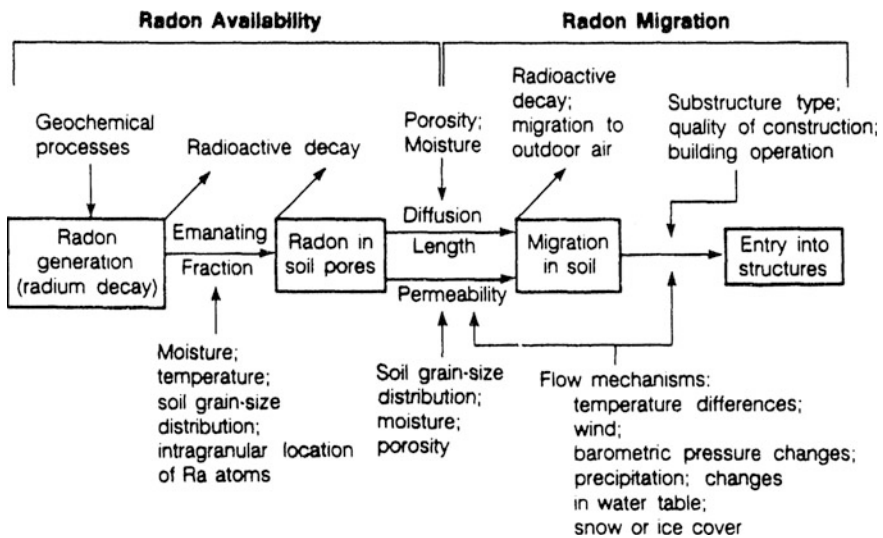
Fig. 11.2 Factors and processes that affect the availability and migration of indoor radon (adapted from Nero et al. 1990)

associated with radon emanation from building materials or well water transport. Shortly following the observation of high indoor radon concentration in a number of homes, soil gas infiltration became recognized as the most important source of indoor radon. Other sources including well water consumption and building materials were considered to be of secondary and tertiary importance. The factors and processes that affect the radon availability and migration of the indoor environment are illustrated in Fig. 11.2.

11.3 Human Lung-Cancer Deaths Related to Radon Exposure

The effects of radon exposure on underground miners were investigated by the Committee on the Biological Effects of Ionizing Radiation (BEIR VI 1999). From eleven cohort studies including 60,000 miners in Asia, Australia, Europe and North America among whom 2,600 deaths from lung cancer had occurred, it was observed that lung cancer rates increased with increasing cumulative radon exposure. As introduced in Chap. 1, for radon-exposed miners, the radon progeny concentrations are given in terms of working levels (WL) and the cumulative exposure of an individual over a working month (170 h/month) is defined as a "working level month (WLM[1])." The BEIR VI (1999) Report indicated that the cancer rate in that group of 60,000 miners (excluding a subset for the Colorado cohort) increased approximately linear with increasing radon exposure (WHO 2009). From a study on lung cancer rates among the former employees of the German uranium mining company, it was found that the percentage increase in lung cancer risk per WLM was larger in non-smokers than in chronic-smokers, but the difference was not statistically significant (BEIR VI 1999).

At an individual level, the risk of radon-induced lung cancer following exposure to a finite radon concentration is much higher among current cigarette smokers than lifelong non-smokers. From the analysis of data from the European residential radon studies, Darby et al. (2005) reported the following: the risk of lung cancer death from indoor radon at the age of 75 for life-long non-smokers were 4, 5 and 10 per thousand when indoor radon concentrations were 0, 100 and 800 Bq m^{-3}, respectively. The corresponding values for life-long smokers were reported to be 100, 120 and 220 per thousand (WHO 2009). It was concluded that for those who have stopped smoking, the radon-related risks are substantially lower than for those who continue to smoke, but they remain considerably higher than the risk of lung cancer death for lifelong non-smokers.

---

[1]One working level is defined as the concentration of any combination of radon progeny that results in the ultimate level of 1.3×10^5 MeV of alpha particle energy.
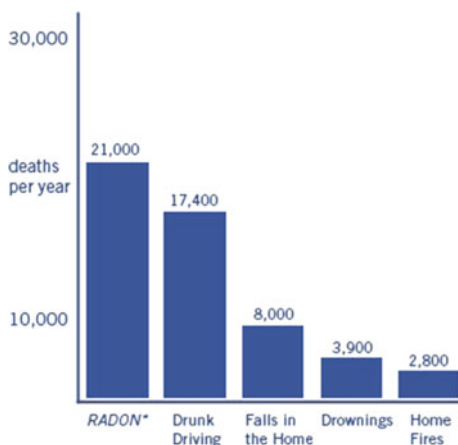
Fig. 11.3 Radon is estimated to cause annually ∼21,000 lung cancer deaths (USEPA 2003). The numbers from deaths from other causes are taken from the Centers for Disease Control in the United States and 2005–2006 National Center for Injury Prevention and Control Report and 2006 National Safety Council Reports (downloaded from http://www.epa.gov/radon/pubs/ciguide.html, downloaded on 5th May 2014)

In the United States, in 2012, the Center for Disease Control reported a total of 157,423 deaths from lung cancer (men: 86,689 and women: 70,734; www.cdc.gov/cancer/lung/statistics/—downloaded on 8th February 2016). In absolute terms, the radon-related lung cancer death rate may be greater than the death rates from many other cancers. The 21,000 lung cancer deaths attributable to radon in the United States is greater than the number of annual deaths for several common cancers including cancer of the ovaries, liver, brain, stomach and melanoma (Fig. 11.3). A comparison of the number of lung cancer deaths relative to deaths from drunk driving, falls in homes, drownings and home fires is shown in Fig. 11.3. In Europe, lung cancer deaths attributable to radon account for approximately 1.8 % of all cancer deaths, amounting to ∼30,000 deaths in 2006 (lung cancer attributable to radon in Canada, Germany, Switzerland, United Kingdom, France and United States are given in Table 11.1, taken from WHO 2009). It is widely known that cancer of the respiratory tract is the most common form of lethal cancer in industrialized countries, accounting for about 20 % of all cancer deaths. Although the cancer can occur in various parts of the respiratory tract, it is found to occur mainly in the lungs, and most lung cancers are associated with smoking. A majority of the lung cancers arise in the bronchial airways and are classified as branchiogenic.

It has been estimated that between 1,000 and 2,000 people in the United Kingdom die each year (15.6–31.2 people per million) from radon-induced lung cancer (Darby et al. 2005). This corresponding figure for the United States is estimated to be

Table 11.1 Estimates of the proportion of lung cancer attributable to radon in selected countries (data is taken from WHO 2009)

Country	Mean indoor radon (Bq/m^3)	Risk estimate used in calculation	Percentage of lung cancer attributed to radon (%)	Estimated no. of deaths due to radon-induced lung cancer each year
Canada (Brand et al. 2005)	28	BEIR VI	7.8	1400
Germany (Menzler et al. 2008)	49	European pooling study[a]	5	1896
Switzerland (Menzler et al. 2008)	78	European pooling study[a]	8.3	231
United Kingdom (AGIR 2009)	21	European pooling study[a]	3.3	1089
		BEIR VI	6	2005
France (Catelinois et al. 2006)	89	European pooling study	5	1234
		BEIR VI	12	2913
United States (BEIR VI 1999)	46	BEIR VI		

[a]After adjustment for year-to-year variation in indoor radon concentration

between 15,000 and 25,000 deaths (47–78 per million). The indoor radon limit set for the UK is 200 Bq m^{-3} (or 5.4 pCi L^{-1}), and in 2010 the new 'target value' was set at 100 Bq m^{-3} (400 Bq m^{-3} in the workplace). In the USA, the level is set at 148 Bq m^{-3} (4.0 pCi L^{-1}). Note that an increased risk of lung cancer cannot be excluded even at levels below 200 Bq m^{-3}, which is the radon concentration level at which action is recommended in many countries. The general distribution of radon potential for the United States is given in Fig. 11.4. On average, the higher potential of radon occurs in the upper regions of the United States from northeastern Washington to Maine, whereas the lowest potential occurs in the southeastern United States. Nero et al. (1986) estimated that there are about a million single-family homes in USA that may have concentrations exceeding 296 Bq m^{-3} (8 pCi L^{-1}), implying that individual's lifetime risk greater than approximately 2 % to long-term occupants. A 0.2–0.3 % average individual risk corresponds to about 10,000 annual cases of lung cancer in the US population (Nero et al. 1986). In some work places, such as water treatment plants, tunnels, caves and mines, elevated levels of radon have also been reported and links have been made between radon levels and incidence of lung cancer in some of these locations.
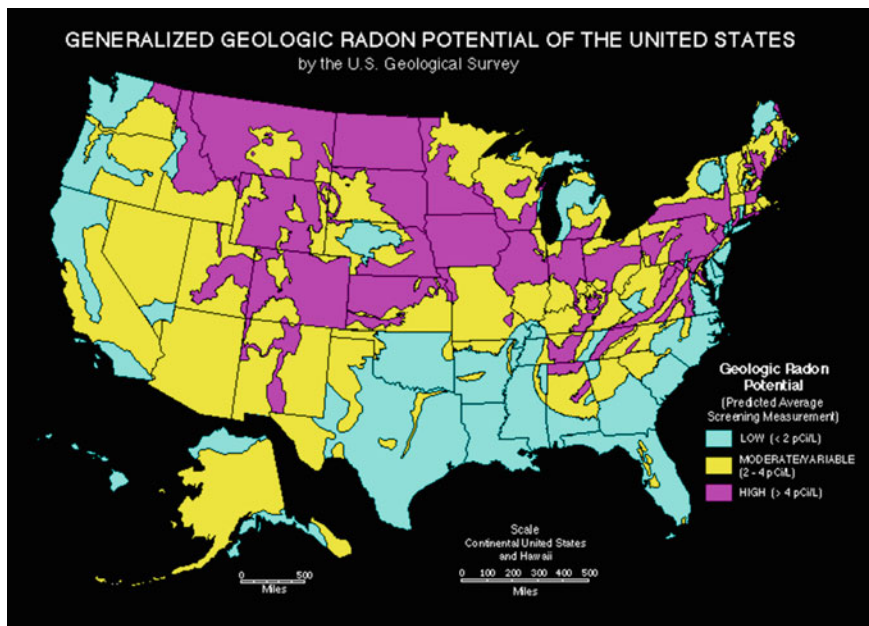
Fig. 11.4 The U.S. Geological Survey has determined the general distribution of radon potential for the United States (see http://energy.cr.usgs.gov/radon/usrnpot.gif). On average, the higher potential of radon occurs in the upper regions of the United States from northeastern Washington to Maine, whereas the lowest potential occurs in the southeastern states. This is a generalized assessment, and does not mean that people living in a high-potential area necessarily are being exposed to elevated levels of radon

11.4   Reference Level for Indoor Radon

A reference level represents the maximum accepted average annual radon concentration in a residential dwelling (WHO 2009). National and global reference levels for indoor radon (the maximum accepted radon concentration in a residential dwelling) vary widely. The reference levels set by various countries do not specify a rigid boundary between safety and danger, but defines a level of risk that a country considers to be too high. The reference level differs from the action level and for a number of years, remediation was only required when the indoor radon levels exceeded the action level. Many countries have developed a radon map based on a combination of indoor radon measurements, aerial radioactivity, geological characteristics, soil permeability and foundation type. In Germany, the radon map was based on radon concentration in soil gas. In Austria, the classification is based upon the mean concentration of radon within a given area.

From a global data synthesis of indoor radon levels, it has been reported that the radon distribution is represented by a log normal distribution, with the majority of the radon concentrations occurring in the lower range. The probability distribution
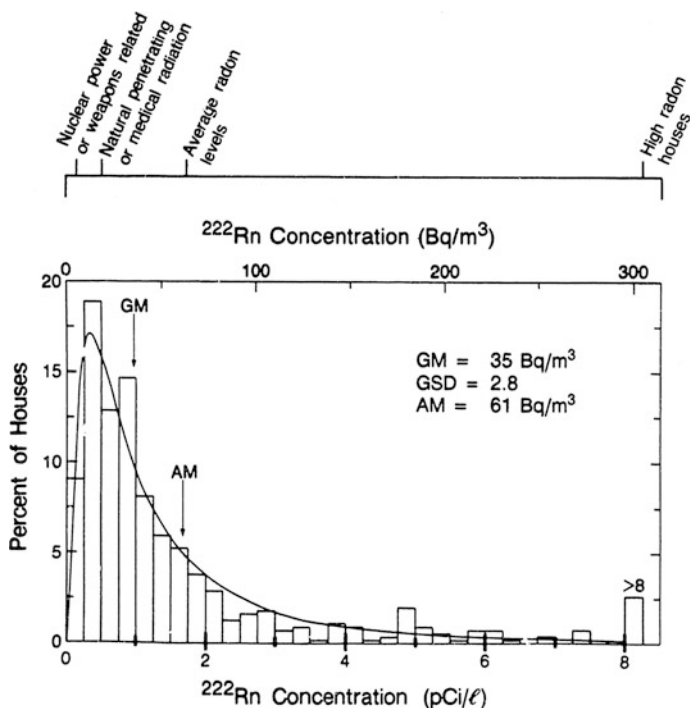
Fig. 11.5 Probability distribution of ^{222}Rn concentrations in U.S. Homes (1 pCi L^{-1} = 37 mBq/l = 37 Bq/m^3). Data resulted from direct aggregation of 19 sets of data, totaling 552 homes from the United States. The smooth curve is a lognormal function with the indicated parameters. The *upper scale* indicates approximately the relative effective doses from radon and other sources of radiation exposure. *GM* Geometric mean; *GSD* Geometric standard deviation; *AM* Arithmetic mean. Adapted from Nero et al. (1990)

of ^{222}Rn concentration from a total of 552 homes, along with a smooth curve of lognormal function and the relative effective doses from radon and other sources of radiation exposure, is given in Fig. 11.5. A vast majority of radon-induced lung cancers are thought to occur following exposure to low and moderate radon concentrations. In a few homes, indoor radon concentrations are extremely high, in the range of 2,000 to 50,000 Bq m^{-3} (e.g. in the Reading Prong area of Pennsylvania and adjoining areas of New Jersey, USA). The number of homes in the extreme tail of the distribution is very small. Most of the time, these high concentrations are often found in home basements in the wintertime. In homes where radon concentrations above the reference levels are found, remedial actions are recommended or required.

In setting a reference level, various country-specific factors such as distribution of radon in outdoor air, number of existing homes with high radon concentrations, average indoor air radon level and the prevalence of smoking are taken into account. From a review of a large number of published research, the World Health

Table 11.2 Indoor radon concentrations in OCED countries (Organization for Economic Co-operation and Development)—data is from WHO (2009)[a] and % dwellings with ^{222}Rn concentrations between 200 and 400 Bq m^{-3} and >400 Bq m^{-3}

Country	Arithmetic mean (Bq m^{-3})	Geometric mean[a] (Bq m^{-3})	% dwellings 200 to 400 Bq m^{-3}	% dwellings > 400 Bq m^{-3}
OECD countries				
Australia	11	8.0 ± 2.1	NA	NA
Austria	99	15	8	4
Belgium	48	38 ± 2	1.7	0.3
Canada	28	11 ± 3.9	NA	NA
Czech Republic	140	44 ± 2	10–15	2–3
Denmark	59	39 ± 2	2.7	0.2
Finland	120	84 ± 2	8.7	3.6
France	89	53 ± 2	6.5	2.0
Germany	49	37 ± 2	2.5	<1.0
Greece	55	44 ± 2	2.0	1.1
Hungary	82	62 ± 2	5.1	0.8
Iceland	10	NA	6.0	1.5
Ireland	89	57 ± 2	6.0	1.5
Italy	70	52 ± 2	3.2	0.9
Japan	16	13 ± 2	NA	NA
Luxembourg	110	70 ± 2	NA	3.0
Mexico	140	90	NA	NA
Netherlands	23	18 ± 2	0.3	0
New Zealand	22	20	NA	NA
Norway	89	40	6.0	3.0
Poland	49	31 ± 2	1.6	0.4
Portugal	62	45 ± 2	NA	NA
Republic of Korea	53	43 ± 2	NA	NA
Slovakia	87	NA	14	11
Spain	90	46 ± 3	4.0	2.0
Sweden	108	56	6–7	3–4
Switzerland	78	51 ± 2	10	7.0
United Kingdom	20	14 ± 3	0.4	0.1
USA	46	25 ± 3	NA	NA
Worldwide average	39			

[a]Geometric standard deviation; *NA* Not available

Organization proposed a reference level of 100 Bq m^{-3} (or 2.7 pCi in 1 L of air) to minimize health hazards due to indoor radon exposure. In countries where the conditions are such that they cannot meet this level, the chosen level should be less than 300 Bq m^{-3} (or 8.1 pCi in 1 L of air), which represents approximately 10 mSv per year of Rn-derived radiation dose, based on calculations by the International Commission on Radiation Protection. Indoor radon concentrations in most of the thirty member countries of the Organization for Economic Co-operation and Development (OECD) are given in Table 11.2. The worldwide arithmetic average value of indoor radon concentration is 39 Bq m^{-3} (WHO 2009), although it varies widely. In twenty of the OECD countries, 0.3–15 % of the homes had indoor ^{222}Rn concentrations of 200–400 Bq m^{-3}, and in 0.1–11 % of the homes, radon levels exceeded 400 Bq m^{-3}, with the largest percentage of high-radon level homes found in Slovakia (Table 11. 2, WHO 2009).

11.5   Factors that Affect the Radon Entry Indoor Air

The product of measured indoor radon concentration and the ventilation rate determine the radon entry at the time of radon measurement. A number of sources of indoor radon have been identified that include outdoor air, building material including concrete, domestic groundwater consumption and soil flux (Fig. 11.6). Figure 11.6 also shows the entry-rate distributions from these sources in various countries.

The two major mechanisms of transport of radon indoors are by molecular diffusion and advection. For a typical volume of homogenous soil unbounded by a concrete slab of finite thickness, and assuming that the generated radon in the soil and concrete migrate solely by molecular diffusion, it is estimated that the diffusive flux contribution accounts for only about 10 % of the mean concentration of radon in single-family dwellings (Nero et al. 1986). Due to the differing half-lives of radon (^{222}Rn, 3.82 d) and thoron (^{220}Rn, 55 s) and for a typical ventilation time scale of $\sim$0.7 h^{-1}, the total indoor concentrations of ^{220}Rn are governed by radioactive decay while the ^{222}Rn concentrations are governed by ventilation. In effect, the ^{220}Rn concentration at any time is determined by the total entry during the past minute, whereas the ^{222}Rn concentration is determined by entry during the past hour.

To assess the radon entry rate indoors from molecular diffusion alone, an estimate can be made as follows: if we assume ^{226}Ra concentration (C_{Ra}) of 30 Bq kg^{-1} in the soil, radon emanation coefficient (f) of 0.2, dry soil density [$\rho = \rho_s(1-\varepsilon)$ where ρ_s is the density of the soil grains, $\sim$2600 kg m^{-3} and ε is the total porosity, $\sim$0.4–0.6] of 1600 kg m^{-3}, the decay constant (λ_{Rn}) of ^{222}Rn = 2.1 × 10^{-6} s^{-1}, the generation rate of mobile ^{222}Rn = C_{Ra} ρ f λ_{Rn} = 72.6 Bq m^{-3} h^{-1}. For a typical volume of a home of 360 m^3 (median for a family of 4), to achieve an indoor ^{222}Rn contribution from soil of 50 Bq m^{-3}, given an air-exchange rate of 0.7 h^{-1}, a ^{222}Rn entry rate from soil is expected to be 12,600 Bq h^{-1}. Since ^{222}Rn can migrate about a meter through soil by molecular diffusion alone, the radon generation rate within a reasonable volume of a typical
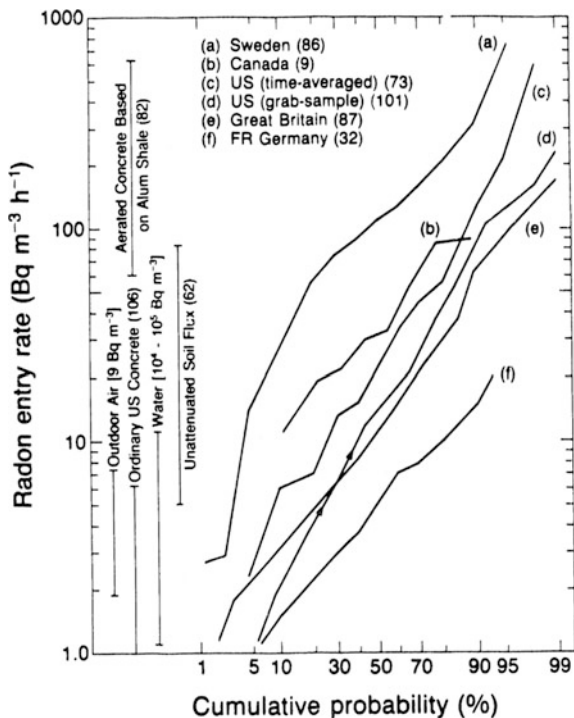
Fig. 11.6 The radon entry rate as a function of cumulative probability. Radon entry rate is determined from the product of simultaneously measured ^{222}Rn concentration and ventilation rate. The number of residences in each sample is indicated in parenthesis. The bars at the left indicate the range of contributions expected from a variety of sources. The following assumptions are made in making this plot: a single-story house of wood-frame construction with a 0.2 m-thick concrete-slab floor; floor area = 100 m^2; floor height = 2.4 m; water usage = 1.2 m^3; use-weighted transfer efficiency for radon to air of 0.55; and the ventilation rate = 0.2–0.8 h^{-1}. Data taken from multiple sources were synthesized for this figure (adapted from Nero et al. 1990)

soil is adequate to account for the typical radon entry rate into a residential building (Nazaroff 1992). Furthermore, weather-induced flow of soil gas through homogenous and isotropic soil and across building substructure penetrations with at least moderate soil permeability can also explain typical ^{222}Rn entry rates in single-family dwellings (Nazaroff 1992).

Although the concentration of soil ^{226}Ra is important, the transport-related parameters (permeability of the soil, diffusivity, etc.) play a stronger role on the amount of radon entry rates indoor (Fig. 11.7). For the entry of radon from soil into buildings, the major transport across the substructure is dominated by pressure-driven flow while the molecular diffusion through a concrete slab is too slow to permit large radon entry rates (Nero and Nazaroff 1984). Since the molecular diffusion process is a slow process, the change in the radon entry rate is also expected to respond slowly; however, rapid and dramatic changes in the radon

entry rates have also been observed (Nazaroff et al. 1985, relevant discussion is also presented in Chaps. 9 and 10). If the molecular diffusion of radon takes from a region of low permeability to a region of high permeability, then, the radon entry rate due to molecular diffusion could be significantly higher than that of advection. However, it is generally anticipated that the radon intrusion by advection is typically a more significant process than diffusion.

Transport of radon from soil through substructure penetrations into buildings is driven by small pressure differences across the building envelope (Fig. 11.7). For a
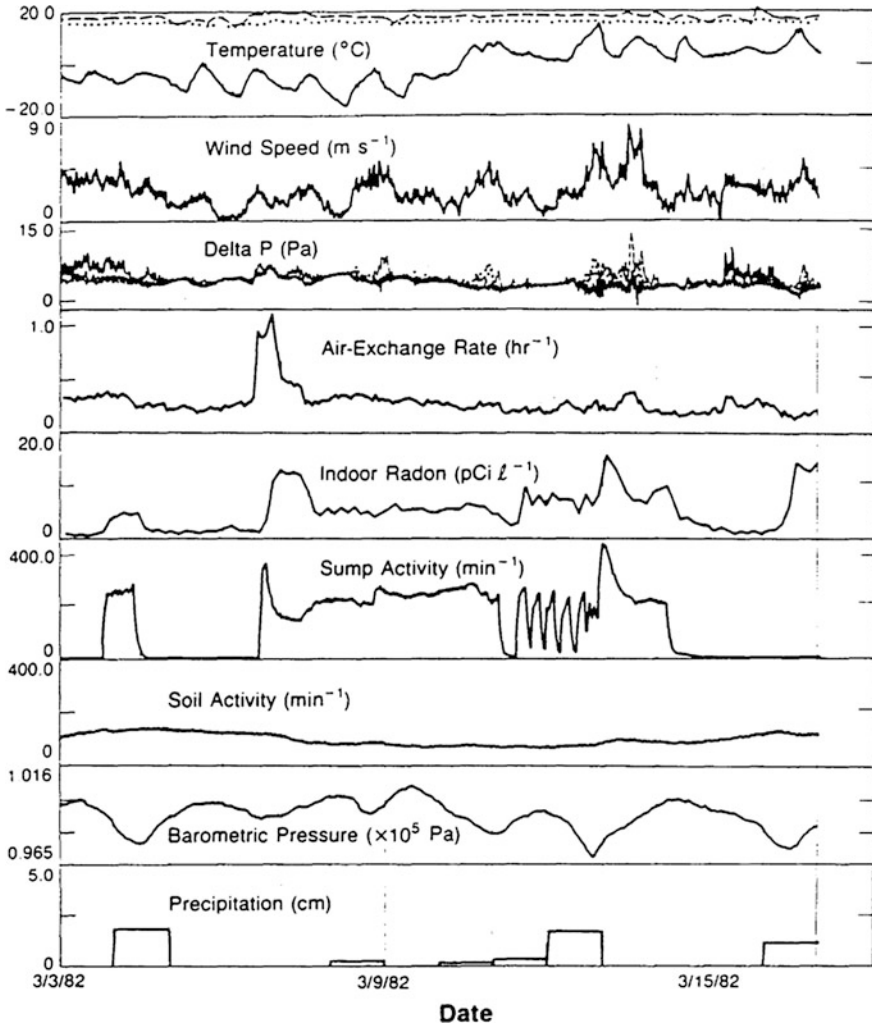
Fig. 11.7 Temporal variations of ^{222}Rn concentration, ventilation rate, and environmental parameters in the basement of a house over two-week period examining the dependence of radon entry on environmental factors (adapted from Nero et al. 1990)

typical wind speed of 3 m s^{-1} and windward drag coefficient of 0.4, and assuming the pressure inside the house is the same as the free stream conditions, Nazaroff (1992) reported a pressure difference across the soil and substructure on the windward side of ~ 2 Pa (which is only of the order of only two ten thousandth of an atmosphere). The pressure difference [ΔP (pressure in the wall—free-stream pressure) $= \frac{1}{2}\,\rho_a\,v^2$ where v is the wind velocity and ρ_a is the air density] varies as the square of the wind speed, with higher wind speeds resulting in larger pressure differences. Since higher wind speeds in outdoor air will lead to increased infiltration rates of outside air, it becomes difficult to say the net effect between infiltration of ^{222}Rn-deficient air into the building and higher ^{222}Rn-enriched soil gas entering the building due to higher wind speed outside (Fig. 11.7).

Air is a compressible fluid and hence its density varies with temperature, and is acted upon by gravity. When there is a gradient in temperature with height indoors, it results in a pressure differential and there is a movement of air vertically upward (stack effect). In addition, operation of building systems such as fireplaces, cloth dryers and exhaust fans, and outdoor changes such as barometric pressure changes and precipitation also can affect pressure changes and may increase the rate of radon entry indoors. For example, during the operation of a fireplace, a high rate of airflow out of the chimney takes place, which may lower the air pressure inside the house and may increase the rate of radon entry. An outdoor-indoor pressure difference of 1 Pa has been reported to be associated with fan operation in an exhaust-ventilated home (Mowris and Fisk 1988).

11.6   Mass Balance of Indoor Radon

A building is regarded as a well-mixed box with the inflow of outside air into the building and exhaust of indoor air to the outdoors, keeping the volume of indoor air constant. The factor E_{ACH}[2] (which is also known as the ventilation rate; ventilation refers to the total supply rate of outdoor air into a building, whether intentional or not) depends on building construction and operation, as well as outside wind velocity and the difference between inside and outside temperatures. Typically, the E_{ACH} values in U.S. single family housing are reported to vary between 0.25 h^{-1} for a 'tight' building, to 1.0 h^{-1} for a 'leaky' building (i.e., all 100 % of the indoor air is exchanged in hour; Fig. 11.8). The indoor concentration as a function of ventilation rate indicates that a 50 % reduction in radon concentration results from a twofold increase in the ventilation rate, from 0.25 to 0.50 ACH or 75 % reduction for a four-fold reduction in radon activity concentration (Fig. 11.8). Note that the time-scale of ventilation is much shorter than the half-life of ^{222}Rn. For a family of four in the United States, the mean volume of the building is V = 360 m^3 and the corresponding area of the basement floor is 80 m^2, hence the air-exchange rate is

---

[2]ACH: air change hour; a value of 0.25 means 25 % of the indoor is exchanged in 1 h.

Fig. 11.8 Indoor ^{222}Rn
concentration as a function of
ventilation rate (ACH). The
time scale of ventilation is
much shorter compared to the
half-life of ^{222}Rn (3.82 days)
and therefore radioactive
decay is a minor sink for
indoor radon
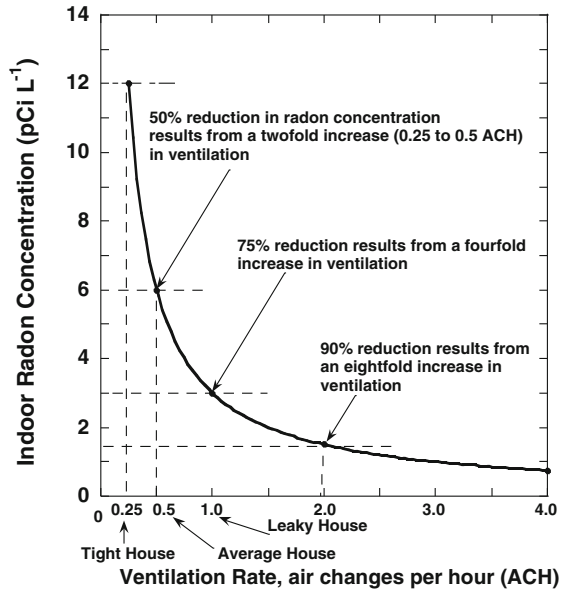
assumed to be 0.7 h^{-1} (Nazaroff 1992). Keeping the right ventilation rate serves the
purpose of controlling odors, diluting the pollutants generated by indoor sources
(e.g., new painting or installation new carpet, etc.), as well as maintaining a proper
balance of metabolic gases.

Radon entry and indoor concentrations can be assessed if the building is viewed
as a well-mixed leaker container. In the United States, Canada and other countries,
in most single-family dwellings infiltration is the major component of ventilation at
times when the outdoor air must be heated or cooled for thermal comfort. The two
factors that drive this infiltration are the outdoor wind and the temperature differ-
ence between the indoor and outdoor air. A steady-state mass balance for ^{222}Rn can
be easily constructed and applied to radon contained within a building. The three
possible sources of indoor radon are: (i) from soil primarily by openings in sub-
structure; (ii) radon released from water consumption; and (iii) radon released from
building materials. If C_{in} and C_{out} are the concentrations of ^{222}Rn (Bq m^{-3}) in
indoor and outdoor air, respectively, Q is the flow rate of outdoor air into the
building (m^3 s^{-1}), V is the building volume (m^3), and R is the rate of first-order
removal of ^{222}Rn from indoor air by processes other than ventilation (e.g., filtration
of air through activated carbon which sorbs radon), then, the mass balance for
indoor ^{222}Rn can be written as follows:

$$Input - Output + \sum sources - \sum sinks = rate\ of\ change\ of\ storage \quad (11.1)$$

(or)

$$C_{outside} \cdot V_{building} \cdot ACH - C_{inside} \cdot V_{building} \cdot ACH + \sum sources - \sum sinks$$
$$= \frac{d(C_{inside})}{dt} \cdot V_{building}$$

To estimate ^{222}Rn concentration inside the building at steady state,

$$\frac{d(C_{inside})}{dt} \cdot V_{building} = 0 \qquad (11.2)$$

$$C_{inside} = \frac{\sum sources}{V_{building} \cdot ACH} \qquad (11.3)$$

The mass balance equation comprised of sources and sinks of indoor radon is given as:

$$S_s(Bq\,s^{-1}) + S_w(Bq\,s^{-1}) + S_b(Bq\,s^{-1}) + V(m^3)C_{out}(Bq\,m^{-3})E_{ACH} - C_{in}(Bq\,m^{-3})V(m^3)E_{ACH}$$
$$- C_{in}(Bq\,m^{-3})V(m^3)\lambda_{Rn}(s^{-1})_{Rn} - C_{in}(Bq\,m^{-3})R(s^{-1})V(m^3) = 0$$

$$(11.4)$$

where S_s, S_w and S_b are the rates of radon entry into the building from soil, water and building materials, respectively, E_{ACH} is the number of air changes per second (usually it is commonly given in air exchanges per hour, for dimensional consistency, it is given in air exchanges per second), R is the removal term by sorption, and λ_{Rn} is the decay constant of ^{222}Rn.

For ^{222}Rn, the term R = 0, as there is virtually very little removal of ^{222}Rn that takes place indoors as radon is an inert gas and very little ^{222}Rn goes through activated graphite material indoors. Also, the amount of ^{222}Rn that undergoes radioactive decay ($C_{in} * V * \lambda_{Rn}$) compared to the amount of ^{222}Rn entering from the outside of the house into the house ($C_{in} * Q$) is negligible (due to differences in mean-life of ^{222}Rn, 5.51 days and typical residence time of indoor air of ~ 2 h). Indoor radon is mostly derived from soil—primarily by advection across openings in substructure. The radon entry from soil is given by:

$$^{222}Rn\,entry\,rate\,(Bq\,s^{-1}) = soil\,gas\,entry\,rate, Q_s\,(m^3s^{-1})$$
$$*^{222}\,Rn\,concentration\,in\,soil\,gas, C_g\,(Bq\,m^{-3}) \quad (11.5)$$

The most important physical parameter of soil relevant to radon migration is, as mentioned earlier, the permeability of the soil—how readily the soil air may flow through it. Permeability of soil depends on the microscopic characteristics that include size, shape, number and orientation of pores and the water content. Fine-grained soils such as clays and silt have low porosities and smaller permeabilities than coarse-grained soils (e.g., sand). Larger grains have larger pores and consequently the resistance to the fluid flow is low and thus they have higher

permeabilities. The permeability of soils ranging in size from coarse sand to silty clay span over six orders of magnitude (Nazaroff 1992). Field measurements of soil permeability near houses show a four order of magnitude range (Nazaroff 1992). There is also anisotrophy in soil permeability. For example, the sedimentary beds deposited in horizontal layers are expected to have higher permeability than those deposited in the vertical direction. Permeability data on samples of water-bearing consolidated soils consisting of clay, silt and sand indicate higher horizontal permeabilities by factors of 1.4 and 7, depending on the site. Differences between horizontal and vertical permeability as high as 1,000 also have been reported (Bowles 1979). Higher permeability in the horizontal direction may lead to a large volume of soil contributing radon to the building.

11.7   Burden of Lung Cancer from Indoor Radon and Its Progeny

As presented in earlier sections, the frequent appearance of homes with relatively high ^{222}Rn concentrations translate to individual lifetime risks of cancer exceeding 1 %, and occasional occurrence of levels much higher (with estimated risks up to an order of magnitude higher), do occur globally. Note that the Rn-originated risks are often large compared to other environmental risks and hence a large amount of studies have been conducted characterizing the indoor ^{222}Rn concentrations and the factors and processes affecting them and their health implications (e.g. Nero and Lowder 1983; Nero et al. 1986). The main health effect of radon is the induction of respiratory tract cancers. Both radon and its progenies emit alpha particles which are highly radiologically hazardous. While radon does not get attached to any tissues, the daughter products (^{218}Po, ^{214}Po as well as ^{214}Pb and ^{214}Bi) are often adsorbed on to tissues inside the human body and yield the majority of the dose to the respiratory system.

As discussed in Chap. 1, the radon concentration can be represented in terms of mole or activity unit. The activity is the actual rate at which atoms undergo radioactive decay (the SI unit Becquerel (Bq) is equal to the amount of radionuclide substance in which one atom decaying per second). For decay products, the collective quantity of its progeny (^{218}Po, ^{214}Pb, ^{214}Bi and ^{214}Po) is used widely and is represented by equilibrium-equivalent-decay-product concentration (EEDC). EEDC is given in terms of the individual decay-product concentration and is based on the alpha decay energies and half-lives of the ^{222}Rn decay series given in Chap. 1. The EEDC is given as:

$$EEDC_{222} = 0.106\,A_{Po\text{-}218} + 0.513\,A_{Pb\text{-}214} + 0.381\,A_{Bi\text{-}214} \qquad (11.6)$$

where $A_{Po\text{-}218}$, $A_{Pb\text{-}214}$ and $A_{Bi\text{-}214}$ are the activity concentrations of Po-218, Pb-214 and Bi-214, respectively. Note that the ^{214}Po (half-life = 164 μs) activity concentration does not contribute significantly to this expression due to its high decay

constant value, which implies very few atoms[3] present in air compared to other three nuclides produced from the decay of ^{222}Rn before production of ^{210}Pb. Note that ^{214}Po alpha energy (7.687 MeV) is the largest contributor to the coefficients of this expression. A similar expression for the ^{220}Rn series, the EEDC$_{220}$ is given as:

$$\text{EEDC}_{220} = 0.913\,A_{\text{Pb-212}} + 0.087\,A_{\text{Bi-212}} \tag{11.7}$$

Note that ^{216}Po (half-life = 0.145 s) and ^{212}Po (half-life = 0.299×10^{-6} s) do not contribute directly to this expression due to very short half-lives (see the foot-note below for short-lived ^{214}Po), although ^{212}Po (8.784 MeV) contributes the dominant alpha energy.

The dose of lung tissue from the inhalation of radon and its progeny cannot be directly measured and is calculated by modeling the sequence of events involved in inhalations, deposition, clearance, and decay of radon progeny within the bronchial airways (James 1988). The dose for a given amount of exposure depends on a number of environmental and personal factors that include aerosol size distribution, rate of breathing and lung size. The structure and airflow in each region determine the fractional deposition of inhaled aerosol particles and of unattached radon progeny (James 1988). The general method to calculate the effective dose equivalent, established by the International Commission on Radiological Protection (ICRP), involves the following steps: (i) evaluate the doses absorbed by tissues for a given intake of a radionuclide; (ii) weigh the doses based on standard estimates of risks from irradiating each tissue; and (iii) summing up the total risk contributed by all irradiated tissues (James 1988). The volume of intake air and the residence time of breathed air inside the human body also plays a significant role in the dose of radiation received.

The maximum amount of air that we can take in and breathe out (known as *vital capacity*, the maximum amount of air a person can expel from the lungs after a maximum inhalation) is approximately 3 L. In addition, some amount of air remains in the respiratory system (residual volume) and the total volume in the respiratory system of a human body can be up to 6 L. The capacity of the lung is typically about 2 L. During the time ^{222}Rn is inside the human body,[4] some of the ^{222}Rn undergoes radioactive decay and the decay of progeny is deposited on the tissues of

---

[3]If one assumes a known amount of ^{222}Rn is kept for about 3 h for its short-lived progeny to reach secular equilibrium, then, after 3 h, the activity of the following will be equal: ^{222}Rn = ^{218}Po = ^{214}Pb = ^{214}Bi = ^{214}Po. However, the ratio of ^{222}Rn atoms to that of ^{214}Po = half-life of ^{222}Rn/half-life of ^{214}Po = 2.01×10^9. This implies that for every 2.01 billion atoms of ^{222}Rn, there will be one atom of ^{214}Po.

[4]One can make an estimate of how many ^{218}Po- alpha particles will be produced from the residence time of air inside the human body: assuming indoor ^{222}Rn activity of 4 pCi L^{-1}, amount of air breathed is 10 L/min, and residence time of air inside human body is 15 s, total radon inside the body will be 10 pCi. This corresponds to 1.76×10^5 ^{222}Rn atoms with ^{218}Po/^{222}Rn activity ratio of 0.054 (or 0.54 pCi of ^{218}Po which corresponds to 0.24 ^{218}Po alpha particle).

the pathway of radon inside human body. When a person is exposed to air containing radon and its decay products, the part of the body that receives the highest dose of ionizing radiation is the bronchial epithelium, although other parts of the body including extra thoracic airways and skin may receive appreciable doses. Ingestion of water with high levels of dissolved radon will result in exposure to the stomach as well (note that the stirring of water and/or treatment during collection and transportation could result in a significant loss of radon). There is no strong evidence suggesting radon causes an increase in mortality from cancers other than lung cancer.

11.8   Radon-220 and Its Decay Products and Their Health Hazards

11.8.1   Effects of Pressure-Driven Advective Flow and Diffusion on the Indoor Activities of ^{222}Rn and ^{220}Rn

Due to the differences in the half-lives of ^{220}Rn and ^{222}Rn and their progeny, and the time scale of ventilation, the indoor ^{220}Rn concentration is expected to be up to two orders of magnitude lower than that of ^{222}Rn (Nazaroff et al. 1992). If the transport of radon is dominated by diffusion, one can compare the diffusive fluxes of ^{222}Rn to ^{220}Rn. The diffusive flux density (J_{Rn}^{d}) of radon activity per unit area of the pore soil (Bq m^{-2} s^{-1}) is given by:

$$J_{Rn}^{d} = -D_e \nabla I_{Rn} \qquad (11.8)$$

where D_e is the effective (or interstitial) diffusion coefficient (this is equivalent to a parameter that relates the gradient of the bulk concentration to the flux density across a geometric area, Nazaroff et al. 1992). For the case of uncovered soil of infinite depth and extent, and assuming the radon concentration to be zero at the soil surface, the steady-state solution to the one-dimensional form of Eq. (11.8) yields the radon activity concentration in the soil pores at a depth of z below the surface (C_{Rn} (z)), and is given by:

$$C_{Rn}(z) = C_{\infty} \left(1 - e^{-z/L}\right) \qquad (11.9)$$

where C_{∞} is the activity concentration (Bq m^{-3}) in the pores at large depths and L is the diffusion length ($= (D_e \, \tau_{Rn})^{1/2}$) and τ_{Rn} is mean-life ($= 1/\lambda_{Rn}$) of radon. Substituting Eq. (11.9) into (11.8) and multiplying by soil bulk porosity ε, Eq. (11.8) can be written as:

$$J_{Rn}^d = \epsilon\lambda\,L\,C_\infty = (D_e\lambda_{Rn})^{1/2}\rho_s f\,A_{Ra}(1 - \epsilon) \tag{11.10}$$

where f is the emanation fraction, ρ_s is the dry density of the soil grains (2.6×10^3 kg m^{-3}) and A_{Ra} is the activity concentration of ^{226}Ra. For a given set of values, one can obtain the ratio of diffusive flux of Rn-220 to that of Rn-222.

$$\text{Diffusive flux of}\,^{220}\text{Rn}/\text{diffusive flux of}\,^{222}\text{Rn} = (\lambda_{Rn\text{-}220}/\lambda_{Rn\text{-}222})^{1/2} = 77. \tag{11.11}$$

The inherent assumption in this estimation is that the specific activities of ^{226}Ra and ^{224}Ra are the same (i.e. activity concentration of ^{238}U and ^{232}Th the same[5]) and the emanation fraction of ^{222}Rn and ^{220}Rn are the same. The calculated radon flux using Eq. (11.10), assuming typical values of ^{222}Rn, $D_e = 2 \times 10^{-6}$ m^2 s^{-1}, $\rho_s = 2{,}600$ kg m^{-3}, f = 0.2, $A_{Ra} = 31$ Bq kg^{-1}, and $\epsilon = 0.5$, is 0.016 Bq m^{-2} s^{-1}. This can be compared to the measured mean ^{222}Rn flux of 0.015 Bq m^{-2} s^{-1} (Wilkening et al. 1972). Assuming the same set of parameters for ^{220}Rn, the calculated diffusive flux ^{220}Rn is 1.27 Bq m^{-2} s^{-1}, which is 77 times (=^{222}Rn diffusive flux * mean-life of ^{222}Rn/mean-life of ^{220}Rn) higher than that of ^{222}Rn. This value can be compared to the average value at six sites in New Mexico of 1.6 ± 0.3 Bq m^{-2} s^{-1} (Crozier 1969).

From the discussion above, the activity of ^{220}Rn can be 77 times higher than that of ^{222}Rn. Whenever radon-related health issues are discussed, it is mostly about radon-222 and not much attention is given to radon-220. Although the radon-220 concentration just above the bare soil (less than 1 m above surface soil—air interface) can be 77 times higher than that of ^{222}Rn, the potential alpha-energy concentration (PAEC$_{212}$, the PAEC from ^{212}Pb, the primary ^{220}Rn decay product, Chap. 1) is estimated to be 4.6 nJ m^{-3} compared to 20 nJ m^{-3} for ^{222}Rn (Table 11.4, Nazaroff et al. 1992); conversion of these units to WL are given in Table 11.3 and comparative concentrations of ^{220}Rn and ^{222}Rn are also given in Table 11.4). The differences in the concentrations and the PAEC for ^{220}Rn and ^{222}Rn are due to differences in the equilibrium factor between them; for ^{222}Rn, it is >0.5, while for ^{220}Rn it is extremely small due to the long half-life of ^{212}Pb ($T_{1/2} = 10.64$ h). The ratio of PAEC$_{220}$/PAEC$_{222}$ has been reported to vary between 0.3 and 0.8 (Europe, Canada and United States, Gunning and Scott 1982; Toth 1984; Schery 1985). This suggests the potential significance of the ^{220}Rn series indoors as a health hazard. In the case of diffusion-dominated entry of both isotopes, assuming that their source concentrations from source materials are similar, then, due to the long half-life of ^{212}Pb compared to other short-lived progeny of ^{222}Rn, the activity concentration of the decay products of ^{220}Rn is expected to be a factor of five or so less compared

---

[5]The concentrations of ^{238}U and ^{232}Th in Upper Continental Crust (UCC) are 2.5 ppm and 10.3 ppm, respectively (Wedepohl 1995); the corresponding activity values are 30.8 mBq g^{-1} rock and 41.7 mBq g^{-1} rock, respectively (i.e., parent-supported ^{220}Rn activity is 1.35 times higher that of parent-supported ^{222}Rn activity).

Table 11.3 SI units and equivalents for traditional units

Parameter, SI unit	Conversion for traditional unit
Activity, Bq	1 Ci = 3.7 × 10^{10} Bq (1 pCi = 0.037 Bq)
Concentration, Bq m^{-3}	1 pCi L^{-1} = 37 Bq m^{-3}
PAEC, J m^{-3}	1 WL = 1.3 × 10^5 MeV/L = 2.08 × 10^{-5} J m^{-3}
EEDC$_{222}$, Bq m^{-3}	1 WL (PAEC) = 3740 Bq m^{-3}
EEDC$_{220}$, Bq m^{-3}	1 WL (PAEC) = 276 Bq m^{-3}
Exposure, J m^{-3} s	1 WLM = 12.97 J m^{-3} s
Exposure, Bq m^{-3} y	1 WLM = 73.9 Bq m^{-3} y
Exposure rate, J m^{-3}	1 WLM/y = 4.11 × 10^{-7} J m^{-3}
Exposure rate, Bq m^{-3}	1 WLM/y = 73.9 Bq m^{-3}

Table 11.4 Comparative concentrations of ^{220}Rn and ^{222}Rn and their decay products

	Indoor		Outdoor (1 m height)	
	Rn (Bq/m^3)	PAEC (nJ/m^3)	Rn (Bq/m^3)	PAEC (nJ/m^3)
^{220}Rn Series	3–4	21	16	5
^{222}Rn Series	15–20	44	6	20

that of ^{222}Rn. Furthermore, the PAEC$_{220}$ is expected to be greater than that of the PAEC$_{222}$ by a factor of two to three (Nazaroff et al. 1992).

In the case of pressure-driven advective flow of air and associated radon, the ratio of ^{220}Rn/^{222}Rn is expected to be the same as the ratio of their decay constants (the activity of ^{222}Rn that leaves the surface = (1/5,936) * activity of ^{220}Rn that leaves the surface) and hence the ^{220}Rn contribution could be quite significant. To summarize, the concentration ratios of ^{220}Rn/^{222}Rn could differ up to two orders of magnitude, depending on whether diffusion or pressure-driven advective flow is the presumed mechanism of transport.

11.9   Radon Prevention and Mitigation

The greatest amount of radon exposure to humans is generally from their homes (perhaps except for miners). Two different general approaches are available for reducing the levels of ^{222}Rn indoors: reducing the rate at which radon enters from its sources or increasing the rate of removal of radon from indoor air. The sources of, and concentrations in, indoor air and transport mechanisms of radon influence the choice of prevention and mitigation strategies. The effectiveness of any radon prevention and mitigation strategies is determined based on final indoor radon concentration (Rahman and Tracy 2009) and the key goal is the overall risk reduction in the population. The strategies to achieve overall risk reduction include both radon reduction in existing buildings (known as mitigation or remediation) and

radon control options in the construction of new buildings (referred as prevention). Radon concentration in a newly-built and unoccupied building can change once the building is occupied due to differences in heating and ventilation. However, testing prior to occupancy can identify problems in advance and is generally easier to address the radon problem at that stage. Hence, it is always recommended to test radon level prior to occupying a house; it is also recommended to monitor the radon level periodically over the life of the structure (Gammage and Wilson 1990). In some countries, they have come up with a radon index after testing individual building sites prior to construction. Such an index is used to define the degree of radon protection needed for building on that site. In a few countries (e.g., USA, United Kingdom, Norway, Switzerland), measurements of indoor radon are already an element in the process of buying and selling homes. Generally, the responsibility to reduce radon concentrations in a home normally rests with the owner of the house. In countries such as Czech Republic, Sweden and Switzerland, there is a requirement to reduce indoor radon levels to below 4,000, 1,000 and 200 Bq m^{-3}, respectively.

Techniques for radon prevention and mitigation in both approach and theory have evolved over the past forty years. Initial attempts were solely focused toward those sites where anthropogenic activities had elevated local concentrations of ^{226}Ra (mainly ^{238}U) resulting from the use of uranium mill tailings as a construction material. Subsequent research findings indicated that elevated radon concentrations could occur in areas of 'normal' radioactivity, and thus mitigation work was found to be necessary to deal with naturally occurring radon. There are two aspects of building design and operation that play important roles in influencing entry of soil radon indoors. The first aspect is the design and operation of the ventilation system, as it may affect the pressures that drive the bulk airflow through the soil. The second aspect is the design and construction of the substructure in a building, as it controls the degree of movement between the air in the soil and the air in the building (Nazaroff et al. 1992). Building practices vary widely even within one country (e.g., sun-belt areas versus northern parts of the United States) and from country to country, principally depending on the climate and the structural and drainage characteristics of the local soil.

The first radon mitigation program was conducted at Grand Junction, Colorado where uranium mill tailings containing up to 480 ppm of ^{238}U (corresponds to 6,000 Bq kg^{-1} of ^{238}U in which ^{238}U and ^{226}Ra are in secular equilibrium) had been used as a replacement for sand as fill. Buildings that stood on a layer of tailings were found to contain indoor radon levels in excess of 200 Bq m^{-3} (5.4 pico Curie per liter of air). Surface and bore-hole gamma-ray surveys along with radon flux measurements from floors and walls indicated the sources of radon. Removal of the uranium mill tailings resulted in a significant reduction in the concentrations of indoor radon. In buildings where the concrete itself had been made with uranium mill tailings instead of sand, seamless epoxy coatings were developed for use as a barrier to prevent radon diffusion, which in turn reduced indoor radon levels. If the concrete floor material has low ^{226}Ra concentration, then, it will serve as an effective barrier against soil gas and hence the diffusion of radon through a concrete floor can

be assumed to be negligible. However, in such cases controlling the movement of soil gas through cracks in a concrete floor becomes essential.

Use of groundwater from a private drilled well for domestic consumption could result in a significant amount of radon released indoors. In such cases, water treatment may help in reducing the indoor air concentration of radon. It has been observed that the health risk associated with radon in water is mostly via the inhalation of radon as opposed to the ingestion of radon. The primary strategies to reduce well water-borne radon at the point of entry to the home are: (i) aeration in a sealed tank where air is bubbled through the water or the water is sprayed into the air over objects, while radon is extracted from the water to the outdoors and (ii) filtration of water through granular activated carbon (WHO 2005).

11.9.1   Basic Mitigation Methods for Radon

The four common mitigation methods for radon include: (i) source removal; (ii) increase in the resistance of the building fabric to soil gas entry, generally called 'sealing'; (iii) increasing the structure ventilation rate; and (iv) soil ventilation. An example of source removal is given above. In conventional building styles, actions during construction often result in many openings through which soil gas containing radon can move freely from the soil to indoors (Scott 1992). Openings are also produced as a side effect of architectural features in houses such as sunken baths, sunken living rooms or unpaved crawl spaces. Concealed openings in floor slabs made to correct errors in plumbing installations can also serve as conduits for the movement of soil gas. The formation of cracks in buildings due to the annual freeze/thaw cycle (as this cycle changes the volume of the upper soil layers over a year) have been reported in northern areas of North America. In the southern areas of the United States, cracks have also formed due to the shrinkage/swell cycle in response to seasonal rainfall variations (Scott 1992). Sealing off the opening in surfaces between the soil and the indoors is a stand-alone mitigation technique which results in limited success. For example, USEPA has reported only one out of 1,500 cases have success with sealing alone and therefore sealing is not recommended (USEPA 1993). Generally, epoxy materials are found to be good sealants, although they are rigid and so strong that new cracks will often form adjacent to the old epoxy-filled joints. Flexible sealants are found to be good and do not produce new stresses that might cause new cracks (Scott 1992).

11.9.2   Design Criteria of Radon Systems to Minimize Indoor Radon Levels

The design criteria that radon systems should possess for the prevention as well as mitigation of indoor radon are the following (WHO 2009):

  (i)   Ability to reduce indoor radon concentration below the reference level;
 (ii)   Durable and functional during the lifetime of the building;
(iii)   Easy radon monitoring of the system;
(iv)   Affordable cost for the installation, operation and maintenance of the system for the public; and
 (v)   Ease to install additional accessories (such as a fan) when needed (e.g., when passive soil depressive systems are used).

The installation and typical annual operating costs of common mitigation techniques can be found in WHO (2009).

A comparison of different radon control systems for new construction that takes design criteria into consideration are given in USEPA (1993). These different options include:

  (i)   Sealing soil contacted surfaces;
 (ii)   Soil gas barriers;
(iii)   Passive ventilation of the unoccupied lower space;
(iv)   Active ventilation of the unoccupied lower space;
 (v)   Active soil de-pressurization;
(vi)   Passive soil depressurization; and
(vii)   Balanced ventilation.

Of these different methods (sealing, ventilation and depressurization), the active soil de-pressurization is one of the most widely used approaches for reducing radon in existing homes. According to a WHO survey, active soil depressurization represented the major radon mitigation method reported by the following countries: Austria, Belgium, Finland, Germany, Norway, Slovenia, Sweden, United Kingdom and the United States of America (WHO 2007). Detailed information on other methods of radon reduction techniques including house ventilation, entry route sealing, house pressure adjustments, air cleaners and well water treatment are given in the second edition of the EPA's technical guidance document (Henschel 1988).

The general principle of the soil depressurization method is to draw radon-containing soil gas away from the house foundation before it can enter and to exhaust this soil gas outdoors (USEPA 1993). The approach in which a fan is used is to create the necessary suction to draw the soil gas radon is referred to as active soil depressurization (ASD) method. There are a number of variations of the ASD process. The first is sub-slab depressurization (SSD), where one or more suction pipes inserted into the aggregate or soil beneath a concrete slab. Suction is then drawn on these pipes using the fan, with the collected soil gas then vented outdoors. Other variations include drain-tile de-pressurization, block-wall de-pressurization (where one or more individual suction pipes are inserted into the void network within a block foundation wall and connected to the fan) and sub-membrane de-pressurization for crawl-space housing with dirt floors. In this last variation, a plastic sheet is placed over some or all the dirt floor, creating a plastic 'slab.' One or more suctioning pipes penetrate this sheeting to draw from the section under the plastic and the soil gas is vented out.

There are three mechanisms by which ASD appears to function, with the primary mechanism being the creation of a negative pressure in the soil or aggregate immediately under the foundation. This occurs either under the concrete floor, inside the hollow-block foundation wall or underneath a membrane laid over the dirt crawl-space floor.

11.10   Future Research

In a majority of the structures, the fraction of indoor radon derived from molecular diffusion occurring in industrially contaminated building fill materials is relatively small and in most cases, radon enters predominantly via the substructure through the combined effects of molecular diffusion and convective flow. Of all the remediation methods, active soil ventilation systems seem to be the best in terms of highest performance/cost ratio. The effects of soil moisture on the radon emanation and transport, and the importance of permeability of subsurface material on soil gas radon, needs more study. The predictive capability of the radon concentration derived from soil gas by diffusive and convective transport needs to be improved by conducting more studies. Post remediation, it is recommended to monitor indoor radon levels periodically once in every 5 years to ensure that radon concentrations remain at acceptable level. Although the indoor $PAEC_{212}$ level is comparable to outdoor $PAEC_{222}$ level, indoor ^{220}Rn series concentrations are less significant compared to outdoor ^{222}Rn concentrations. A better understanding of the behavior of ^{220}Rn series is useful and could even serve as a tool to understand fully the mechanisms of transport of radon into the indoor environment. Under typical indoor exposure conditions, the dose due to thoron decay products is about one order of magnitude less than that from radon decay products. However, special circumstances have been identified where thoron-dose contributions can exceed that from radon and more research needs to be conducted in identifying those situations.

References

Biological Effects of Ionizing Radiation IV Report (Committee on the Biological Effects of Ionizing Radiation) (1988) Health Effects of Radon and Other Internally Deposited Alpha-Emitters. BEIR, National Academy of Sciences, Washington
Biological Effects of Ionizing Radiation VI Report (1999) Health effects of exposure to indoor radon. BEIR, National Academy Press, Washington D.C.
Bowles JE (1979) Physical and geotechnical properties of soils. McGraw-Hill, New York, p 213

Crozier WD (1969) Direct measurements of radon-220 (thoron) exhalation from the ground. J Geophys Res 74:4199. doi:10.1029/JB074i017p04199

Darby S, Hill D, Auvinen A et al. (2005) Radon in homes and risk of lung cancer: collaborative analysis of individual data from 13 European case-control studies. BMJ 330(7485):223–226. doi:10.1136/bmj.38308.477650.63

Gammage R, Wilson D (1990) Performance experience with radon mitigation systems. In: The Fifth International Conference on Indoor Air Quality and Climate, Toronto

Gunning C, Scott AG (1982) Radon and thoron daughters in housing. Health Phys 42:527–528

Henschel DB (1988) Radon reduction techniques for detached houses: technical guidance, 2nd edn. EPA/625/5-87/019 (NTIS PB88-184908), January 1988

James AC (1988) Lung dosimetry. In: Nazaroff WW, Nero AV (eds) Radon and its decay products in indoor air. Wiley (1992, Ch. 259–310)

Mowris RJ, Fisk WJ (1988) Modeling the effects of exhaust ventilation on 222Rn entry rates and indoor 222Rn concentrations. Health Phys 54:491–501

Nazaroff WW (1992) Radon transport from soil to air. Rev Geophys 30(2):137–160

Nazaroff WW, Feustel H, Nero AV, Revzan KL, Grimsrud DT, Essling MA, Toohey RE (1985) Radon transport into a detached one-story house with a basement. Atmos Environ 19:31–46

Nazaroff WW, Moed BA, Sextro RG (1992) Soil as a source of indoor radon: generation, migration and entry. In: Nazaroff WW, Nero AV (eds) Radon and its decay products in Indoor Air. Wiley (1992, Ch. 257–112)

Nero AV, Lowder WM (1983) Special issue—Indoor Radon—preface. Health Phys 45(2):273–275

Nero AV, Nazaroff WW (1984) Characterizing the source of radon indoors. Radlat. Prot. Dosim. 7:23–39

Nero AV, Schwehr MB, Nazaroff WW, Revzan KL (1986) Distribution of airborne radon-222 concentrations in U.S. homes. Science 234:992–997

Nero AV, Gadgil AJ, Nazaroff WW, Revzan KL (1990) Indoor radon and decay products: concentrations, causes and control strategies, Tech. Rep. DOE/ER-0480P, 138 pp, U.S. Dep. Of Energy, Washington, D.C.

Rahman NM, Tracy BL (2009) Radon control systems in exisiting and new construction: a review. Radiat. Prot. Dosimetry 135(4):243–255. doi:10.1093/rpd/ncp112. Epub 2009 Jul 21

Schery SD (1985) Measurements of airborne 212Pb and 220Rn concentrations at varied indoor locations within the United States. Health Phys 49:1061–1067

Scott AG (1992) Preventing radon entry. In: Nazaroff WW, Nero AV (eds) Radon and its decay products in Indoor Air. Wiley (1992, Ch. 10, 407–433)

Toth A (1984) A simple field method for determination of 220Rn and 222Rn daughter energy concentrations in room air. Radiat Prot Dosim 7:247–250

UNSCEAR (United Nations Scientific Committee on the Effects of Atomic Radiation) (2000) Sources and Effects of Ionizing Radiation. UNSCEAR 2000 Report to the General Assembly, with Scientific Annexes. UNSCEAR, United Nations, New York

USEPA (United States Environmental Protection Agency) (1993) Radon reduction techniques for existing detached homes. Technical Guidance for Active Soil Depressurization systems. EPA/625/R-93–011, October 1993

USEPA (United States Environmental Protection Agency) (2003) Radon report 2003: USEPA Publication 402-R-03-003, (http://www.epa.gov/radon)

WHO (World Health Organization) (2005) Guidelines for drinking-water quality, 3rd edn. WHO, Geneva

WHO (World Health Organization) (2007) Effective Media Communication during Public Health Emergencies. WHO, Geneva

WHO (World Health Organization) (2009) WHO handbook on indoor radon—a public health perspective. In: Hajo Z, Ferid S (eds)

Wilkening MH, Clements WE, Stanley D (1972) Radon-222 flux measurements in widely separated regions. In: Adams JAS, Lowder WM, Gesell TF (eds) Proceedings natural radiation environment II, Conf-720805, U.S. Dept. of Commerce, National Technical Information Service, Springfield, VA, p 717

Wedepohl KH (1995) The composition of the continental crust. Geochim Cosmochim Acta 59:1217–1232

Index